Republic of Iraq
Ministry of Higher Education and Scientific Research
Middle Technical University
Engineering Technical College- Baghdad

Evaluation of hybrid Cooling System Models for Battery Pack of Electric Vehicle under Hot Zones Conditions

A Dissertation Submitted to
the Council of the Engineering Technical
College-Baghdad in a Partial Fulfillment
of the Requirements for the Degree of
Doctor of Philosophy (Ph.D.) in Thermal Engineering

By
Hareth Maher Abd
BSc 2004
MSc 2012

Supervisor	Supervisor
Dr. Ahmed J. Hamad	**Dr. Abdul Hadi N. Khalifa**
Professor	**Professor**

December 2024 Jumada al-Akhirah 1446

بِسْمِ اللَّهِ الرَّحْمَٰنِ الرَّحِيمِ

﴿ يَا أَيُّهَا الَّذِينَ آمَنُوا إِذَا قِيلَ لَكُمْ تَفَسَّحُوا فِي
الْمَجَالِسِ فَافْسَحُوا يَفْسَحِ اللَّهُ لَكُمْ وَإِذَا قِيلَ
انْشُزُوا فَانْشُزُوا يَرْفَعِ اللَّهُ الَّذِينَ آمَنُوا مِنْكُمْ
وَالَّذِينَ أُوتُوا الْعِلْمَ دَرَجَاتٍ وَاللَّهُ بِمَا تَعْمَلُونَ
خَبِيرٌ ﴿11﴾ ﴾

صدق الله العظيم

[سورة المجادلة]

Supervisors Certification

We certify that this dissertation was prepared under our supervision as a partial fulfillment of requirements for the degree of Doctor of Philosophy in Thermal Engineering Technology.

Signature:
Name: Dr. Ahmed J. Hamad
Title: Professor
(Supervisor)
Date: / / 2024

Signature:
Name: Dr. Abdul Hadi N. Khalifa
Title: Professor
(Supervisor)
Date: / / 2024

Linguistic Certification

I certify that I have read this dissertation entitled **"Evaluation of hybrid Cooling System models for Battery Pack of Electric Vehicle under Hot Zones Conditions"**, and I examined the language of the dissertation in my opinion, it is adequate as a dissertation for a degree Doctor of Philosophy in Thermal Engineering Technology.

Signature:
Name: Dr. Ammar A. Hussain
Title: Professor
Date: / / 2024

Signature:
Name: Dr. Haidar A. Hussein
Title: Assistant Professor
Head of Engineering Power Mechanics Department
Date: / / 2024

In view of the available recommendation, I forward this dissertation for debating by the examining committee.

Signature:
Name: Dr. Sabah Khammass Hussein
Title: Professor
(Deputy Dean for Scientific Affairs, Students and Postgraduates Studies)
Date: / / 2024

<u>**Certification**</u>

We are the members of the Examining Committee certify that after reading this dissertation, **"Evaluation of hybrid Cooling System models for Battery Pack of Electric Vehicle under Hot Zones Conditions"** and examining the student **"Hareth Maher Abd"** in its contents. We think it is adequate for the award of the *Doctor of Philosophy in Thermal Engineering Technology.*

Signature: John
Name: Dr. Johain Jawdet Faraj
Title: Assistant Professor
(Member)
Date: / / 2024

Signature:
Name: Salah H. Abid Aun
Title: Assistant Professor
(Member)
Date: / / 2024

Signature: Safaa
Name: Dr. Safaa Abdulwahid Ghadhban
Title: Assistant Professor
(Member)
Date: 29/12/2024

Signature:
Name: Dr. Kadhum Audaa Jehhef
Title: Assistant Professor
(Member)
Date: 29/12/2024

Signature:
Name: Dr. Salah Sabeeh Abed Alkareem
Title: Professor
(Chairman)
Date: 29/12/2024

Signature:
Name: Dr. Ahmed J. Hamad
Title: Professor
(Supervisor)
Date: / / 2024

Signature:
Name: Dr. Abdul Hadi N. Khalifa
Title: Professor
(Supervisor)
Date: / / 2024

Signature:
Name: Dr. Nabil Jamil Yasin
Title: Professor
(Dean)
Date: 30/12/2024

Dedication

To My Homeland

To My Family

To My Supervisors

To My Teachers

To My friends

With Respect

Hareth Maher Abd

2024

ACKNOWLEDGMENTS

Praise be to God, who gave me the opportunities, ability, health, strength, and perseverance to complete this thesis.

I would like to express my great appreciation to my supervisors, "***Prof. Dr. Ahmad Jassim Alhamad and Prof. Dr. Abdul Hadi N. Khalifa***" for their scientific guidance, kind advice, continuous follow-up, and encouragement throughout the research period and writing of this thesis.

Special thanks go to my teachers in the faculty for being such a supportive group, especially ***Assist. Prof. Dr. Johain J. Faraj, Dr. Asim Sahib Alawy, Dr. Ahmed Qassim Mohammed, Prof. Dr. Ammar A. Hussain*** *and* ***Prof. Dr. Hani Aziz Ameen.***

Also, I would like to thank the deanship, professors, and staff of my college of Engineering Technical / Mosul for the support they provided me during the study period.

I am thankful to my parents, my brothers, and my friends for always supporting me, guiding me, and pushing me to do my best in life. And my most enormous thanks to my family for all the support you have shown me through this research. Thanks to my devoted wife, for all your support. My appreciation also goes out to my friends for their encouragement and support throughout my studies.

Hareth Maher Abd

2024

List of Contents

Chapter One: Introduction

Section	Subjects	Page
1.1	Background	1
1.2	Li-ion Batteries	1
1.2.1	lithium-ion Battery Structure	2
1.2.2	lithium-ion Battery Operation	3
1.2.3	Geometrical Types of Lithium-ion Batteries	4
1.2.4	Temperature Effectiveness and Thermal Runaway	5
1.3	Battery Thermal Management System Types	7
1.3.1	Air-cooling system	8
1.3.2	Liquid cooling system	9
1.3.3	Heat pipe cooling system	9
1.3.4	Phase change material for cooling system	11
1.3.5	Compound cooling system	13
1.4	Motivations	14
1.5	Objectives of the Current Work	15

Chapter Two: Literature Review

Section	Subjects	Page
2.1	Introduction	16
2.1.1	Air cooling system studies	16
2.1.2	Liquid cooling system studies	18
2.1.3	heat pipe cooling system studies	19
2.1.4	Phase change material cooling system studies	23
2.1.5	Compound cooling system studies	28

2.2	Conclusions Obtained from Previous Research	34
2.3	Scope and Originality of the Current Work	36

Chapter Three: Numerical Simulation

Section	Subjects	Page
3.1	Introduction	38
3.2	Battery Pack Cooling Models	38
3.2.1	Air-Model	38
3.2.2	PCM-Model	40
3.3.3	PCM/Fin-Air-Model	41
3.3.4	HP-Model	43
3.3.5	HP/PCM-Model	44
3.4	Assumptions	45
3.5	Governing Equations	46
3.6	Initial Conditions and Boundary	51
3.7	Grid Independence	56

Chapter Four: Experimental Work

Section	Subjects	Page
4.1	Introduction	63
4.2	Test Rig	64
4.2.1	Air-Model	66
4.2.2	PCM-Model	68
4.2.3	PCM/Fin-Air-Model	69
4.2.4	HP-Model and HP/PCM-Model	70
4.3	Battery Heat Generation	74
4.4	HP Thermal Resistance Behavior	75

4.5	Measurement Devices and Complementary Instruments	75
4.5.1	Battery discharge electronic load tester	75
4.5.2	Adjustable DC power supply	76
4.5.3	Temperature measurement	77
4.5.4	Vacuum pump	77
4.5.5	Airflow and pressure drops measurement	78
4.5.6	Battery electric internal resistance measurement	79
4.6	Experimental Procedures	79
4.7	Uncertainty Analysis	81

Chapter Five: Results and Discussion

Section	Subjects	Page
5.1	Introduction	83
5.2	Experimental Results	83
5.2.1	Thermal performance of the Air-Model under various u_{in} and C-rates	84
5.2.2	Thermal performance of the PCM-Model under various C-rates	85
5.2.3	Thermal performance of the PCM/Fin-Air-Model under various u_{in} and C-rates	86
5.2.4	Thermal performance of the HP-Model under various u_{in} and C-rates	88
5.2.5	Thermal performance of the HP/PCM-Model under various u_{in} and C-rates	89
5.2.6	Effectiveness of the present hybrid models compared with other models	90

5.2.7	Effect of C-rates on the battery pack discharge voltage and T_{max}	94
5.2.8	Battery heat generation	95
5.2.9	HP thermal resistance behavior	96
5.2.10	Pressure drops and power consumption	98
5.2.11	Experimental results comparison with the previous study	100
5.3	Numerical Results	101
5.3.1	Effect of T_{in} variation on the T_{max} using the Air-Model	101
5.3.2	Effect of u_{in} variation on the T_{max} and ΔT_{max} using the Air-Model	102
5.3.3	Effect of u_{in} variation on the ΔP using the Air-Model	105
5.3.4	Effect of T_{amb} variation on the T_{max} and the PCM liquid fraction using the PCM-Model	107
5.3.5	Effect of T_{amb} variation on the temperature distribution using the PCM-Model	112
5.3.6	Effect of T_{in} variation on the T_{max} using the PCM/Fin-Air-Model	113
5.3.7	Effect of u_{in} variation on the temperature distribution using the PCM/Fin-Air-Model	115
5.3.8	Effect of u_{in} variation on the PCM liquid fraction using the PCM/Fin-Air-Model	118
5.3.9	Effect of u_{in} variation on the ΔP using the PCM/Fin-Air-Model	121
5.3.10	Effect of T_{in} variation on the T_{max} using the HP-Model	123
5.3.11	Effect of u_{in} variation on the T_{max} and ΔT_{max} using the HP-Model	124
5.3.12	Effect of u_{in} variation on the Δp using the HP-Model	127

5.3.13	Effect of T_{in} variation on the T_{max} using the HP/PCM-Model	128
5.3.14	Effect of u_{in} variation on the T_{max} and ΔT_{max} using the HP/PCM-Model	129
5.3.15	Effect of u_{in} variation on the PCM liquid fraction and temperature distribution using the HP/PCM-Model	132
5.3.16	Numerical results comparison with the previous studies	136
5.4	Numerical and Experimental Results Validation	136

Chapter Six: Conclusions and Recommendations

Section	Subjects	Page
6.1	Conclusions	138
6.2	Recommendations for Future Work	139

References

Section	Subjects	Page
-	References	141

List of Figures

Figure	Title	Page
1.1	Specific power and specific energy of various battery kinds [3].	2
1.2	Schematic of the one-dimensional electrochemical process of Li-ion battery [6].	3
1.3	Internal structure of the cylindrical Li-ion battery module [10].	4
1.4	Internal structure of different types of battery, (A) cylindrical battery (B) coin battery (C) prismatic battery (D) pouch battery [11].	5
1.5	Thermal runaway process [20].	7

1.6	Battery air-cooling system in Toyota Prius [26].	8
1.7	Liquid battery cooling (A) Tesla liquid tube cooling [30] (B) Chevrolet Spark liquid cooling plates [26].	9
1.8	Heat pipe structure [34].	10
1.9	Schematic diagram of the PCM's Phase Change transition	11
1.10	PCM cooling system [36].	12
1.11	Generalized categories of phase change materials (PCMs) [37].	12
1.12	Compound cooling system (A) PCM and active air-cooling combinations system [44], (B) PCM and liquid cooling combinations system [16].	14
3.1	Schematic diagram of the battery pack of Air-Model	39
3.2	Schematic diagram of the battery pack of PCM-Model	40
3.3	Schematic of the battery pack PCM/Fin-Air model. (A) Top view of the complete model, (B) top view of a selected row, and (C) 3D view of the selected row.	42
3.4	Schematic diagram of the HP-Model	44
3.5	Schematic diagram of the HP/PCM-Model	45
3.6	Boundary conditions of (A) Air-Model, (B) PCM-Model, (C) PCM/Fin-Air-Model, (D) HP-Model, and (E) HP/PCM-Model.	55
3.7	Variation of the T_{max} with the mesh numbers of (A) Air-Model, (B) PCM-Model, (C) PCM/Fin-Air-Model, (D) HP-Model, and (E) HP/PCM-Model.	58

3.8	Meshing structure of (A) Air-Model, (B) PCM-Model, (C) PCM/Fin-Air-Model, (D) HP-Model, and (E) HP/PCM-Model.	61
3.9	Flow chart of the numerical solution	62
4.1	Schematic diagram of the experimental system.	65
4.2	Photograph of the test rig**.**	65
4.3	Photograph of Type-I air duct with PCM/Fin-Air-Model	66
4.4	Photograph of Type-II air duct with HP/PCM-Model	66
4.5	Schematic diagram of the Air-Model (A) Top view (B) Front view. (dimensions unit are in mm).	67
4.6	Photograph of the Air-Model.	67
4.7	PCM-Model test section with temperature sensor location (A) Schematic diagram (B) Photograph (All dimensions are in mm).	68
4.8	PCM/Fin-Air-Model schematic drawing (A) Top view (B) Front view (dimensions unit are in mm).	69
4.9	Photograph of PCM/Fin-Air-Model.	70
4.10	Photograph of the HP-Model: (A) copper tube of the HP, (B) fins, (C) HP after fabrication, and (D) HP with Li-ion battery connections.	72
4.11	Schematic diagram of the HP/PCM-Model and temperature sensor location (A) front view (B) side view (C) top view (D) bottom view (F) HP evaporator cross-section. (All dimensions are in mm).	73
4.12	Electronic Load Tester	76
4.13	Adjustable DC power supply	76

4.14	Multi-channel temperature meter	77
4.15	Vacuum pump	78
4.16	Digital pitot tube	78
4.17	Battery internal resistance measurement device	79
5.1	Variation of (A) T_{max} and (B) ΔT_{max}, under various u_{in} and C-rates at T_{in} of 40 °C using the Air-Model.	85
5.2	Variation of (A) T_{max} and (B) ΔT_{max}, under various C-rates at T_{amb} of 40 °C using the PCM-Model.	86
5.3	Variation of (A) T_{max} and (B) ΔT_{max}, under various u_{in} and C-rates at T_{in} of 40 °C using the PCM/Fin-Air-Model.	88
5.4	Variation of (A) T_{max} and (B) ΔT_{max}, under various u_{in} and C-rates at T_{in} of 40°C using the HP-Model.	89
5.5	Variation of (A) T_{max} and (B) ΔT_{max}, under various u_{in} and C-rates at T_{in} of 40°C using the HP/PCM-Model.	90
5.6	Variation of T_{max} and ΔT_{max} under various C-rates at T_{in} of 40°C and $u_{in} = 1.5\ m/s$ using five models, (A) T_{max} under 1C, (B) ΔT_{max}under 1C (C) T_{max} under 2C, (D) ΔT_{max}under 2C, (E) T_{max} under 3C, (F) ΔT_{max}under 3C	92
5.7	Largest value of (A) T_{max} and (B) ΔT_{max}, using five models at various u_{in} and C-rates.	93
5.8	Battery discharge voltage and T_{max} at T_{in} of 40 °C and various C-rates using the PCM/HP-Model.	95
5.9	Battery heat generation rates under various C-rates at T_{in} of 40°C using the Air-Model	96
5.10	Variation of (A) R_{th}, Q_{HP} and (B) ΔT_{HP} for HP, at various C-rates at T_{in} of 40°C using the HP-Model.	97

5.11	Comparison of (A) HP-Model against Liu et al. [48] and (B) PCM/Fin-Air-Model against Qin et al. [77].	100
5.12	Variation of the T_{max} using the Air-Model at u_{in} of 0.75 m/s under various C-rates and T_{in} of (A) T_{in}=25 ºC (B) T_{in}= 30 ºC (C) T_{in}= 35 ºC (D) T_{in}= 40 ºC.	102
5.13	Variation of T_{max} and ΔT_{max} using the Air-Model at T_{in} of 40°C, under various u_{in} and C-rates. (A) T_{max} at 2C, (B) ΔT_{max} at 2C, (C) T_{max} at 3C, (D) ΔT_{max} at 3C.	104
5.14	Temperature distribution contours for the Air-Model at the end of the discharge period under 3C rate and T_{in} of 40°C with various $u_{in}$of (A) $u_{in} = 0.75\, m/s$ (B) $u_{in} = 1.5\, m/s$ (C) $u_{in} = 2.25\, m/s$ (D) $u_{in} = 3\, m/s$.	105
5.15	Pressure distribution contour for the Air-Model with various $u_{in}$of (A) $u_{in} = 0.75\, m/s$ (B) $u_{in} = 1.5\, m/s$ (C) $u_{in} = 2.25\, m/s$ (D) $u_{in} = 3\, m/s$.	106
5.16	Variation of T_{max} using the PCM-Model under various C-rates and T_{amb} of (A) $T_{amb} = 25$ ℃, (B) $T_{amb} = 30$ ℃, (C) $T_{amb} = 35$ ℃, (D) $T_{amb} = 40$ ℃.	108
5.17	Variation of the average liquid fraction using the PCM model under various T_{amb} and C-rates of (A) 2C and (B) 3C.	109
5.18	PCM liquid fraction contours for the PCM-Model at the end of the discharge period under 2C rate with various T_{amb} of (A) $T_{amb} = 25$ ℃, (B) $T_{amb} = 30$ ℃, (C) $T_{amb} = 35$ ℃, (D) $T_{amb} = 40$ ℃.	110
5.19	PCM liquid fraction contours for the PCM-Model at the end of the discharge period under 3C rate with various T_{amb} of (A)	111

	$T_{amb} = 25$ °C, (B) $T_{amb} = 30$ °C, (C) $T_{amb} = 35$ °C, (D) $T_{amb} = 40$ °C.	
5.20	Variation of ΔT_{max} using the PCM-Model under various T_{amb} and C-rates of (A) 2C and (B) 3C.	112
5.21	Temperature distribution contours for the PCM-Model at the end of the discharge period under 3C rate with various T_{amb} of (A) $T_{amb} = 25$ °C, (B) $T_{amb} = 30$ °C, (C) $T_{amb} = 35$ °C, (D) $T_{amb} = 40$ °C.	113
5.22	Variation of T_{max} using the PCM/Fin-Air-Model at u_{in} of 0.75 m/s and various C-rates under (A) $T_{in} = 25$ °C, (B) $T_{in} = 30$ °C, (C) $T_{in} = 35$ °C, (D) $T_{in} = 40$ °C.	115
5.23	Variation of (A) T_{max} and (B) ΔT_{max}, at 3C rate and T_{in} of 40 °C under various u_{in} using the PCM/Fin-Air-Model.	116
5.24	Temperature distribution contours for the PCM/Fin-Air-Model at the end of the discharge period under 3C rate and T_{in} of 40°C with various $u_{in}$of (A) $u_{in} = 0.75\ m/s$ (B) $u_{in} = 1.5\ m/s$ (C) $u_{in} = 2.25\ m/s$ (D) $u_{in} = 3\ m/s$.	117
5.25	Variation of the average liquid fraction using the PCM/Fin-Air-Model at T_{in} of 40 °C under various u_{in} and C-rates of (A) 2C and (B) 3C.	118
5.26	PCM liquid fraction contours for the PCM/Fin-Air-Model at the end of the discharge period under 2C and T_{in} of 40 ºC with various u_{in} of (A) $u_{in} = 0.75\ m/s$, (B) $u_{in} = 1.5\ m/s$, (C) $u_{in} = 2.25\ m/s$, (D) $u_{in} = 3\ m/s$.	120
5.27	PCM liquid fraction contours for the PCM/Fin-Air-Model at the end of the discharge period under 3C and T_{in} of 40 ºC, with	121

	various u_{in} of (A) $u_{in} = 0.75\ m/s$, (B) $u_{in} = 1.5\ m/s$, (C) $u_{in} = 2.25\ m/s$, (D) $u_{in} = 3\ m/s$.	
5.28	Pressure distribution contours for PCM/Fin-Air-Model with various u_{in} of (A) u_{in}=0.75 m/s (B) u_{in}=1.5 m/s (C) u_{in}=2.25 m/s (D) u_{in}=3 m/s.	122
5.29	Variation of T_{max} using the HP-Model at u_{in} of 0.75 m/s and various C-rates for (A) $T_{in} = 25$ ℃, (B) $T_{in} = 30$ ℃, (C) $T_{in} = 35$ ℃, (D) $T_{in} = 40$ ℃.	124
5.30	Variation of (A) T_{max} and (B) ΔT_{max}, at 3C rate and T_{in} of 40 °C under various u_{in} using the HP-Model.	125
5.31	Temperature distribution contours for the HP-Model at the end of the discharge period under 3C and T_{in} of 40 ºC with various u_{in} of (A) u_{in}=0.75 m/s (B) u_{in}=1.5 m/s (C) u_{in}=2.25 m/s (D) u_{in}=3 m/s.	126
5.32	Pressure distribution contours for HP-Model with various $u_{in}$of (A) $u_{in} = 0.75\ m/s$, (B) $u_{in} = 1.5\ m/s$, (C) $u_{in} = 2.25\ m/s$, (D) $u_{in} = 3\ m/s$.	128
5.33	Variation of T_{max} using the HP/PCM-Model at u_{in} of 0.75 m/s and various C-rates under (A) T_{in}=25 ºC (B) T_{in}= 30 ºC (C) T_{in}= 35 ºC (D) T_{in}= 40 ºC.	129
5.34	Variation of (A) T_{max} and (B) ΔT_{max}, at 3C rate and T_{in} of 40 °C under various u_{in} using the HP/PCM-Model.	130
5.35	Temperature distribution contours for the HP/PCM-Model at the end of the discharge period under 3C and T_{in} of 40 ºC, and various u_{in} of (A) $u_{in} = 0.75\ m/s$, (B) $u_{in} = 1.5\ m/s$, (C) $u_{in} = 2.25\ m/s$, (D) $u_{in} = 3\ m/s$.	131

5.36	Variation of the average liquid fraction using the HP/PCM-Model at T_{in} of 40 °C under various u_{in} and C-rates of (A) 2C and (B) 3C.	132
5.37	PCM liquid fraction contours for the HP/PCM-Model at the end of the discharge period under 2C and T_{in} of 40 ºC, and various u_{in} of (A) $u_{in} = 0.75\ m/s$, (B) $u_{in} = 1.5\ m/s$, (C) $u_{in} = 2.25\ m/s$, (D) $u_{in} = 3\ m/s$	134
5.38	PCM liquid fraction contours for the HP/PCM-Model at the end of the discharge period under 3C and T_{in} of 40 ºC, and various u_{in} of (A) $u_{in} = 0.75\ m/s$, (B) $u_{in} = 1.5\ m/s$, (C) $u_{in} = 2.25\ m/s$, (D) $u_{in} = 3\ m/s$.	135
5.39	Comparison of (A) HP/PCM-Model against Sutheesh et al. [97] and (B) PCM/Fin-Air-Model against Kavasogullari et al. [44].	136
5.40	Comparison of T_{max} variation with time between the experimental and numerical results for (A) Air-Model, (B) PCM-Model, (C) PCM/Fin-Air-Model (D) HP-Model (E) HP/PCM-Model.	137

List of Tables

Table	Title	Page
1.1	Li-ion battery properties of common cathode kind [9].	3
2.1	Summary of previous studies.	34
3.1	Thermo-physical properties of the battery [88, 89].	39
3.2	Thermo-physical properties of the PCM (RT47).	41
3.3	The values of the Reynolds number for each model.	50

3.4	Mesh independence number of different models.	61
4.1	Specifications for Li-ion batteries type 18650-type $LiCoO_2$ [88].	64
4.2	Thermo-physical properties of the acetone [93].	74
4.3	Discharge rates and equivalent current values.	80
4.4	Device's precisions.	81
5.1	Measured and evaluated parameters at various u_{in} and C-rates using five cooling models.	99

List of Appendices

Section	Subjects	Page
A.1	Thermocouples Calibrations	A-1
A.2	Pressure and Velocity Device Calibration	A-3
B.1	PCM Data Sheet	B-1
C.1	Calculation of the Uncertainty	C-1

List of Symbols

Symbol	Definition	Unit
A	Area	m^2
c_p	Specific heat	J/kg. K
C-rate	Discharge rate	C
D_h	Hydraulic diameter	m
H	Height	m
h	Convection heat transfer coefficient	W/ m^2. K
h_n	Natural heat transfer coefficient	W/ m^2. K
I	Current	Amp.
$\mathbf{I}$	Unit diagonal matrix	-
k	Turbulent kinetic energy	m^2/s^2

k	Thermal conductivity	W/ m. K
L	Latent heat	kJ/kg
m	Mass	kg
$\dot{m}$	Mass flowrate	kg/s
P_{fan}	Fan power consumption	W
P	Pressure	Pa
Q	heat transfer rate	W
$\dot{Q}_{gen}$	Volumetric heat generation	W/m^3
R_{th}	Thermal resistance	K/W
R	Electric Resistance	Ω
S_t	Traverse separation	m
S_L	Longitudinal batteries separation	m
T	Temperature	°C
t	Time	s
$\mathbf{u}$	Velocity vector, $ui + vj + wk$	m/s
u	Air velocity	m/sec
V_d	Discharge voltage	V
V_o	Open-circuit voltage	V
W	Width	m
w_y	Indirectly uncertainty	-
w_{x_i}	Direct uncertainty	-
x_i	Directly measured parameter	-
y	Indirectly measured parameter	-

List of Greek letters

Greek letters	Definition	Unit
ρ	Density	kg/m^3
Δ	Difference	-
∇	Del or Nabila (gradient operator), $\frac{\partial}{\partial x}i + \frac{\partial}{\partial x}j + \frac{\partial}{\partial x}k$	-
∂	Partial differential operators	-
θ_l	Percentage of liquid in phase change material	-
θ_s	Percentage of solid in phase change material	-
μ	Dynamic viscosity	Pa. s
μ_{T}	Turbulent viscosity of fluid	Pa. s
ε	Turbulent Dissipation rate	m^2/s^3

List of Abbreviations

Abbreviations	Definition
$BTMS$	Battery Thermal Management System
EVs	Electric Vehicles
EG	Expanded Graphite
k-ε	k-epsilon model
Li-ion	Lithium-ion batteries
$LiCoO_2$	lithium Cobalt Oxides
$LiFePO_4$	lithium Iron Phosphate
$LiMn_2O_4$	lithium Manganese Oxides
PCM	Phase Change Materials
Re	Reynold number
SEI	Solid Electrolyte Interface

List of Subscripts

Subscripts	Definition
a	air
amb	ambient
Al	Aluminum
atm	atmospheric
b	battery
d	air duct
f	fin
gen	generation
HP	Heat Pipe
h	hydraulic
in	inlet
irr	irreversible
l	liquid
max	maximum
n	number
out	outlet
rev	reversible
s	solid

Abstract

The charges/discharges of Li-ion batteries generate excessive heat, especially at high charge/discharge rates, which represent the main barrier to Li-ion battery usage. Therefore, using an effective battery thermal management system is quite essential to ensure optimal operation of lithium-ion batteries. Furthermore, a hybrid cooling system from an active and passive cooling system can provide more temperature control and uniformly throughout the battery cell than solely a passive or active cooling system.

Therefore, in this study, an experimental and numerical investigation of two novel hybrid cooling systems using phase change material as a passive cooling system combined with other cooling systems is studied. The first cooling model (PCM/Fin-Air-Model), uses phase change material combined with aluminum fins and forced air. While the second model (HP/PCM-Model), uses a new model of flat heat pipes having a finned condenser and double circular grooved evaporator in addition to the usage of phase change material integration in the evaporator section. The HP was charged with acetone as a working fluid with 40 % filling ratio. Phase change material type Rubitherm-RT47 with a melting temperature range of 41-48 °C is selected. The present hybrid models are designed for cooling a battery pack consisting of 12 cylindrical batteries 18650-type $LiCoO_2$ arranged with three batteries in parallel and four batteries in series. The thermal performance of the novel models are compared with other conventional models of passive phase change material model (PCM-Model), forced air model (Air-Model), and the same heat pipe without the phase change material combination (HP-Model). All models are examined using various discharge rates (C-rate) of 1, 2, and 3C, and various inlet air velocities (u_{in}) of (0.75, 1.5, 2.25, and 3 m/s), and various operating temperatures (T_{in}) of (25, 30, 35 and 40 °C).

Numerical simulation is achieved using three-dimensional models built using COMSOL Multiphysics 5.6 and comprehensively validated with experiment results. The experimental results indicated that the novel hybrid models display a good cooling performance, especially at a high C-rate compared with the conventional models which became insufficient for battery cooling at a 3C. The PCM/HP-Model reduces the maximum operating temperature at 3C by 18.9, 26.6, and 9.8%, while the PCM/Fin-Air-Model reduces it by 15.2, 23.3, and 4.6%, compared to the Air-Model, PCM-Model and HP-Model, respectively. Furthermore, the largest maximum temperature difference for the PCM/HP-Model and PCM/Fin-Air-Model did not exceed 4.2 and 1.9 °C, respectively. Additionally, the HP/PCM-Model has the lowest pressure losses and fan power consumption (P_{fan}) than other models.

The numerical result shows that the increase of the air velocity has a slight effect on the battery cooling using the novel hybrid models while it has a significant effect on the battery cooling using Air-Model, where the T_{max} reduces by 5.3, 12.8 and 30 % as the u_{in} increases from 0.75 to 3 m/s for PCM/HP-Model, PCM/Fin-Air-Model, and Air-Model respectively. The increasing of u_{in} from 0.75 to 3 m/s reduces the PCM liquid fraction from 0.877 to 0.772 and from 1.0 to 0.748 at the end of the 3C rate period of the PCM/HP-Model and PCM/Fin-Air-Model, respectively. The usage of PCM-Model is not recommended for a 3C rate even at a low operation temperature of 25 °C.

Moreover, the result demonstrated that the HP/PCM-Model exhibits a better thermal performance and lower power consumption, especially at a high C-rate, as well as it can offer a safe working temperature for the Li-ion batteries.

The numerical results show good agreement with the experimental data, with maximum deviations of 3.8, 6, 2.3, 2, and 2.4% for the Air-Model, PCM-Model, PCM/Fin-Air-Model, HP-Model, and HP/PCM-Model, respectively.

Chapter One

Introduction

Chapter One

Introduction

1.1 Background

Lithium-ion batteries are widely used in many applications, such as electric vehicles, smartphones, and laptops, as well as consider a new way to store electrical energy from alternative energy sources, due to their high energy density, long cycle life, and reliability. However, their performance and safety are highly sensitive to operating temperature. When Li-ion batteries operate outside their optimal temperature range, problems such as reduced capacity, accelerated aging, and safety risks like thermal runaway can arise. This necessitates the need for a battery thermal management system to regulate the battery within the operating temperature. A well-designed BTMS ensures uniform temperature distribution, improves battery performance, extends its lifespan, and prevents both overheating and excessive cooling, making it an essential component for the safe, reliable, and efficient operation of Li-ion batteries.

1.2 Li-ion Batteries

Among all kinds of batteries, Li-ion batteries are the most popular because of their unique features comprising; the long cycle life, high voltage capability, fast charging/discharge rate, high specific power of more than 10000 W/kg, and high specific energy (70-170 Wh/kg) compared with other batteries for similar size and weight [1-3]. The specific power is the maximum available power divided by the battery mass, while the specific energy is the nominal battery energy per unit mass. Figure (1.1) demonstrates the relation between various types of batteries.

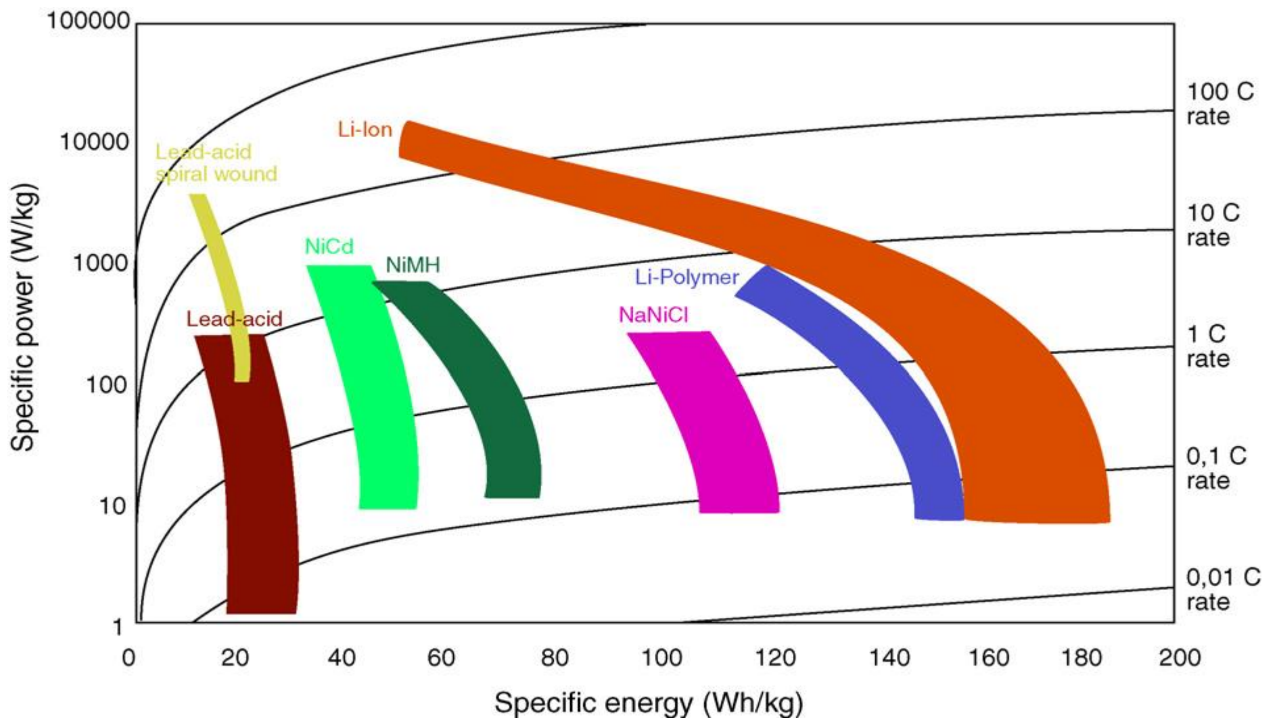

Figure (1.1) Specific power and specific energy of various battery kinds [3]**.**

1.2.1 Lithium-ion battery structure

Like most batteries, lithium-ion batteries consist of positive and negative electrodes separated by a liquid electrolyte, allowing the free passage of ions. In a typical modern lithium-ion battery, the negative terminal, or anode, is made of a carbon compound (usually graphite), and the cathode, or positive terminal, is made of a lithium-metal oxide compound, which determines the battery type [4, 5].

The popular materials used in cathode construction include; lithium manganese oxides ($LiMn_2O_4$), lithium cobalt oxides ($LiCoO_2$), and lithium iron phosphate ($LiFePO_4$). The electrolyte comprises complex lithium salts dissolved in a non-aqueous solvent [6-7]. The battery types of LiCoO2, $LiMn_2O_4$, $LiFePO_4$, and Lithium Nickel Manganese Cobalt Oxide ($LiNiMnCoO_2$) are considered the most common kinds of Li-ion batteries that are candidates to use for electric vehicles [8, 9]. The characteristics of various cathode materials are illustrated in Table (1.1).

Table (1.1) Li-ion battery properties of common cathode kind [9].

property	$LiCoO_2$	$LiNiO_2$	$LiMn_2O_4$	$LiFePO_4$
Practical capacity (Ah/kg)	150	170	120	155
Energy density (Wh/kg)	180	170	100	130
Nominal voltage (V)	3.7	3.5	4	3.3
Cycling capability (Cycles)	>500	>500	>500	>2000

1.2.2 lithium-ion battery operation

As the Li-ion battery discharges, the lithium atoms split into electrons and lithium ions in the anode. The Lithium ions go through the electrolyte from the anode to the cathode, whereas the electrons cannot pass through the electrolyte because the electricity insulation of the separator forms, which causes the electrons to move over the external circuit to the cathode. However, they move in the opposite direction during the charging process [6]. The schematic of the one-dimensional electrochemical process and the internal structure of the cylindrical lithium-ion battery model are shown in Figures (1.2) and (1.3), respectively.

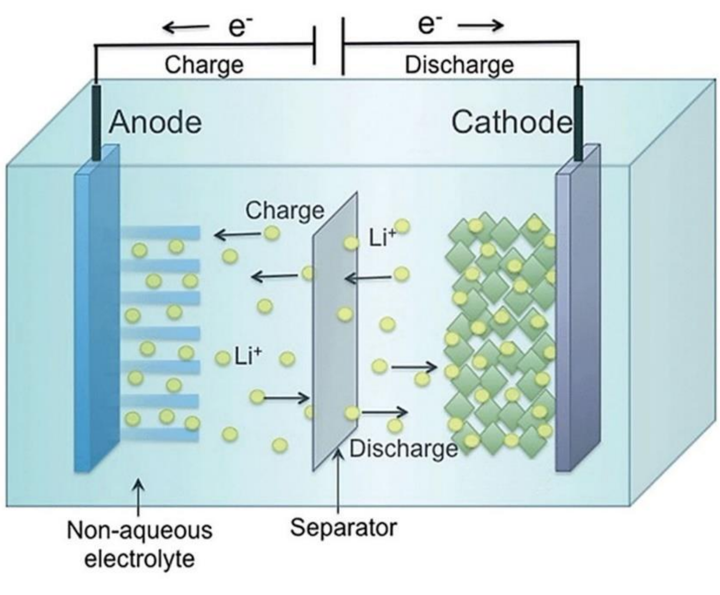

Figure (1.2) Schematic of the one-dimensional electrochemical process of Li-ion battery [6].

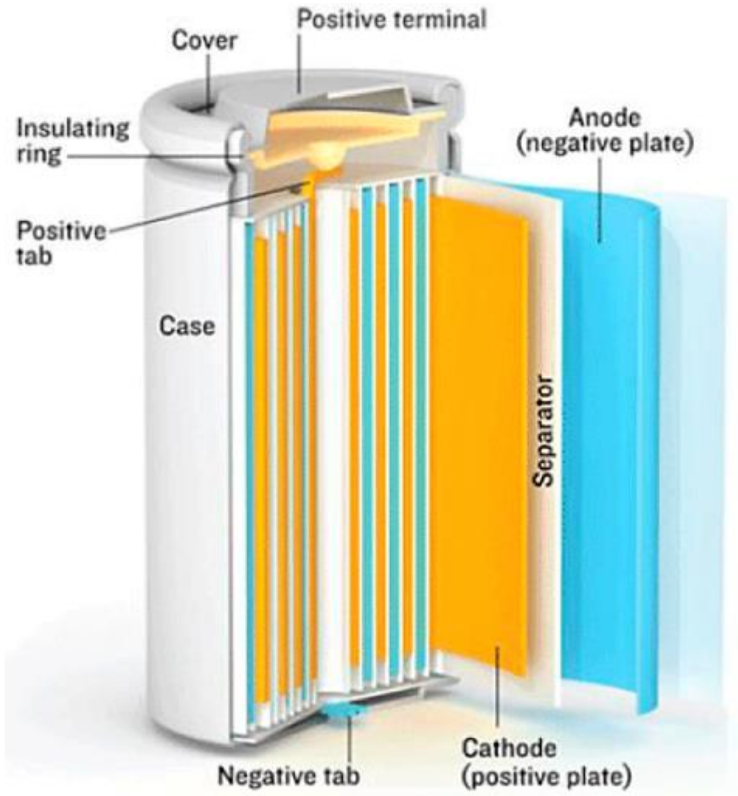

Figure (1.3) Internal structure of the cylindrical Li-ion battery module [10].

1.2.3 Geometrical types of Lithium-ion batteries

There are various configurations of lithium-ion batteries. Figures (1.4 A-D) show the interior layout of the different battery configurations. The cylindrical and prismatic batteries have multiple electrochemical cells within and are constructed from wound electrodes and separators submerged in electrolytes. The pouch battery has a flat design like the coin battery; however, it contains multiple electrochemical cells as opposed to the coin battery's single electrochemical cell. Since the positive and negative electrodes have a larger area, automotive applications frequently use cylindrical, prismatic, and pouch packaging [11].

The packaging chosen by the automaker depends on the battery's expected working conditions. For example, the Tesla Model S vehicle uses cylindrical batteries, and the Chevrolet Volt and Nissan Leaf vehicles use pouch batteries [12].

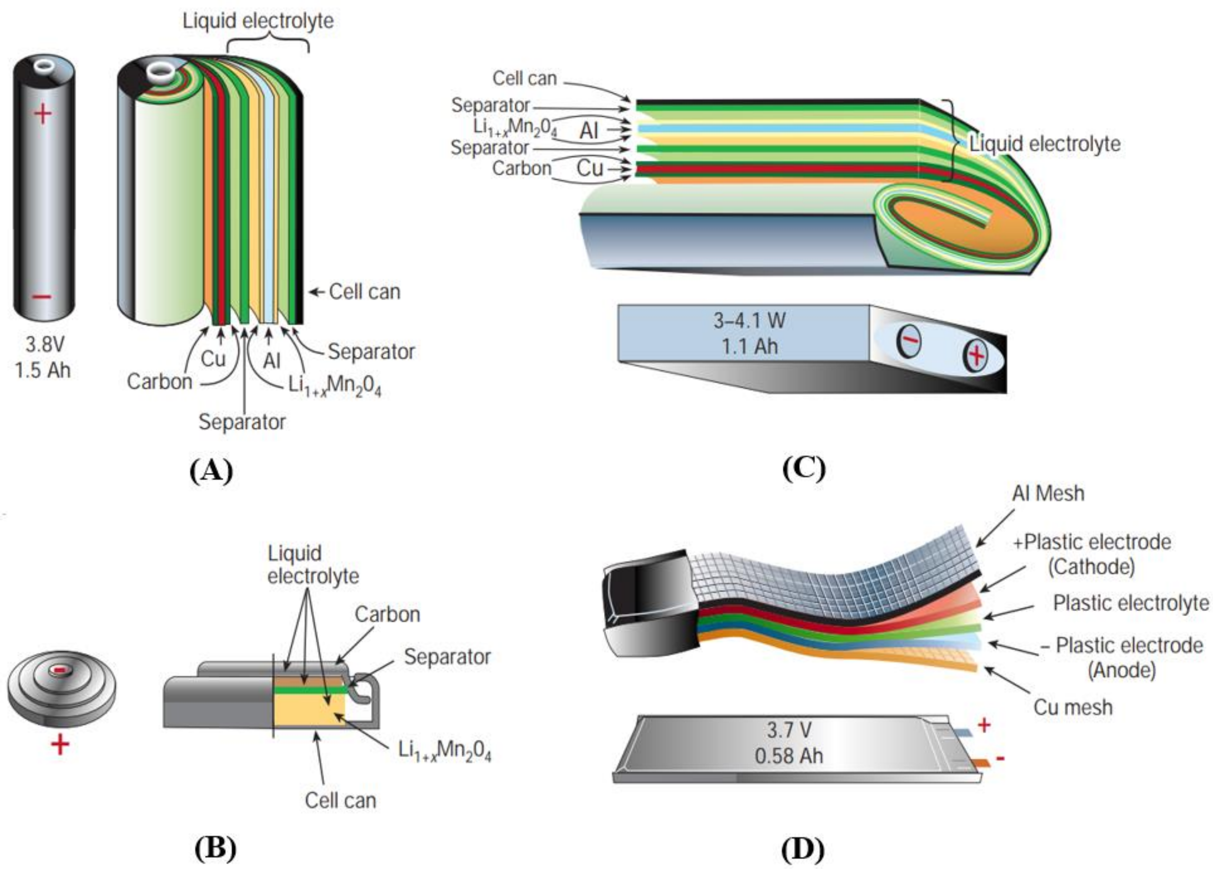

Figure (1.4) Internal structure of different types of battery, (A) cylindrical battery (B) coin battery (C) prismatic battery (D) pouch battery [11].

1.2.4 Temperature effectiveness and thermal runaway

Li-ion batteries generate excessive heat during charging and discharging operations because of electrochemical reactions, especially at high C-rates [13]. The C-rate represents the amount of charging/discharging power rate of the battery cell relative to its maximum capacity [14]. For example, if a battery has a capacity of 2,500 mAh, a 1C rate means charging or discharging at 2,500 mA, which will fully charge or discharge the battery in 1 hour. A 2C rate means charging or discharging at 5,000 mA, which will take 0.5 hours to fully charge or discharge, and so on.

Consequently, the battery surface temperature increases, and the temperature distribution becomes non-uniform in the battery pack representing the main barriers to Li-ion battery usage due to its impact on battery lifetime and vehicle safety. Generally, the acceptable range for the Li-ion battery's operation temperature is (−20 to 60 °C), while the high temperature in the battery cell leads to an elevation in the cell's internal resistance and an increase in the Li-ion battery degradation, which reduces the cell output power [1].

The safe and optimal operating temperatures for Li-ion batteries should range between 20 and 50 °C, and the maximum temperature variance in a battery pack should be kept within 5 °C, whereas the operation outside these ranges will negatively affect the lifetime and performance of the batteries [15-17]. Zadeh et al., 2022 [18] noted when the maximum temperature was limited to less than 45 °C, it leads to the slightest negative impression on the battery life through charge/discharge cycles, while the battery loses 70% of its capacity after 500 cycles at 55 °C. Furthermore, the cells that work at high temperatures have a higher loss capacity after each cycle in comparison with the cell that operates at low temperatures [14, 19].

However, Thermal runaway is started at around 90°C when the SEI decomposes. The SEI is a protection between the negative electrode and liquid electrolyte. With SEI destruction, the electrolyte and electrode would react with each other at around 100 °C and produce a lot of heat and gas. Consequently, this reaction will cause a greater increase in the temperature. When the battery's temperature exceeds 150 °C, the separator melts, and a chain reaction occurs leading to thermal runaway [20]. Figure (1.5) demonstrates the thermal runaway process.

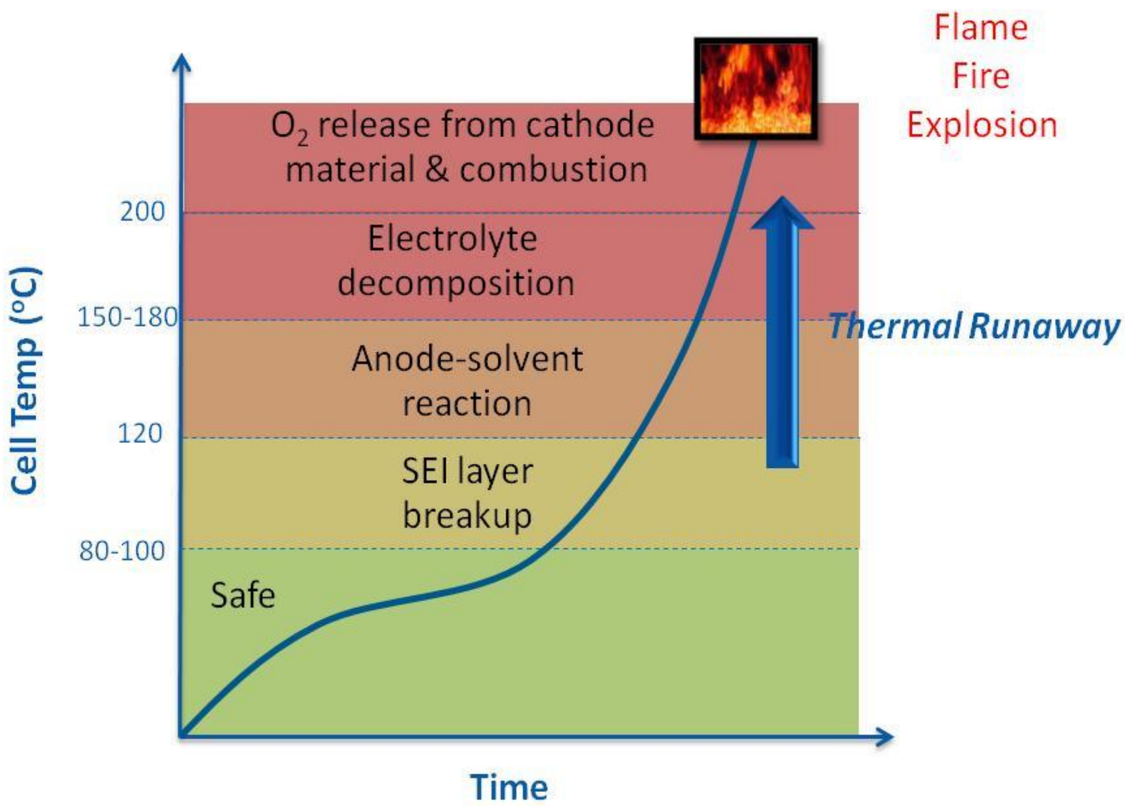

Figure (1.5) Thermal runaway process [20].

1.3 Battery Thermal Management System Types

As mentioned, the efficient BTMS is essential for electric vehicles to control the battery pack temperature with a safety operation limit during the charge/discharge process and reduce the degradation in the Li-ion battery's performance that occurs with increased temperatures. Furthermore, the accumulation of heat inside the battery pack without a sufficient dissipation mechanism will deteriorate the battery capacity or may lead to a thermal runaway that causes the battery explosion [21].

Based on the cooling mediums, there are currently five main types of cooling systems: air cooling, liquid cooling, heat pipe cooling, phase change cooling, and compound cooling systems [22]. These systems can be described as follows:

1.3.1 Air-cooling system

The main features of BTMS that use air-cooling systems are the lightweight, simple design, ease of maintenance, and direct access [23]. In addition, air-cooling systems are considered safer and more economical to install and control [24]. The air-cooling may be achieved either by forced convection or natural convection. Natural convection is not sufficient at high C-rates owing to the larger temperature increase [25]. The forced convection of the airflow is divided into a series flow cooling system and a parallel flow cooling system. In the series flow, the air flowing in a continuous channel is heated by the first cells, consequently leading to less ability to cool the other cells. In contrast, in the parallel flow, the airflow is split into several branches that require a highly accurate design of the air channels [20].

In contrast, air-cooling systems have some disadvantages like a low heat capacity and the difficulty of obtaining a uniform air distribution. These limit the use of this system, mainly when operating at high C-rates. However, they are employed in commercial vehicles like Toyota, Nissan, Mitsubishi, and Honda [26, 27]. Figure (1.6) shows the air-cooling structure used in the Toyota Prius car.

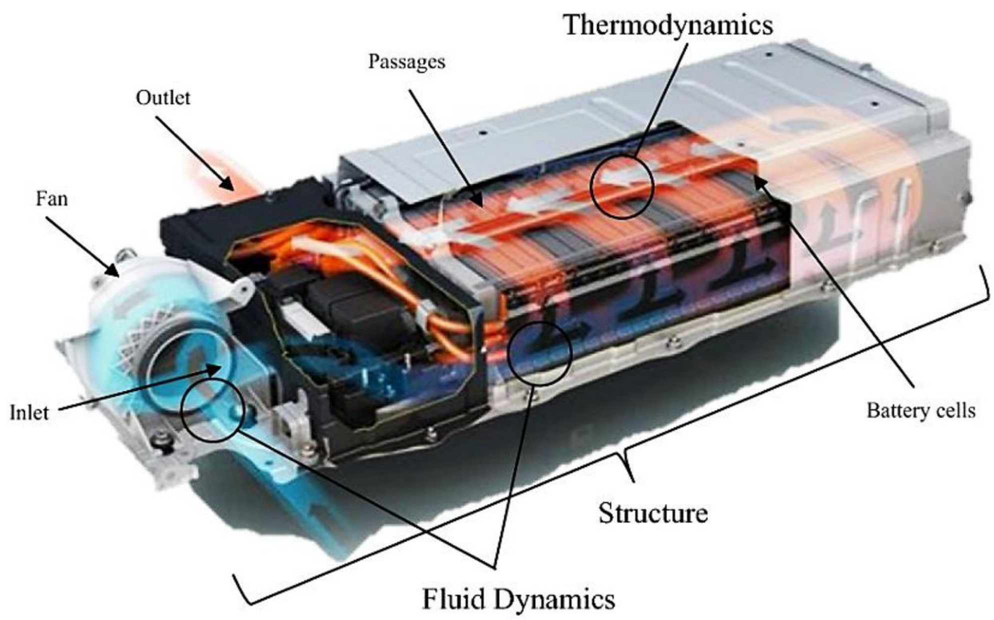

Figure (1.6) Battery air-cooling system in Toyota Prius [26].

1.3.2 Liquid cooling system

Liquid cooling for BTMS in electric vehicles has received significant attention due to its large thermal conductivity and specific heat capacity compared to air-cooling systems [28, 29]. In liquid cooling, the batteries may be cooled directly by submerging them in the coolant fluid or indirectly cooled using pipes or cooling plates like that is used in Tesla and General Motors [26, 30]. Figures (1.7 A and B) show the liquid cooling systems used in Tesla and Chevrolet Spark EV cars, respectively. However, the liquid cooling system has several disadvantages being overweight, adding complexity to the EV by requiring additional components such as pumps, radiators, hoses, and reservoirs, as well as, having a possibility risk of liquid leakage, pump maintenance, and liquid replacement, and it needs more power consumption for the water pump [27, 31].

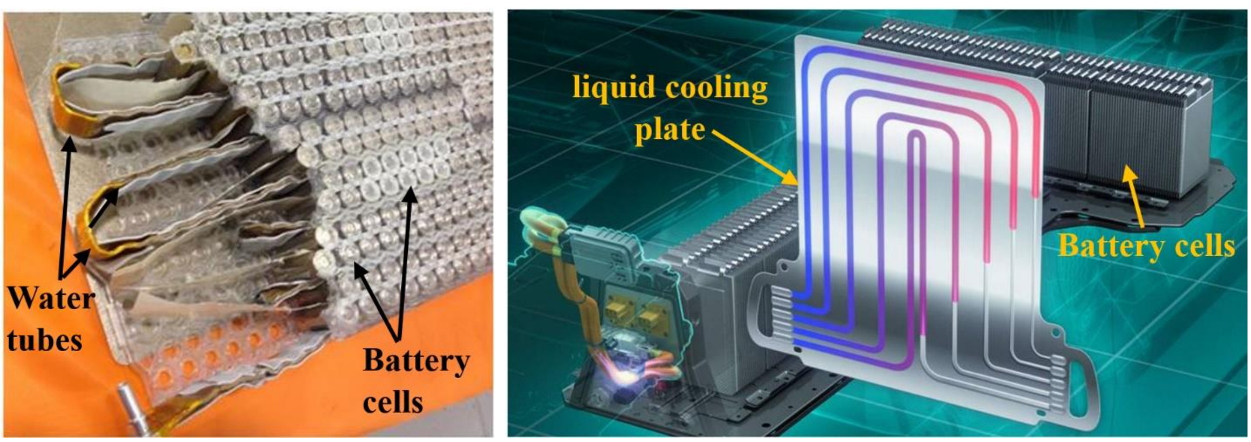

(A) **(B)**

Figure (1.7) Liquid battery cooling (A) Tesla liquid tube cooling [30] (B) Chevrolet Spark liquid cooling plates [26].

1.3.3 Heat pipe cooling system

Heat pipes (HPs) become one of the most effective technologies used in cooling systems. They are used in numerous cooling applications owing to their thermal super-conductor properties, minimal maintenance, low price, long lifespan, and passive design [14]. For these features, many researchers investigated using them in BTMS to regulate the temperature of battery pack cells.

They are manufactured usually from a copper tube with different shapes and types, depending on the available space, and working principle. They are filled with a certain amount of a working fluid that transfers the heat from the evaporator to the condenser sections. The HP has a large thermal conductivity due to the working fluid's latent heat of phase change [32, 33].

However, as the HP is heated in the evaporator section, the working fluid inside the HP absorbs heat and transforms into vapor form. Consequently, the pressure builds up, causing the vapor to flow into the condenser section, where the vapor condenses and releases heat to the surrounding air; then, the condensed fluid flows back to the evaporation section due to gravity or capillary action of the wick. Figure (1.8) shows the thermosyphon HP structure and heat flow. The working fluid's phase change depends on HP's vacuum pressure and the working fluid's saturation temperature [34]. Nonetheless, they haven't yet been used in BTMS of commercial EVs.

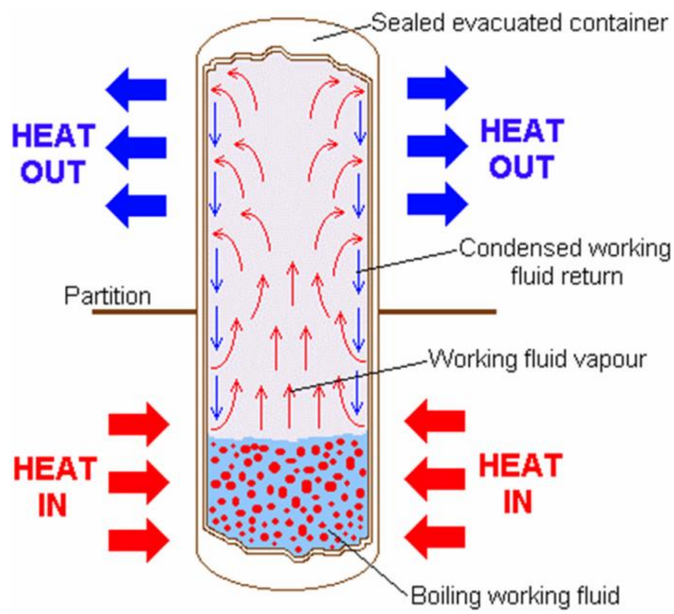

Figure (1.8) Heat pipe structure [34].

1.3.4 Phase change material for cooling system

Phase change materials (PCMs) store and release significant amounts of energy during the melting and solidification processes, maintaining nearly constant temperatures within their phase change temperature range due to their high heat of fusion, as illustrated in Figure (1.9).

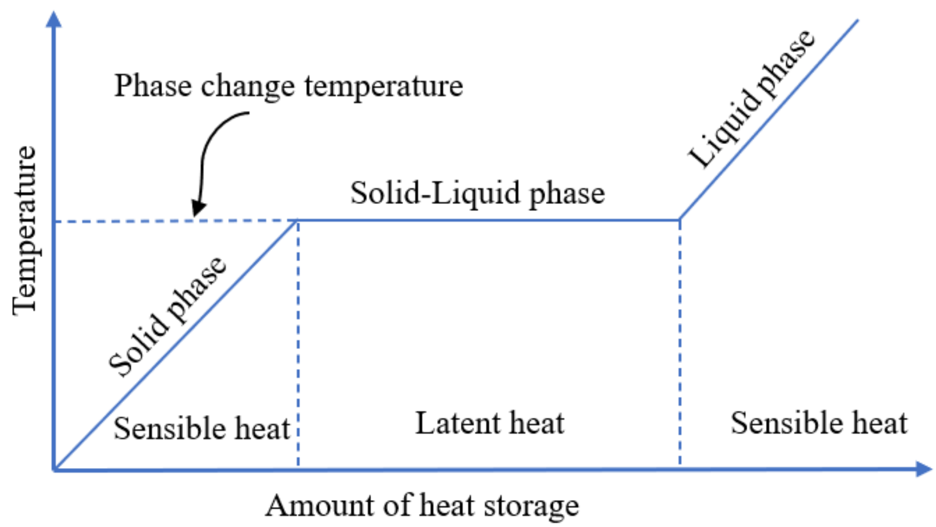

Figure (1.9) Schematic diagram of the PCM's Phase Change transition.

Therefore, they have been used to hold the battery packing within a normal operating temperature for a specific long time without using external power by immersing the battery cells in the PCM as presented in Figure (1.10). Furthermore, it is used to keep the temperature gradient through the battery packing uniformly [35]. This feature has attracted the interest of many researchers to utilize this advantage in cooling batteries and improving them.

However, PCMs suffer from low thermal conductivity that can be improved by adding a filler combination such as expanded graphite, metal foam having high thermal conductivity, or integrated with metal fins [36].

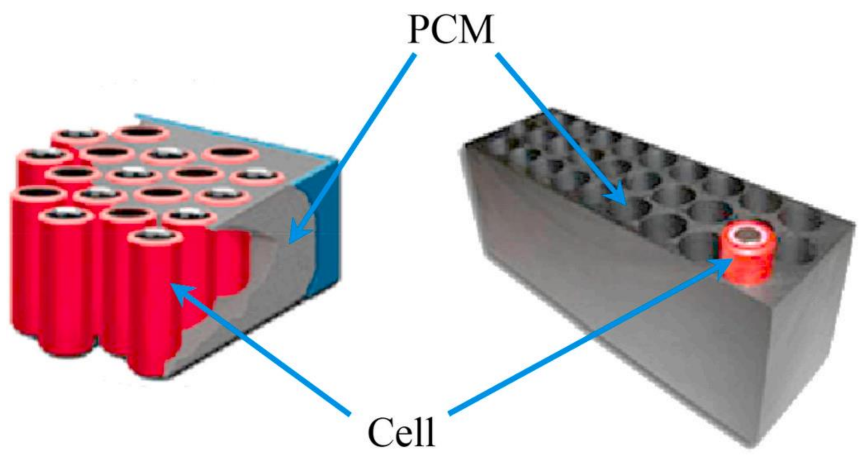

Figure (1.10) PCM cooling system [36].

PCMs depending on the phase change of substances before/after the changing process can be classified into four types; Solid–solid PCMs, solid-liquid PCMs, solid–gas PCMs, and liquid–gas [2]. Among them, solid-liquid PCMs have a large latent heat of fusion, are easy to obtain, and have a slight change in volume during the phase change, making them the most widely used in many applications [37]. Moreover, a solid-liquid PCM is classified into three main groups organic, inorganic, and eutectics as shown in Figure (1.11).

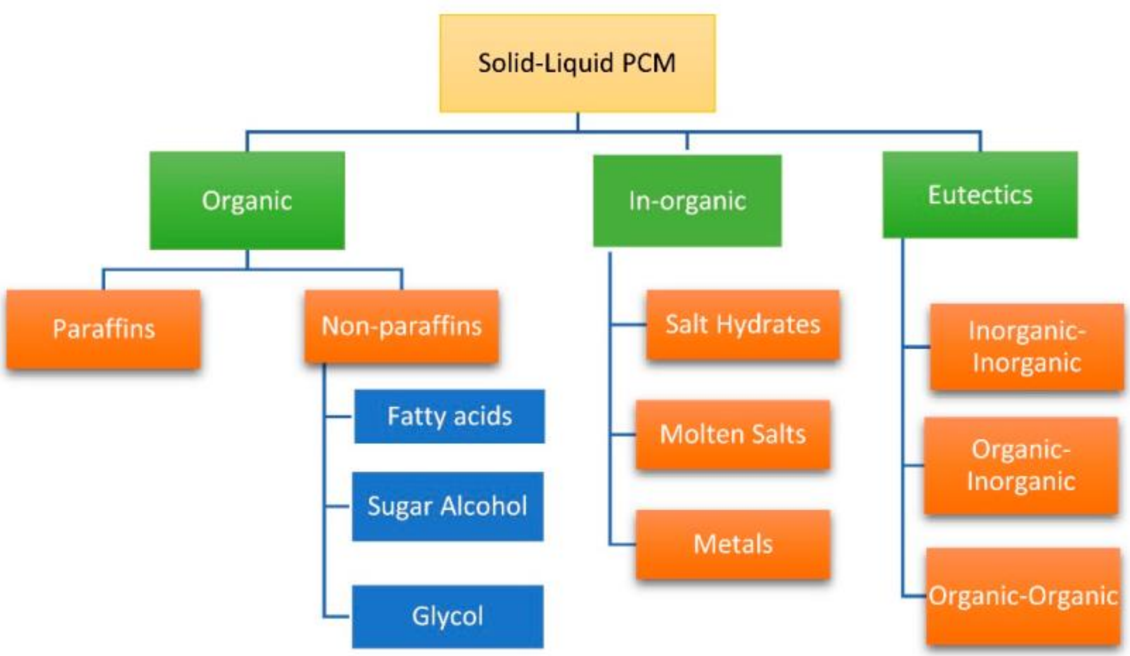

Figure (1.11) Generalized categories of phase change materials (PCMs) [37].

Based on what has been mentioned, and to use the PCM in Li-ion battery cooling systems, the following requirements must be available for PCM [38, 39]:

(1) Melting point temperature drops within the desired range.

(2) High specific heat, latent heat, and thermal conductivity.

(3) Small volume expansion during phase change.

(4) Non-flammable, non-poisonous, no corrosiveness, and chemically stable.

(5) Availability and low cost.

1.3.5 Compound cooling system

In this model, two or more cooling systems are combined. Generally, the combination consists of passive and active cooling systems to take the benefits of their features and improve their thermal behavior. Furthermore, the combination of different cooling systems can enhance the overall efficiency of the BTMS, since, each system can handle a specific aspect of heat generation and dissipation, leading to increased energy saving and producing a more effective system [40-42].

Many researchers found that combining cooling systems have considerable efficiency and are more effective than single BTMS since the individual system always suffers from some weakness [36, 43]. Other researchers noted a compound cooling system can give more temperature uniformity across the battery pack [44-45]. Moreover, the compound system can operate passively when the battery pack generates a small rate of heat at low charge/discharge rates and operates actively at high charge/discharge rates [46]. Hence, the most common combinations include:

(1) PCM and Active/Passive Air-cooling combinations system, as shown in the Figure (1.12A) [44].

(2) PCM and Liquid cooling combinations system, as shown in Figure (1.12B) [16].

(3) Liquid and Active/Passive Air-cooling combination system [47].

(4) HPs and Active/Passive Air-cooling combinations system [48].

(5) HPs and Liquid cooling combinations system [49].

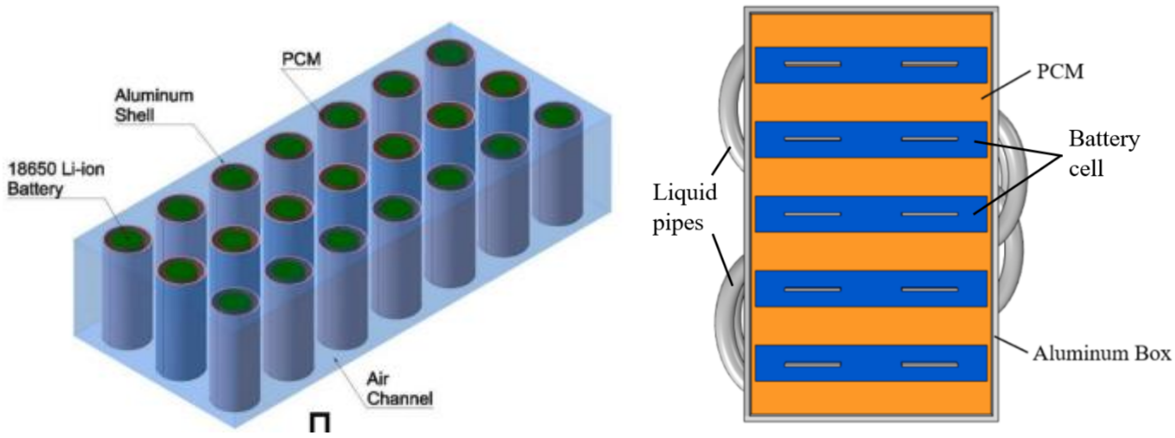

(A) (B)

Figure (1.12) Compound cooling system (A) PCM and active air-cooling combinations system [44], (B) PCM and liquid cooling combinations system [16].

1.4 Motivations

The improvement of BTMS is driven by several key motivations, which may list some of them:

(1) Maintaining the battery pack's temperature within the optimal range across various environmental conditions enhances energy production, reliability, and lifespan, thereby improving efficiency and ensuring safe operation. This is particularly important in applications like EVs and systems requiring high-energy-density batteries, as it helps prevent risks such as high temperatures and thermal runaway.

(2) Reducing the power consumption of cooling systems enhances overall efficiency, prompting many researchers to develop cooling technologies with low energy consumption, such as PCMs, which absorb and release significant amounts of latent heat during phase transitions, and HPs, which transfer more heat than copper with minimal energy consumption

Overall, combining PCMs with other thermal management systems represents an innovative approach to addressing the complex thermal challenges associated with modern battery technologies.

1.5 Objectives of the Current Work:

The aims of this work include the following:

(1) Enhance the thermal performance of BTMS that use a PCM by adding aluminum fins to increase the thermal conductivity as well as use the forced air combination to reject the heat storage in the PCM.

(2) Improving the HP structure by adding copper fins to the condenser section, as well as, using an arc evaporator shape to get direct contact with the cylindrical battery.

(3) Study the effectiveness of the present hybrid models by comparing their results with those obtained from standard models: one using pure PCM without the aluminum fins combination, and the other using forced air cooling only.

(4) Reduce the power consumption of the cooling fan by reducing the pressure losses of the flowing air.

(5) Examine the thermal performance of the present models with high-ambient temperatures up to 40 °C, different discharge rates (1, 2, 3C), and different cooling air velocities of (0.75, 1.5, 2.25, and 3 m/s).

(6) Developing a numerical simulation using COMSOL software to study a wider range of operating temperatures and air-cooling velocities, and comparing the results with experimental data to validate the numerical model.

Chapter Two

Literature Review

Chapter Two

Literature Review

2.1 Introduction

There are various adopted battery thermal management systems (BTMSs) that are aimed at addressing the thermal challenges faced by Li-ion batteries. It uses multiple cooling technologies and cooling mediums, including air-cooling systems, liquid cooling systems, heat pipe cooling systems, phase change material cooling systems, and hybrid cooling systems, which consist of a combination of two or more systems. Furthermore, this literature review highlights the significance of BTMS in battery performance, safety, and longevity. However, the objective of this chapter is to produce a review of the main experimental and theoretical study related to the BTMSs. The literature review is divided into five sections based on the type of cooling mediums: air cooling system studies, liquid cooling system studies, heat pipe cooling system studies, phase change material cooling system studies, and compound cooling system studies.

2.1.1 Air cooling system studies

Hakeem and Solyali, 2020 [50] examined experimentally the thermal performance of BTMS using forced air to cool cylindrical packing batteries consisting of 100 cells 18650-type. The investigation included three airflow velocities of 1.4, 2.4, and 3.4 m/s. Two different charge/discharge rates of 0.5 and 0.75C were used. Their results showed the T_{max} was 36.1 °C during a 0.75C charge/discharge rate at 22 °C ambient temperature and 1.4 m/s air velocity. As well as the T_{max} can be reduced by 54.28 % by increasing the air flow rate from 1.4 to 3.4 m/s in the 0.75C charge. The temperature difference between the observed cells ΔT transcends 5 °C at 1.4 m/s airflow velocity while staying under 5 °C at 2.4 m/s and 3.4 m/s airflow velocity.

Kirad and Chaudhari, 2021 [51] studied numerically the effectiveness of longitudinal and transverse distances between the battery cells on T_{max} and ΔT. The study was achieved at airflow velocities ranging between (2 to 10 m/s) and various discharge rates of (1, 2, 3, 4, and 5 C) at 25 ºC ambient temperature using ANSYS Fluent software. They note the T_{max} and ΔT were affected majorly by the longitudinal batteries separation (S_L) more than the traverse batteries separation of airflow (S_t), where the T_{max} and ΔT decreases with the increment of (S_L), while the reduction in the (S_t) value increases the pressure drop, which consequently leads to more energy consumption to keep the cooling air rate value. Furthermore, the system efficiency in this study module was better for 8 m/s air velocity with S_t = 38 mm and S_L = 23 mm.

Saechana and Dhuchakallaya, 2022 [18] investigated numerically the thermal performance of BTMS using air-cooling. The simulation was achieved with ANSYS Fluent software using a standard k-ε turbulence model. The effect of the airflow velocity of (1, 2, 4 m/s) and battery discharge rate of (0.5, 1, 2C) on the cooling performance was simulated. They observed that the increase in the airflow velocity enhances the cooling performance of the battery pack. Furthermore, the force convection was insufficient for cooling the battery at a 2C rate using a simple thermal management system, and the natural convection can maintain the battery temperature at a low discharge rate of 0.5C.

Nazar et al., 2023 [52] used natural air cooling, forced air cooling, and PCM cooling systems to cool a cylindrical cell 26650-type. $Na_2SO_4 10H_2O$ was used as a PCM with a melting temperature of 32.4 ºC. The battery was tested under a discharge rate of 1C and at room temperature around 28 ºC. The experimental result shows that active air-cooling can reduce the ΔT of the cylindrical-26650 cells to 6 ºC compared with passive cooling, which may reach up to 10 ºC. Moreover, the using of PCM can reduce the ΔT to 3.5 ºC, which can enhance the battery cell lifetime and safety. The T_{max} were 41, 33.5, and 31.2 ºC for natural air cooling, forced air cooling, and PCM cooling, respectively.

2.1.2 Liquid cooling system studies

Rao et al., 2017 [28] investigated the thermal performance of mini-liquid channels drilled in aluminum blocks to get a large contact area. The simulation model consists of 24 li-ion batteries, 18650-type, arranged in a 4P6S configuration. The impact of water velocity, direction, and aluminum block length were simulated. The numerical result shows that the system with variable contact surface can significantly enhance the battery temperature uniformity and both the T_{max} and ΔT decrease with the increase of aluminum block length and water velocity. The T_{max} can be controlled under 40 °C at a water velocity of 0.05 m/s and ambient temperature of 22.5 °C.

Zhou et al., 2019 [53] proposed a liquid cooling method based on a half-helical pipe to cool cylindrical lithium-ion batteries. The effects of inlet mass flow rate, pitch and number of helical pipes, diameter of the helical pipe, and fluid flow direction on the thermal performance of the battery at a 5 C rate and 25 °C ambient temperature were analyzed numerically. The results showed that the maximum temperature and temperature difference decreased with an increase in the inlet mass flow rate. The pitch and number of helical pipes have no significant improvement in cooling performance. If the diameter of the half-helical pipe was varied from 2.0 mm to 3.8 mm, the temperature difference remained within 4.3 °C, but the maximum temperature increased slightly from 30.5 °C to 30.9 °C. Compared to thermal management using the jacket liquid cooling method, the half-helical pipe liquid cooling method proved to be more effective due to its lower fluid volume and absence of stagnant zones.

Wei et al., 2024 [54] numerically studied the effects of liquid-cooling plate connections on the thermal performance of battery packs under different layouts. Scheme A used six liquid micro-channel plates arranged in parallel. Scheme B used six micro-channel plates arranged in a combination of three in parallel and two in series. Scheme C consisted of two sets of liquid micro-channel plates, each set arranged with three in parallel and one in series. The study also examined the effects of inlet coolant temperatures (16, 19, 22, 25, and 28 °C) under various discharge rates (0.5, 1, 2, and 3 C) at a coolant inlet flow rate of 5 L/min. The results indicated that Scheme C effectively reduced the maximum temperature of the battery pack from 48.73 °C to 30.75 °C while controlling the maximum temperature difference to 3.98 °C at the end of discharge. Furthermore, a reduction in the coolant inlet temperature led to a decrease in the maximum battery pack temperature, though it increased the maximum temperature difference.

Jha et al., 2024 [55] used an L-grooved channel cold plate design to cool Li-ion battery packs and compared it with a reference design to evaluate thermal performance. The study was done by varying parameters such as the number of channels, channel width, and coolant type at an ambient temperature of 25 °C. The best thermal performance was achieved with five 6 mm wide channels engraved on the aluminum cold plate by circulating 1 % Al2O3 in 20:80 ethylene glycol-water nanofluid as the coolant. At the 5C rate, the proposed cooling system drastically reduces the maximum temperature of the battery pack from 68.25 °C to 27.55 °C at the end of discharge.

2.1.3 heat pipe cooling system studies

Rao et al., 2013 [56] investigated experimentally the thermal design of BTMS based on HP for rectangular batteries. An electrical heater, like a real LiFePO4 battery, was used for heat generation. Four wicked HPs filled with water as a working fluid with a 50 % filling ratio were used. The T_{max} increasing rate and ΔT were studied at an operating temperature of around 22 °C. The results showed HP can control the T_{max} below 50 °C when the heat rate was below 50 W. Whereas, the maximum ΔT becomes lower than 5 °C when a heat rate does not exceed 30 W.

Greco et al. 2014 [57] developed an analytical and 3D numerical model of HPs arranged in a sandwiched configuration for cooling a prismatic Li-ion battery. The BTMS consists of eighteen HPs with an internal grooved structure to transfer the working fluid, a 10 mm outside diameter, and a 0.8 mm gap between them. All HPs were inserted in a copper structure to get a large conductive heat transfer with the battery cell at the evaporator sections. The HP condenser sections were cooled using natural and forced air convection with 20 °C ambient temperature. They found that the higher surface contact area of the HPs allows for better thermal management compared to forced convection cooling, where the predicted T_{max} was 51.5 °C when forced convection was applied.

Liu et al., 2016 [48] used thin micro-HPs with a fined condenser to cool a rectangular Li-ion battery under discharge rates of 1, 2, and 3C. A natural and forced convection was used to cool the condenser section at 30 °C ambient temperature. The results show the use of PHs can decrease the T_{max} by 7.1 °C at 2C as compared without HPs. Thin micro-HPs with forced convection can effectively deal with the instant increases in battery heat generation rate compared to forced convection without HPs under the same air velocity. The HP model can keep the T_{max} below 40 °C under 2C discharge rate.

Nasir et al., 2019 [58] investigated experimentally the thermal performance of BTMS using HP. The model consists of two proxy cells having an electrical heater with a heat generation range of (10-35 W/cell). The evaporator section was made from two cylindrical HP crammed in an aluminum plate and inserted between the proxy cells to ensure maximum contact with the cells' surface. The condenser section was cooled with forced water and natural convection air. The HP is partially filled with water as a working fluid with approximately a 10% filing ratio. The effect of heat rate, condenser length, and water flow rate on the T_{max}, and ΔT have been investigated. The results showed that the HP can reduce the cells' surface temperature by 39.1 % compared to the natural convection air and maintain the T_{max} under 50 °C and the ΔT below 5 °C if the heat generation rate was less than 20 W.

Liu et al., 2019 [59] developed BTMS using HPs having new fin structures to cool 28 Li-ion batteries 18650-type under discharge rates of 2, 3, and 5C at 25 °C ambient temperature. Arc fins with 1.5 mm thickness were attached to the HP evaporator section to get more contact area with battery cells. The HP condenser section was cooled in two ways (forced air-cooling and water-cooling). The result shows that increased contact area with battery cells enhances temperature control. In addition, the water cooling produces a lower T_{max} and more temperature uniformity as compared with forced air-cooling.

Gan et al., 2020 [49] utilized a wave-shaped aluminum sleeve coupled with HP to increase the contact area between cylindrical batteries and HPs. A cold plate was used to cool the HP at the condenser section. The effect of cooling fluid flow rate, condenser HP length, and aluminum sleeve height on BTMS performance was numerically investigated and verified experimentally. The results indicated that the cooling fluid flow rate has a clear influence on the T_{max} while it has a slight effect on the temperature distribution. The increase in the HP condenser length and aluminum sleeve height can decrease the T_{max} and enhance the ΔT through the battery pack, which can be kept below 5 °C.

Alihosseini and Shafaee, 2021 [60] investigated experimentally the performance of BTMS using a flat HP to get the best contact area between the HP and prismatic batteries. The experiments were conducted at a 1C rate at ambient temperatures between (18-33 °C) with a water-cool condenser HP. Moreover, the results were proved using the numerical simulation model (COMSOL software). They found the maximum increase in the T_{max} does not exceed 8 °C and the use of force convection in the HP condenser can uniform the temperature distribution among the cells and control the battery surface temperature below 40 °C. However, the T_{max} increased to 45 °C without using HP.

Wang et al., 2021 [61] studied experimentally the BTMS performance using a new type of flat thermosyphon HP (with no wick structure) made from aluminum as a U-shape. The HP was charged with Freon (R-134a) as a working fluid with a 90 % filling ratio and coupled with two water-cooling plates. The model was used for cooling ten rectangular battery cells under charging rates of 1 and 1.5C. Their results showed the T_{max} of the battery, the surface can be kept less than 50 °C under a charge rate of 1.5C and less than 37 °C under 1C with 24 °C inlet water temperature, while the maximum ΔT was below 3 and 7 °C under 1.5 and 1C charge rate, respectively.

Jiaqiang E. et al., 2021 [62] analyzed the dissipation performance of BTMS-based HP consisting of 12 Li-ion batteries 18650-type. The effect of fin thickness of (1.6, 1.8, 2, 2.2, and 2.4 mm) and space between fins of (4, 5, 6, 7, and 8 mm) on the heat transfer coefficient, T_{max}, and ΔT under various battery discharge rates were investigated. The theoretical results showed that the 2 mm fin thickness and 5 mm space between fins give a better thermal performance. The T_{max} increasing rate was 9 °C only, while the maximum ΔT at 1, 2, and 4C discharge rates were 0.11, 0.44, and 1.6 °C, respectively. The increasing rate of the airflow velocity from 4 to 16 m/s led to an increase in the heat transfer coefficient of the fins from 7.6 to 11.9 W/m^2.K.

Han et al. 2023 [63] conducted a comparative study on the thermal performance of two types of HPs integrated with fin structures. The first model consists of five straight HPs, while the second model consists of five HPs bent into an L-shape. Each model was coupled with five aluminum fins in an L-shape and associated with a baseline cooling plate. The two models were used to cool a rectangular 16 A Li-ion battery under a 3C discharge rate at an operating temperature of 25 °C. The results show that the L-shaped HPs can lower the T_{max} by more than 3 °C compared to the straight HPs. The L-shaped HPs can reduce the thermal resistance to 28.0 % by decreasing the coolant temperature from 25 °C to 15 °C.

Zheng et al., 2023 [64] studied numerically and experimentally the thermal performance of BTMS based on tubular HP. The system consists of tubular HPs, rectangular Li-ion batteries, cooling plates, and fins. The system was simulated at 30 °C ambient temperature under 1 and 2C discharge rates. The results show the T_{max} was reached 35.6 °C at 1C, while it was become 54 °C at 2C and the maximum ΔT was reached 7 °C at 2C.

2.1.4 Phase change material cooling system studies

Azizi and Sadrameli, 2016 [35] studied experimentally and theoretically the thermal performance of the PCM combined with aluminum wire mesh. Poly Ethylene Glycol 1000 with a melting range of 35-40 °C has been used as a PCM. The combination was used to enhance the thermal conductivity of the PCM and achieve a uniform temperature distribution in the battery cells. The PCM melting point is between 35 and 40 °C. The charge/discharge rates range between 1 and 3C. A mathematical model has been developed to verify the experimental data using COMSOL 5.1. The obtained results showed the use of the combination of the PCM and aluminum wire mesh can reduce the battery's surface temperature remarkably, where the maximum ΔT was 2.6 °C using the PCM combined with aluminum mesh, 4 °C with PCM only, and 6.7 °C without a thermal management system. Moreover, the combined system can reduce the T_{max} by 19, 21, and 26 % for the discharge rates of 1, 2, and 3 C, respectively.

Sun et al., 2019 [65] enhanced experimentally and numerically the thermal conductive of PCM by adding different numbers of longitudinal metal fins. The effects of the fins' position and number under different rates of heat generation on the BTMS performance were evaluated. The experimental result showed a better performance than the pure PCM system. The fin structures can enhance the heat conductive through the PCM and control the temperature rise. Moreover, the optimal PCM ring thickness was 3.6 mm and recommended dimensionless distance between rings and batteries was 0.2, while the ideal number of rings and fins were 1 and 8, respectively. Additionally, it has been noticed that the PCM-Fin system can regulate the rise in the battery's temperature even at a 20 W heat generation rate.

Also, Zheng et al., 2020 [66] studied experimentally and numerically the effect of adding fins on improving the thermal performance of the PCM. The experiment was performed using a cylindrical heater located in the PCM container with and without aluminum fins. The effect of fins' geometrical factors (number, thickness, and length) and materials (steel, Al alloy, nylon, titanium, and copper) was studied numerically using ANSYS Fluent software. The result showed that the fins can improve the working time by 75, 68, and 61% compared to those without using the fins under a heat generation rate of 10, 12.5, and 15 W, respectively. The simulation results indicated that aluminum fins with 8 fins and a thickness of 0.5 mm provide the greatest performance.

Srivastava et al., 2022 [67] studied experimentally and numerically the effectiveness of the PCM thickness around the battery cell under various discharging rates 1, 2, and 3C. Three different PCMs (Paraffin wax, Eicosane, and Capric acid) with 5 and 10 mm thicknesses were used to inspect their effect on the battery surface temperature. The results confirmed that using PCM can reduce the cell's temperature by 21.5 % compared to the rate without PCM at the discharging 3C rate. The T_{max} of battery cell with Paraffin wax reached a maximum value of 43 °C compared to 40 °C using Eicosane. The surface temperature remained uninfluenced by the change in the thickness of the PCM layer from 5 to 10 mm.

Behi et al., 2022 [68] enhanced the thermal conductivity of the PCM using a composite of PCM-graphite. The PCM melting temperature ranged between (35-42 °C) with latent heat of 220 kJ/kg. The BTMS model consists of 24 cylindrical batteries and was directly immersed in the PCM. The systems were tested under a 1.5C discharge rate at an ambient temperature of 25 °C. The results showed a slight difference in the T_{max} of the batteries model between pure PCM and PCM-graphite cooling systems, which were 40.4, and 39 °C, respectively. Moreover, they obtained a large temperature uniformity using the PCM-graphite.

Li et al., 2022 [69] studied experimentally the use of fluorinated liquid immersion as a gas-liquid phase change material for cooling a single li-ion battery 18650-type. The boiling point of a fluorinated liquid was 33.4 ºC. They compared it with forced air-cooling under 2 and 4C at an ambient temperature of about 30 °C. Their result found that immersion liquid cooling was better than forced air-cooling, especially under 4C discharging. Where the maximum cell temperature rise was 14.06 ºC for the forced air-cooling, while it was 4.97 ºC for the immersion cooling under 4C discharge rate.

Budiman et al. 2022 [70] studied experimentally three different arrangements of carbon tubes filled with PCM and located between twenty Li-ion batteries 18650-type. The experiment was conducted under discharge rates of 1, 2, and 4C at 25 °C operating temperature. The results show that the three configuration models can maintain the average temperature of no more than 40 and 55 °C for discharge rates of 1 and 2C, respectively. In contrast, all arrangements cannot keep the average battery temperature with an acceptable limit at a 4C discharge rate.

Chen et al., 2022 [71] increased the thermal performance of the PCM cooling and reduced the T_{max} during the discharging process by adding several circular fins around the cylindrical battery and submerging it in the PCM-filled container. COMSOL Multiphysics software was used to build the physical model. The simulation results showed that the fins increase the PCM melting performance at the start of the cooling process and reduce the T_{max} of the battery. Furthermore, the simulation results demonstrated the minimum value of the T_{max} and the largest volume fraction of the PCM liquid can be obtained with a fins number equal to 9, whereas the battery T_{max} rises when the fins number exceeds nine.

Sun et al., 2023 [72] enhanced the PCM thermal conductivity using copper foam. The experiment was conducted under a 3C discharge rate using sixteen thermal dummy cells instead of real cells 21700-type. The thermal performance of copper foam/PCM compares with natural air and pure PCM cooling models. The results showed the T_{max} of copper foam/PCM model can be reduced from 57.4 to 51.4 °C compared with pure PCM. In addition, the maximum ΔT in the cells was maintained at less than 5 °C at an operating temperature of 25 and 35 °C. Furthermore, the T_{max} increase using the natural air-cooling model was significantly larger than in the other models and it exceeded the safety limit.

Li et al., 2023 [73] conducted a numerical simulation using dual PCMs integrated with a fin arrangement for cooling a single Li-ion battery 18650-type. The dual PCMs are pure paraffin and paraffin composites with expanded graphite. The radial thickness of the PCM is 9 mm. The dual PCMs are separated by eight aluminum fins and surrounded by an external aluminum shell. The thermal performance of the dual PCMs model at various ambient temperatures and discharge rates was examined. The results show the T_{max} were 29.87, 32.89, 34.69, 36.84, and 39.41 °C at an ambient temperature of 25 °C and under discharge rates of 1, 2, 3, 4 and 5C, respectively. The symmetric fin arrangement reduces the T_{max} and ΔT_{max} by 29.19 and 42.76 %, respectively, at ambient temperature of 40 °C.

Sudhakaran et al., 2023 [74] studied the effect of PCM thicknesses of 2, 4, 6, and 8 mm; the volume percentage of copper foam were 1, 3, 5, and 7% on the heat transfer performance of BTMS using a various type of PCMs (Capric Acid, RT-55, RT-42, and RT-35). The simulation was conducted using ANSYS Fluent software for a cylindrical battery having a heat generation rate of 94,023.84 W/m^3 at an ambient temperature of 25 °C. The results showed that the Capric Acid has a lower cell temperature of 30 °C, and the PCM material with 8 mm thickness has a lower cell temperature. Moreover, the most effective parameter regarding the cooling performance of BTMS used PCM was the PCM material of 35.4 % followed by material thickness of 35.13 %, PCM heat transfer coefficient of 13.98 %, and the added ingredient percentage of 5.09 %.

Wang et al. 2023 [75] numerically enhanced the PCM by adding expanded graphite and examined the effect of phase transition temperatures of composite PCM on BTMS performance. Three paraffin waxes with different melting points (45, 48, and 54 °C), mixed with EG, were used to make three different types of composite PCM. The numerical simulation model is carried out in COMSOL 5.2 software. The study was performed under 1, 2, and 3C discharge rates for cylindrical Li-ion batteries 18650-type at 20 °C ambient temperature. The most appropriate transition temperature was equal to 48 °C, and the optimal parameters were 4.4 mm for battery spacing, 0.8 W/m^2 K for convective heat transfer coefficient, and 10.9 % for mass fraction.

2.1.5 Compound cooling system studies

Jiang et al., 2017 [76] designed a hybrid BTMS of composite paraffin/expanded graphite (EG) and forced air as a tube-shell configuration system. The model consists of aluminum tubes containing battery cells surrounded by composite paraffin/EG. These tubes are then placed inside a cylindrical baffled shell to examine the forced airflow direction. The result shows the model significantly reduces the temperature increase and keeps the ΔT lower than 2 °C. The existence of baffles improves the heat transfer efficiency by changing the airflow direction.

Huang et al. 2018 [41] used three types of BTMSs to cool Li-ion batteries 18650-type under discharge rates of 1, 2, and 3C at 35 °C ambient temperature. The three models include the Pure PCM model, a flat HP coupled with air-cooling, and the PCM model. The third model was a flat HP coupled with liquid cooling and PCM. The result showed that the use of a flat HP coupled with PCM could maintain the T_{max} at 50 °C under a 3C discharge rate and produce a good temperature uniformly. The HP with liquid flow can reduce the ΔT by 3 °C than other models.

Qin et al., 2019 [77] proposed a hybrid BTMS of PCM combined with forced air convection. The model consists of four cylindrical Li-ion batteries 18650-type, twelve PCM containers, and nine aluminum ducts allowing airflow. It was tested experimentally and theoretically by COMSOL Multiphysics 5.2 under 1, 2, 3, and 4C discharge rates and at 22 °C ambient temperature. The passive and active approach to the BTMS performance was also compared. The results showed the combined model can control the T_{max} and ΔT within a recommended limit. Furthermore, the active mode has superior thermal performance compared to the passive mode. Where the active mode can reduce the T_{max} and ΔT by 16 and 1.2 °C under 3 C rate, respectively. Also, the recommended gap between the batteries was 5 mm for application.

Kong et al., 2019 [78] improved theoretically the BTMS by integrating the composite phase change material with liquid cooling. The system was simulated under a 3C discharging rate and 0.5C charging rate using COMSOL software. The effect of cell gaps, liquid cooling velocity, and channel number was studied. Then, the proposed model was designed experimentally to confirm the effectiveness of the coupled system. The simulation results demonstrated the new model can hold the T_{max} and ΔT of the battery cell at 41.1 and 4 °C during 3C discharge rate and ambient temperature up to 30 °C. Also, they noticed thermal performance enhanced by increasing the cell gap up to 5 mm. Furthermore, the integrated system enhanced the thermal performance of the batteries at different ambient temperatures and reduced the cooling power consumption significantly.

Jilte et al., 2019 [79] modified numerically a conventional passive PCM cooling system to stimulate the effect of active and passive PCM cooling on the BTMS. The packing cell was arranged in several rows, each consisting of 6 Li-ion batteries 18650-type. Each cell was surrounded by a 4 mm cylindrical shell of the PCM. The model tested at discharge rates of 2 and 4C and ambient temperatures of 27, 35, and 40 °C. The simulation results confirm the PCM around each cell, which led to better heat removal and enhanced the temperature distribution in the model. Where the ΔT between the battery cell was within 0.05 °C at a 2C rate and 0.12 °C at a 4C discharge rate. Furthermore, the PCM thickness of 4 mm around each cell is sufficient for heat dissipation.

Wang et al., 2020 [40] introduced an experimental study of a hybrid cooling for BTMS consisting of HP and PCM integration. The model consists of 40 cylindrical Li-ion batteries 18650-type, 14 aluminum HP charged with a 40 % filling ratio of acetone as a working fluid, and 13 aluminum tubes filled with paraffin as a PCM. The HPs have four circular grooves in the evaporator section to ensure tight contact with battery cells and four annular fins in the condenser section to enhance the HP heat rejection. The experiment was performed at a 2C discharge rate and using natural air convection with 25 °C ambient temperature. They found the hybrid model could keep the T_{max} and ΔT across the battery pack within 47.7 and 2.5 °C, respectively.

Huang et al., 2020 [80] examined experimentally and numerically the effect of integrated composite PCM and forced air on BTMS performance. The investigation was conducted under various air velocities of (0, 1, 2, 3 m/s) and discharge rates of (1, 2, 3, 4C) at an ambient temperature of 25 ºC. They concluded that the PCM as a passive cooling system, cannot continue to absorb the heat produced by the cell once the PCM has entirely melted. Furthermore, they found the active combined cooling system from the PCM and forced air-cooling give more temperature uniformity through the cell than the passive cooling system. Where the T_{max} and ΔT could be limited to 63 °C and 4.8 °C, respectively under a 4C discharge rate using a 3 m/s forced air convection.

Yang et al., 2020 [47] investigated the thermal performance of a combination of mini-channel water cooling with forced air at a 4C discharge rate. The effectiveness of water flow rate, direction, tube space, and air-cooling velocity were studied. The results displayed that the T_{max} and ΔT reduce with the water flow rate increase following a significant rise in power consumption. At suitable values of the system parameters can keep the ΔT within 4.13 °C and decrease the T_{max} to 32 °C at an operating temperature of 25 °C. The cooling tube amount has slightly improved the cooling performance. Moreover, the high air-cooling velocity could reduce the T_{max} and ΔT of a battery model.

Hu et al., 2020 [81] studied the effectiveness of the HP integrated with PCM on temperature control for the prismatic Li-ion battery cell under the 3C discharging rate. The integrated system was compared with the use of HP without integration. The condenser HP section was cooled by water at a 25 °C inlet temperature. The results show that the maximum temperature of HP-integrated PCM was 40 °C, but it was 45.5 °C for HP use only. Moreover, the ΔT was decreased by 1.02 °C using the HP integration system.

Chen et al., 2020 [10] studied theoretically the thermal performance of forced air-cooling and PCM cooling. A two-dimensional thermal model consisting of sixteen cylindrical 26650-type was built using COMSOL multi-physics modeling software. The study was achieved at airflow velocities range between (0 to 8 m/s) and various ambient temperatures range from 0 ºC to 50 ºC. The results show that forced air cooling was more effective than pure PCM cooling, especially at high operating temperatures. However, forced air-cooling has a lower temperature uniformity at low air velocities. Moreover, the researchers suggested a combination of forced air-cooling and PCM to extend the battery's life and obtain the best temperature uniformity through the Li-ion battery pack. The battery cycle life can extend by 600% as compared with PCM cooling, owing to the lower temperature field in air-cooling conditions.

The thermal behavior of natural convection cooling, natural convection combined with PCM cooling, and forced convection combined with PCM cooling were investigated by Yang et al. 2021 [15] and compared under different discharge-charge rates. The simulation is conducted using COMSOL multiphasic software. The models cool four Li-ion batteries 18650-type arranged in a staggered array at 26.5 ºC ambient temperature. Each battery is surrounded by a 2 mm PCM thickness. The results demonstrated that the T_{max} reached 53.94 ºC under a 1C discharge rate with natural convection which exceeds the optimal temperature. The combined forced air and PCM cooling system can effectively reduce the T_{max} by 18 ºC compared with the natural convection system. The simulation results showed that T_{max} of the passive combined cooling system exceeds the safety limit under the 2C discharge rate. Active cooling with a PCM combination is recommended for battery cooling under a 2C discharge rate.

Abbas et al., 2021 [13] proposed two compact BTMS modules consisting of flat HPs integrated with paraffin as PCM. Each module was comprised of two parts: the lower part contains the HP evaporator section and PCM that fills the gaps between the HP and battery cells, while the upper part contains the HP condenser section, which was cooled by cooling water. One model contains five HPs with a gap of 4.5 mm, while the second model contains seven HPs without gaps to establish direct contact between the HP and batteries. The results confirmed that the direct-contact HP model reduced the T_{max} by 31% compared to the indirect-contact HP model under a heat generation rate of 6 W. The PCM melting process occurs under high heat generation rates of 4 and 6 W.

Anqi et al., 2022 [82] studied the effectiveness of the PCM as an active cooling system to cool a single Li-ion battery 18650-type. The battery cell was surrounded by two different shapes of circular and hexagonal chambers and simulated using the COMSOL software. The models were put in an air duct to examine the effect of air velocity variation between 0.1 and 0.4 cm/s with an air-cooling temperature of 30 °C. They noted that the hexagonal chamber produced more liquefied PCM than the circular chamber. Also, they observed that the increasing air velocity increases the heat transfer coefficient and decreases the volume fraction of the PCM.

Leng et al., 2022 [45] tested three BTMS models for cooling a prismatic Li-ion battery; one used HP only, the second used PCM only, and the third used HP coupled with PCM. The HP was flattened to get closely attached to the battery. The

PCM melting temperature ranged between (42-44 °C) with latent heat of 178 kJ/kg. The simulation was performed at 22 °C operating temperature for 20 W battery heat generation. The theoretical result confirmed that a couple of flat HPs and PCM can achieve a more temperature-controlled time and lower surface temperature than a single PCM and HP. Furthermore, this coupling gave more energy-saving.

Gu et al., 2022 [83] used composite PCM (paraffin and expanded graphite) coupled with air-cooling and fins. It has been found that the composite PCMs can cool the Li-ion battery at 20 °C ambient temperature and natural convection under 2C discharge. Experimentally, the optimal axial and radial thicknesses of composite PCMs found were 45 and 8 mm. While the composite PCMs coupled with four fins and 1.23 m/s air velocity can keep the T_{max} below 60 at 30 °C ambient temperature and 4C discharge rate. Moreover, a numerical simulation was conducted under high discharge rates and different fin structures using COMSOL Multiphasic. The simulation results show the fins could effectively decrease the flow dead zone model.

Kavasogullari et al., 2023 [44] investigated the thermal performance of a hybrid BTMS using forced air integrated with PCM having 43 °C melting temperature and 165 kJ/kg latent heat of fusion. The simulation model consists of twenty-one battery cells 18650-type arranged in a 3P7S configuration. Each battery has been wrapped in aluminum shells filled with PCM and placed in the air duct. The simulation was carried out using different PCM thicknesses of (4, 6, and 8 mm), two PCM types, and various Reynolds numbers of (100, 200, and 400) at 20 °C ambient temperature using COMSOL Multiphysics software. The results show the model gives a better cooling performance as compared without the use of PCM and it can keep the ΔT below 5 °C.

2.2 Conclusions Obtained from Previous Research

From the previous studies mentioned above, some important research related to improving the PCM heat conduction, HP configuration, and coupling system performance, are summarized in Table (2.1).

Table (2.1) Summary of previous studies.

No.	Author and Year	Study type	BTMS types	Parameters	Results
1	Rao et al., 2013 [3]	Experimental	Wicked HPs	Heat generation was equal to 50 W, T_{amb}=22 °C	The model controls the T_{max} below 50 °C
2	Wang et al., 2020 [50]	Experimental	HP and PCM integration	2C-rate and T_{amb}=25 °C	The T_{max} and ΔT across the battery pack were 47.7 and 2.5 °C, respectively.
3	Wang et al., 2021 [4]	Experimental	Flat thermosyphon HP with water cooling	1 and 1.5C-rate and $T_{water,in}$=24 °C	T_{max} and ΔT can be kept less than 50 and 7 °C under 1.5C-rate and less than 37 and 3 °C under 1C-rate, respectively.
4	Yang et al. 2021 [8]	Simulation	Passive air, passive air combined with PCM, and active air combined with PCM	1 and 2C-rate and T_{amb}=26.5 °C	T_{max} exceeds the safety limit under a 1C-rate. Active combined cooling can be kept. T_{max} under a 2C-rate
5	Leng et al., 2022 [18]	Simulation	Three models; HP only, PCM only, and HP coupled with PCM	Heat generation was equal to 20 W, T_{amb}=22 °C	The coupled model can achieve a more temperature-controlled and lower T_{max} and more energy-saving
6	Kavasogullari et al., 2023 [15]	Simulation	forced air integrated with PCM	different PCM thicknesses, two PCM types, and various Re No.	Better performance compared to without PCM integrated and it can keep ΔT below 5 °C.
7	Azizi and Sadrameli, 2016 [24]	Experimental and simulation	PCM combined with aluminum wire mesh	Effect of adding fins on PCM under 1, 2, and 2C-rate	ΔT equal to 2.6, 4, and 6.7 °C using the integration, PCM only, and without any BTMS, respectively

8	Qin et al., 2019 [28]	Experimental and simulation	Integration of PCM with forced air	1, 2, 3, and 4C-rates, T_{amb} = 22 °C	A model can reduce the T_{max} and ΔT by 16 and 1.2 °C under 3 C rate, respectively
9	Huang et al., 2020 [27]	Experimental and simulation	Integration of composite PCM with forced air	Effect of integration under 4C-rate, T_{amb}=22 °C, air velocity=3 m/s	T_{max} and ΔT could be limited to 63 and 4.8°C, respectively
10	Zheng et al., 2020 [66]	Experimental and simulation	PCM with and without aluminum fins	Effect of heat generation rate of 10, 12.5, and 15 W	Using 8 fins can improve the working time by 61% compared to without fins under a 15 W heat rate.
11	Alihosseini and Shafaee, 2021 [34]	Experimental and simulation	Flat HP with water cool condenser	Comparing between using HP and without HP	T_{max} equal to 40 °C and 45 °C with and without HP, respectively
12	Abbas et al., 2021 [35]	Experimental and simulation	Two models of flat HPs integrated with paraffin as PCM	Effect of direct and indirect contact condenser HPs with batteries	Direct-contact HP model reduced the T_{max} by 31% compared to the indirect-contact HP

Furthermore, the following conclusions can be made from the studies mentioned above:

(1) Most of the investigations on active cooling systems combined from the PCM and forced air on a cylindrical battery were achieved theoretically.

(2) The majority of experiments consisting of a pure PCM or PCM metal form combination were reported for Prismatic cells or at a low ambient temperature.

(3) Battery systems based on cylindrical cells embedded in the PCM were generally a single cell surrounded by the PCM or multi-cells with the PCM filled in between them.

(4) Numerous investigations using the HP with the Li-ion battery were made. However, the investigation of the HP strategy for the cylindrical battery pack contacting the surface in the evaporator section was seldom presented in previous studies.

(5) Due to their classification with maximum self-heat rate and potential hazards of thermal runaway, very few studies have focused explicitly on cylindrical lithium cobalt oxide (LiCoO2)-type cells. However, they possess the highest energy density [84, 85], which is a crucial factor for Li-ion batteries. Additionally, major EV manufacturers currently employ $LiCoO_2$ batteries for some of their car models such as the Tesla Roadster and Daimler Smart Fortwo [23]. Moreover, $LiCoO_2$ batteries find applications in various other devices such as digital cameras, cellular phones, and laptops [86].

2.3 Scope and Originality of the Current Work

The objective of the present work is to enhance the performance of the Li-ion battery cooling system under high ambient temperatures (up to 40 °C). This can be achieved through:

1- Developing two novel configurations of hybrid cooling models for the BTMS, consisting of twelve cylindrical Li-ion batteries type 18650-type $LiCoO_2$ with a capacity of 2600 mAh.

2- The first model integrates PCM and aluminum fins with a forced air-cooling system. The aluminum fins are used to enhance thermal conduction within the PCM and accelerate heat transfer to the cooling air, while the PCM is employed to store excess heat generated by the batteries.

3- The second model employs a flat HP with a finned condenser and an arc-shaped evaporator to get direct contact with the cylindrical batteries, improving heat dissipation efficiency.

4- Comparing the thermal performance of the two proposed models with standalone systems using pure PCM and air cooling to evaluate their effectiveness.

5- Conducting experiments at different battery discharge rates (1, 2, 3C) and varying cooling air velocities (0.75, 1.5, 2.25, and 3 m/s).

6- Developing a numerical simulation using COMSOL Multiphysics software to model the proposed configurations and validate the simulation results against experimental data.

Chapter Three

Numerical Simulation

Chapter Three

Numerical Simulation

3.1 Introduction

In this chapter, five different BTMSs are numerically investigated to examine the thermal performance of these models. The numerical analysis is achieved using COMSOL Multiphysics software (version 5.6) depending on the finite element method. This approach is chosen to simulate and solve the hybrid cooling models due to its highly precise results and ability to use a couple of multi-physics tests [87]. 3D-simulation models with time-dependent and multi-physics interface solvers are used. The five models considered in this study include the usage of various cooling systems: one employs a passive cooling system, two utilize active cooling systems, and the remaining two feature hybrid cooling systems. The models are analyzed under different conditions of Li-ion battery discharge rates (C-rate) of 1, 2, and 3C, various operating temperatures (T_{in}) of 25, 30, 35, and 40 ºC, various inlet air velocities (u_{in}) of 0.75, 1.5, 2.25, and 3 m/s, and Reynold numbers range from 1,850 to 13,400 for active and hybrid cooling systems.

3.2 Battery Pack Cooling Models

3.2.1 Air-Model

The Air-Model of the Li-ion battery pack consists of twelve batteries of 18650-type $LiCoO_2$ with a diameter of 18.2 mm and a height of 65 mm as shown in Figure (3.1). The batteries are arranged in three rows with four batteries in each row and located in the air duct of a cross-section area (70 x 80) mm². The longitudinal (SL) and traverse (St) distances between the adjacent batteries are 23 and 25 mm, respectively. The cooling air flows from the left side of the duct (inlet) to the right side (outlet) through the gaps between batteries at specified values of velocities and temperatures. The heat is generated from the batteries with a certain amount depending on the discharge rate and transferred to the cooling air. The battery's thermo-physical properties that are used in the present simulation are listed in Table (3.1). Moreover, the effectiveness of positive and negative battery electrode structures is ignored to simplify the modeling process and to reduce the computational time of the numerical solution.

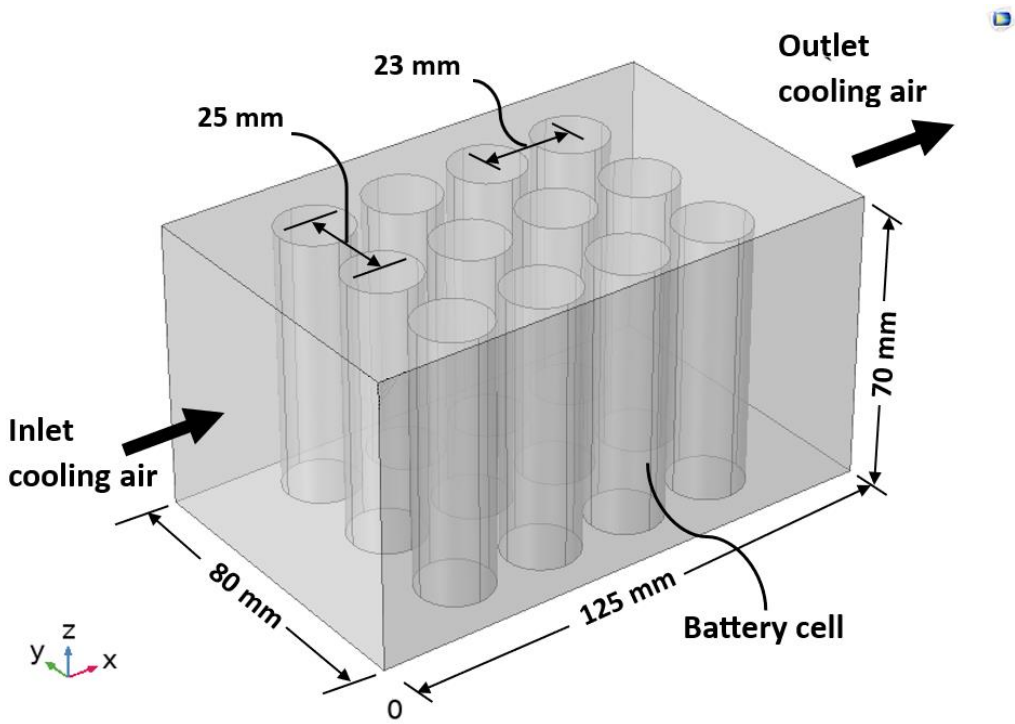

Figure (3.1) Schematic diagram of the battery pack of Air-Model.

Table (3.1) Thermo-physical properties of the battery [88, 89]**.**

Parameter	Value	Unit
Density	2720	[kg/m³]
Specific heat capacity	830	[J/kg. °C]
Thermal conductivity	0.55	[W/m °C]

3.2.2 PCM-Model

In this model, a BTMS based on phase change material cooling is simulated. The purpose of this model is to examine the effectiveness of passive cooling on battery thermal management and compare it with other cooling systems. Therefore, a three-dimensional model using a pure PCM of type Rubitherm-RT47 with a melting range of (41-48 °C) is simulated. The selection of PCM was to be suitable for high-temperature operation, maintain the battery pack temperature within the optimal operating temperature limit, and store the greatest possible amount of heat generated within this temperature range.

The configuration of the battery pack and dimensions are arranged as in the Air-Model for results comparison. The battery pack is submerged in a PCM container of dimensions (65×75×92) mm^3 as shown in Figure (3.2). The PCM thermo-physical properties are illustrated in Table (3.2). The upper boundary of batteries and PCM are exposed to free convection of coefficient $h = 5\ \mathrm{W/m^2K}$ [68, 74]. The other outer walls are assumed insulated surfaces without heat exchange with the surroundings.

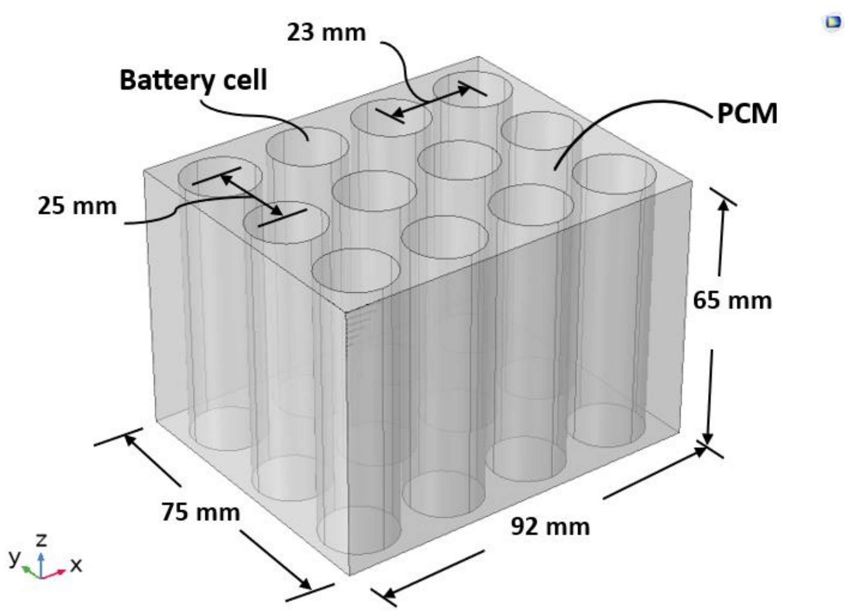

Figure (3.2) Schematic diagram of the battery pack of PCM-Model.

Table (3.2) Thermo-physical properties of the PCM (RT47).

Parameter	Value	Units
Melting range	41-48	[°C]
Latent heat of fusion	160	[kJ/kg]
Specific heat capacity	2	[kJ/kg °C]
Solid phase density	880	[kg/m^3]
Liquid phase density	770	[kg/m^3]
Heat conductivity (both phases)	0.2	[W/m °C]

3.3.3 PCM/Fin-Air-Model

In this model, a three-dimensional hybrid cooling system is simulated. The model consists of PCM integrated with aluminum fins and forced air. The purpose of fins is to increase the heat transfer surface area and improve the temperature distribution of the PCM. Additionally, the use of forced air is to remove the heat transfer and remove the heat generated by the battery pack. The battery pack was arranged in a symmetrical model thus the middle battery row is considered in modeling the cooling system to reduce the computation time of the numerical solution. Figure (3.3) shows the battery row considered in the numerical analysis which consists of 4 batteries 18650-type arranged in series and surrounded by two PCM jackets of 62 mm height and 104 mm length.

Each PCM container is made of 0.5 mm thick aluminum plates equipped with 6 aluminum fins of dimension (62 x 11 x 0.5) mm^3 and filled with a pure PCM of type Rubitherm-RT47. The interval distance between adjacent batteries in each row is 8 mm, while the air gap between adjacent rows is 6 mm in width. The hybrid cooling system was located inside the air duct to examine the cooling air velocities and operating temperature variations. The inlet cooling air flows from the inlet to the outlet of the duct through the gaps between battery rows at constant velocity and temperature. The other two sides of the model are simulated as symmetrical walls for heat transfer and fluid flow.

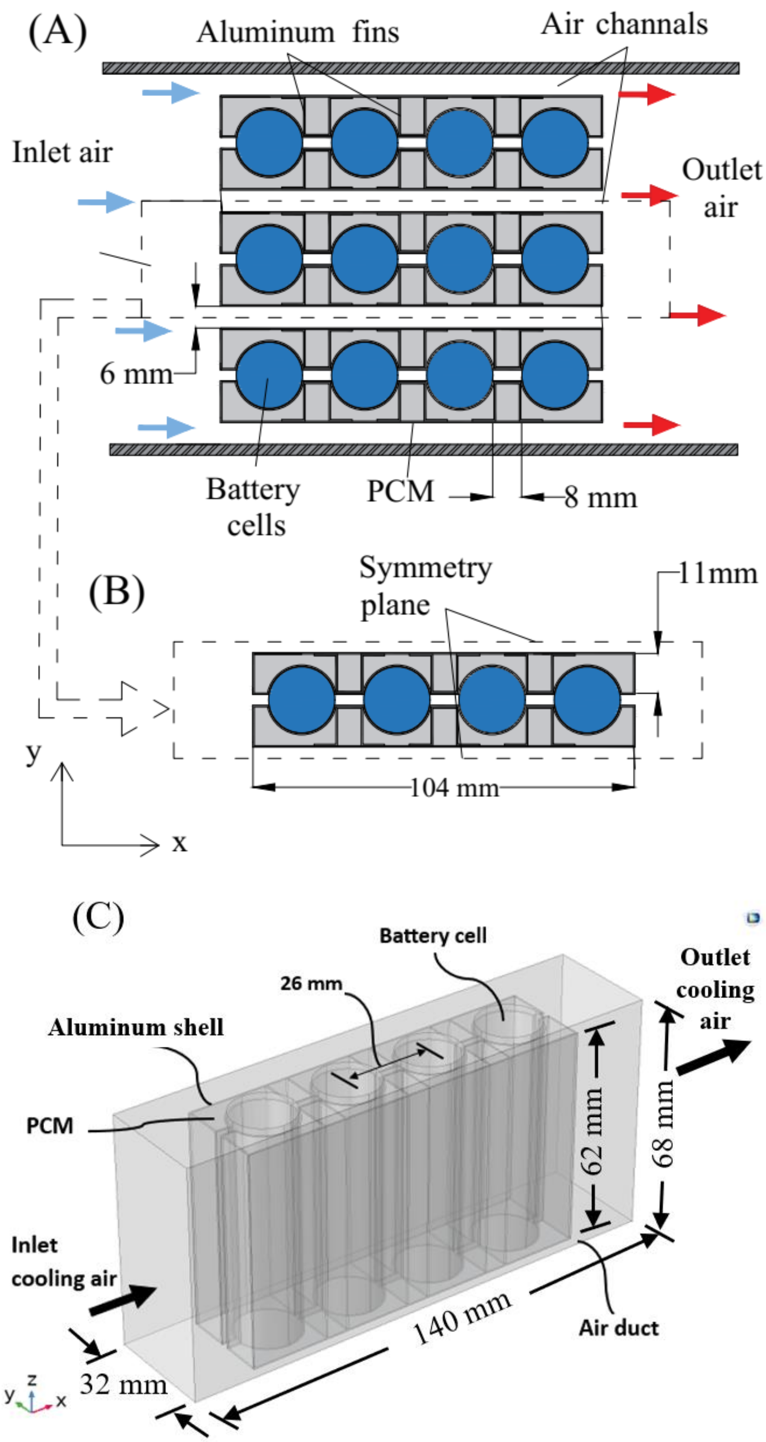

Figure (3.3) Schematic of the battery pack PCM/Fin-Air model. (A) Top view of the complete model, (B) top view of a selected row, and (C) 3D view of the selected row.

3.3.4 HP-Model

In this model, the effectiveness of the heat pipe (HP) with a compact contact area on the performance of the battery thermal management is studied. Therefore, a three-dimensional model of HPs with a double-groove evaporator is simulated. The grooved evaporator was made to get direct contact with the cylindrical battery surface on each side which increases the heat transfer area and reduces the thermal resistance. Due to the symmetry of the battery pack model, only half of the battery model consisting of three HPs with six battery 18650-type was modeled as shown in Figure (3.4).

The condenser sections of the HPs are equipped with ten rectangular copper fins of dimension (88 x 40 x 0.35) mm^3 with a space of 2.3 mm between two adjacent fins. The condenser section is placed in the air duct with cross-sectional dimensions of (30 × 44) mm^2 to examine the cooling air velocity and temperature variations. The total length of the HP is 140 mm while the condenser and evaporator lengths are 30 and 65 mm, respectively. To simplify the model calculation, the HPs are simulated as a metal plate with a thermal conductivity of 700 W/m. K, which is measured experimentally.

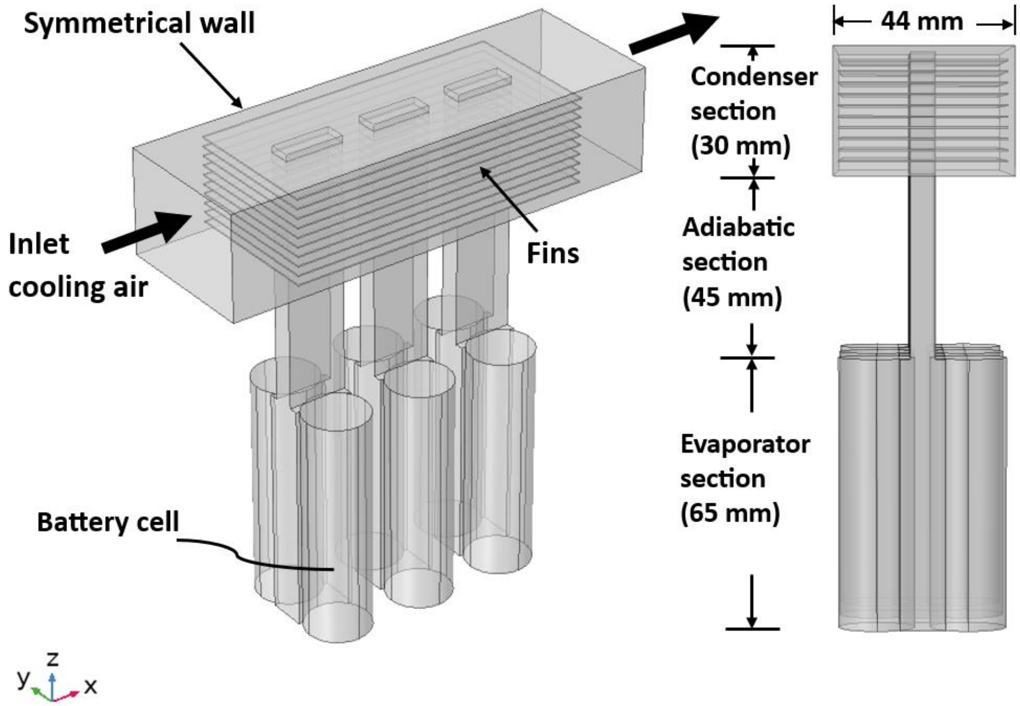

Figure (3.4) Schematic diagram of the HP-Model.

3.3.5 HP/PCM-Model

In this model, the effectiveness of HP that is used in the previous HP-Model with PCM integration on the performance of the battery thermal management is studied. Therefore, the structure and dimensions of HPs are similar to that used in the HP model. In contrast, the HPs evaporator section and battery pack are submerged in a PCM container of dimension (76 × 47 × 65) mm^3 as shown in Figure (3.5). A pure PCM of type Rubitherm-RT47 is used in this model.

Consequently, there are two ways to remove the heat generated from the battery cell during the battery discharging process: the first is using PCM to absorb the extra heat from battery cells, while the second way is using HP to release the heat to the environment. Moreover, in this simulation model only one-half of the battery pack is considered in the numerical analysis due to the battery model symmetry, and to reduce computation time. Therefore, the left wall of the air duct and evaporator section is assumed as a symmetrical wall.

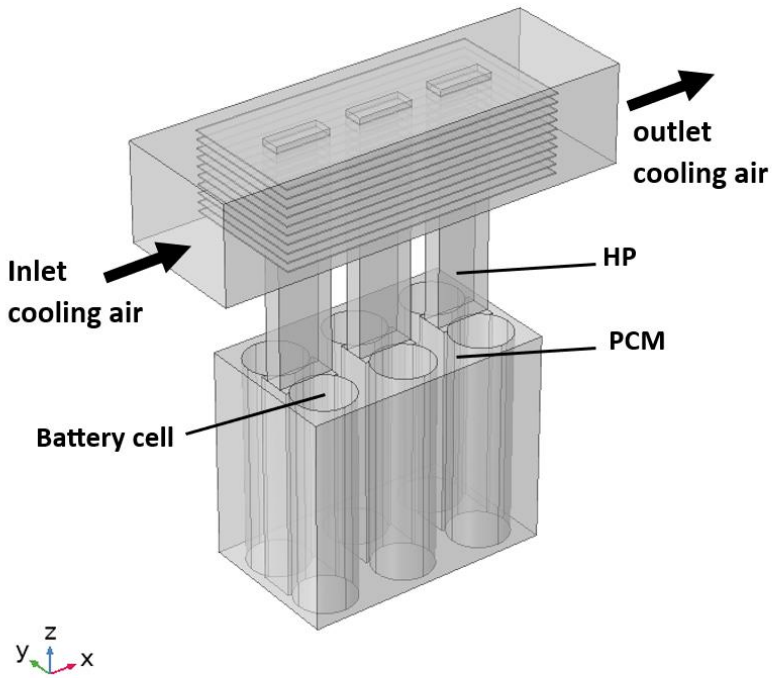

Figure (3.5) Schematic diagram of the HP/PCM-Model.

3.4 Assumptions

To simplify the numerical simulation of the present battery cooling models the following assumptions are considered:

1) Unsteady heat transfer and steady fluid flow.
2) The thermal radiation and the buoyancy effect in all models are neglected.
3) Three-dimensional and incompressible cooling airflow are considered for both laminar and turbulent flows.
4) The volumetric variation of PCM through the melting process is neglected.
5) The thermo-physical properties of PCM are assumed constant for both phases except the density that changes with phase change.

6) Conductive heat transfer is considered to govern the heat transfer in the PCM, while the convection heat transfer and gravitational effects are ignored.
7) The thermal resistances between the PCM and battery cells are neglected.
8) The structure of the positive and negative battery electrode connection is ignored to enhance the computational speed of the numerical solution.
9) All battery cells are modeled as a solid body having the same volumetric heat generating.

3.5 Governing Equations

Three-dimensional modeling is considered in the simulation of the all-cooling models for the Li-ion battery pack. The finite element method is used to solve governing equations, and all variables were solved using linear discretization, unsteady for heat transfer and steady for airflow. Furthermore, the governing equations for the air side are solved by considering the air flow regime as laminar or turbulent depending on the value of the Reynolds number. The heat transfer in solid and fluid modules, which involves non-isothermal flow, multi-physics, and time-dependence, is used to solve the energy equations in the air, HPs, copper fins, aluminum shells, PCM, and battery cells. The relative tolerance was selected to be 0.005. For cooling air simulation, the k-epsilon model is used in solving the simulated turbulent flow of the battery cooling system due to its stability, relatively lower computational time, and acceptable accuracy [25].

The governing equation can be listed as follows:

1) The momentum equation in the liquid PCM is not considered, and the heat transfer through the PCM, battery, and solid regions is governed by the energy conservation equation as follows:

The battery energy equation is simulated as [49, 73]:

$$\rho_b C_{p,b} \frac{\partial T_b}{\partial t} - \nabla . k_b \nabla T_b = \mathrm{Q_{gen}} \tag{3.1}$$

Where ρ_b is the battery density (kg/m³), $C_{p,\mathrm{b}}$ is the battery specific heat (J/kg. K), k_b is the battery thermal conductivity (W/m. K), T_b is the battery's absolute temperature (K), $\mathrm{Q_{gen}}$ is the battery volumetric heat generation (W/m³).

The PCM energy equation is simulated as [66, 73]:

$$\rho_{PCM} c_{p,PCM} \frac{\partial T_{PCM}}{\partial t} - \nabla . (k_{PCM} \nabla T_{PCM}) = 0 \tag{3.2}$$

$$c_{p,PCM} = \theta_s c_{p,s} + \theta_l c_{p,l} + L_{PCM} \frac{\partial \alpha_m}{\partial T} \tag{3.3}$$

$$\alpha_m = \frac{1}{2} \frac{\theta_l - \theta_s}{\theta_s + \theta_l} \tag{3.4}$$

$$\theta_s + \theta_l = 1 \tag{3.5}$$

Where ρ_PCM, k_PCM and L_{PCM} are the density (kg/m³), thermal conductivity (W/m. K), and latent heat (J/kg) of PCM, respectively. θ_s and θ_l are the percentage of solid and liquid in the PCM, respectively.

The solid region of the heat pipe and fins domain, the energy equations are simulated as [44]:

$$\rho_{HP} C_{p,HP} \frac{\partial T_{HP}}{\partial t} - \nabla . k_{HP} \nabla T_{HP} = 0 \tag{3.6}$$

$$\rho_f C_{p,f} \frac{\partial T_f}{\partial t} - \nabla . k_f \nabla T_f = 0 \tag{3.7}$$

Where ρ_{HP} and $C_{p,HP}$ are the heat pipe average density and specific heat which are equal to 2650 kg/m³ and 1020 J/kg. K, respectively, based on a weighted average method for acetone and copper pipe. k_{HP} is the heat pipe equivalent thermal conductivity which is equal to 700 W/m. K which is measured experimentally. ρ_f, $C_{p,f}$, k_f and T_f are the density (kg/m³), specific heat (J/kg. K) thermal conductivity (W/m. K), and absolute temperature (K) of fins, respectively.

2) For the cooling air domain, the heat transfer and fluid flow are governed by the continuity, momentum, and energy conservation equations as follows [13]:

Continuity equation:

For the incompressible steady flow, the continuity equation is expressed as:

$$\rho_{\mathrm{a}}\nabla\mathbf{u} = 0 \tag{3.8}$$

Where ρ_a is the air density (kg/m³) and **u** is the velocity vector (m/s).

Momentum equation:

For the unsteady, compressible, Newtonian fluid and laminar flow, the momentum equation is expressed as [90]:

$$\rho_a \frac{\partial \mathbf{u}}{\partial t} + \rho_a \mathbf{u}.\nabla\mathbf{u} = -\nabla p + \nabla.\left[\mu(\nabla\mathbf{u} + (\nabla\mathbf{u})^T) - \frac{2}{3}\mu(\nabla.\mathbf{u})\mathbf{I}\right] + \rho_a g \tag{3.9}$$

Where μ is the air dynamic viscosity (Pa. s), p is the air pressure (Pa), and **I** is the unit diagonal matrix (unit tensor), and $(\nabla\mathbf{u})^T$ is the velocity gradient tensor.

For steady the ($\frac{\partial \mathbf{u}}{\partial t} = 0$) and for incompressible flows, the divergence of the velocity vector is zero ($\nabla \cdot \mathbf{u} = 0$), and for neglection the buoyancy effect ($\rho_a g = 0$), the equation (3.9) reduces to:

$$\rho_a \mathbf{u}.\nabla\mathbf{u} = -\nabla p + \nabla.\left[\mu(\nabla\mathbf{u} + (\nabla\mathbf{u})^T)\right] \tag{3.10}$$

For the unsteady, compressible, and turbulent flow, the momentum equation is expressed as [90]:

$$\rho_a \frac{\partial \mathbf{u}}{\partial t} + \rho_a(\mathbf{u}.\nabla)\mathbf{u} = \nabla.\left[-p\mathbf{I} + (\mu + \mu_\mathrm{T})(\nabla\mathbf{u} + (\nabla\mathbf{u})^T) - \frac{2}{3}(\mu + \mu_\mathrm{T})(\nabla.\mathbf{u})\mathbf{I} - \frac{2}{3}\rho_a k\mathbf{I}\right] \quad (3.11)$$

Where μ_T is the air turbulent dynamic viscosity (Pa. s),

For the steady, incompressible, and turbulent flow, the momentum equation (3.11) reduces to:

$$\rho_a(\mathbf{u}.\nabla)\mathbf{u} = -\nabla p + \nabla.[(\mu + \mu_\mathrm{T})(\nabla\mathbf{u} + (\nabla\mathbf{u})^T)] \quad (3.12)$$

The k-epsilon (k-ε) model is used in solving the simulated turbulent flow. Where k is the turbulent kinetic energy ($\mathrm{m}^2/\mathrm{s}^2$) and ε is the dissipation rate (1/s). These are calculated as:

$$\rho_a(\mathbf{u}.\nabla)k = \nabla.\left[(\mu + \frac{\mu_\mathrm{T}}{\sigma_k})\nabla k\right] + \mathrm{P}_k - \rho_a\varepsilon \quad (3.13)$$

$$\rho_a(\mathbf{u}.\nabla)\varepsilon = \nabla.\left[(\mu + \frac{\mu_\mathrm{T}}{\sigma_\varepsilon})\nabla\varepsilon\right] + \mathrm{C}_{\varepsilon 1}\frac{\varepsilon}{k}\mathrm{P}_k - \mathrm{C}_{\varepsilon 2}\rho\frac{\varepsilon^2}{k} \quad (3.14)$$

The values of parameters $\mathrm{C}_{\varepsilon 1}$, $\mathrm{C}_{\varepsilon 2}$ σ_ε and σ_k are 1.44, 1.92, 1.3 and 1 [90], respectively. μ_T and P_k are the turbulent viscosity and turbulence production, respectively, which are calculated as:

$$\mu_\mathrm{T} = \rho\mathrm{C}_\mu\frac{k^2}{\varepsilon} \quad (3.15)$$

$$\mathrm{P}_k = \mu_\mathrm{T}[\nabla\mathbf{u}:(\nabla\mathbf{u} + (\nabla\mathbf{u})^T] \quad (3.16)$$

$$\mathrm{C}_\mu = 0.09$$

Energy equation:

For unsteady heat transfer, the energy equation for the air domain is expressed as:

$$\rho_a C_{p,a}\frac{\partial T_a}{\partial t} + \rho_a C_{p,a}\mathbf{u}.\nabla T_a - \nabla.(k_a\nabla T_a) = 0 \quad (3.17)$$

Where k_a, $C_{p,a}$ and T_a are the air thermal conductivity (W/m. K), specific heat capacity (J/kg. K), and absolute temperature (K), respectively.

The Reynolds numbers (Re) *is* calculated as

$$Re = \frac{\rho_a u_a D_h}{\mu_a} \tag{3.18}$$

Where u_a is the inlet airflow velocity at the inlet section for each model, μ_a is the average dynamic viscosity of air, D_h is the hydraulic diameter of the air channel which is determined as:

$$D_h = \frac{4A_d}{P_d} = \frac{4(H_d \times W_d)}{2(H_d + W_d)} \tag{3.19}$$

Where H_d and W_d are the height and width of the air channels.

The airflow is considered in the laminar regime when the Reynolds number is (Re < 2300), while it becomes in the turbulent flow regime for (Re > 2300) [90]. Depending on the values of the Reynolds number shown in Table (3.3) the airflow is considered in the laminar regime for HP-Model at $u_{in} = 0.75\ \mathrm{m/s}$ only and in the turbulent regime for other values of u_{in}. In contrast, the flow is considered in the turbulent regime for all airflow velocities for Air-Model and PCM/Fin-Air-Model.

Table (3.3) Reynolds number values for the cooling models**.**

Model	*Re*			
	$u_{in} = 0.75$ (m/s)	$u_{in} = 1.5$ (m/s)	$u_{in} = 2.25$ (m/s)	$u_{in} = 3$ (m/s)
Air-Model	3,127	6,254	9,381	12,508
PCM/Fin-Air-Model	3,350	6,700	5,515	13,400
HP-Model	1,851	3,702	5,553	7,404

3.6. Initial and Boundary Conditions

1) The initial temperatures of batteries, PCM, fins, and HP are all set at the same temperature as the initial operation temperatures that are used in the simulation. The computational domain of the present models are shown in Figures (3.6 A-E).

$$\mathrm{t} = 0 \qquad \mathrm{T_b} = \mathrm{T_{PCM}} = \mathrm{T_{fin}} = \mathrm{T_{HP}} = \mathrm{T_0} \tag{3.20}$$

Where $\mathrm{T_b}, \mathrm{T_{PCM}}, \mathrm{T_f}, \mathrm{T_{HP}}, \mathrm{T_0}$ are the battery, PCM, fin, HP, and operation temperatures, respectively.

2) The T_{in} is simulated to be constant at specific values of 25, 30 35, and 40 ºC which is equal to the operation temperature.

$$T_{in} = T_0 \tag{3.21}$$

3) The u_{in} is set to be constant at specific value*s* of 0.75, 1.5, 2.25, and 3 m/s, while outlet air condition is set to have a pressure equal to atmospheric pressure.

$$u_{in} = 0.75, 1.5, 2.25, 3 \ (\frac{\mathrm{m}}{\mathrm{s}}) \tag{3.22}$$

$$\mathrm{P}_{out} = \mathrm{P}_{atm} \tag{3.23}$$

4) The outer surfaces of the duct are assumed as thermally insulated surfaces, and the other parts of HP-Model boundaries located outer the duct are thermally insulated.

$$-\mathrm{n.q} = 0 \tag{3.24}$$

where n denotes the outward normal vector on the boundary of the domain.

5) Symmetric flow condition is imposed in the air duct of HP and Fin/PCM-Air-Models [44].

$$-\mathrm{n.q} = 0 \tag{3.25}$$

$$\mathrm{u.n} = 0 \tag{3.26}$$

$$\mathrm{K_n} - (\mathrm{K_n.n})\mathrm{n} = 0, \mathrm{K_n} = \mathrm{kn} \tag{3.27}$$

6) No slip boundary condition is considered between the inside wall surface of the channel and airflow.

$$u_w = 0 \tag{3.28}$$

7) The boundary conditions at the contact surface between batteries-solid surface, batteries-PCM, and solid surface-PCM are defined by the energy conversation equations as follows [44]:

$$-k_b \frac{\partial T_\mathrm{b}}{\partial n} = -k_\mathrm{s} \frac{\partial T_\mathrm{s}}{\partial n} \tag{3.29}$$

$$-k_b \frac{\partial T_\mathrm{b}}{\partial n} = -k_\mathrm{PCM} \frac{\partial T_\mathrm{PCM}}{\partial n} \tag{3.30}$$

$$-k_\mathrm{s} \frac{\partial T_\mathrm{s}}{\partial n} = -k_\mathrm{PCM} \frac{\partial T_\mathrm{PCM}}{\partial n} \tag{3.31}$$

Where k_b, k_s and k_PCM are thermal conductivity of the battery, solid surface of the aluminum fin and heat pipe, and PCM (W/m K), respectively. $\frac{\partial T}{\partial n}$ is the temperature gradient.

8) The boundary conditions of the external wall (batteries and fins) that are cooled by forced air is defined as [73]:

$$-k_b \frac{\partial T_\mathrm{b}}{\partial n} = \mathrm{h}(\mathrm{T_b} - \mathrm{T_a}) \tag{3.32}$$

$$-k_\mathrm{s} \frac{\partial T_\mathrm{s}}{\partial n} = \mathrm{h}(\mathrm{T_f} - \mathrm{T_a}) \tag{3.33}$$

Where h is the heat transfer coefficient of air (W/m² K). T_s and T_b are the solid surface and battery surface temperatures.

9) The upper boundary of batteries and PCM for the pure PCM-Model are defined as exposed to free convection as [73]:

$$-k_{PCM}\frac{\partial T_{PCM}}{\partial n} = h_n(T_{PCM} - T_a) \tag{3.34}$$

$$-k_b\frac{\partial T_b}{\partial n} = h_n(T_b - T_a) \tag{3.35}$$

Where h_n is the free convection heat transfer coefficient of 5 W/m^2K [78].

10) The heating generation source was applied to the battery bodies in each model.

$$Q_{gen} = Q_{gen,1C}, Q_{gen,2C}, Q_{gen,3C} \tag{3.36}$$

Where Q_{gen} is the volumetric heat generation in W/m^3, which were determined experimentally for battery cell 18650-type $LiCoO_2$, as in equation (5.2).

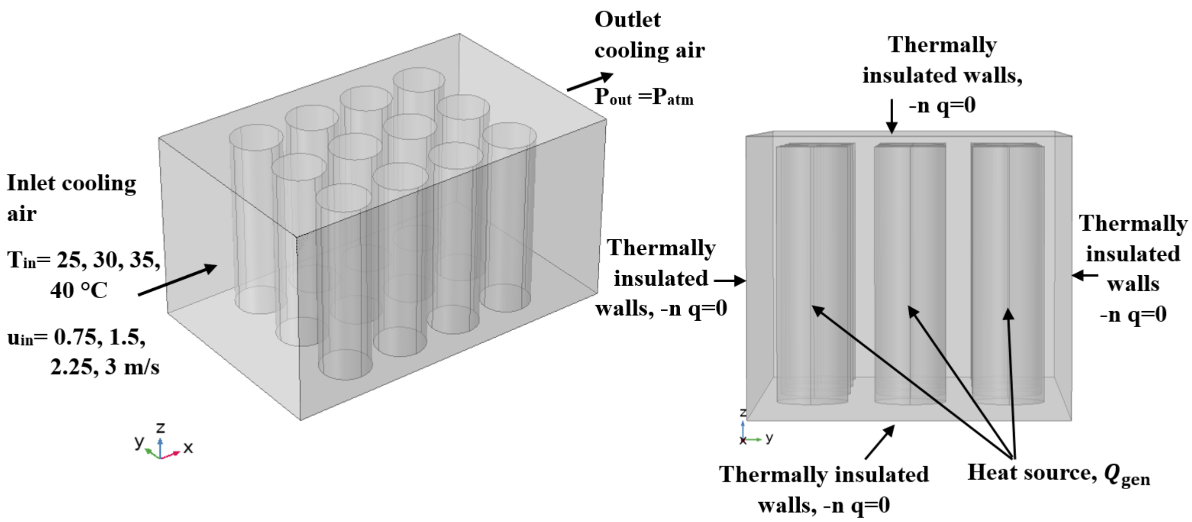

(A)

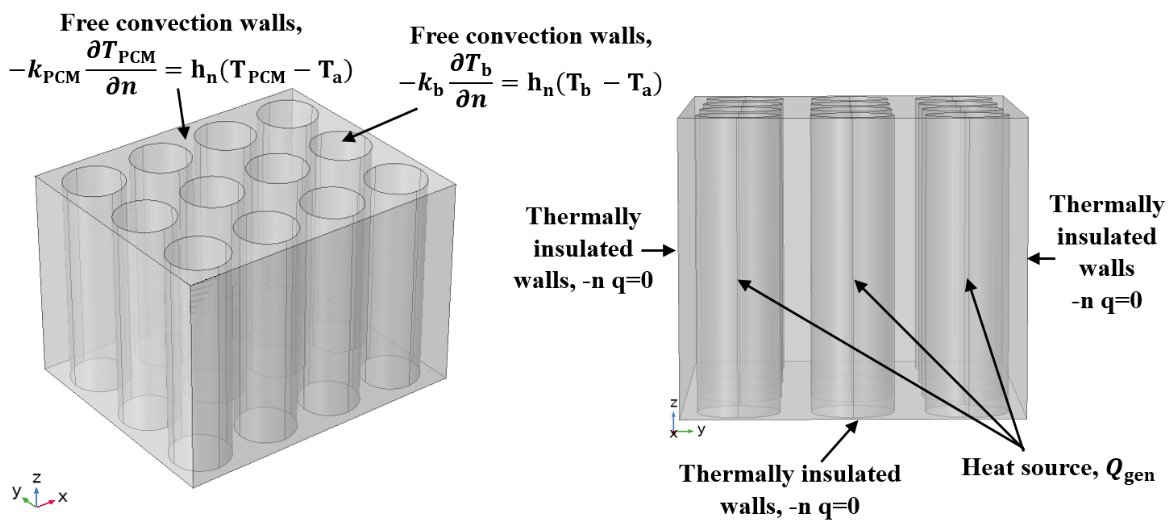

(B)

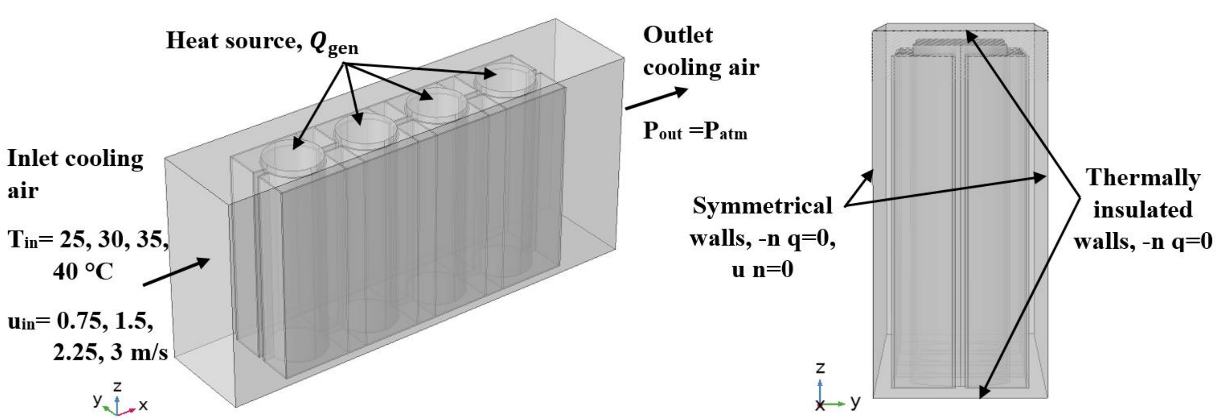

(C)

Continuous

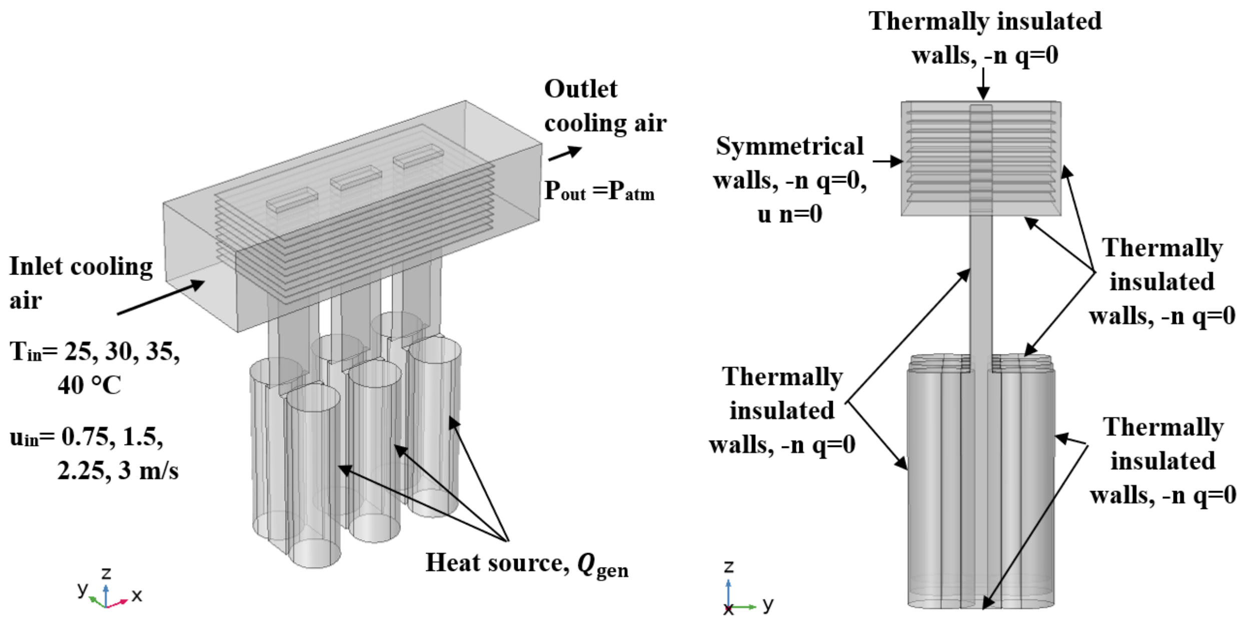

(D)

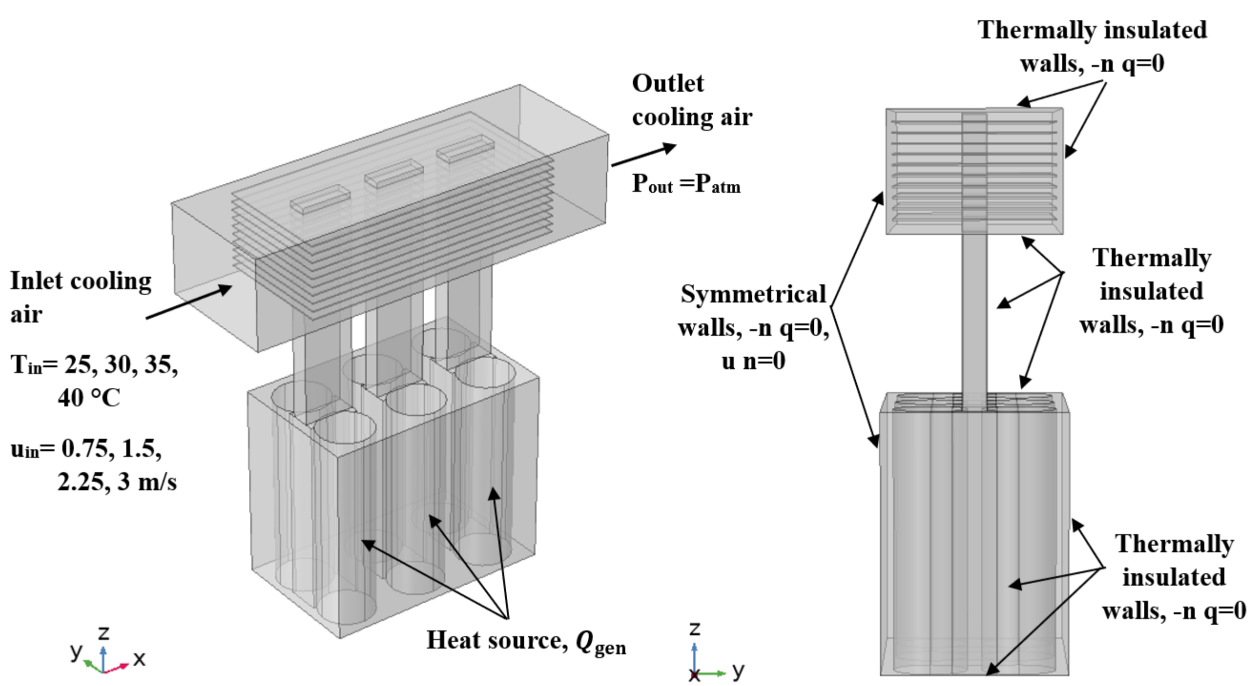

(E)

Figure (3.6) Boundary conditions of (A) Air-Model, (B) PCM-Model, (C) PCM/Fin-Air-Model, (D) HP-Model, and (E) HP/PCM-Model.

3.7 Grid Independence

The proper grid number is selected depending on the maximum temperature variation of the probe point on the battery's surface. To simplify the model, the tab of the battery is ignored and the battery is represented as a cylindrical cell. The physically-controlled mesh is applied for the different models to find the mesh size and a tetrahedral grid density is considered for each model. The mesh independence size has been conducted for air velocity of 1.5 m/s, 3C rate, 40 ºC ambient temperature, and various mesh sizes.

Figures (3.7 A-E) show the variation of the T_{max} with the number of meshes for different cooling models. It is observed that the T_{max} become more stable when the number of grids reached 899073, 435072, 1714672, 1447276, and 1513462 for Air-Model, PCM-Model, PCM/Fin-Air-Model, HP-Model, and HP/PCM-Model, respectively, and the maximum deviation percentage in the T_{max} of the battery was within 0.11, 0.04, 0.24, 0.16, and 0.15% as the grid number increased to the selected number for these models, respectively. Therefore, these grid numbers are considered in the computation.

Subsequently, a personal computer equipped with a Core i7 processor and a total memory capacity of 32 GB (RAM) was used to achieve the simulation models. The meshing structure of the five battery cooling models is shown in Figures (3.8 A-E). The duration of the computation varied between 2 and 21 hours, depending on the model type. Figure (3.9) shows the schematic of the flow chart of the numerical solution steps implemented by COMSOL software.

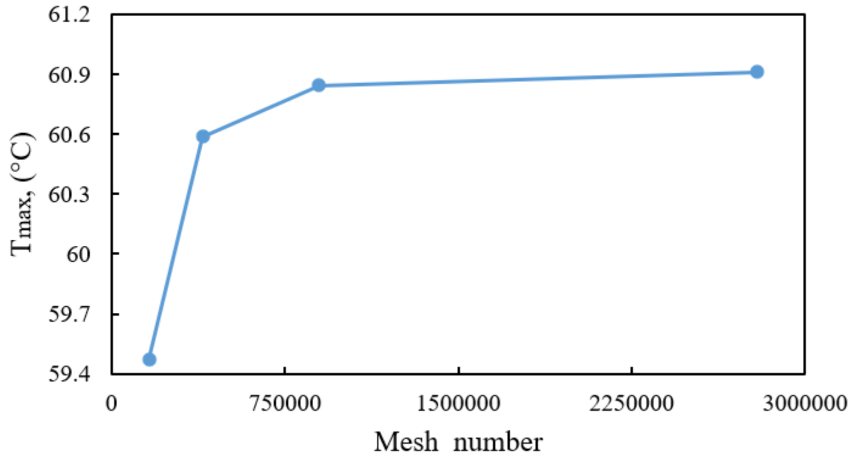

(A)

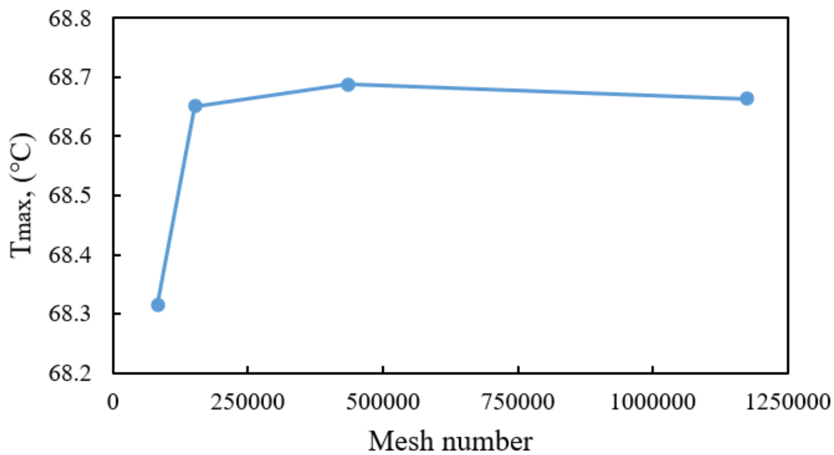

(B)

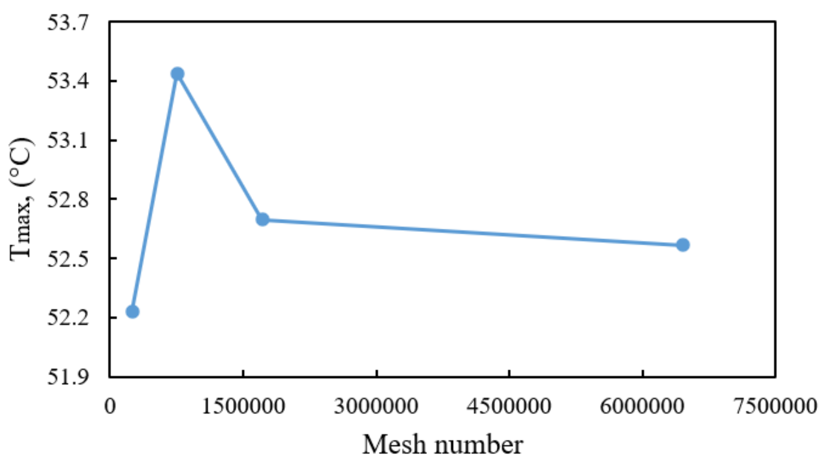

(C)

Continuous

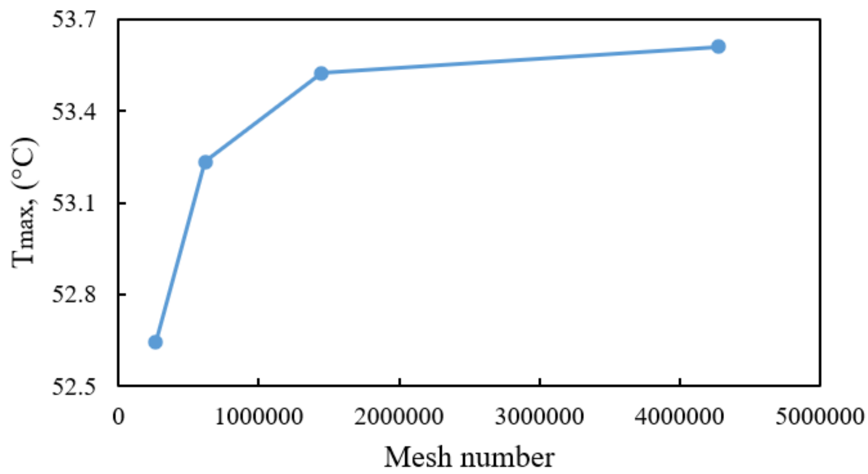

(D)

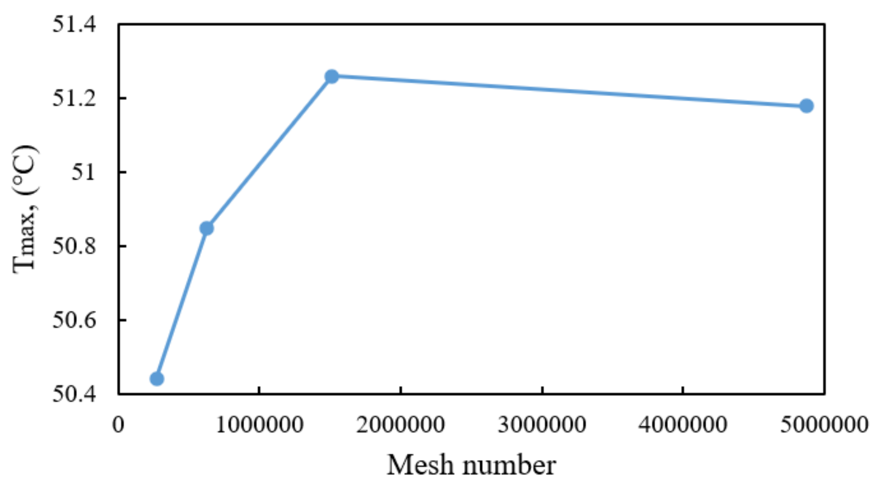

(E)

Figure (3.7) Variation of the T_{max} with the mesh numbers of (A) Air-Model, (B) PCM-Model, (C) PCM/Fin-Air-Model, (D) HP-Model, and (E) HP/PCM-Model.

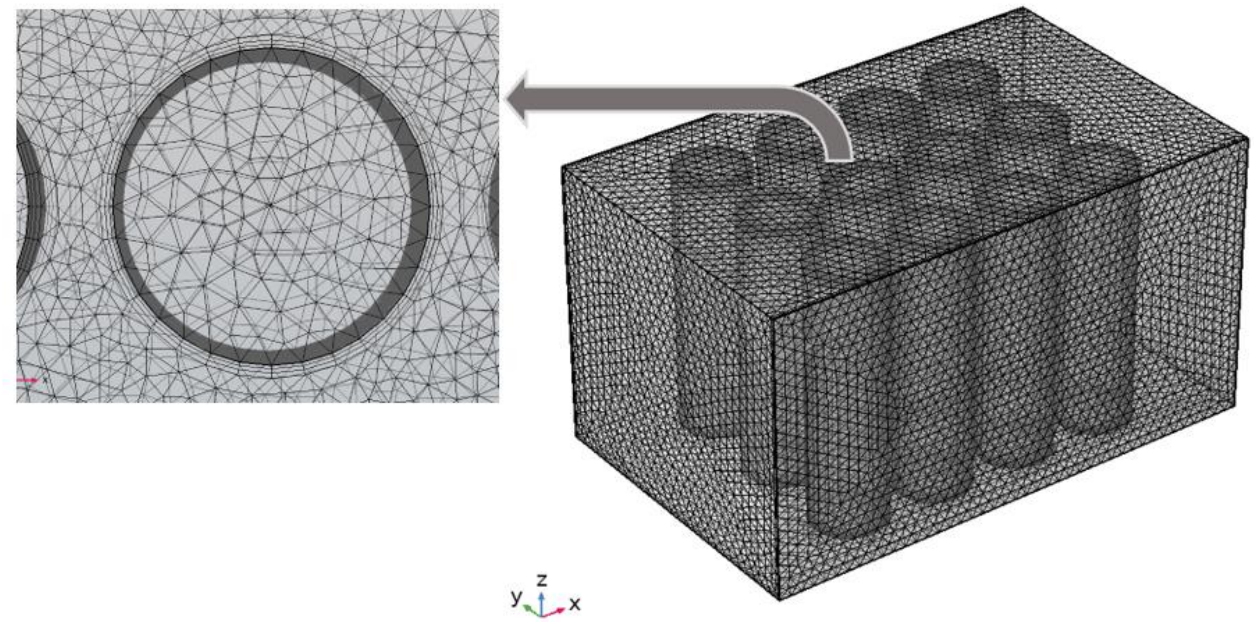

(A)

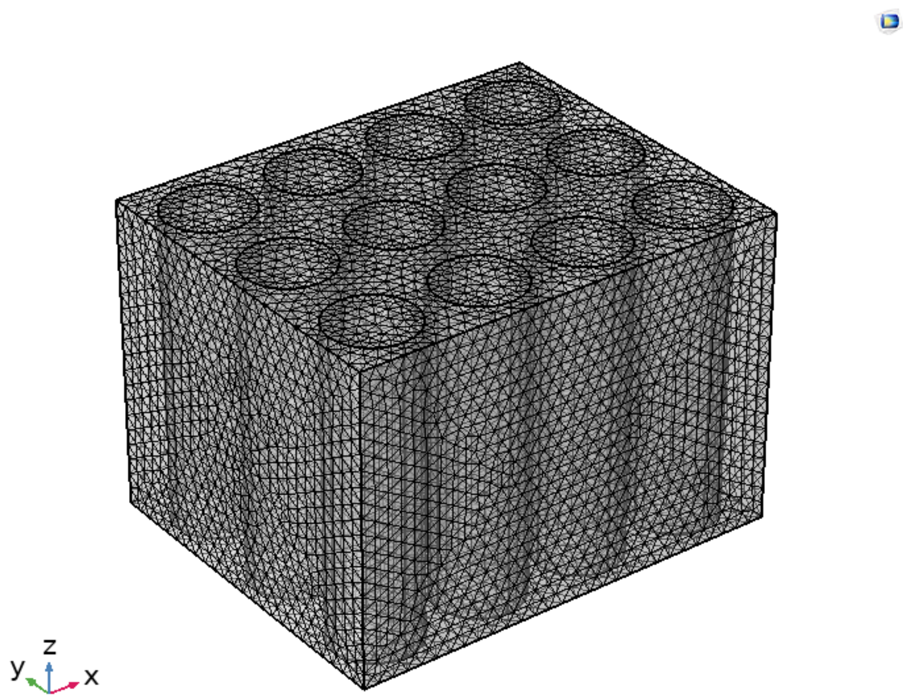

(B)

Continuous

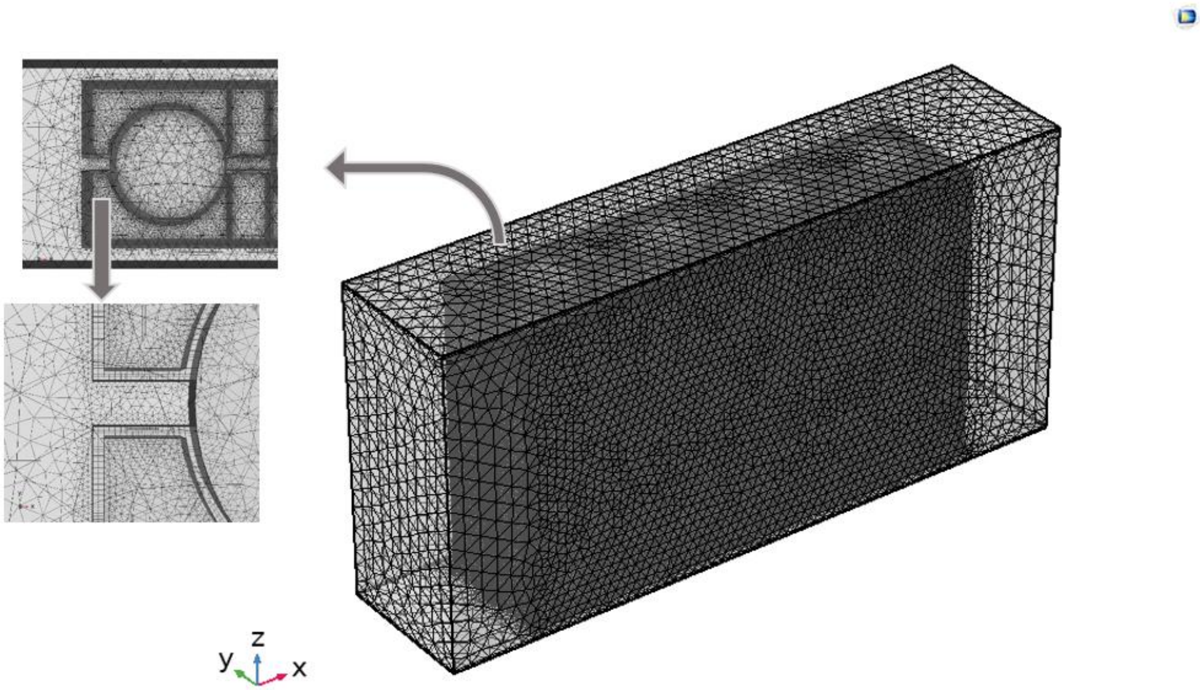

(C)

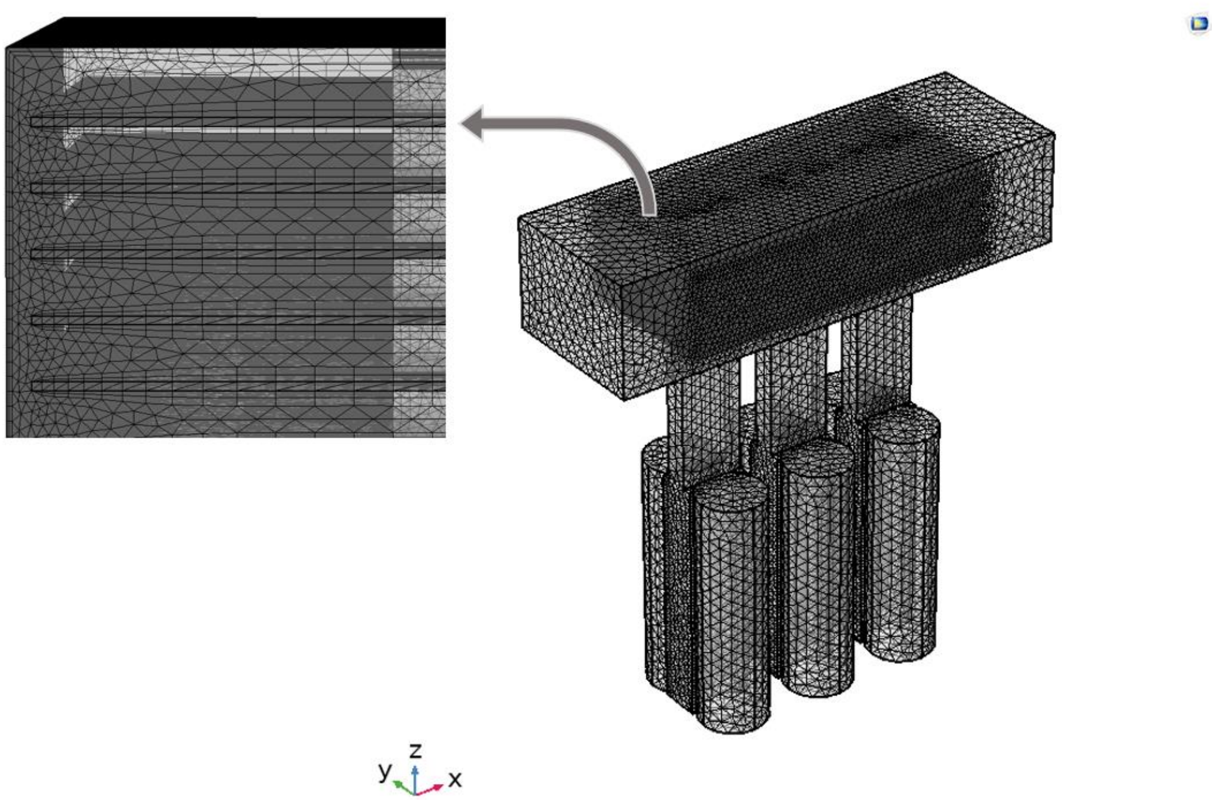

(D)

Continuous

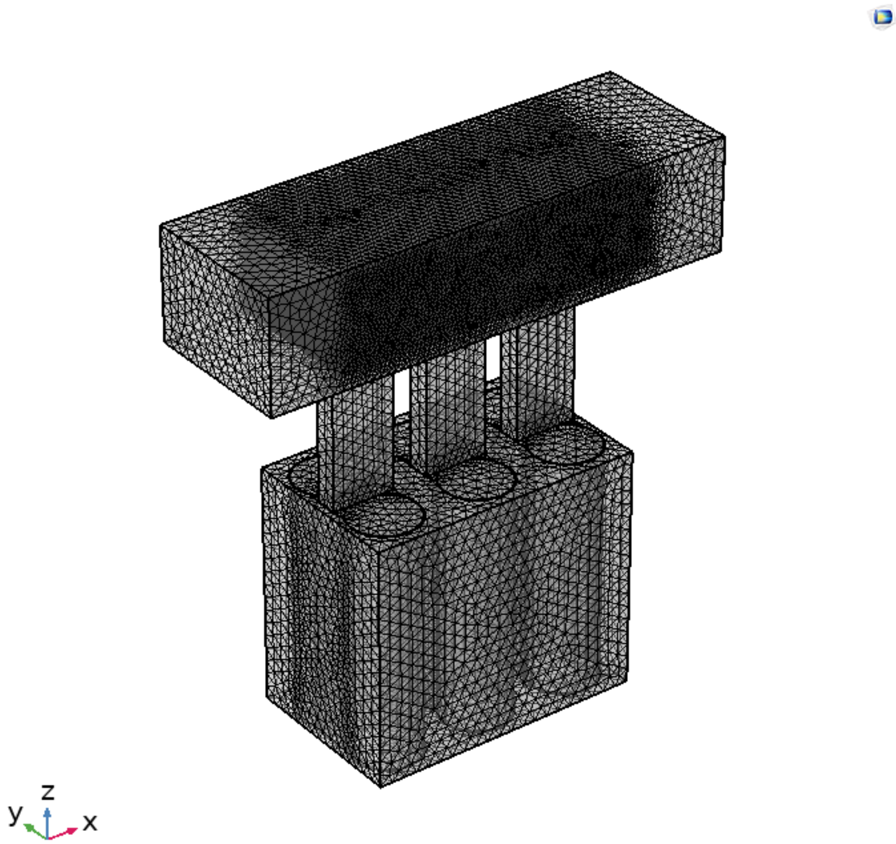

(E)

Figure (3.8) Meshing structure of (A) Air-Model, (B) PCM-Model, (C) PCM/Fin-Air-Model, (D) HP-Model, and (E) HP/PCM-Model.

Table (3.4) Mesh independence number of different models.

Model type	No. of element	Variation percentage in T_{max}
Air-Model	899,073	0.11%
PCM-Model	435,072	0.04%
PCM/Fin-Air-Model	1,714,672	0.24 %
HP-Model	1,447,276	0.16
HP/PCM-Model	1,513,462	0.15 %

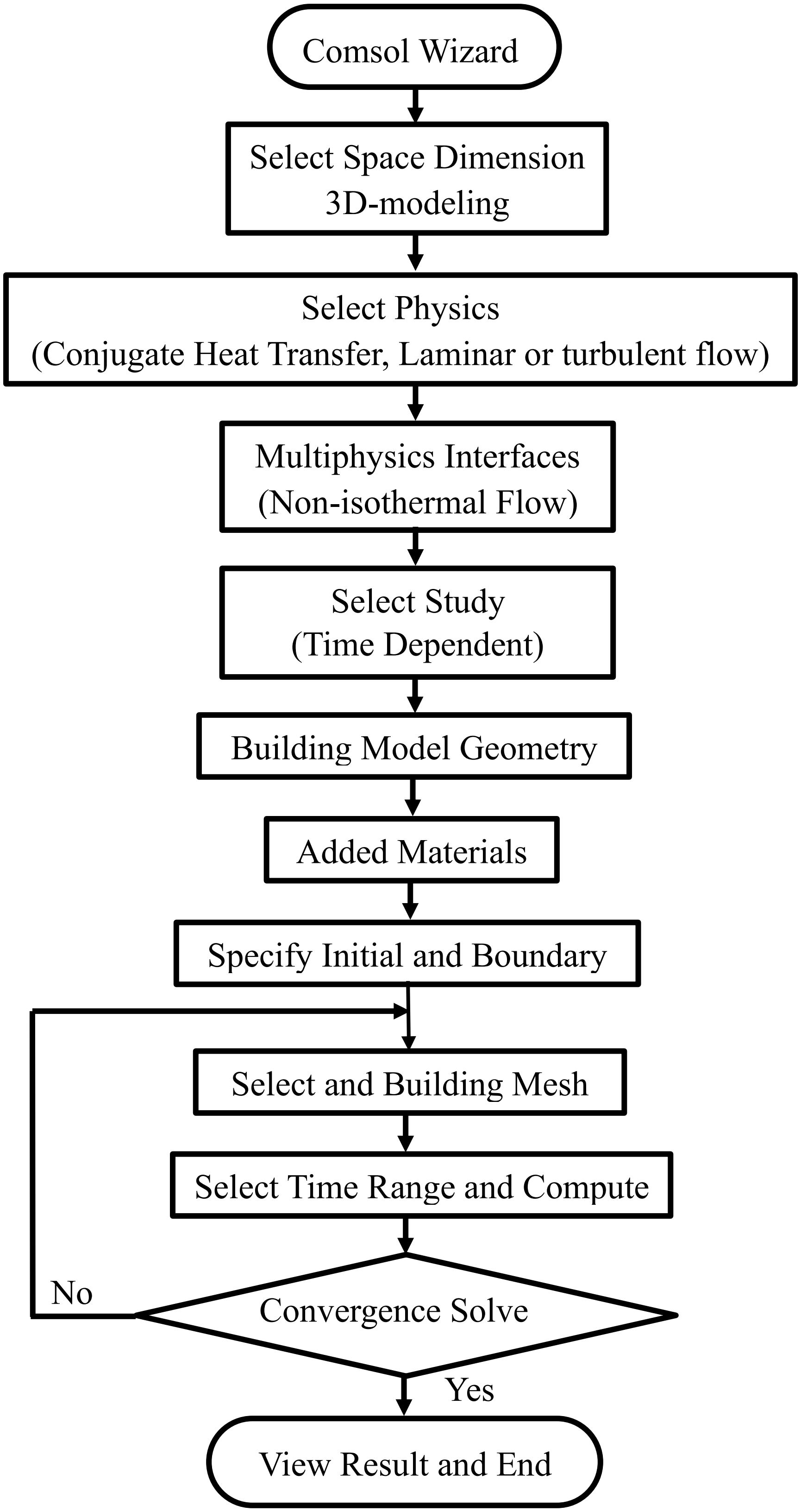

Figure (3.9) Flow chart of the numerical solution.

Chapter Four

Experimental Work

Chapter Four

Experimental Work

4.1 Introduction

In this work, the battery surface temperature and temperature distribution at various operation conditions of discharge rates of 1, 2, and 3C, inlet air velocities of 0.75 and 1.5 m/s at ambient temperature of 40 °C using five different models are investigated experimentally. Also, the battery heat generation and discharge voltage are measured.

The five models included two standard models and three novel models. The two standard models are used standalone PCM refers as (PCM-Model) and forced air refers as (Air-Model) to cool the battery pack, while the first novel model refers as (PCM/Fin-Air-Model), uses aluminum fins coupled with PCM and forced air, the second novel model refers as (HP-Model) uses a special design of a flat HP having a double circular grooved evaporator and finned condenser, the third novel model refer as (HP/PCM-Model) is same as second model HP-Model in addition to use of the PCM combination in the evaporator section.

The purpose of usage standard models is to assess the performance of new hybrid models, as well as the results acquired from these novel models were compared with other literature studies that employed hybrid models of PCM and forced air combination to verify the effectiveness of the present modes. All tested models consist of twelve cylindrical batteries of 18650-type $LiCoO_2$ arranged as three batteries in parallel electrical connection and four batteries in series electrical connection. The main specifications of the Li-ion batteries are presented in Table (4.1).

Table (4.1) Specifications for Li-ion batteries type 18650-type $LiCoO_2$ [88].

Properties	Specifications	Units
Nominal capacity	2600	[mAh]
Dimension (diameter × length)	18.2×65	[mm]
Mass	46	[g]
Heat capacity	830	[J/kg °C]
Positive electrode	Lithium cobalt oxide ($LiCoO_2$)	
Negative electrode	Graphite	
Nominal voltage	3.7	[V]
Cut-off voltage	2.5-4.2	[V]
Internal resistance	41-43	[m Ω]

4.2 Test Rig

Figures (4.1) and (4.2) illustrate the experimental system's schematic diagram and the photograph of the test rig, respectively. The system consists of the following components: air duct, DC load tester, power supply, temperature sensor with data logger, battery resistance meter, digital Pitot tube, air blower, gate valve, laptop, and test section.

Two air cooling ducts (Type-I and Type-II) are utilized in the present study to evaluate the effectiveness of cooling air velocity on the models, as shown in Figures (4.3) and (4.4). The ducts differ only in cross-sectional area, while the other configurations remain symmetrical. Type-I has a cross-sectional dimension of (110 × 70) mm² and is used for the Air-Model and PCM/Fin-Air-Model. Type-II, with a cross-sectional dimension of (30 × 88) mm², is employed for cooling the condenser section of the HP-Model and HP/PCM-Model. Both ducts feature a conical entrance with a 3.5º incline angle to ensure uniform air distribution [92]. Additionally, they are equipped with an air blower and an adjustable gate valve to regulate air velocity.

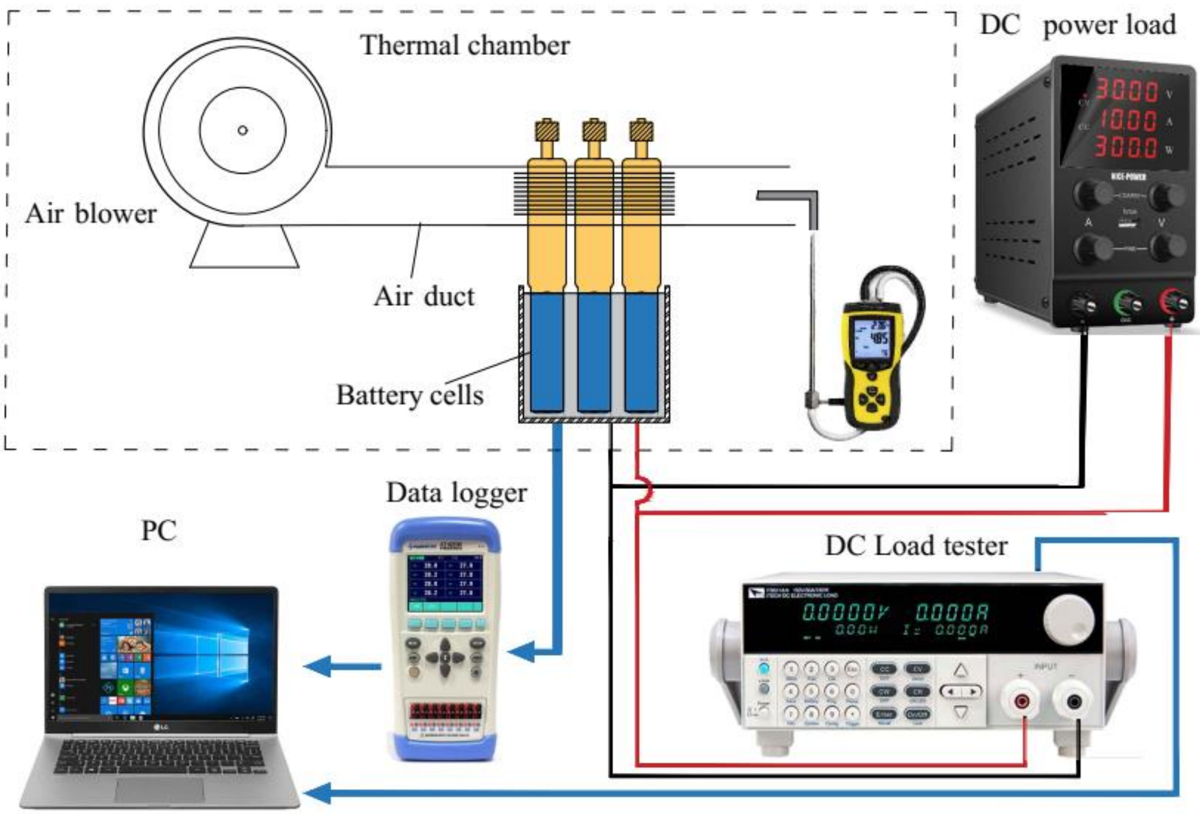

Figures (4.1) Schematic diagram of the experimental system.

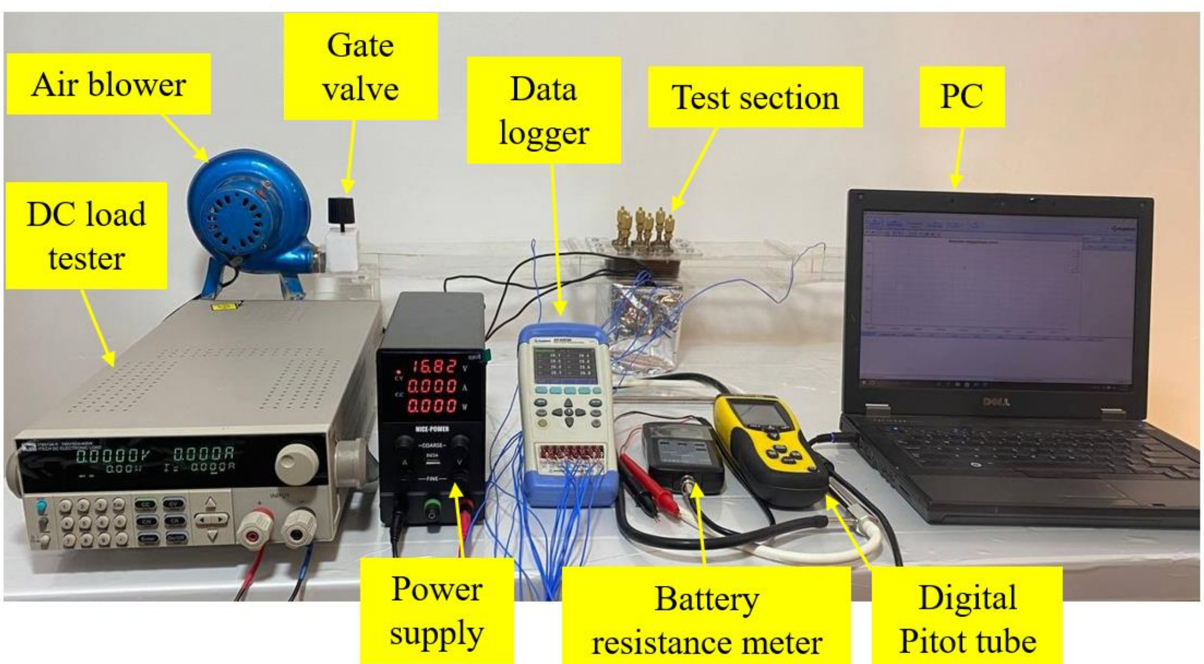

Figures (4.2) Photograph of the test rig**.**

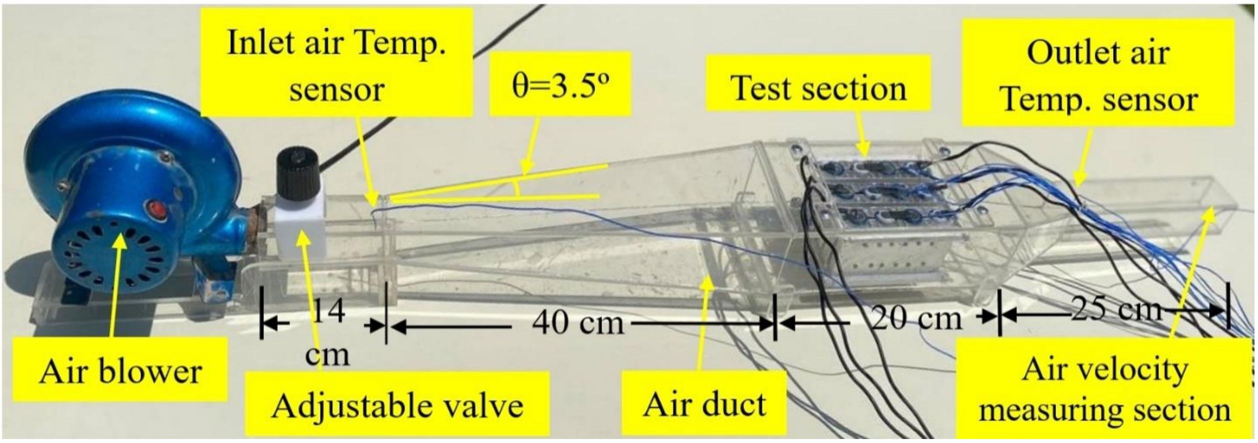

Figures (4.3) Photograph of Type-I air duct with PCM/Fin-Air-Model.

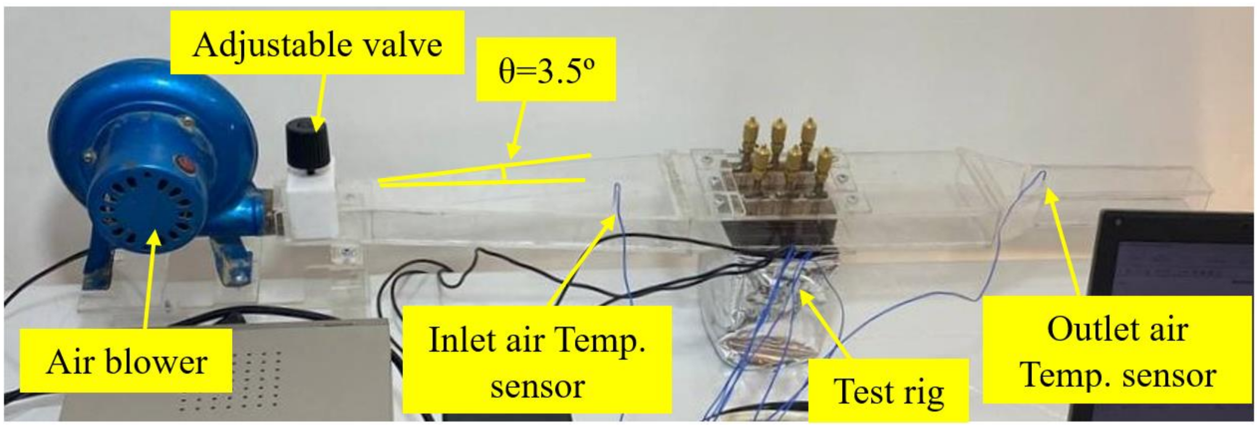

Figures (4.4) Photograph of Type-II air duct with HP/PCM-Model.

4.2.1 Air-Model

The Air-Model involves the use of forced air convection only. It consists of twelve batteries connected in three batteries in parallel and four batteries in series. The distance between each adjacent cell is 23 mm in longitudinal battery separation (SL) and 25 mm in transverse battery separation (St). The schematic diagram and Photograph of the Air-Model are depicted in Figures (4.5) and (4.6), respectively. The model is positioned in a Type-I air duct to test forced-air velocities and measure air temperatures at the inlet and outlet.

To record temperature, eight K-type thermocouples with 0.2 °C accuracy were employed. Two thermocouples are utilized to measure the temperature of the cooling air before and after the battery pack, while six thermocouples are affixed to the middle point of the batteries' surface at various locations to measure T_{max} and ΔT_{max}, as illustrated in the Figure (4.5A). The thermocouple sensors are connected to a temperature data logger of the Applent-AT4208 type, which automatically records temperature readings and transmits them to the computer.

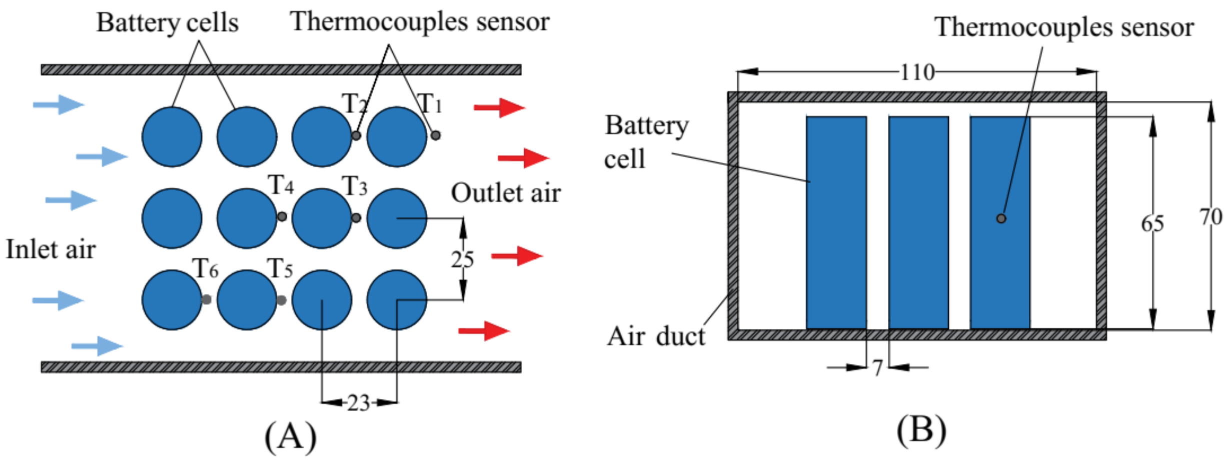

Figure (4.5) Schematic diagram of the Air-Model (A) Top view (B) Front view. (dimensions unit are in mm).

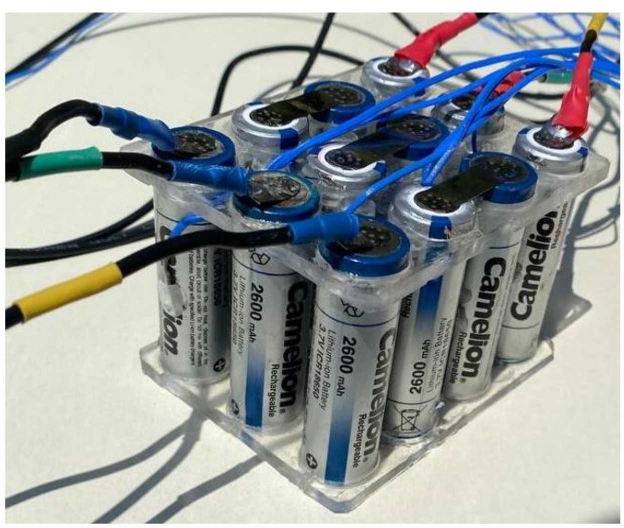

Figure (4.6) Photograph of the Air-Model.

4.2.2 PCM-Model

The present model is based only on the passive cooling technique. Where the heat generated from the battery pack is absorbed by the PCM without using an external power source owing to the high latent heat of its phase change. The arrangement and distance between each adjacent cell of the PCM-Model is the same as the Air-Model only the gaps between the battery cells are filled with PCM as shown in Figures (4.7 A and B).

A PCM type Rubitherm-RT47 having a melting area between (41-48 °C) is used in this model. The selection of PCM was to be suitable for high-temperature operation and maintain the battery pack temperature within the optimal operating temperature limit (50 °C). The PCM properties are listed in Table (3.2). The model is completely covered by a 1.5 cm thickness of thermal wool insulation. Moreover, six K-type thermocouples were employed to record battery surface temperature and distribution at the same location in the Air-Model as shown in Figure (4.7A).

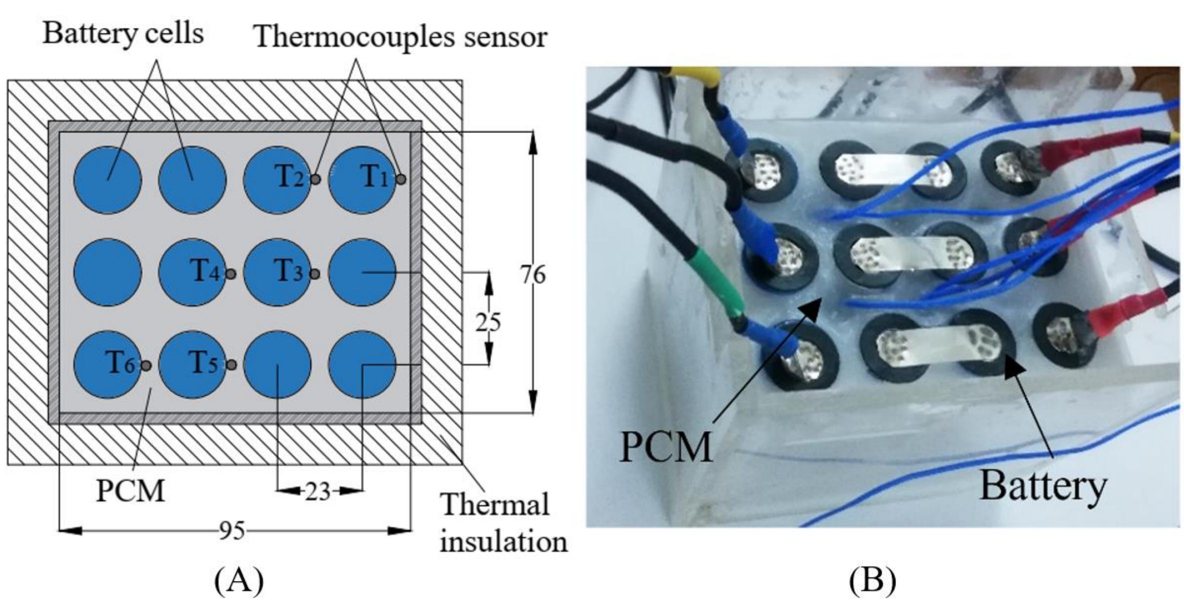

Figure (4.7) PCM-Model test section with temperature sensor location (A) Schematic diagram (B) Photograph (All dimensions are in mm).

4.2.3 PCM/Fin-Air-Model

In this model, a new hybrid cooling system combined of active and passive cooling are used. The model consists of twelve batteries arranged in three batteries in parallel and four batteries in series. All batteries are enclosed with six shells made from aluminum plates with a thickness of 0.48 mm. Each shell is filled with 0.03 kg of pure PCM-type Rubitherm-RT47 and provided with six aluminum fins to enhance heat transfer through the PCM layer. Each battery row was almost surrounded by two aluminum shells on each side to improve heat conduction between the batteries and the aluminum shell surfaces. A 6 mm air channel was left between the rows to allow cooling air passage, as depicted in Figures (4.8) and (4.9).

The batteries and aluminum shell's contact areas are covered with a small amount of thermal conductive oil to decrease interfacial thermal resistance. Eight K-type thermocouples were employed, two thermocouples to record cooling air temperature at the inlet and outlet and six thermocouples to record batteries surface temperature which is distributed at the same location in the Air-Model as shown in Figure (4.8A). The model is positioned in a Type-I air duct to test forced-air velocities and measure air temperatures at the inlet and outlet.

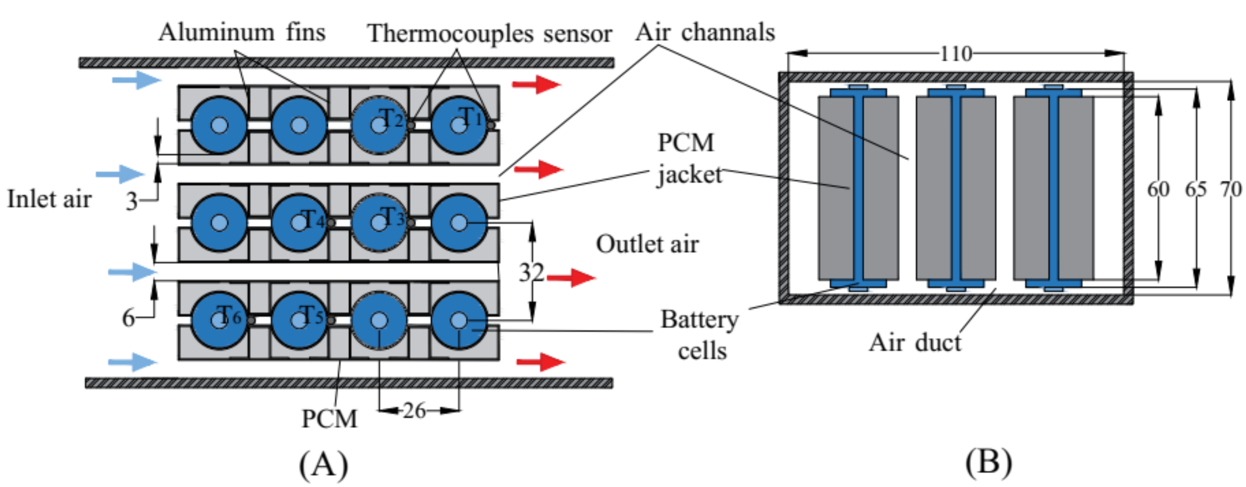

Figure (4.8) PCM/Fin-Air-Model schematic drawing (A) Top view (B) Front view (dimensions unit are in mm).

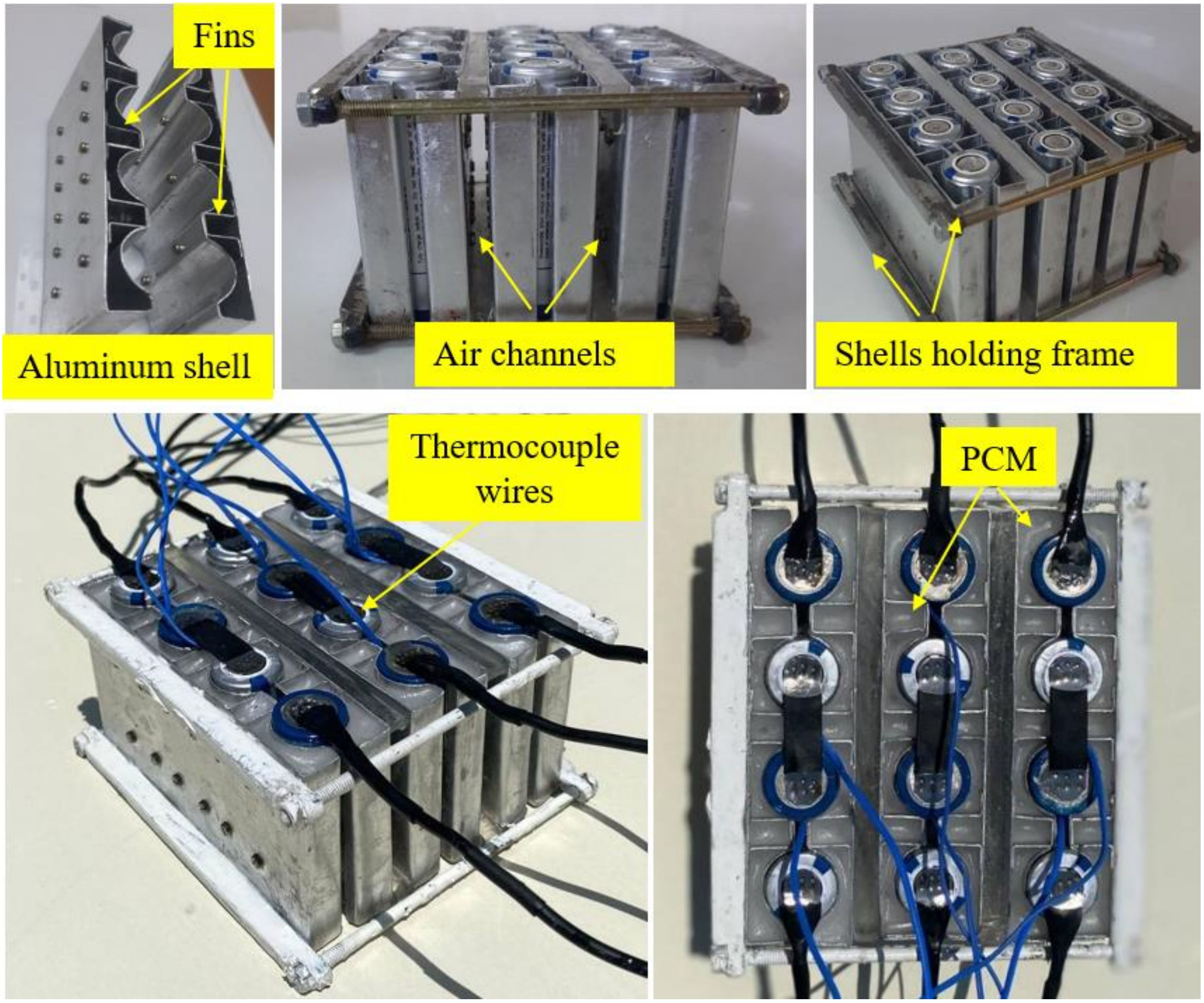

Figure (4.9) Photograph of PCM/Fin-Air-Model.

4.2.4 HP-Model and HP/PCM-Model

The second (HP-Model) and third (HP/PCM-Model) novel models consist of six flat HPs, in addition to the use of PCM integration for the HP/PCM-Model only. HPs work depending on the thermosyphon effect of vapor pressure difference and the gravity effect between the evaporator and condenser sections (without using the wick structure). So, when the working fluid inside the HP absorbs the heat and evaporates, the vapor pressure difference is rapidly formed between the evaporation section and the condensation section, which moves the hot vapor to the condensation section where the heat is released and the condensed vapor returns to the evaporation section due to gravity.

Each HP is made from a cylindrical copper tube with an outer diameter of 15.8 mm and an inner diameter of 14.6 mm. The HP has been formed to get a double circular groove with an arc angle of (θ=120°) in the outer surface of the evaporator section and an oval cross-sectional of (21 × 5) mm^2 in the condenser section. The two circular groove shapes were made to get direct contact with the two cylindrical battery surfaces which increases the heat transfer area and reduces the thermal resistance, while the oval cross-sectional reduces the pressure losses in the forced air convection. The contact areas between the HP evaporator and batteries are coated with a thin layer of thermal conductive silicone to reduce heat resistance. The Photograph of HPs is shown in Figure (4.10), while the schematic diagram of the HPs and PCM combination is shown in Figure (4.11).

Furthermore, ten pieces of rectangular copper fins (88 × 40 × 0.35 mm^3) were welded on the condenser section to enhance the heat transfer with a space of 2.3 mm between two adjacent fins. The total length of the HP is 140 mm while the condenser and evaporator lengths are (30 and 65 mm), respectively. The filling ratio of 40±5% with acetone as a working fluid was used, and a vacuum pump was used to produce the vacuum inside the HP through the service valve located at the top of the HP. The thermal properties of acetone are presented in Table (4.2).

The condenser section is placed in the Type-II air duct to examine the air velocity variation effect and record the inlet and outlet air temperatures. Thermal wool insulation with 1.5 cm thickness was used to insulate the evaporator and adiabatic sections of HP in addition to the upper part that contains the service valve. Furthermore, 0.03 kg of pure PCM type Rubitherm-RT47 is used to submerge the battery pack and the evaporator section in the HP/PCM-Model. The usage of PCM integration in the HP/PCM-Model is to get more temperature uniformly and control, as well as, to assess the effectiveness of PCM adding.

(A) (B)

(C) (D)

Figure (4.10) Photograph of the HP-Model: (A) copper tube of the HP, (B) fins, (C) HP after fabrication, and (D) HP with Li-ion battery connections.

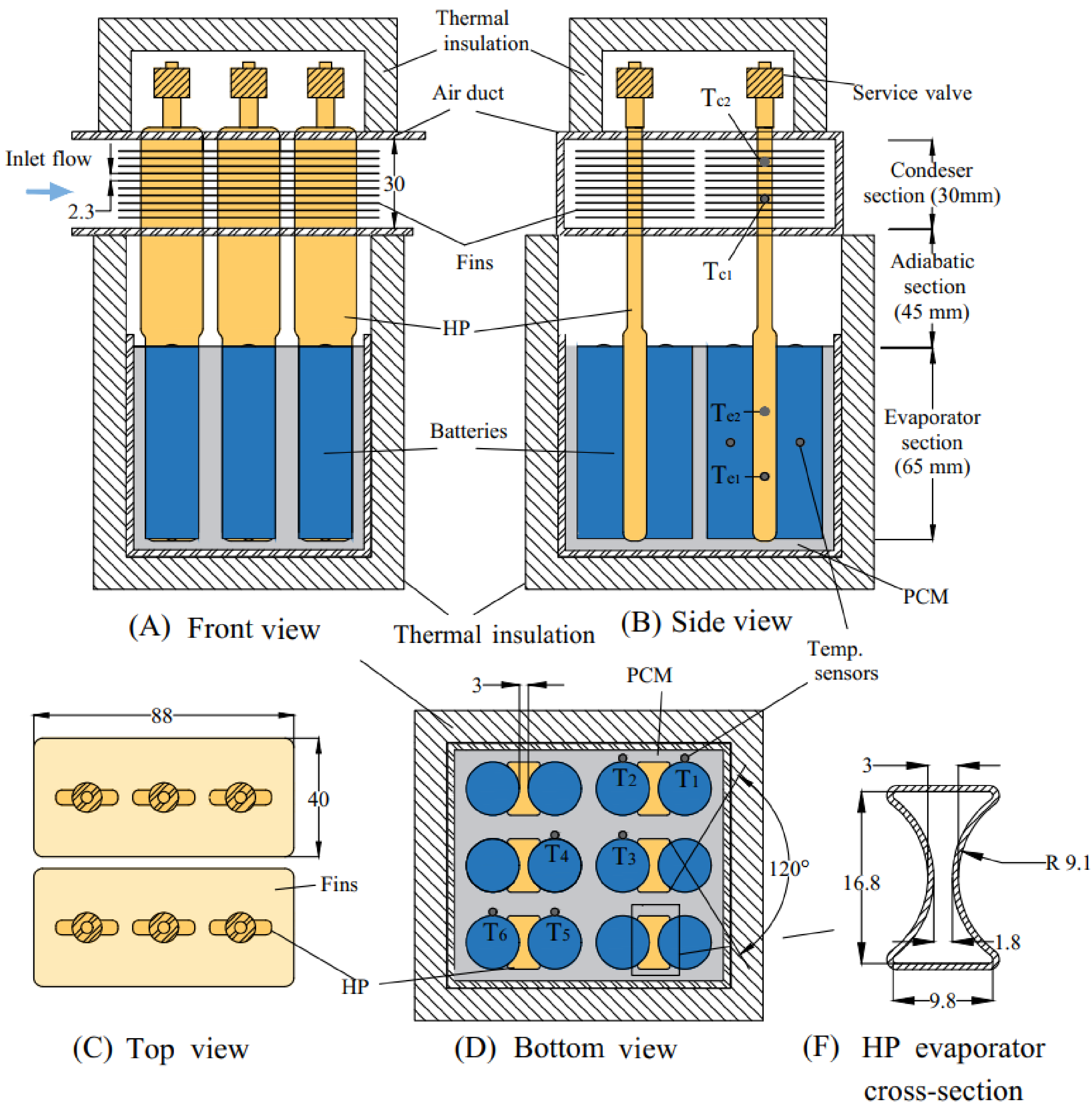

Figure (4.11) Schematic diagram of the HP/PCM-Model and temperature sensor location (A) front view (B) side view (C) top view (D) bottom view (F) HP evaporator cross-section. (All dimensions are in mm).

Twelve K-type thermocouples with a 0.2°C precision were used to record the temperature. Six thermocouples were attached to the middle of the outer surface of the batteries at different locations on the batteries to measure the surface temperature of the batteries and the temperature difference between them. Four thermocouples were used to measure the average temperature of HP sections, two at the condenser section and two at the evaporator section. Furthermore, two thermocouples were used to measure the cooling air temperature at the inlet and outlet of air ducts. The locations of thermocouples are illustrated in the Figure (4.11).

Table (4.2) Thermo-physical properties of the acetone [93].

Parameter	Value	Units
Boiling point	56.3	[°C]
Latent heat of vaporization	532.4	[kJ/kg]
Thermal conductivity of liquid	0.176	[W/m °C]
Specific heat capacity of liquid	2.15	[kJ/kg °C]
Liquid phase density	791	[kg/m³]

4.3 Battery Heat Generation

The volumetric heat generation $\dot{Q}_{gen}$ from the battery cell in (W/m³) can be determined by summing the heat dissipation with air Q_a, and the variation in heat battery capacity Q_b dividing on the batteries volume V_b [7,48]:

$$\dot{Q}_{gen} = \frac{1}{V_b}(Q_a + Q_b) \tag{4.1}$$

The heat dissipation through forced air convection can be calculated as follows [17]:

$$Q_a = \dot{m}_a \times cp_a \times \left(T_{a,out} - T_{a,in}\right) \tag{4.2}$$

The term cp_a is the air heat capacity, $T_{a,in}$ and $T_{a,out}$ are the inlet, and outlet air cooling temperatures, $\dot{m}_a$ is the mass flow rate of air cooling that is calculated as:

$$\dot{m}_a = \rho_a \times u \times A_d \tag{4.3}$$

Where ρ_a and u represents the air density and velocity, while A_d is the cross-sectional area of the air duct.

The variation of thermal battery capacity is found using:

$$Q_b = m_b \times cp_b \times \frac{\Delta T}{\Delta t} \tag{4.4}$$

The m_b and cp_b are the battery mass in kg and battery-specific heat capacity, while the $\Delta T/\Delta t$ describes the battery temperature variance with time.

4.4 HP Thermal Resistance Behavior

In particular, the thermal resistance of the HP is considered the most important parameter that explains the heat and mass transfer behavior of the HP [36]. In the present study, the total thermal resistance of HP (R_{th}), which includes several resistances, can be determined using [94]:

$$R_{th} = \frac{\Delta T_{HP}}{Q_{HP}} \tag{4.5}$$

Where the ΔT_{HP} is the average temperature difference between the evaporator and condenser surface of HP.

While Q_{HP} is the amount of heat transmission by each HP. Since, there are six HPs to transmit the heat to the condenser section, the Q_{HP} is equal to the heat released by the forced air divided by the number of HPs (six):

$$Q_{HP} = Q_a/6 \tag{4.6}$$

And the amount of heat absorbed by the forced air (Q_a) can be found based on Equation (4.2).

4.5 Measurement Devices and Complementary Instruments

4.5.1 Battery discharge electronic load tester

Battery discharge electronic load tester that is shown in Figure (4.12) type IT8513A+ series single channel with high resolution, and automatic test function is used for the discharge battery pack. The maximum voltage, current, and power of the model are

150V, 60A, and 400W, respectively. It has four operating modes; Constant Voltage (CV), Constant Current (CC), Constant Resistance (CR), and Constant Power (CP). It has a voltage measurement resolution of up to 0.1mV / 0.1mA

Figure (4.12) Electronic Load Tester.

4.5.2 Adjustable DC power supply

An adjustable DC power supply shown in Figure (4.13) is used to charge the battery pack. It has two types of power output modes: constant voltage output (CV) and constant current output (CC). The output voltage and current are (0-30V) and (0-10A), respectively. The current and voltage stabilities are lower than 0.2%+3mA and 0.1%+3mV, respectively.

Figure (4.13) Adjustable DC power supply.

4.5.3 Temperature measurement

Two AT4208 Multi-channel temperature meter devices with 8 thermocouples Type-K with a temperature range of (−50 to 800°C), 0.1 ºC resolution, and an accuracy of 0.2 ºC were used to measure the temperature in different locations in the models, and the rig. The temperature reader and thermocouple are shown in the Figure (4.14). All thermocouples were connected to acquisition devices through consenting wires. The data collected from thermocouples and data acquisition devices was sent to a laptop PC via USB cable and stored for the next analysis. AT4208 Multi-channel has been certified calibration test report in Appendix A-2.

Figure (4.14) Multi-channel temperature meter.

4.5.4 Vacuum pump

A two-stage evacuated pump type VALUE with high performance as shown in Figure (4.15) is used to purge each HP from air and non-condensable gases after the charging of working fluid (acetone). The vacuum pump can achieve a high vacuum level of -15 psi.

Figure (4.15) Vacuum pump.

4.5.5 Airflow and pressure drops measurement

A digital pitot tube anemometer meter (Model TA400) shown in Figure (4.16) is used for measuring the amount of air velocity and pressure drop through the battery pack. The data was collected from a digital pressure anemometer device sent to a laptop PC via a USB cable and stored for analysis. A digital pressure anemometer provides accurate and fast readings with a wide range of (0 to 80 m/s), with resolution and accuracy amount of 0.01 m/s ± 2.5 % and 1 Pa ± 0.3 % for velocity and pressure, respectively. The digital pressure anemometer has been certified calibration test report as shown in Appendix A.

Figure (4.16) Digital pitot tube.

4.5.6 Battery electric internal resistance measurement

The battery internal resistance measurement device shown in Figure (4.17) is used to measure the internal electrical resistance of individual battery cells or battery packs, as well as, to ensure that all individual battery cells have the same internal electrical resistance before each cycle of operation. It has an internal resistance measurement range between 0~200Ω with a minimum resolution of 0.01 mΩ and a minimum accuracy of 0.7%.

Figure (4.17) Battery internal resistance measurement device.

4.6 Experimental Procedures

In the present study, the five cooling systems were examined at the same operation conditions and several necessary procedures were considered to obtain experimental data can be summarized by following steps:

1- All models were positioned in an environmental room to regulate the operating temperature, which was set at 40 °C with a variation of ±1 °C.

2- The batteries are charged using a DC Power Supply at a constant current charge rate of 0.5C (3.9 A) until the voltage of the battery pack reaches the cut-off charge value of 16.8V, and then the batteries are charged at a constant voltage of 16.8V allowing the charging current to steadily drops to a very low value. This method of charging is regarded as a standard approach that does not damage the batteries [16].

3- The air velocities are maintained at a specific speed of (0.75 and 1.5 m/s) using an adjustable gate valve and measured using a Digital TA400 Pitot-tube anemometer before each experiment.

4- Programmable DC Electronic Load type IT8513A+ is used to discharge the battery at a constant current and a specific discharge rate of (1C, 2C, and 3C), where C refers to the rate of battery discharge relative to its maximum capacity. The discharge rate and their corresponding current are shown in Table (4.2).

5- Every minute, the temperatures and voltages are recorded and saved on the computer.

The battery pack consists of twelve cylindrical 18650-type $LiCoO_2$ Li-ion batteries with a maximum and minimum cut-off voltage of 4.2 V and 2.5 V, respectively, Since the batteries are connected as three batteries in parallel and four batteries in series, the maximum and minimum cut-off voltage the battery pack is ($4\times4.2=16.8$ V) and ($4\times2.5=10$ V), respectively. Through the discharge process, the terminal voltage of the battery pack drops from 16.8 V to its cut-off terminal voltage, which is set at 10 V to avoid the battery's damage. Table (4.3) lists the reading devices' precisions and measuring ranges.

Table (4.3) Discharge rates and equivalent current values.

Discharge Rate	Constant Current	Time of discharge process
1C	7.8 A	60 min
2C	15.6 A	30 min
3C	23.4 A	20 min

Table (4.4) Device's precisions.

Devices	Range	Resolution	Accuracy
Programmable DC-load tester type IT8513A+	0-60A 0.1-150 V	0.1 mA 0.1 mV	±0.05%
Velocity and pressure digital Pitot tube type TA400	1-80 m/s 0-5000 Pa	0.01 m/s 1 Pa	±2.5% ±0.3%
Temperature data logger type Applent-AT4208	200 to 1300 ºC	0.1 ºC	±0.2%
Battery resistance meter type YR1035	0.0003-200 Ω	0.01 mΩ	0.6%

4.7 Uncertainty Analysis

The **Abd et al., 2022** [95] method is used to evaluate the indirect uncertainties of the measuring amount which formed as:

$$w_y = \left\{\sum\left[\left(\frac{\partial y}{\partial x_i}\right)^2 w_{x_i}^2\right]\right\}^{1/2} \tag{4.7}$$

Where w_y, y, x_i, and w_{xi} represent the overall uncertainty, displayed functions, independent variables, and uncertainty of various variables, respectively.

Hence the overall uncertainties of the ΔT_{max}, $m^{\cdot}$, $Q^{\cdot}_{gen}$, Q_{HP} and R_{th} are determined as follows:

$$w_{\Delta T_{max}} = \left[\left(\frac{\partial \Delta T_{max}}{\partial T_{max}}\right)^2 w_{T_{max}}^2 + \left(\frac{\partial \Delta T_{max}}{\partial T_{min}}\right)^2 w_{T_{min}}^2\right]^{1/2} \tag{4.8}$$

Where ΔT_{max} equal to, $(\Delta T_{max} = T_{max} - T_{min})$. T_{max} and T_{min} the maximum and minimum battery surface temperature, respectively.

$$w_{\dot{m}_a} = \left[\left(\frac{\partial \dot{m}_a}{\partial \rho}\right)^2 w_\rho^2 + \left(\frac{\partial \dot{m}_a}{\partial u}\right)^2 w_u^2 + \left(\frac{\partial \dot{m}_a}{\partial A_d}\right)^2 w_{A_d}^2\right]^{1/2} \tag{4.9}$$

Where $\dot{m_a}$, ρ and v the mass flow rate, density, and velocity of cooling air, respectively. A is the area of the duct.

$$w_{\dot{Q_{gen}}} = \left[\left(\frac{\partial \dot{Q_{gen}}}{\partial m_b}\right)^2 w_{m_b}^2 + \left(\frac{\partial \dot{Q_{gen}}}{\partial cp_b}\right)^2 w_{cp_b}^2 + \left(\frac{\partial \dot{Q_{gen}}}{\partial \Delta T_b}\right)^2 w_{\Delta T_b}^2 + \left(\frac{\partial \dot{Q_{gen}}}{\partial \dot{m}_a}\right)^2 w_{\dot{m}_a}^2 + \left(\frac{\partial \dot{Q_{gen}}}{\partial cp_a}\right)^2 w_{cp_a}^2 + \left(\frac{\partial \dot{Q_{gen}}}{\partial \Delta T_a}\right)^2 w_{\Delta T_a}^2\right]^{1/2} \quad (4.10)$$

Where $\dot{Q_{gen}}$ is the battery heat generation. m_b, cp_b and ΔT_b are the mass, specific heat, and temperature increase of batteries, respectively. cp_a and ΔT_a the specific heat and temperature increase of cooling air.

$$w_{Q_{HP}} = \left[\left(\frac{\partial Q_{HP}}{\partial \dot{m}_a}\right)^2 w_{\dot{m}_a}^2 + \left(\frac{\partial Q_{HP}}{\partial cp_a}\right)^2 w_{cp_a}^2 + \left(\frac{\partial Q_{HP}}{\partial \Delta T_a}\right)^2 w_{\Delta T_a}^2\right]^{1/2} \quad (4.11)$$

Where Q_{HP} is the heat transfer by the heat pipe which equal to $\frac{1}{6}Q_a$.

$$w_{R_{HP}} = \left[\left(\frac{\partial R_{HP}}{\partial \Delta T_{HP}}\right)^2 w_{\Delta T_{HP}}^2 + \left(\frac{\partial R_{HP}}{\partial Q_{HP}}\right)^2 w_{Q_{HP}}^2\right]^{1/2} \quad (4.12)$$

Where R_{HP} is the overall thermal resistance of the heat pipe which is determined as $(R_{HP} = \frac{\Delta T_{HP}}{Q_{HP}})$. ΔT_{HP} is the temperature difference between the evaporator and condenser of HP.

Consequently, the indirect uncertainty of ΔT_{max}, $\dot{m}_a$, and $\dot{Q_{gen}}$, Q_{HP} and R_{th} based on the present study have been estimated to be 2.7%, 4.4%, 5.9%, 4.8%, and 5.7% respectively, in the current measurement.

The uncertainty symbols of the measurement variables have been determined, as Appendix D shows.

Chapter Five

Results and Discussion

Chapter Five

Results and Discussion

5.1 Introduction

In this chapter, the effectiveness of the BTMS using the five cooling configuration systems at different inlet air temperatures (T_{in}), inlet air velocities (u_{in}) and different discharge rates (C-rates) were experimentally and theoretically investigated. The drop in the battery pack temperature and temperature gradient between the batteries are considered the major problems for enhancing the BTMS. Therefore, our study focused on reducing the maximum operating temperature (T_{max}) of battery surfaces and the maximum temperature difference (ΔT_{max}) within the battery pack, which represents the difference between the maximum and minimum temperature of the battery surfaces through the battery pack.

Furthermore, the pressure drops (Δp) in the airflow across the models were determined experimentally and theoretically. Moreover, the drop in the working voltage of the battery pack and the amount of HP thermal resistance were calculated experimentally.

5.2 Experimental Results

The primary purpose of the experimental section was to investigate the effectiveness of using five cooling configuration models on the BTMS thermal performance. The experimentation was performed at T_{in} of 40 °C, u_{in} of 0.75 and 1.5 m/s, and C-rates of 1, 2, and 3C. The T_{max} , ΔT_{max} and ΔP within the battery pack was recorded for each model.

Furthermore, the drop in the working voltage of the battery pack and the amount of HP thermal resistance were calculated.

5.2.1 Thermal performance of the Air-Model under various u_{in} and C-rates

The effect of direct forced air using various u_{in} of 0.75 m/s and 1.5 m/s and C-rates of 1, 2, and 3C on T_{max} and ΔT_{max} at $T_{in} = 40$ ℃ is tested using the Air-Model. Figures (5.1 A and B) demonstrate that air velocity plays a significant role in reducing T_{max} and ΔT_{max}, particularly at a higher C-rate. With increasing the u_{in}, the rate of heat transfer rises, consequently improving heat removal.

At the 1C rate, the highest recorded values of T_{max} were 47.9 and 45.8 °C at the end of the discharge process (t=60 min) for the u_{in} of 0.75 and 1.5 m/s, respectively, as demonstrated in Figure (5.1 A). Conversely, ΔT_{max} reaches its highest values of 2.9 and 1.7 °C at u_{in} of 0.75 and 1.5 m/s, respectively, as demonstrated in Figure (5.1 B).

The 2C rate clearly shows the effectiveness of u_{in} on the T_{max} because the heat accumulates in the case of low velocities and becomes unsuitable for battery operation where it reaches 59.7, and 53.9 °C at the end of the discharge process (t=30 min), while the ΔT_{max} increase to 5.4 and 3.1 °C for u_{in} of 0.75, and 1.5 m/s, respectively.

Furthermore, at the 3C rate, a larger increase in the T_{max} occurs for all u_{in} values, reaching 62.4 °C for $u_{in} = 1.5\ m/s$ at the end of the discharge process (t=20 min), while peaking at 69 °C at a time of 17 s for $u_{in} = 0.75\ m/s$ at which the battery was automatically disconnected, as each battery has an automatic disconnector circuit for overheating, which was set at 70±2 to protect the battery cell, while the ΔT_{max} reaches 7.4 °C at $u_{in} = 0.75\ m/s$ and 5.7 °C at $u_{in} = 1.5\ m/s$. Based on the displayed results, it can be inferred that the use of a $u_{in} = 0.75\ m/s$ is insufficient for efficient battery cooling, mainly at high C-rates this is due to the large heat accumulation.

Furthermore, the results indicate that the T_{max} reduces by 2.1 °C (4.4%), 5.8 °C (9.7%), and 6.6 °C (9.5%) for 1, 2, and 3C rates, respectively, at the end of the discharge process with the increase in u_{in} from 0.75 to 1.5 m/s.

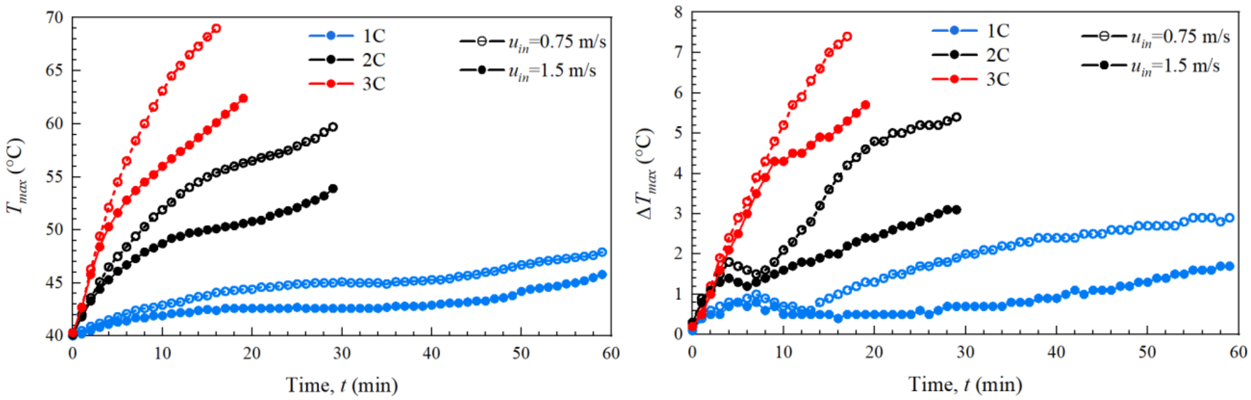

(A) (B)

Figure (5.1) Variation of (A) T_{max} and (B) ΔT_{max}, under various u_{in} and C-rates at T_{in} of 40 °C using the Air-Model.

5.2.2 Thermal performance of the PCM-Model under various C-rates

The impact of using pure PCM on T_{max} and ΔT_{max} at an operating temperature of 40 °C and under 1, 2, and 3C rates are illustrated in Figures (5.2 A and B). As observed in Figure (5.2 A), T_{max} exhibits a slow rise at a 1C rate compared to other discharge rates due to the small rate of heat generated, which is stored in the PCM as latent heat during discharge. However, at a 2C rate, T_{max} begins to rise more quickly, initially mirroring the pattern that was recorded at 1C, followed by a slight increase in the middle period due to phase transition in the PCM, and a rapid increase towards the end of the period, indicating complete melting in the PCM around the battery pack.

Under a 3C rate, T_{max} display a sharp increase, reaching its peak value before the end of the discharge period. This can be attributed to the amount of PCM heat storage does not adequately match the heat dissipation from the battery at the 3C rate, as well as the small thermal conductivity of PCM, which negatively affects the heat transfer rate to all parts of the PCM. The highest recorded values of T_{max} were 47.1, 53.5, and 69 °C for 1, 2, and 3C rates, respectively.

Furthermore, the ΔT_{max} between the batteries has similar behavior to that of T_{max} as shown in Figure (5.2 B). Consequently, extreme values of ΔT_{max} at 1, 2, and 3C rates were measured as 2.2, 3.5, and 6.7 °C, respectively. Thus, PCM can effectively distribute temperature at a lower C-rate below 2C rate. Nevertheless, as the C-rate increases to 3C, the battery's temperature rises more rapidly, exceeding the recommended limit.

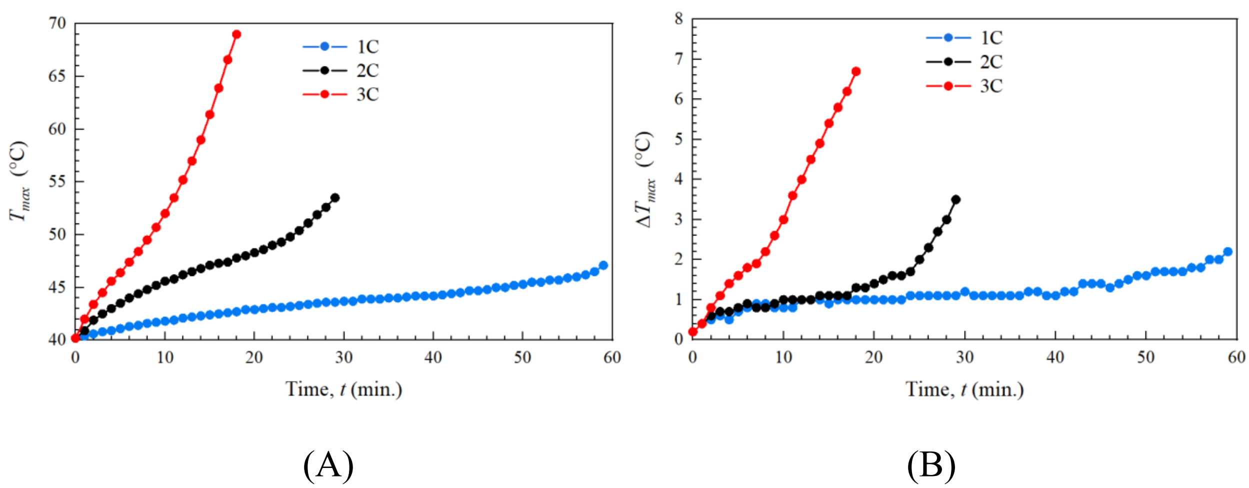

Figure (5.2) Variation of (A) T_{max} and (B) ΔT_{max}, under various C-rates at T_{amb} of 40 °C using the PCM-Model.

5.2.3 Thermal performance of the PCM/Fin-Air-Model under various u_{in} and C-rates

The impacts of using PCM integrated with aluminum fins and forced air on the T_{max} and ΔT_{max} at 40 °C and under various C-rates are depicted in Figures (5.3 A and B). The results illustrate a rise in both T_{max} and ΔT_{max} as the C-rate increases. Additionally, u_{in} of 0.75 and 1.5 m/s exhibit a slight impact on T_{max} and ΔT_{max}, especially at a 1C rate, where the battery temperature remains within the PCM melting area. As displayed in Figure (5.3 A), at the 1C rate, the highest recorded values of T_{max} were 45 and 44.3 °C for u_{in} of 0.75 and 1.5 m/s, respectively, while the highest recorded values of ΔT_{max} were 1.6 and 1.1 °C for the respective air velocities, as shown in Figure (5.3 B).

Along with the discharge increase to the 2C rate, the highest recorded values of T_{max} become 48.8 and 48.4 °C for u_{in} of 0.75 and 1.5 m/s, respectively, while the highest recorded values of ΔT_{max} become 2.2 and 1.4 °C, respectively. Furthermore, it can be noted from Figure (5.3 B) a sudden increase in the ΔT_{max} for 2 and 3C rates at times of 28 and 18 min, respectively, which can be attributable to the difference in the phase change transition time for the PCM around the batteries due to some difference in the amount of battery heat generation, as the PCM has a small heat conductivity, that leads to a sharp increase in batteries temperature for the batteries that firstly completed the PCM phase change while the other batteries have a slightly temperature increase due to existing of some amount of PCM which have not complete the phase change process.

Moreover, at a 3C rate, the highest recorded values of T_{max} were 55.2 and 52.9 °C for u_{in} of 0.75 and 1.5 m/s, respectively, while the highest recorded values of ΔT_{max} were 4.2 and 3.1 °C respectively. These results emphasize the PCM/Fin-Air-Model can maintain the ΔT_{max} and T_{max} closely to the recommended temperature range throughout all operational cycles, attributed to the presence of aluminum fins and PCM that enhance the thermal performance of the cooling system.

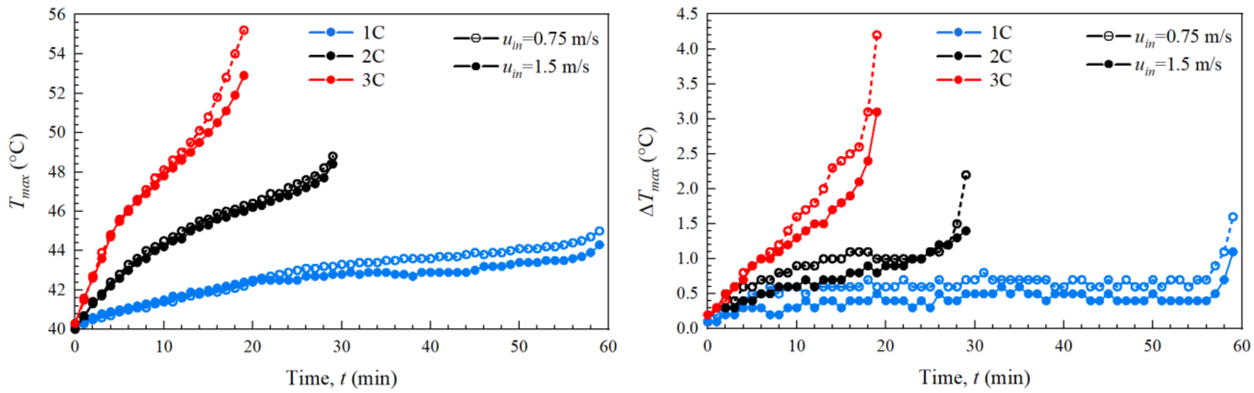

(A) (B)

Figure (5.3) Variation of (A) T_{max} and (B) ΔT_{max}, under various u_{in} and C-rates at T_{in} of 40 °C using the PCM/Fin-Air-Model.

5.2.4 Thermal performance of the HP-Model under various u_{in} and C-rates

The effects of the new HP-Model on the T_{max} and ΔT_{max} at 40 °C, using various C-rates of 1, 2, and 3C, and u_{in} of 0.75 and 1.5 m/s are shown in Figures (5.4 A and B). The results indicate an increase in the T_{max} and ΔT_{max} as the C-rate increases, while the air velocities have a marginal impact on the T_{max} at 1C and a significant impact at 2 and 3C, as shown in Figure (5.4 A). As the C-rate increases, the battery heat generation increases, and this causes a rise in the temperature difference between the cooling air and the HP condenser, which causes more heat exchange with an increase in air velocity. The largest values of T_{max} were 45.5, 51.8, and 59.9 °C at $u_{in} = 0.75\ m/s$ and C-rates of 1, 2, and 3C, respectively, where they were 44.4, 49.3 and 56.1 °C at $u_{in} = 1.5\ m/s$ and C-rates of 1, 2, and 3C, respectively.

On the other hand, the temperature difference of the battery pack varies a little with the air velocity change, where the largest values of ΔT_{max} were 1.1, 2.1, and 3.1 °C for $u_{in} = 0.75\ m/s$, respectively, and 1.2, 1.8 and 2.9 °C for $u_{in} = 1.5\ m/s$ respectively as shown in Figure (5.4 B). These results confirm that the new model of HP can keep the ΔT_{max} within the recommended range over all the periods of operation, while it can keep the T_{max} within the recommended range at 1 and 2C rates, and a slight increase over the recommended range at 3C.

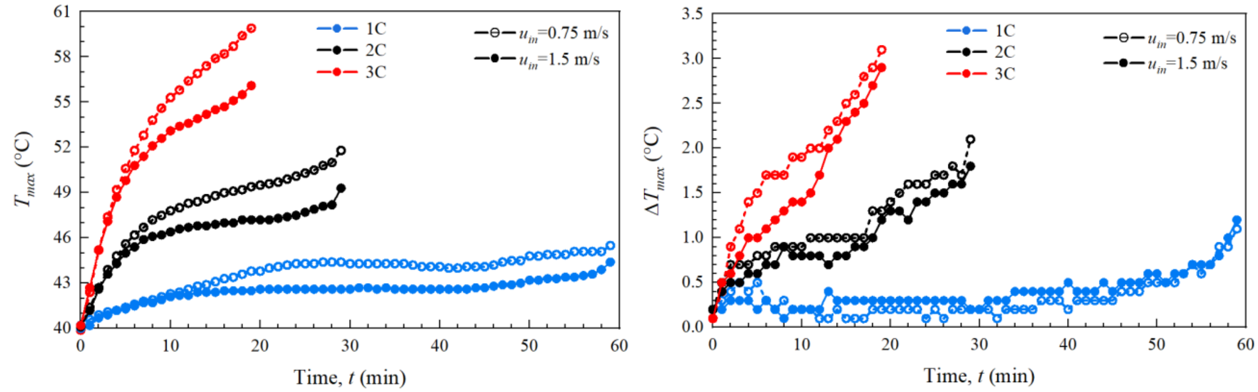

(A) (B)

Figure (5.4) Variation of (A) T_{max} and (B) ΔT_{max}, under various u_{in} and C-rates at T_{in} of 40°C using the HP-Model.

5.2.5 Thermal performance of the HP/PCM-Model under various u_{in} and C-rates

The impacts of the new model of HP coupled with PCM on the T_{max} and ΔT_{max} at 40 °C, under different C-rates of 1, 2, and 3C and u_{in} of 0.75 and 1.5 m/s are shown in Figures (5.5 A and B). The result indicates an increase in the T_{max} and ΔT_{max} with the C-rate increases, and the u_{in} has a slight effect on the T_{max} at 1C and a significant impact at 2 and 3C, as shown in Figure (5.5 A). The largest values of T_{max} were 44.7, 48, and 51.9 °C at $u_{in} = 0.75\ m/s$ and C-rates of 1, 2, and 3C respectively, where they were 44.4, 47.5, and 50.6 °C at an air velocity of $u_{in} = 1.5\ m/s$ and C-rates of 1, 2, and 3C respectively.

On the other hand, the largest values of ΔT_{max} were 0.9, 1.6, and 1.9 °C for air velocities of $u_{in} = 0.75\ m/s$, respectively, and 0.7, 1.5 and 1.8 °C for air velocities of $u_{in} = 1.5\ m/s$, respectively as shown in Figure (5.5 B). These results confirm that the HP/PCM-Model can keep the T_{max} and ΔT_{max} within the recommended range over all the discharge periods of 1, 2, and 3C.

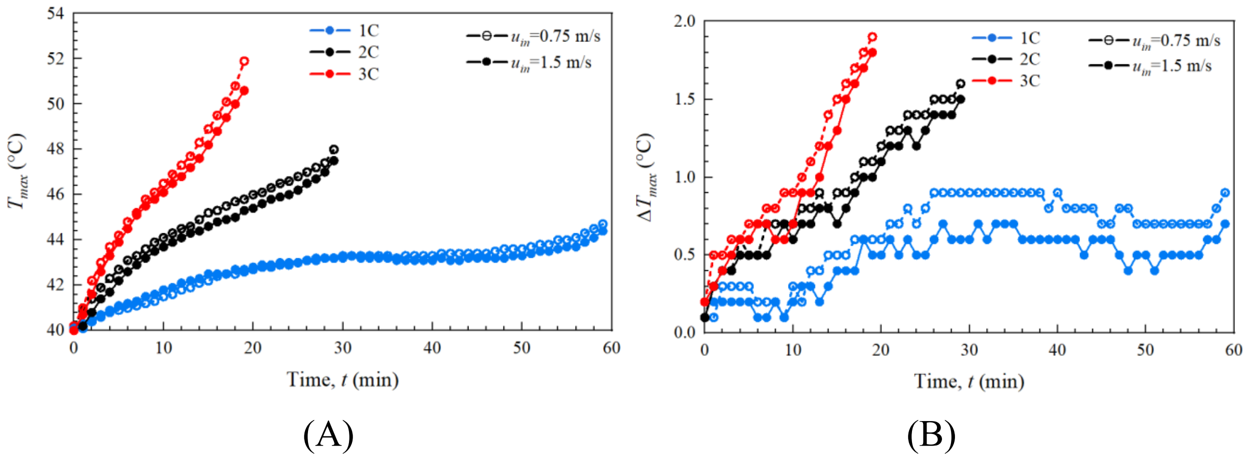

Figure (5.5) Variation of (A) T_{max} and (B) ΔT_{max}, under various u_{in} and C-rates at T_{in} of 40°C using the HP/PCM-Model.

5.2.6 Effectiveness of the present hybrid models compared with other models

The effectiveness of the present hybrid models (PCM/Fin-Air-Model and HP/PCM-Model) compared to other models (Air-Model, PCM-Model, and HP-Model) in reducing T_{max} and ΔT_{max} at $u_{in} = 1.5\ m/s$ and various C-rates are displayed in Figures (5.6 A-F).

At 1C rate, as shown in Figure (5.6 A), the PCM/Fin-Air-Model records the lowest T_{max} minimized by 1.5, 2.8, 0.1, and 0.1°C compared to the Air-Model, PCM-Model, HP-Model, and HP/PCM-Model, respectively. While the HP/PCM-Model could produce a lower ΔT_{max} as demonstrated in Figure (5.6 B).

As increasing the discharge to 2C rate, the HP/PCM-Model records a significant decrease in both T_{max} and ΔT_{max} compared to the Air-Model, PCM-Model, and HP-Model, and a slight decrease compared to the PCM/Fin-Air Model, as illustrated in Figures (5.6 C and D). Additionally, the Air-Model displays a fast initial increase in both T_{max} and ΔT_{max} compared to other models, owing to the lower thermal conductivity of air in comparison to PCM, aluminum fins, and HP. On the other hand, the T_{max} and ΔT_{max} continuous increase slightly until t=23 min in the PCM-Model, after that, they take a rapid increase form.

Furthermore, the HP-Model displays a large initial increase in T_{max} until t=7 min, then it became slightly constant until the end of discharge. In contrast, the T_{max} take a slight increase form in the HP/PCM-Model and PCM/Fin-Air-Model until the end of discharge. Furthermore, the results demonstrated that the HP/PCM-Model can reduce the T_{max} at the end of 2C rate by 6.4, 6, 1.8, and 0.9 °C compared to Air-Model, PCM-Model, HP-Model, and PCM/Fin-Air-Model, respectively. While the PCM/Fin-Air-Model can reduce the T_{max} at the end of 2C rate by 5.5, 5.1, and 0.9 °C compared to Air-Model, PCM-Model and HP-Model, respectively.

Moreover, when the discharge increases to a 3C rate, the HP/PCM-Model also records a significant decrease in both T_{max} and ΔT_{max} compared to the Air-Model, PCM-Model, and HP-Model, and a slight decrease compared to the PCM/Fin-Air Model, as illustrated in Figures (5.6 E and F). In contrast, the PCM-Model exhibits a faster rise in the middle period than the other models. The results indicate that the use of HP/PCM-Model can reduce T_{max} by 11.8, 18.4, 5.5, and 2.3 °C at the end of 3C rate compared to Air-Model, PCM-Model, HP-Model, and PCM/Fin-Air-Model, respectively. While the PCM/Fin-Air-Model can reduce the T_{max} at the end of 3C rate by 9.5, 16.1, and 3.2 °C compared to Air-Model, PCM-Model and HP-Model, respectively. Moreover, the largest value of ΔT_{max} using the HP-Model, HP/PCM-Model, and PCM/Fin-Air-Model remains below 3.1 ℃ through all C-rates, which falls within the recommended range, while it exceeds 5 °C in the Air-Model and PCM Model.

Additionally, for a clearer comparison among these models, the highest values of T_{max} and ΔT_{max} at various C-rates and u_{in} are condensed in Figures (5.7 A and B). Accordingly, these results indicate that the HP/PCM-Model gives a good cooling performance, especially at high discharge rates, which provides better protection for the battery pack. This is because the heat generation is absorbed effectively by the grooved evaporator and released by the large area of the fined condenser, as well as, more heat generation can be stored in the PCM through the discharge process.

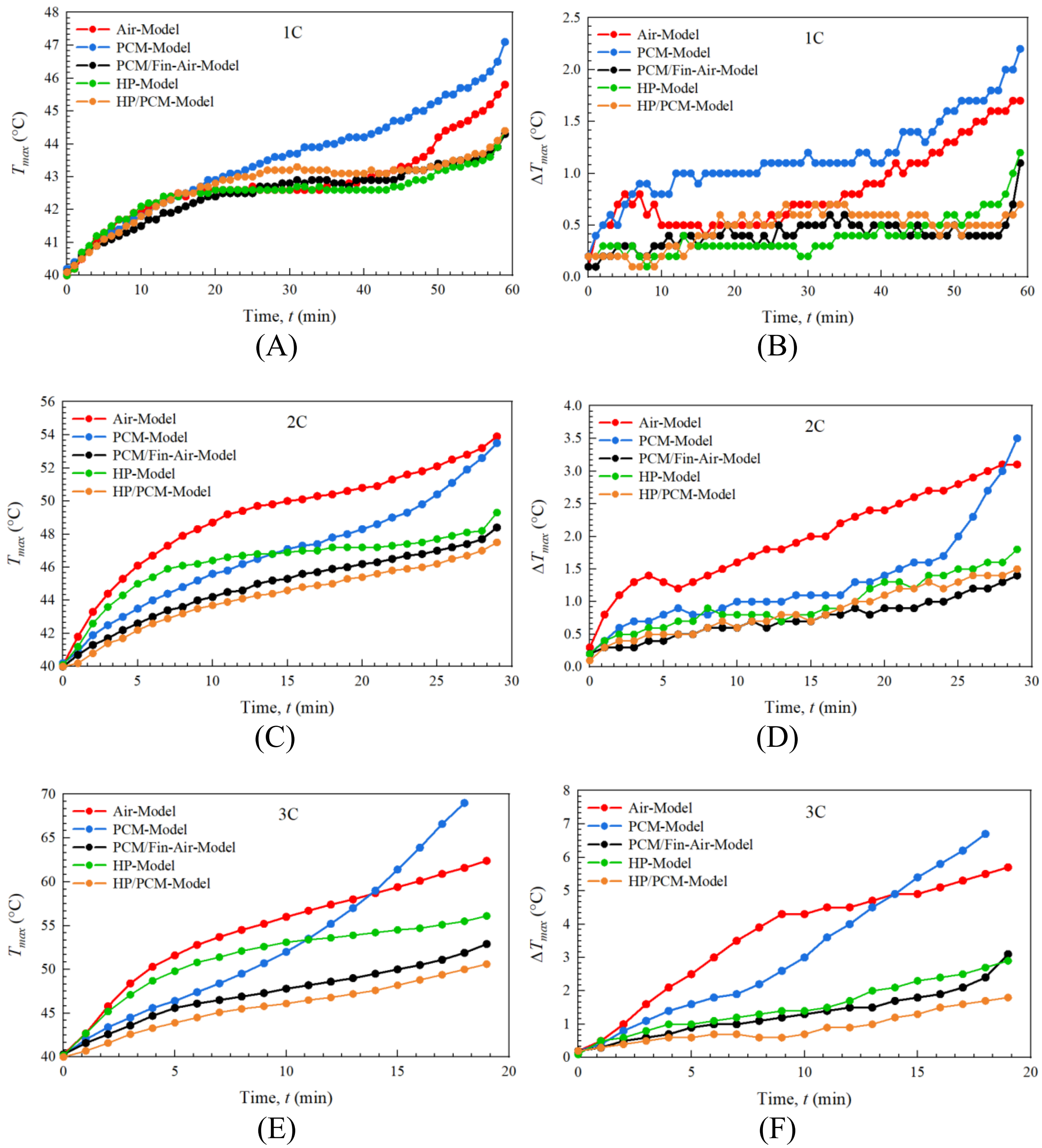

Figure (5.6) Variation of T_{max} and ΔT_{max} under various C-rates at T_{in} of 40°C and $u_{in} = 1.5\ m/s$ using five models, (A) T_{max} under 1C, (B) ΔT_{max} under 1C (C) T_{max} under 2C, (D) ΔT_{max} under 2C, (E) T_{max} under 3C, (F) ΔT_{max} under 3C.

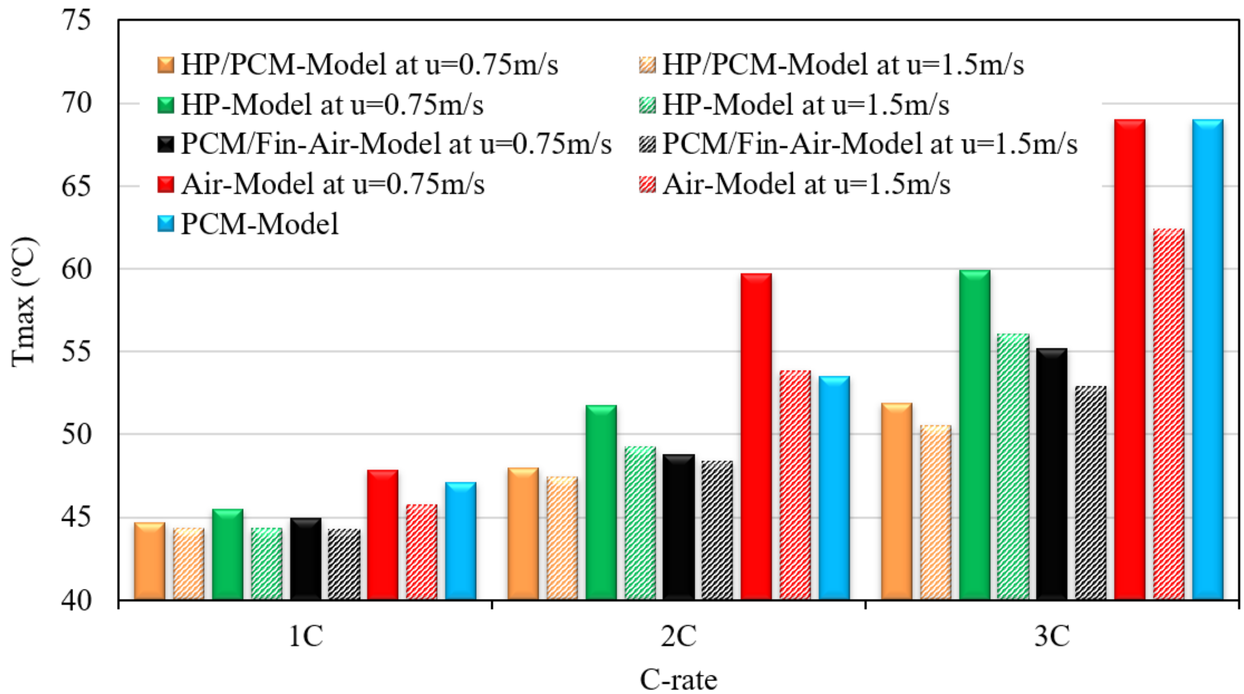

(A)

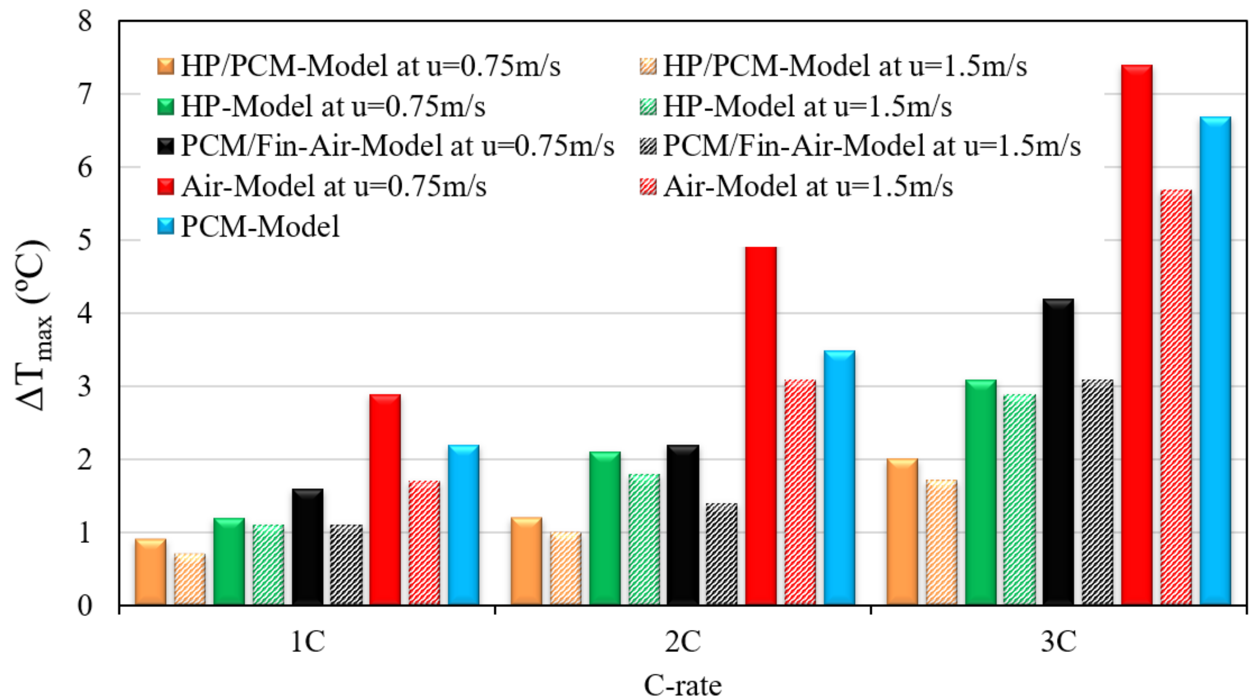

(B)

Figure (5.7) Largest value of (A) T_{max} and (B) ΔT_{max}, using five models at various u_{in} and C-rates.

5.2.7 Effect of C-rates on the battery pack discharge voltage and T_{max}

Figure (5.8) shows the battery pack discharge voltage and T_{max} curves of the PCM/HP-Model at different C-rates as a function of time at T_{in} of 40 °C. The choice of the PCM/HP-Model model was due to its better thermal performance compared to the other models. The discharge processes of 1, 2, and 3C rates are carried out at constant currents of 7.8, 15.6, and 23.4 A, respectively. While the C-rate increases, the voltage of the batteries decreases.

Furthermore, the figure shows a sudden drop in the voltage at the start of the discharge process, particularly, this happens in the cases of high C-rates, that is due to transmission from the open-circuit voltage which represents the voltage of the battery pack with no load to the discharge voltage under external load, and then gradually drops until times of 56, 27, and 17 min for 1, 2, and 3C rates, respectively. After that, the batteries' voltage dramatically drops as a result of the polarization phenomena of the battery concentration. The operation is programmed to stop once the voltage reaches 10 V to protect the batteries. In contrast, as the voltage drops, the temperature of the batteries rises steadily until it reaches its highest values of 44.4, 47.5, and 50.6 °C, at the end of processes for 1, 2, and 3C rates, respectively.

Furthermore, the increase in the discharge rate from 1 to 3C leads to an increase in the heat generation amount from the battery cell due to the increase in the current flow rate which has a positive effect on the heat generation rate based on the formula of battery heat generation that follows as [96]:

$$q_{gen} = I[(V_o - V_d) + T\frac{dV_o}{dT}] \tag{5.1}$$

Where I is the current flow, U and V are the battery open-circuit voltage and discharge voltage, respectively. T is the battery temperature and dU/dT is the temperature coefficient. Consequently, the increase in the battery heat generation causes a faster temperature rise.

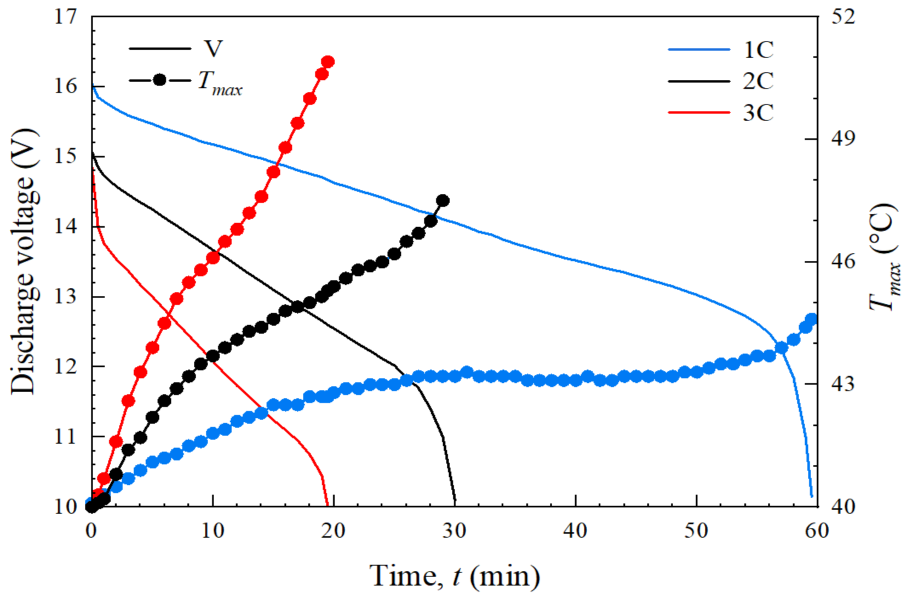

Figure (5.8) Battery discharge voltage and T_{max} at T_{in} of 40 °C and various C-rates using the PCM/HP-Model.

5.2.8 Battery heat generation

The amount of volumetric battery heat generation rate in (W/m³), using Equation (4.1), for a single battery cell at various C-rates using the Air-Model, is presented in Figure (5.9). The figure illustrates a direct correlation between C-rate and heat generation rate, with an increase observed as the C-rate rises. Moreover, there is a sharp increase in the heat generation at the start of the process, attributed to the current flow in the electrolyte resulting in a significant voltage drop, as indicated in Figure (5.8), leading to a rapid increase in ohmic heat [50]. Subsequently, there is a gradual rise over time due to the reversible heat generated by entropy changes.

Consequently, the average volumetric heat generation rates for a single battery cell 18650-type $LiCoO_2$ at 40 °C operating temperature and 1, 2, and 3C rates were 31,400, 119,200, and 234,600 W/m³, respectively. Additionally, the equations describing the non-uniform heat generation rates (W/m³) of the battery have been derived in terms of battery discharge time (min) from the experimental data:

$$\dot{Q}_{gen} = \begin{cases} 0.96t^3 - 94.1t^2 + 3024.8t + 1339.5, & \text{(for 1C)} \\ 19.1t^3 - 967.1t^2 + 16486t + 28710, & \text{(for 2C)} \\ 107.3t^3 - 3817.2t^2 + 45840t + 60848, & \text{(for 3C)} \end{cases} \tag{5.2}$$

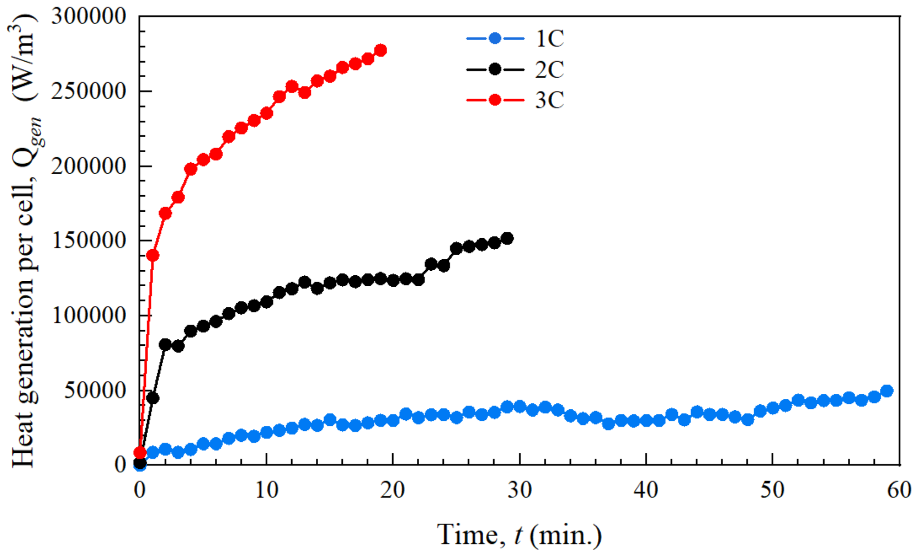

Figure (5.9) Battery heat generation rates under various C-rates at T_{in} of 40°C using the Air-Model.

5.2.9 HP thermal resistance behavior

The amount of heat transmission per HP (Q_{HP}) and the HP thermal resistance (R_{th}), calculated using Equations (4.6) and (4.5), of the HP-Model, respectively, at various C-rates of 1, 2, and 3C are presented in Figure (5.10 A). On the other hand, the average temperature difference between the evaporator and condenser surface of the HP is shown in Figure (5.10 B).

From the figures, we can observe a direct influence of C-rate on Q_{HP} and the temperature difference between the evaporator and condenser section ΔT_{HP} where they increase as the C-rate increases, while the R_{th} decreases as the C-rate increases. As the C-rate increases the heat generation from the battery increases [50] causing an increase in the temperature difference between the evaporator and condenser section ΔT_{HP} as shown in Figure (5.10 B).

Furthermore, it can be noticed from Figure (5.10 A) that R_{th} has a sharp increase at the beginning of the discharge process. This phenomenon is due to a sudden increase in the heat generation from the batteries at the beginning of the discharge period [17] which causes a sharp increase in the battery surface temperature which by its role leads to a larger increase of ΔT_{HP} than the Q_{HP} increase. Therefore, according to Equation (4.5), R_{th} value jumped at this moment since the ΔT_{HP} has a positive effect on the R_{th}.

Thereafter, the R_{th} significantly decreases with time due to the increase of the Q_{HP}, and then shortly, it settles to nearly constant values of 2.5, 1.7, and 1.2 °C/W at discharge rates of 1, 2, and 3C, respectively.

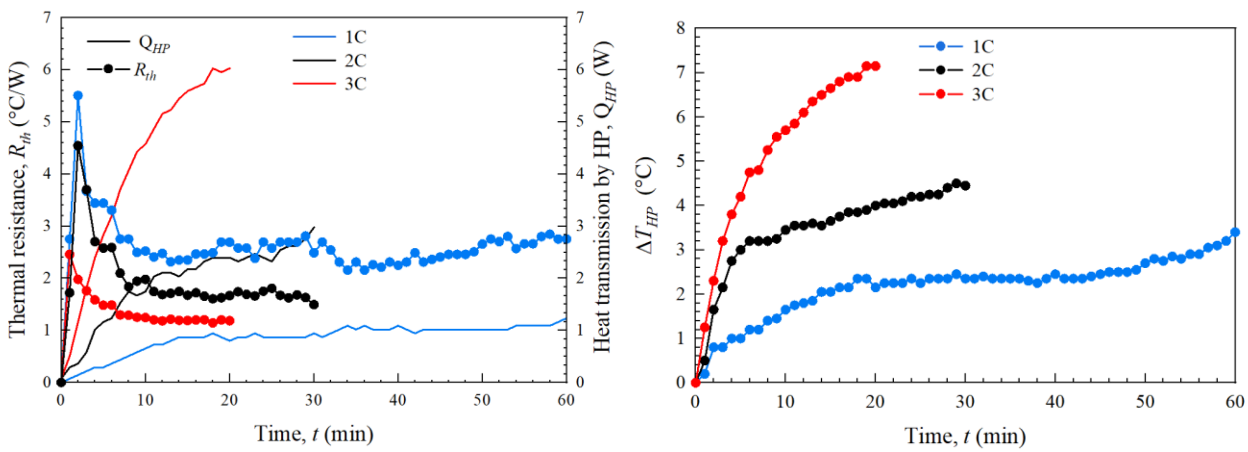

(A) (B)

Figure (5.10) Variation of (A) R_{th}, Q_{HP} and (B) ΔT_{HP} for HP, at various C-rates at T_{in} of 40°C using the HP-Model.

5.2.10 Pressure drops and power consumption

The airflow pressure drops (ΔP) across the battery pack and the air-cooling power consumption of the fan (P_{fan}) have important considerations in the feasibility of cooling systems. Table (5.1) shows the ΔP, P_{fan}, ΔT_{max} and T_{max} corresponding to different inlet air velocities for the various cooling models. Where the P_{fan} can be calculated using the formula [10]:

$$P_{fan} = \Delta P \times u_{in} \times A_d \tag{5.3}$$

It is easy to observe from Table (5.1) that the increase in the air velocity from 0.75 to 1.5 m/s results in a significant rise in ΔP, which leads to an increase in P_{fan}. Additionally, the using of the PCM/Fin-Air-Model causes a significant increase in both ΔP and P_{fan}, as compared to the HP-Model, HP/PCM-Model, and Air-Model at the same air inlet velocity. In contrast, the HP/PCM-Model has the lowest ΔP, and P_{fan} than other models, as well as, has the lowest T_{max} and ΔT_{max}, where it can minimize the percentage energy consumption by 94 and 90% than PCM/Fin-Air-Model and Air-Model, respectively, at u_{in} equal 1.5 m/s.

Furthermore, it should be noticed that there is a slight difference in the T_{max} when using the HP/PCM-Model and PCM/Fin-Air-Model for various C-rates as the air velocity increases from 0.75 to 1.5 m/s. Therefore, it could be used in the case of the lower air inlet velocity of 0.75 m/s at low C-rates of 1 and 2C which has the significant advantage of minimizing energy consumption.

Conversely, air velocity significantly affects the reduction of T_{max} in the Air-Model, especially at 2 and 3C rates. Furthermore, it requires more than 1.5 m/s at 3C to reduce the T_{max} in the Air-Model is the same as in the HP/PCM-Model and PCM/Fin-Air-Model which inevitably causes more pressure drop and then more power consumption.

Table (5.1) Measured and evaluated parameters at various u_{in} and C-rates using five cooling models.

Cooling model	C-rate [C]	u_{in} [m/s]	T_{max} [°C]	ΔT_{max} [°C]	ΔP [Pa]	P_{fan} [W]
Air-Model	1	0.75	47.9	2.9	9	0.052
	1	1.5	45.8	1.7	36	0.416
	2	0.75	59.7	5.4	9	0.052
	2	1.5	53.9	3.1	36	0.416
	3	0.75	69	7.4	9	0.052
	3	1.5	62.4	5.7	36	0.416
PCM-Model	1	0	47.1	2.2	0	0
	2	0	53.5	3.5	0	0
	3	0	69	6.7	0	0
PCM/Fin-Air-Model	1	0.75	45	1.6	15	0.086
	1	1.5	44.3	1.1	57	0.658
	2	0.75	48.8	2.2	15	0.086
	2	1.5	48.4	1.4	57	0.658
	3	0.75	55.2	4.2	5	0.086
	3	1.5	52.9	3.1	57	0.658
HP-Model	1	0.75	45.5	1.1	3	0.006
	1	1.5	44.4	1.2	10	0.04
	2	0.75	51.8	2.1	3	0.006
	2	1.5	49.3	1.8	10	0.04
	3	0.75	59.9	3.1	3	0.006
	3	1.5	56.1	2.9	10	0.04
HP/PCM-Model	1	0.75	44.7	0.9	3	0.006
	1	1.5	44.4	0.7	10	0.04
	2	0.75	48	1.6	3	0.006
	2	1.5	47.5	1.5	10	0.04
	3	0.75	51.9	1.9	3	0.006
	3	1.5	50.6	1.8	10	0.04

5.2.11 Experimental results comparison with the previous study

To assess the experimental results of the HP-Model and PCM/Fin-Air-Model, their results are compared with the experimental previous results found by Liu et al. [48] and Qin et al. [77]. Liu et al. used a flat HP equipped with copper fins in the condenser section and cooled with forced air. It is inserted between the Li-ion battery cells close to the cell surfaces. In contrast, Qin et al. used a hybrid cooling model consisting of twelve aluminum shells filled with PCM, associated with nine air channels to pass the forced air between the aluminum shells and the Li-ion battery. They conducted their study under different C-rates at a low ambient temperature of 30 and 23 °C, respectively. Nevertheless, due to variation in the operation temperature between the present work and the previous studies, the comparison is conducted using the increase in the maximum temperature of batteries $T_{max,rise}$ over the ambient temperature T_{amb}.

The comparison is specifically conducted for the 3C rate. As illustrated in Figure (5.11 A and B), the current HP-Model and PCM/Fin-Model exhibit favorable cooling performance compared to Liu's and Qin's models. Additionally, the present models demonstrate a significant reduction in $T_{max,rise}$.

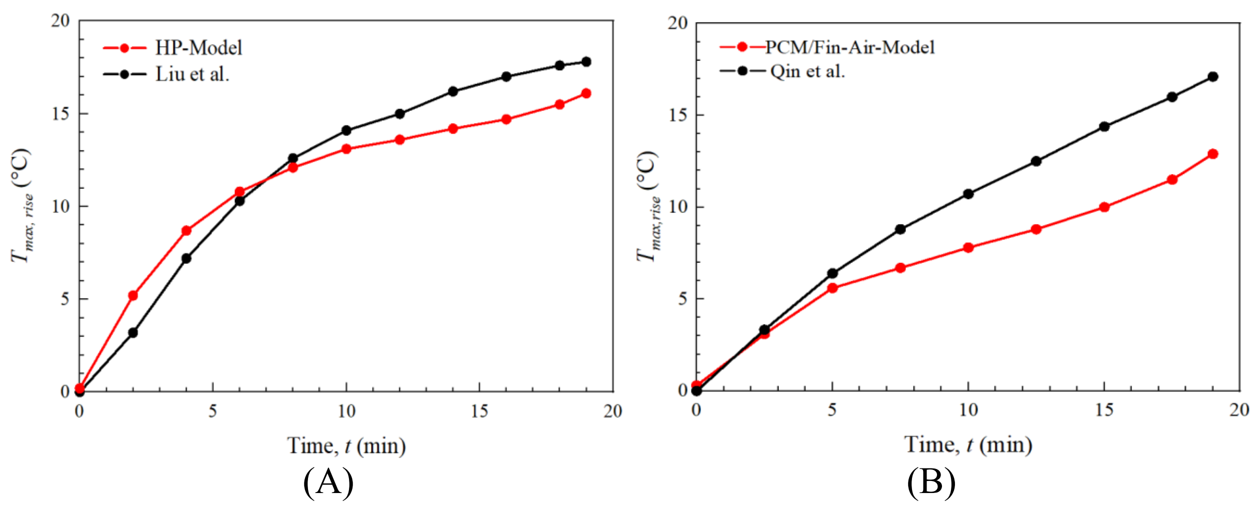

Figure (5.11) Comparison of (A) HP-Model against Liu et al. [48] and (B) PCM/Fin-Air-Model against Qin et al. [77].

5.3 Numerical Results

In this section, the heat transfer and airflow conjugate were simulated for five cooling models and analyzed numerically using COMSOL-5.6 Multiphysics software. The effectiveness of cooling models on the battery pack's T_{max} and ΔT_{max} under different conditions of C-rates of 1, 2, and 3 C, T_{in} of 25, 30 35, and 40 ºC, and u_{in} of 0.75, 1.5, 2.25, and 3 m/s were assessed. Furthermore, the liquid fraction of the PCM and the airflow pressure drop across the battery pack using the Air-Model, Fin/PCM-Air-Model, and HP-Model were simulated.

5.3.1 Effect of T_{in} variation on the T_{max} using the Air-Model

Figures (5.12 A-D) show the effect of T_{in} variation of 25, 30, 35, and 40 ºC on the T_{max} at u_{in} of 0.75 m/s and C-rates of 1, 2, and 3C. At 1C the figure shows a minimum increase in the T_{max} for all operating temperatures where the maximum increase in the T_{max} does not exceed 7.1 ºC.

At 2C the T_{max} show a fast increase from the beginning until t=11 min, then it takes a slow increase until the end of the discharge period. The maximum increase in the T_{max} through the discharge period does not exceed 19.6 ºC for all operating temperatures.

At 3C, the figure shows that the T_{max} has a higher increase rate and it continuously increased rapidly until the end of the discharge period for all operating temperatures. This increase is attributed to the large heat generation that accumulates in the battery cells, due to the lower conductivity of the air. The increasing rate of the T_{max} until the end of the discharge period is reached 33.9 ºC.

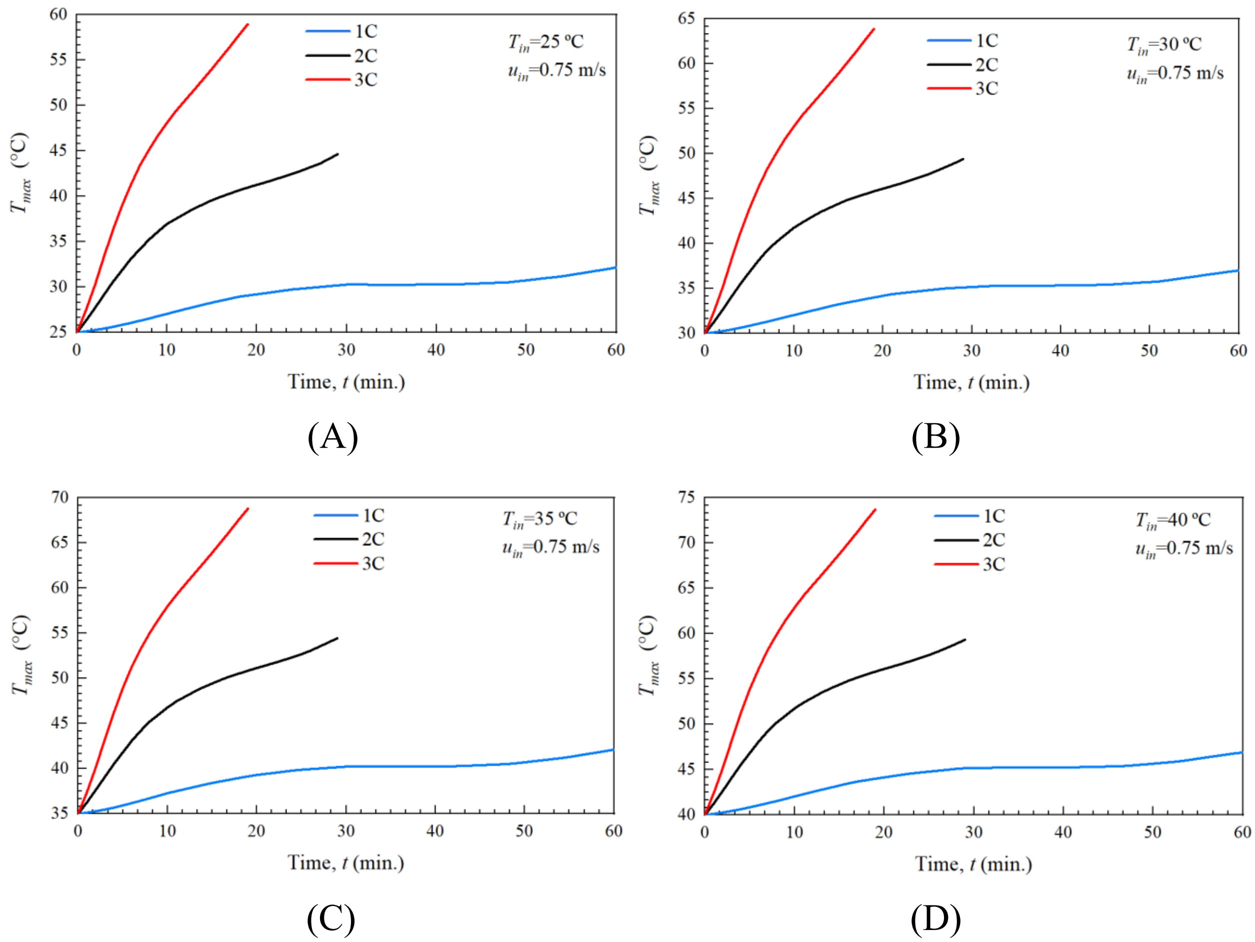

Figure (5.12) Variation of the T_{max} using the Air-Model at u_{in} of 0.75 m/s under various C-rates and T_{in} of (A) T_{in}=25 ºC (B) T_{in}= 30 ºC (C) T_{in}= 35 ºC (D) T_{in}= 40 ºC.

5.3.2 Effect of u_{in} variation on the T_{max} and ΔT_{max} using the Air-Model

Figures (5.13 A-D) show the T_{max} and ΔT_{max} variation at T_{in} of 40 ºC under 2 and 3C rates using various u_{in} of 0.75, 1.5, 2.25 and 3 m/s. At the 2C rate, as shown in Figure (5.13 A), the T_{max} decrease from 59.3 ºC to 46.1 ºC at the end of the discharge period as the u_{in} increase from 0.75 to 3 m/s, while the ΔT_{max} decrease from 6.5 to 2.4 ºC at the end of the discharge period as shown in Figure (5.13 B). This is due to the increase in the convection heat transfer coefficient between airflow and batteries at higher inlet air velocities.

The increase in the u_{in} decreases the thermal resistance between the airflow and battery pack, which accelerates the heat transfer and reduces the battery's temperature during operation. Furthermore, the increase in u_{in} ensures that heat is equally dissipated, which reduces the localized hotspots and enhances the temperature uniformity. The largest value of T_{max} at the end of the 2C rate period are 59.3, 51.9, 47.8, and 46.1 ºC for u_{in} of 0.75, 1.5, 2.25, and 3 m/s, respectively.

At the 3C rate, as shown in Figures (5.13 C and D), the T_{max} and ΔT_{max} decrease from 73.7 to 51.6 ºC and from 10.2 to 4.5 ºC at the end of the discharge as the u_{in} increase from 0.75 to 3 m/s. Also, it is observed that the u_{in} increase in the range of 0.75-1.5 m/s has a more significant effect on T_{max} and ΔT_{max} compared to increases in the range of 2.25-3 m/s. This means that the cooling model reached its thermal stability and the temperature difference between the batteries surface and air cooling became lower. The largest value of T_{max} at the end of the 3C rate period are 73.7, 62.5, 54.9, and 51.6 ºC for u_{in} of 0.75, 1.5, 2.25, and 3 m/s, respectively.

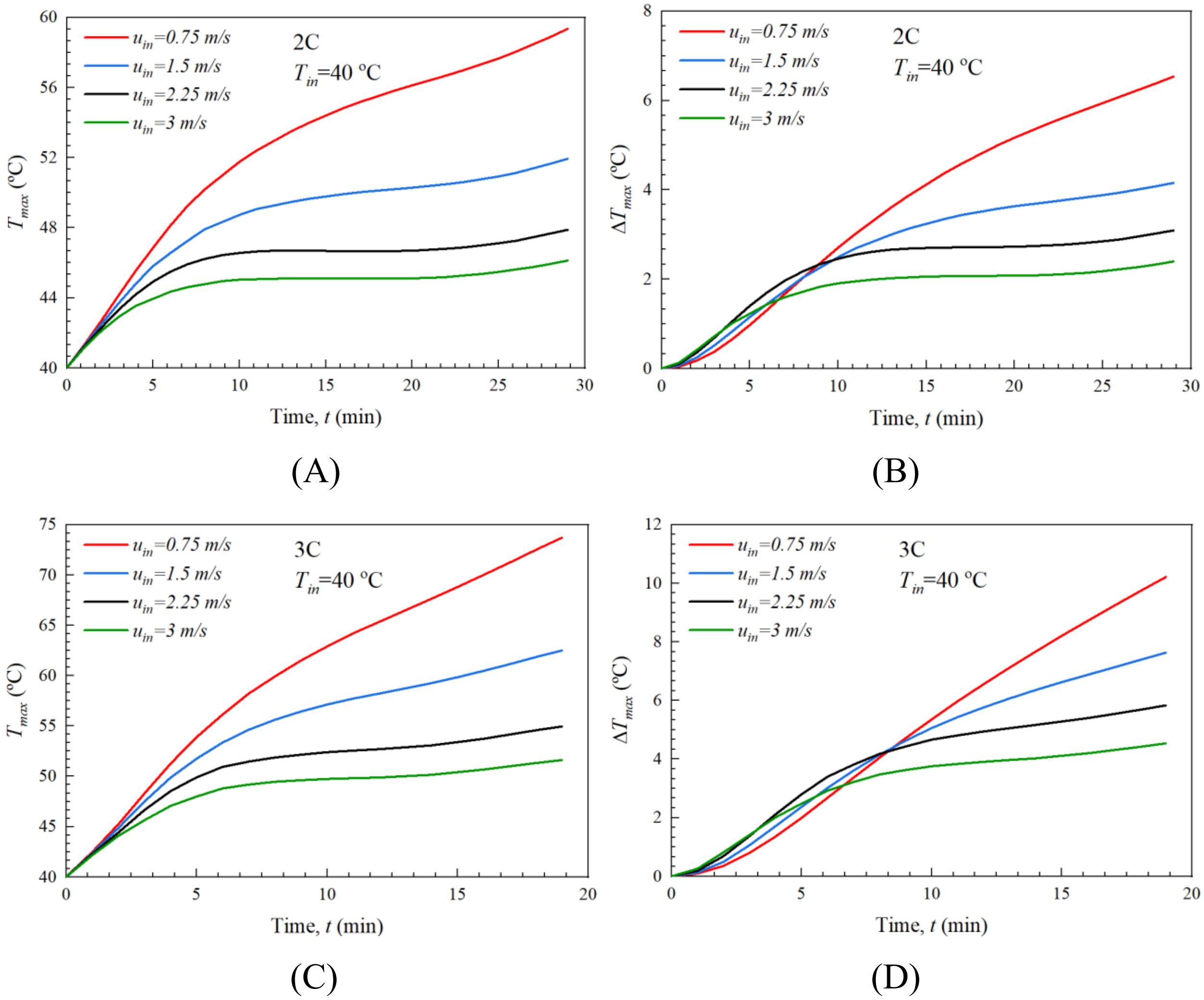

Figure (5.13) Variation of T_{max} and ΔT_{max} using the Air-Model at T_{in} of 40°C, under various u_{in} and C-rates. (A) T_{max} at 2C, (B) ΔT_{max} at 2C, (C) T_{max} at 3C, (D) ΔT_{max} at 3C.

Moreover, the temperature distribution within the battery pack under 3C rate, $T_{in} = 40$ ℃ and various u_{in} at the end of the discharge period is shown in Figures (5.14 A-D). The figure demonstrated that the first column has the lower temperature due to its location next to the airflow inlet section, then the air moves toward the outlet section absorbing heat from each column as it flows, causing progressively increases in the air flow temperature that leading to progressively increase in the battery surface temperature toward the last column which has the largest temperature, as well as, the figure demonstrated that the increasing in the inlet air velocity reduce the overall temperature across the battery pack.

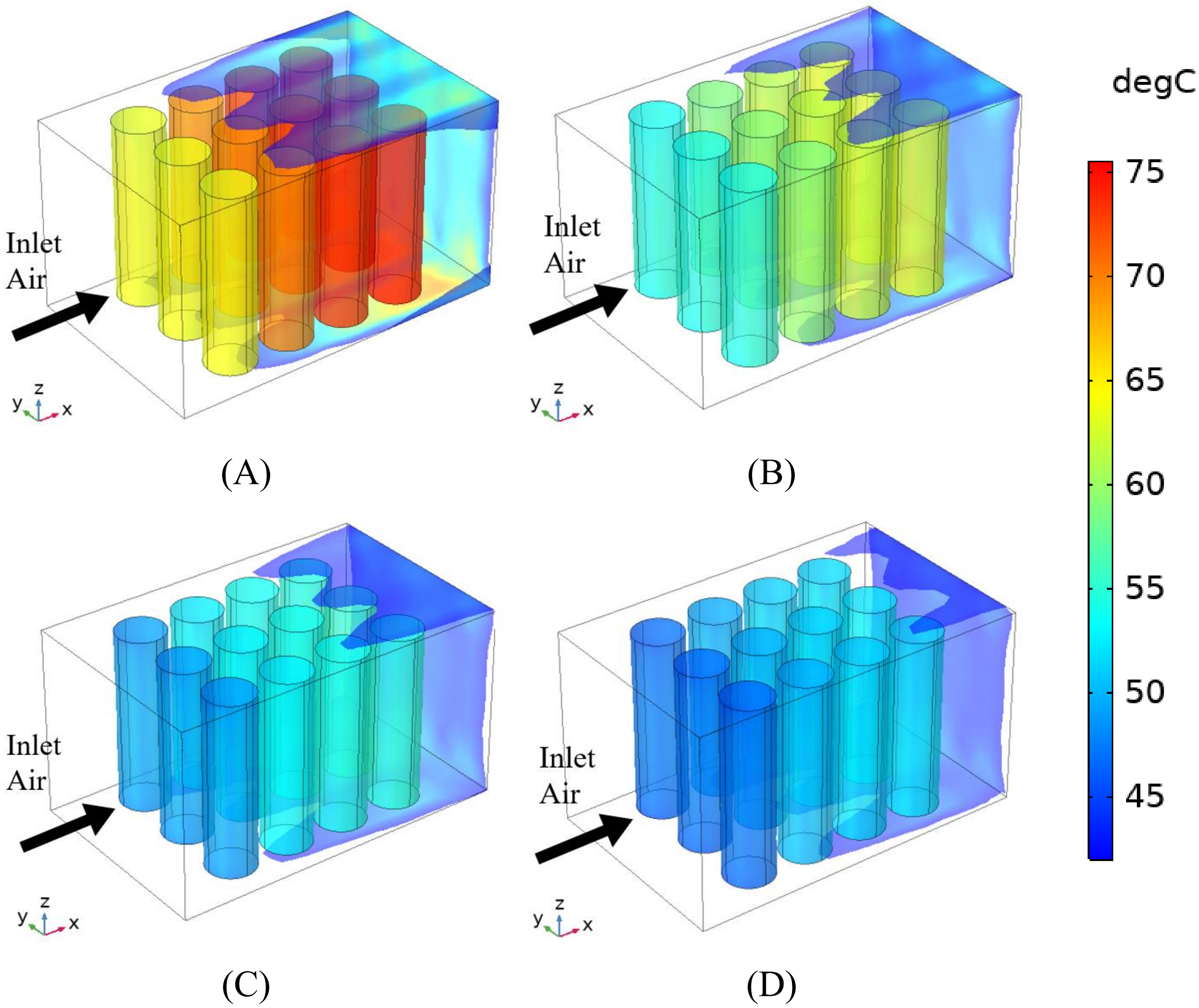

Figure (5.14) Temperature distribution contours for the Air-Model at the end of the discharge period under 3C rate and T_{in} of 40°C with various u_{in} of (A) $u_{in} = 0.75\ m/s$ (B) $u_{in} = 1.5\ m/s$ (C) $u_{in} = 2.25\ m/s$ (D) $u_{in} = 3\ m/s$.

5.3.3 Effect of u_{in} variation on the ΔP using the Air-Model

Figures (5.15 A-D) show the pressure distribution contours at various u_{in} using Air-Model. It displays an increase in the pressure at the inlet section of the first battery column owing to the convergence of the airflow area, then the airflow tends to pass through the gap space between battery rows, resulting in an increase in the airflow velocity and a decrease in the pressure. Then the pressure decreases gradually toward the exit section due to the friction losses until it leaves the battery pack. Moreover, the increases in the inlet air velocity also led to an increase in the ΔP across the battery pack. The maximum pressure drops across the battery pack were 8, 31, 69, and 123 Pa for u_{in} of 0.75, 1.5, 2.25, and 3 m/s, respectively.

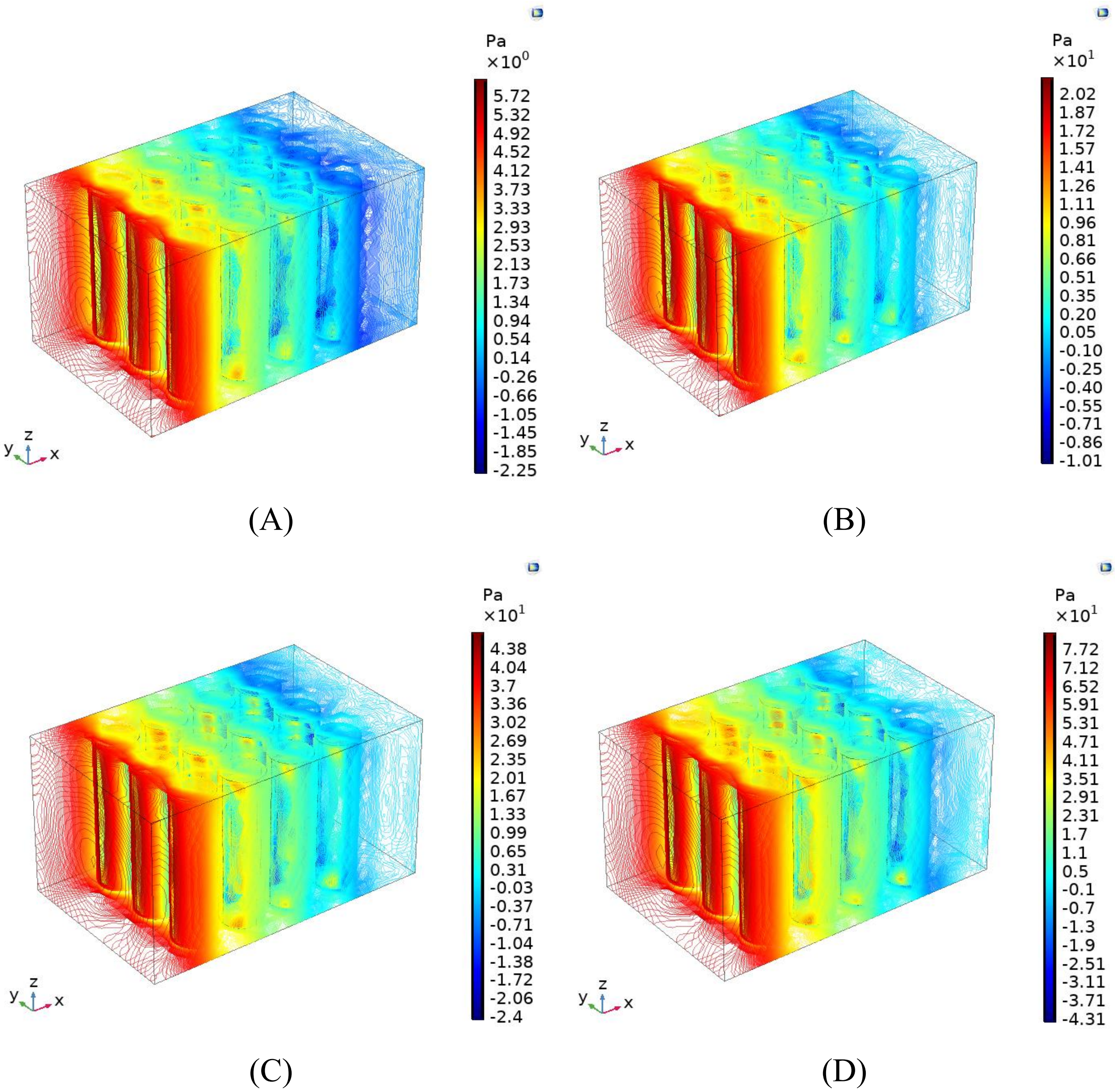

Figure (5.15) Pressure distribution contour for the Air-Model with various u_{in} of (A) $u_{in} = 0.75\ m/s$ (B) $u_{in} = 1.5\ m/s$ (C) $u_{in} = 2.25\ m/s$ (D) $u_{in} = 3\ m/s$.

5.3.4 Effect of T_{amb} variation on the T_{max} and the PCM liquid fraction using the PCM-Model

Figures (5.16 A-D) show the variation in the T_{max} under various T_{amb} of 25, 30 35, and 40 ºC and various C-rate of 1, 2, and 3C. At the 1C rate, the figures display the lowest increasing rate in T_{max} due to the reduced heat generation. Furthermore, the increasing rate in the T_{max} at T_{amb} of 40 ºC has the lowest value, as shown in Figure (5.16 D), owing to the cooling system's operating temperature becoming close to the melting point of the PCM. The T_{max} remains below the safety temperature limit throughout these discharge periods where the largest values of T_{max} at T_{in} of 25, 30, 35, and 40 ºC were 43.5, 44.5, 45.3 and 46.2 ºC, respectively.

At the 2C rate, the increase in T_{max} occurs in three distinct stages related to the PCM melting process. In the first stage, the T_{max} rises rapidly as the battery pack temperature is below the PCM melting temperature range due to the low heat storage rate associated with sensible heat. This stage occurs from the start of the T_{amb} of 25, 30, 35, and 40 ºC until times of 16, 12, 7, and 2 min, respectively, where the average liquid fraction of the PCM remains zero as shown in Figure (5.17 A).

The second stage then starts and continues until the end of T_{amb} equal to 25 ºC and the times of 27, 25, and 22 min for T_{amb} of 30, 35, and 40 ºC, respectively. This stage displays a lower increasing rate in T_{max} as the battery temperature approaches the PCM melting temperature range due to the use of latent heat associated with the PCM phase change. After that, the third stage displays and continuous until the remaining time for the T_{amb} of 30, 35, and 40 ºC indicating the completion of the PCM melting around the battery cells, although the PCM has not fully melted due to its lower thermal conductivity, as shown in Figure (5.18 A-D). The largest values of T_{max} at T_{in} of 25, 30, 35, and 40 ºC were 47.6, 49.8, 51.6 and 54.2 ºC, respectively.

At a 3C rate, In the first stage, the T_{max} also display a rapidly increasing rate but with a higher rate as compared to the 2C rate due to the increased rate in the battery heat generation. This stage is particularly evident at the beginning of T_{amb} of 25, 30, and 35 ºC continuing until the time of 7, 5, and 3 min, respectively, where the PCM liquid fraction remains zero. After that, in the second stage, the PCM begins to melt, as shown in the average liquid fraction results in Figure (5.17 B). In the third stage, the T_{max} continues to increase rapidly, reflecting the completion of the PCM melting around the battery cells. The largest values of T_{max} at T_{in} of 25, 30, 35, and 40 ºC were 56.5, 58.7, 62.9 and 67.2 ºC, respectively.

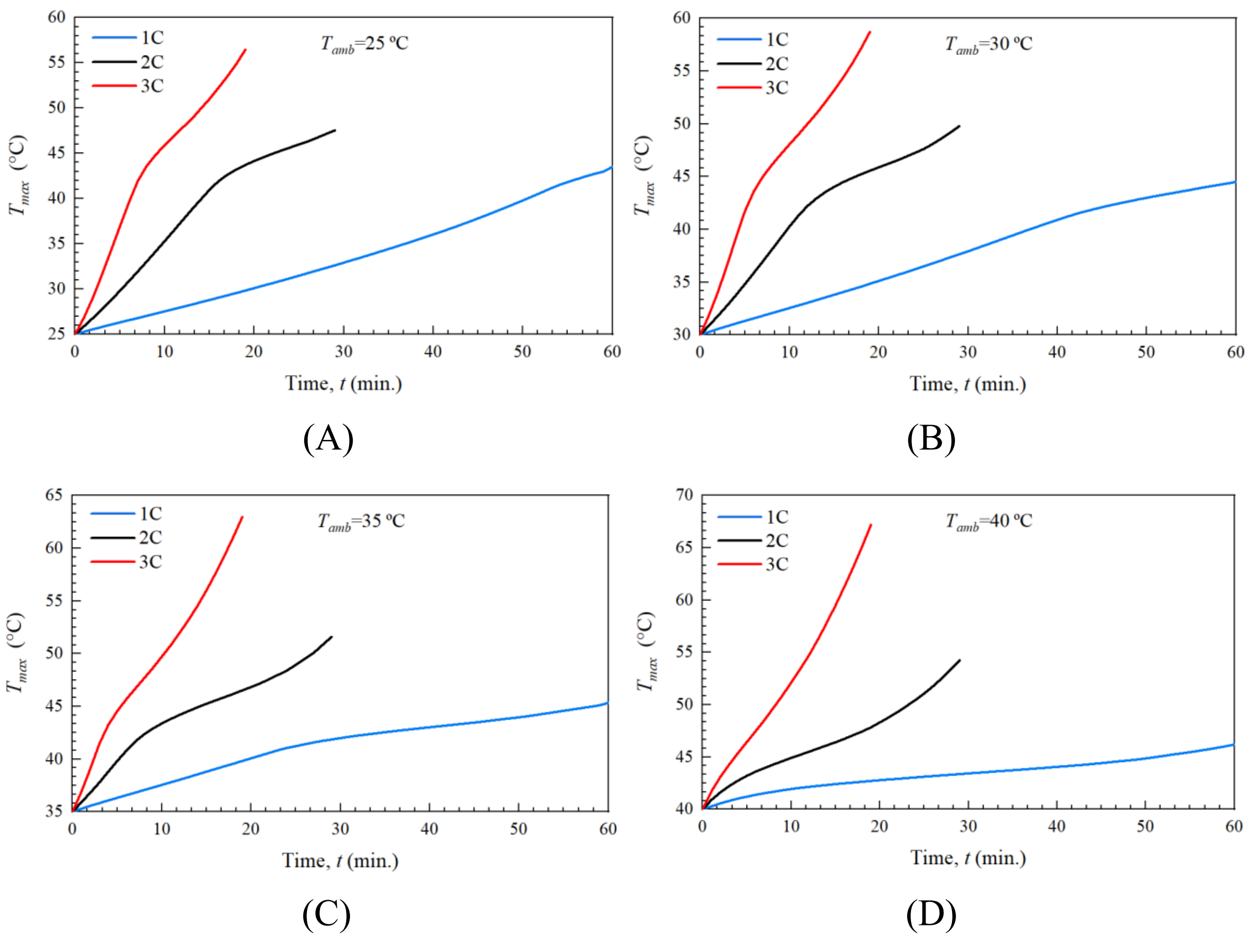

Figure (5.16) Variation of T_{max} using the PCM-Model under various C-rates and T_{amb} of (A) T_{amb} = 25 °C, (B) T_{amb} = 30 °C, (C) T_{amb} = 35 °C, (D) T_{amb} = 40 °C.

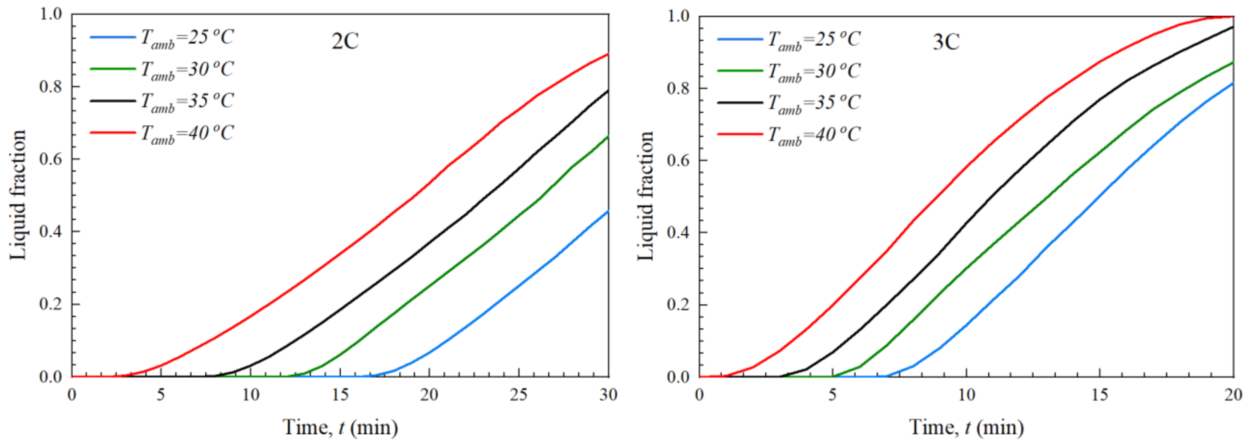

(A) (B)

Figure (5.17) Variation of the average liquid fraction using the PCM model under various T_{amb} and C-rates of (A) 2C and (B) 3C.

For further clarity, Figures (5.18) and (5.19) show the contours of the PCM liquid fraction within the battery pack at the end of the discharge period of 2C and 3C rates at various T_{amb}, respectively. Figures (5.18 A-D) show an increase in the layer thickness of the liquid PCM as T_{amb} increase. In addition, the figures show a large variation in the PCM liquid fraction within the battery pack, that attributed to the low thermal conductivity of the PCM. As the discharge rate increases to 3C, as shown in Figures (5.19 A-D) the thickness of the liquid PCM layer increases. This thickness increases also with the T_{amb} increase until the solid PCM disappeared, as shown in Figure (5.19 D).

Furthermore, Figures (5.19 A-C) display a quantity of solid PCM at the end of the discharge period, although the T_{max} greatly exceeds the melting point of the PCM. This can be attributed to the low thermal conductivity of PCM, which must be taken into consideration in the design of battery cooling systems.

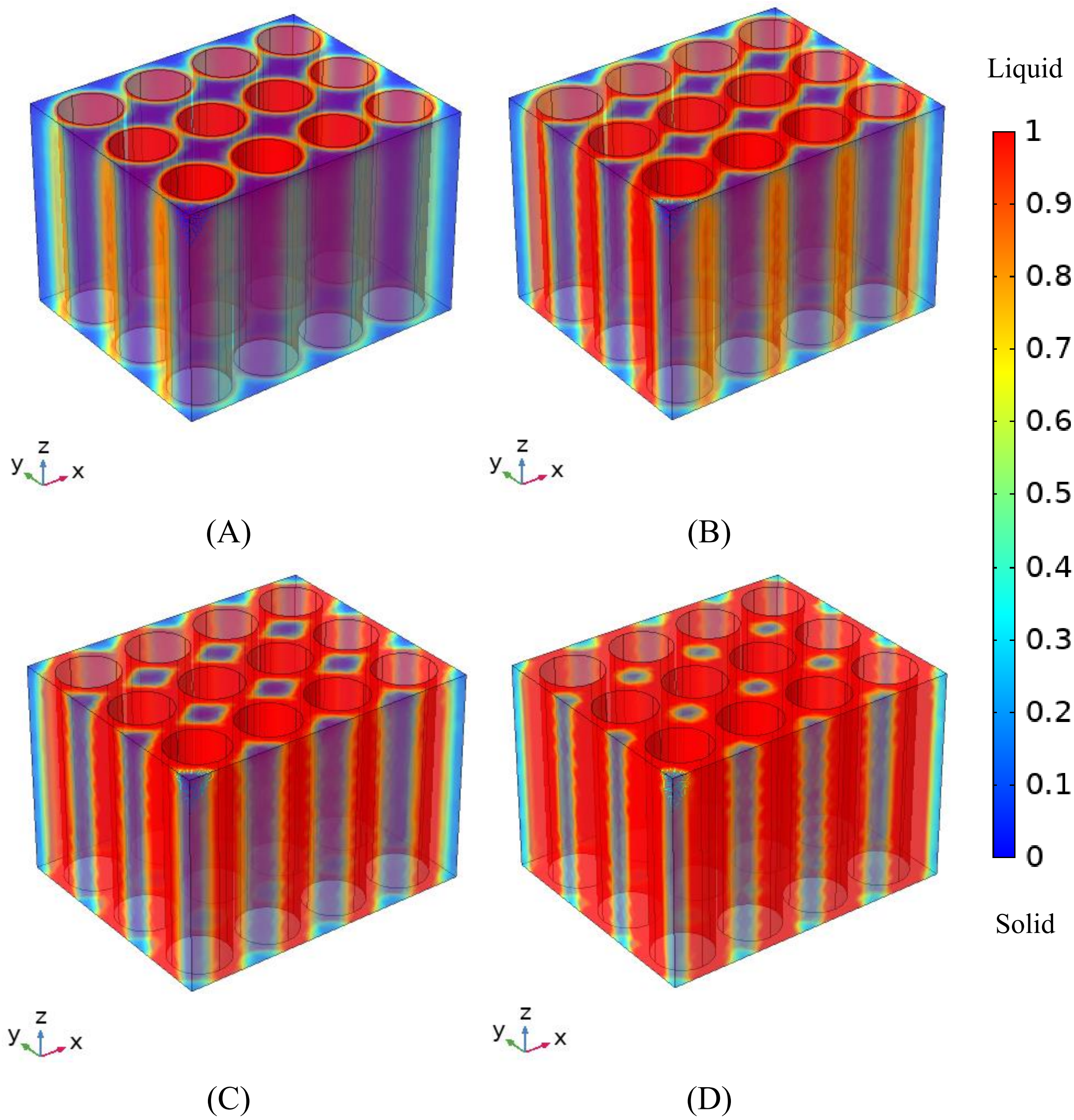

Figure (5.18) PCM liquid fraction contours for the PCM-Model at the end of the discharge period under 2C rate with various T_{amb} of (A) $T_{amb} = 25$ ℃, (B) $T_{amb} = 30$ ℃, (C) $T_{amb} = 35$ ℃, (D) $T_{amb} = 40$ ℃.

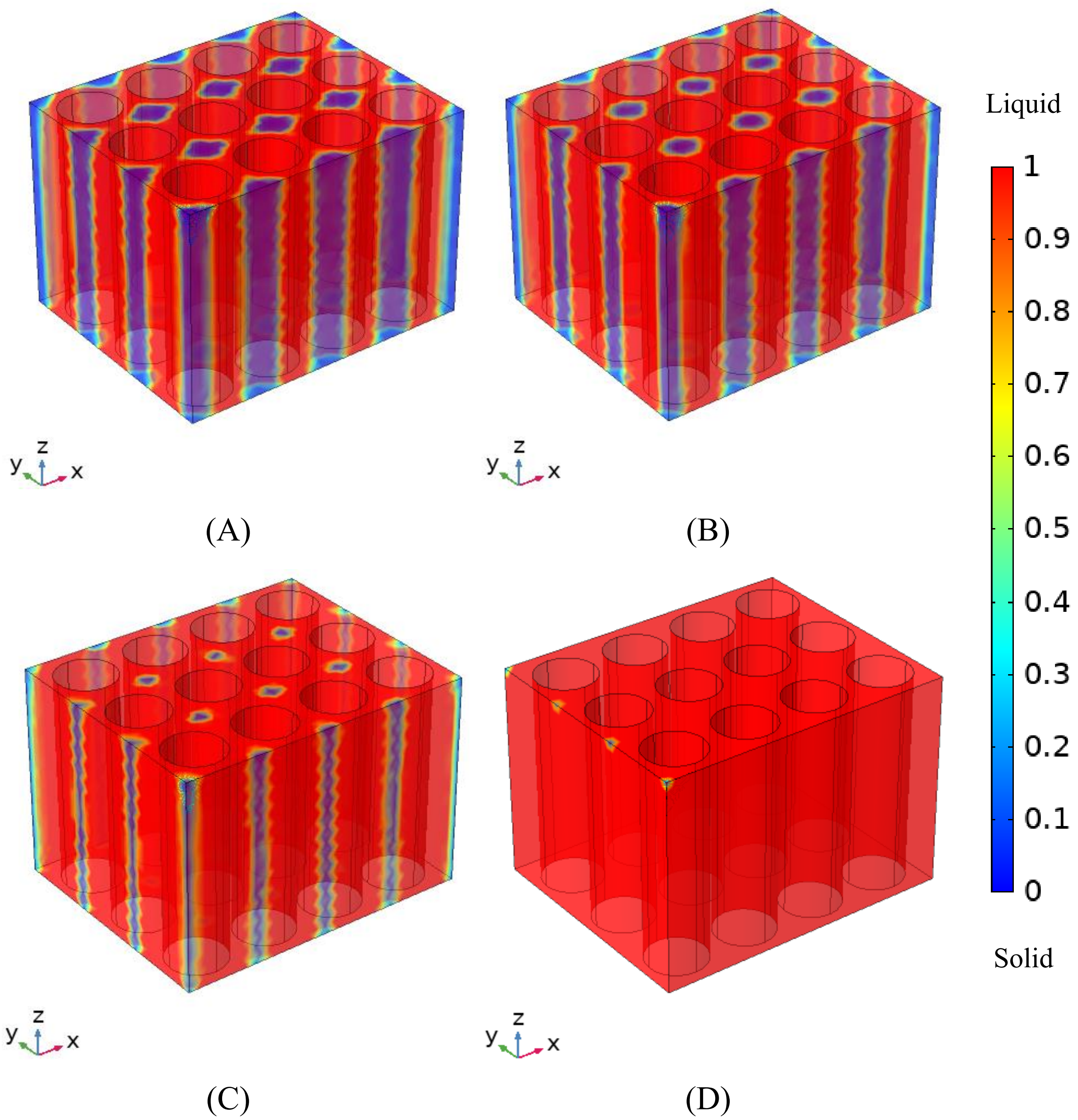

Figure (5.19) PCM liquid fraction contours for the PCM-Model at the end of the discharge period under 3C rate with various T_{amb} of (A) $T_{amb} = 25$ ℃, (B) $T_{amb} = 30$ ℃, (C) $T_{amb} = 35$ ℃, (D) $T_{amb} = 40$ ℃.

5.3.5 Effect of T_{amb} variation on the temperature distribution using the PCM-Model

Figures (5.20 A and B) show the ΔT_{max} at various T_{amb} under 2 and 3C rates using PCM-Model. The ΔT_{max} has started with a low value and then began to increase until the PCM melting process occurred. This led to reducing the ΔT_{max} indicating that PCM cooling can achieve better temperature uniformity than air cooling. Where the maximum value of ΔT_{max} for all T_{amb} and under 2 and 3C rates are below 2.2 and 4.5 ºC, respectively.

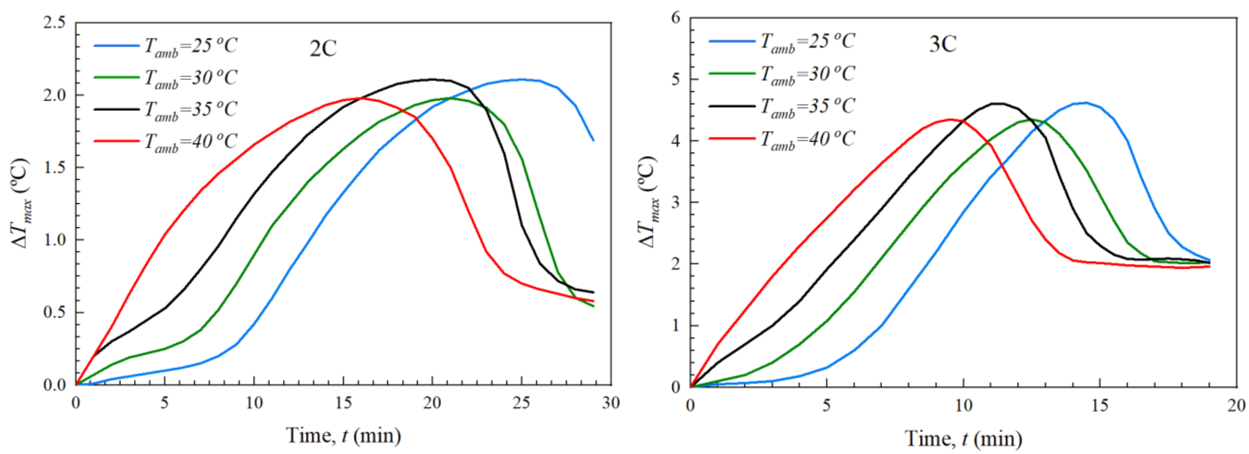

(A) (B)

Figure (5.20) Variation of ΔT_{max} using the PCM-Model under various T_{amb} and C-rates of (A) 2C and (B) 3C.

Moreover, Figures (5.21 A-D) show the temperature distribution at the end of the 3C-rate operating period at various T_{amb}. It illustrated that the temperature distribution has a diagonal gradient around the battery cell, where the temperature decreases as it moves away from the battery surface. Furthermore, the figure illustrated a large temperature gradient across the PCM domain that reached around 24 ºC, this is due to the low thermal conductivity of PCM. This gradient causes non-uniform melting of the PCM and increases the temperature of the battery cell, despite the presence of some unmelted PCM.

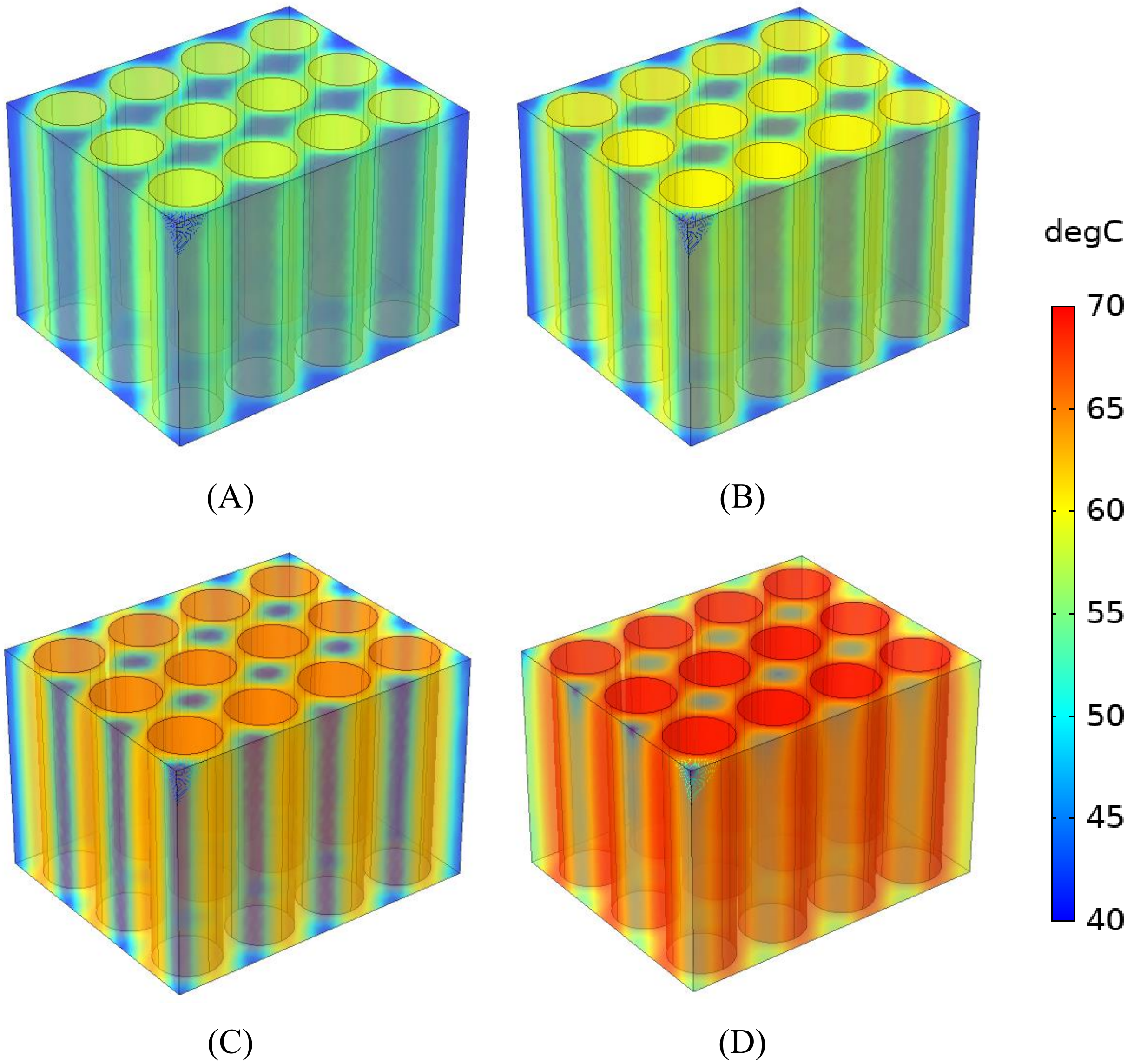

Figure (5.21) Temperature distribution contours for the PCM-Model at the end of the discharge period under 3C rate with various T_{amb} of (A) $T_{amb} = 25$ ℃, (B) $T_{amb} = 30$ ℃, (C) $T_{amb} = 35$ ℃, (D) $T_{amb} = 40$ ℃.

5.3.6 Effect of T_{in} variation on the T_{max} using the PCM/Fin-Air-Model

Figures (5.22 A-D) show the variation in the T_{max} at u_{in} of 0.75 m/s and various T_{in} of 25, 30 35, and 40 ºC under C-rates of 1, 2, and 3C. The figures show an increase in the T_{max} with increasing the T_{in} and discharge rates. At 1C the T_{max} remains below the safety temperature limit where the largest value of T_{max} was 44.68 ºC at

T_{in} of 40 ºC as shown in Figure (5.22 D). As well as, the increasing rate in T_{max} does not exceed 6 ºC during the discharge period for all T_{in} which indicates the battery pack can operate safely for a 1C rate at a u_{in} of 0.75 m/s.

At the 2C the T_{max} of the battery cell stay below the upper limit of the acceptable temperature of 50 ºC, where the largest values of T_{max} were 40.7, 44.8, 46.6 and 48.2 ºC for T_{in} of 25, 30, 35, and 40 ºC, respectively, as shown in Figures (5.22 A-D). In contrast, the increasing rate in T_{max} at the end of the discharge period reduced from 15.2 ºC at the low T_{in} of 25 ºC to 8 ºC at a high T_{in} of 40 ºC. This reduction in the temperature increase is due to the cooling system's operating temperature becoming close to the melting point of the PCM, where the cooling model adsorbs the largest amounts of heat generated during its phase change, that reduces the increasing rate in the battery temperature.

At the 3C the T_{max} of the battery cell remains within the safety temperature limit at low T_{in} of 25 ºC, 30 ºC, and 35 ºC, where the largest values of T_{max} were 47.2, 48.7, and 50.5, respectively, as shown in Figures (5.22 A-C). In contrast, it exceeds the upper level of safety temperature limit at the high T_{in} of 40 ºC, where it was reached to 55.3 ºC, as shown in Figure (5.22 D). This increase in the T_{max} is attributed to the completion of the PCM melting process before the end of the discharge period. This is evident from the average liquid fraction results shown in Figure (5.25 B) for an air velocity of 0.75 m/s, as well as from Figure (5.27 A), which illustrates the complete melting of PCM within the battery pack.

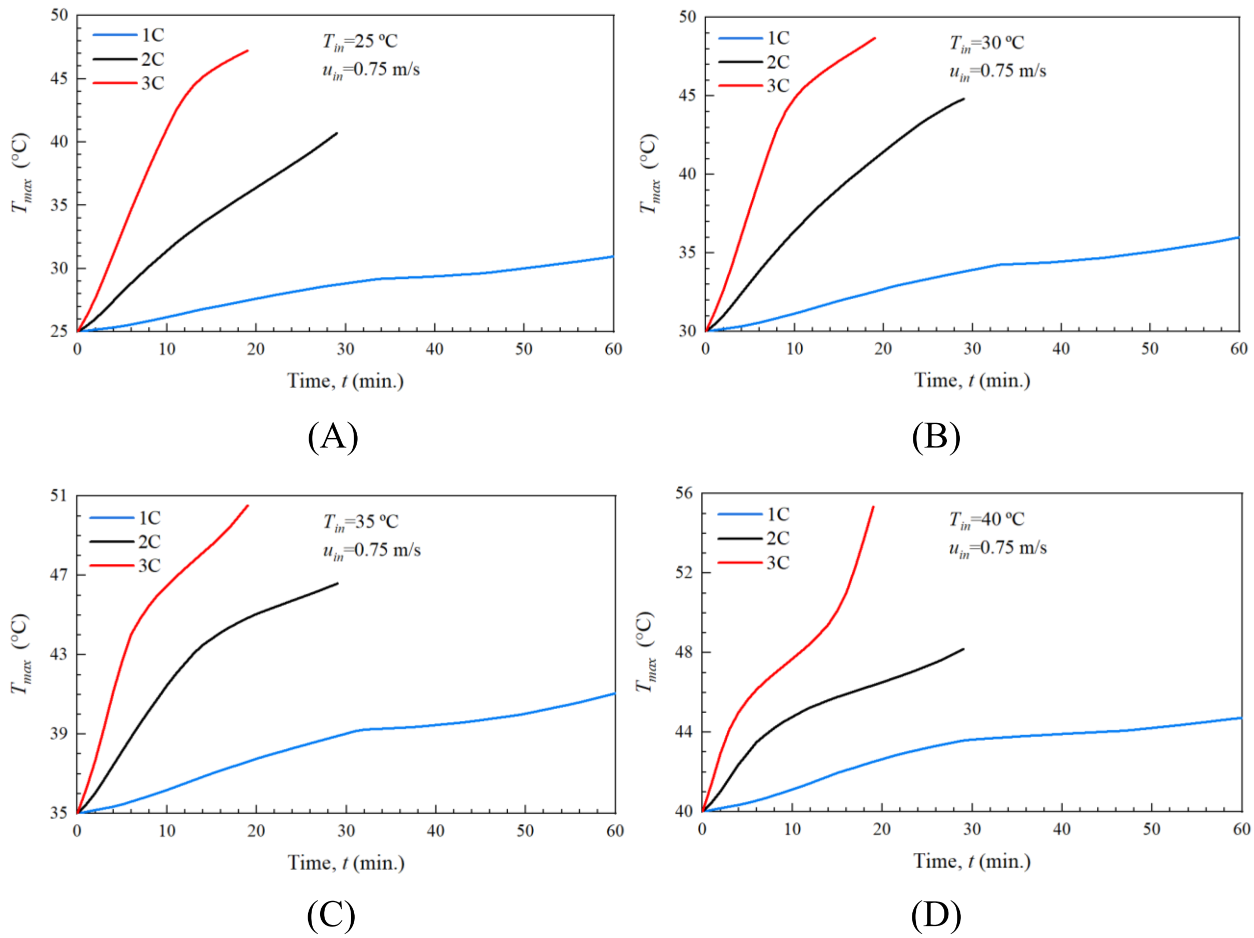

Figure (5.22) Variation of T_{max} using the PCM/Fin-Air-Model at u_{in} of 0.75 m/s and various C-rates under (A) $T_{in} = 25$ ℃, (B) $T_{in} = 30$ ℃, (C) $T_{in} = 35$ ℃, (D) $T_{in} = 40$ ℃.

5.3.7 Effect of u_{in} variation on the temperature distribution using the PCM/Fin-Air-Model

Figures (5.23 A and B) show the variation in the T_{max} and ΔT_{max} at T_{in} value of 40 ºC and various u_{in} values of 0.75, 1.5, 2.25, and 3 m/s under 3C rates. As shown in Figure (5.23 A), the changes in u_{in} has a relatively low influence on T_{max} at the first half period of the operation due to the phase change occurring in the PCM. Thereafter, the variation in the T_{max} increases continuously until the end of the discharge period due to completing the PCM melting process before the end of the discharge period at low air velocities.

Hence, the T_{max} can be reduced from 55.34 to 48.22 ºC by increasing the u_{in} from 0.75 m/s to 3 m/s. The largest values of T_{max} at the end of the discharge period were 55.3, 52.15, 48.89, and 48.22 ºC for u_{in} of 0.75, 1.5, 2.25, and 3 m/s, respectively. In contrast, it is observed a good temperature distribution throughout the battery cells where the maximum temperature difference between the battery cells does not exceed 2.8 ºC at the end of the discharge period for all air velocities as shown in Figure (5.23 B), which is still below the recommended limit of temperature difference (5 ºC). It can be concluded that using the u_{in} value of 0.75 m/s is sufficient for 1 and 2C rates at T$_{in}$ of 40 ºC, while it should increase to 2.25 m/s for a 3C rate to avoid the accumulation of heat and then completing the PCM melting process that causes a sharp increase in the T_{max}.

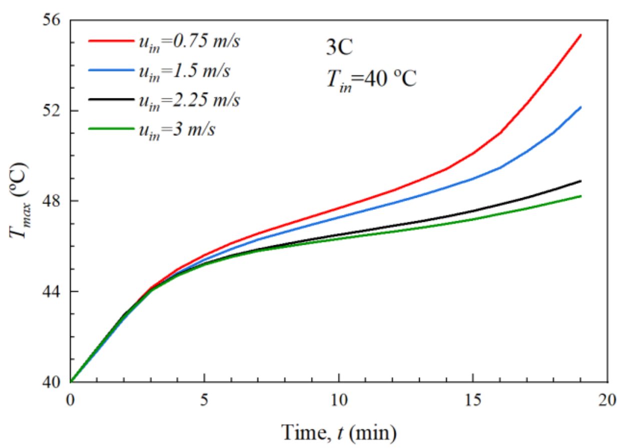

(A)

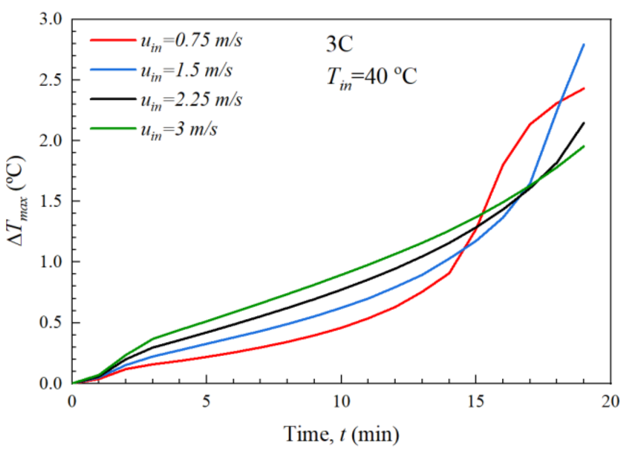

(B)

Figure (5.23) Variation of (A) T_{max} and (B) ΔT_{max}, at 3C rate and T_{in} of 40 °C under various u_{in} using the PCM/Fin-Air-Model.

Furthermore, Figures (5.24 A-D) show the temperature contours at the end of the discharge rate for the 3C rate, across the battery row using various u_{in} values and T_{in} of 40 ºC. As the discharge rate progresses, the heat generation from the battery cells is continuously transferred outwards. Some of this heat is stored in the PCM, while the other is removed by the cooling air across the PCM and aluminum fins. Moreover, these figures show the path of heat dissipation, where the temperature continuously increases from the battery cells toward the air channel, and from the inlet toward the outlet due to the continuous heat exchange between the battery cells and flowing cooling air. Therefore, the largest value of T_{max} can be shown around the last battery cell in the row, while it was the lowest around the first battery cell.

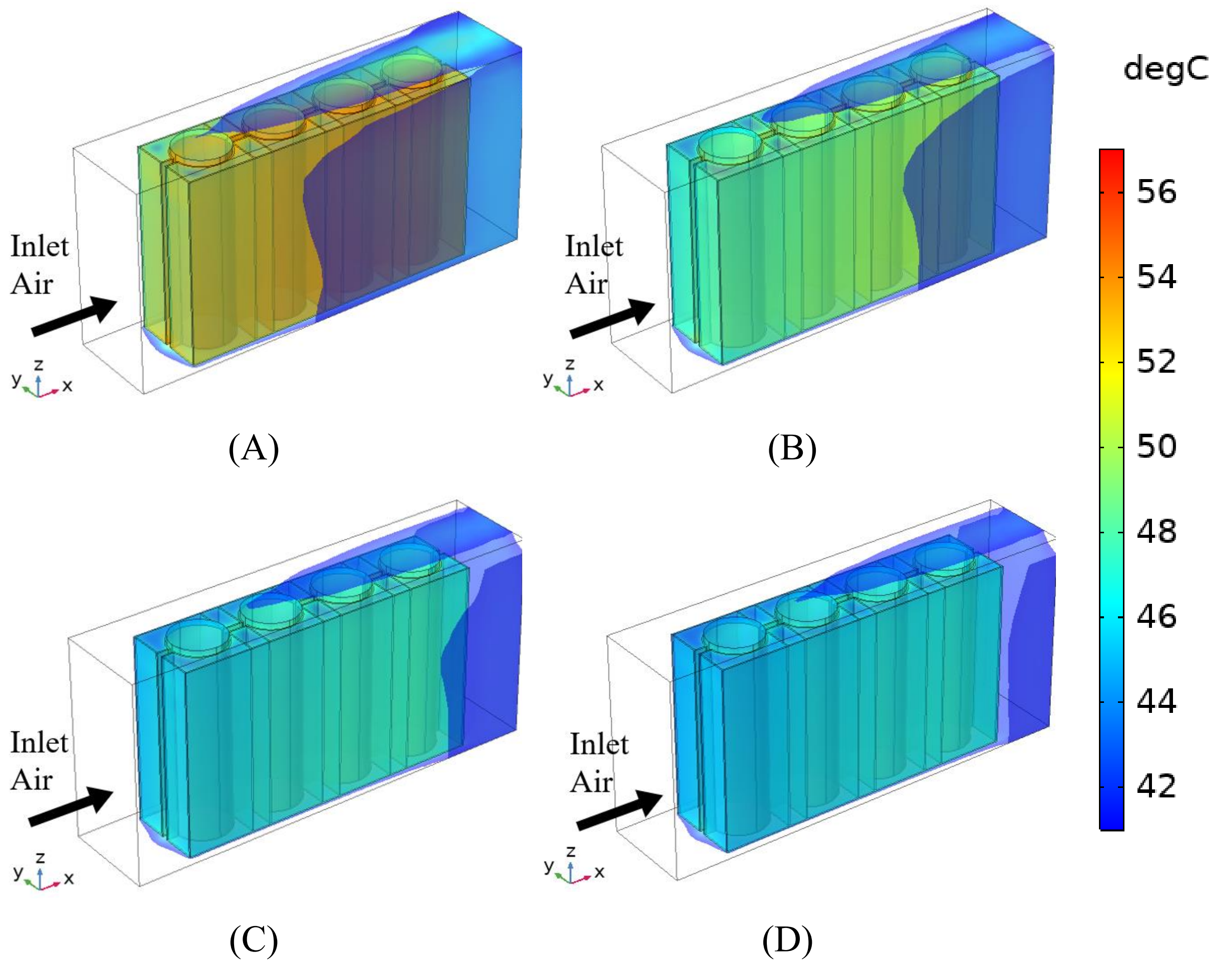

Figure (5.24) Temperature distribution contours for the PCM/Fin-Air-Model at the end of the discharge period under 3C rate and T_{in} of 40°C with various u_{in} of (A) $u_{in} = 0.75\ m/s$ (B) $u_{in} = 1.5\ m/s$ (C) $u_{in} = 2.25\ m/s$ (D) $u_{in} = 3\ m/s$.

5.3.8 Effect of u_{in} variation on the PCM liquid fraction using the PCM/Fin-Air-Model

Figures (5.25 A and B) illustrate the variation in the average liquid fraction of PCM at T_{in} of 40 ºC and various u_{in} of 0.75, 1.5, 2.25, and 3 m/s under 2C and 3C discharge rates. The figures show that the increase in the u_{in} can effectively reduce the PCM liquid fraction rate where the increase in the u_{in} from 0.75 to 3 m/s can reduce the liquid fraction of PCM at the end of the discharge period from 0.679 to 0.24 for 2C, as shown in Figure (5.25 A) and from 1.0 to 0.748 for 3C, as shown in Figure (5.25 B).

Furthermore, the figure demonstrated the liquid fraction of PCM remains less than 0.679 for all u_{in} at a 2C rate, while it reaches 1.0 before the end of the discharge period using a 0.75 m/s air velocity under a 3C discharge rate.

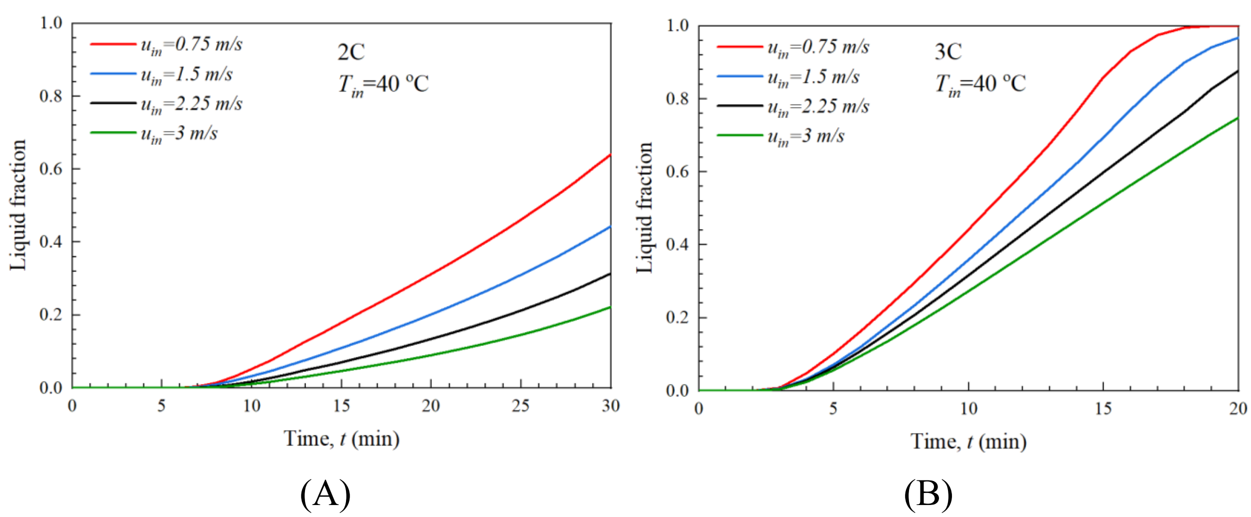

Figure (5.25) Variation of the average liquid fraction using the PCM/Fin-Air-Model at T_{in} of 40 °C under various u_{in} and C-rates of (A) 2C and (B) 3C.

For further clarity, Figures (5.26) and (5.27) show the contours of the PCM liquid fraction within the battery pack at the end of the discharge period under 2C and 3C rates at T_{in} of 40 ºC and various u_{in}. Figures (5.26 A-D) illustrate the liquid fraction at a 2C rate with various u_{in} values of 0.75, 1.5, 2.25, and 3 m/s, respectively. At a low u_{in} of 0.75 m/s, a thick layer of liquid PCM is formed close to the battery cells due to the low heat rejection rate. As u_{in} increases to 1.5 m/s, the amount of liquid PCM is reduced, especially around the first battery cell. With further increases in u_{in} to 2.25 and 3 m/s, the amount of liquid PCM becomes minimal with a thin layer close to the last cells.

In contrast, Figures (5.27 A-D) illustrate the liquid fraction at a 3C rate with various u_{in} values of 0.75, 1.5, 2.25, and 3 m/s, respectively. It demonstrates that the PCM melting process is completed at low u_{in} values of 0.75 and 1.5 m/s, which explains the increase in T_{max} at these u_{in} values. In contrast, a small amount of solid PCM remains at a higher u_{in} values of 2.25 and 3 m/s.

Furthermore, Figures (5.27 A and B) show the homogeneously of the PCM melting process at the end of the discharge period owing to the existence of aluminum fins that get more reliable to the present model.

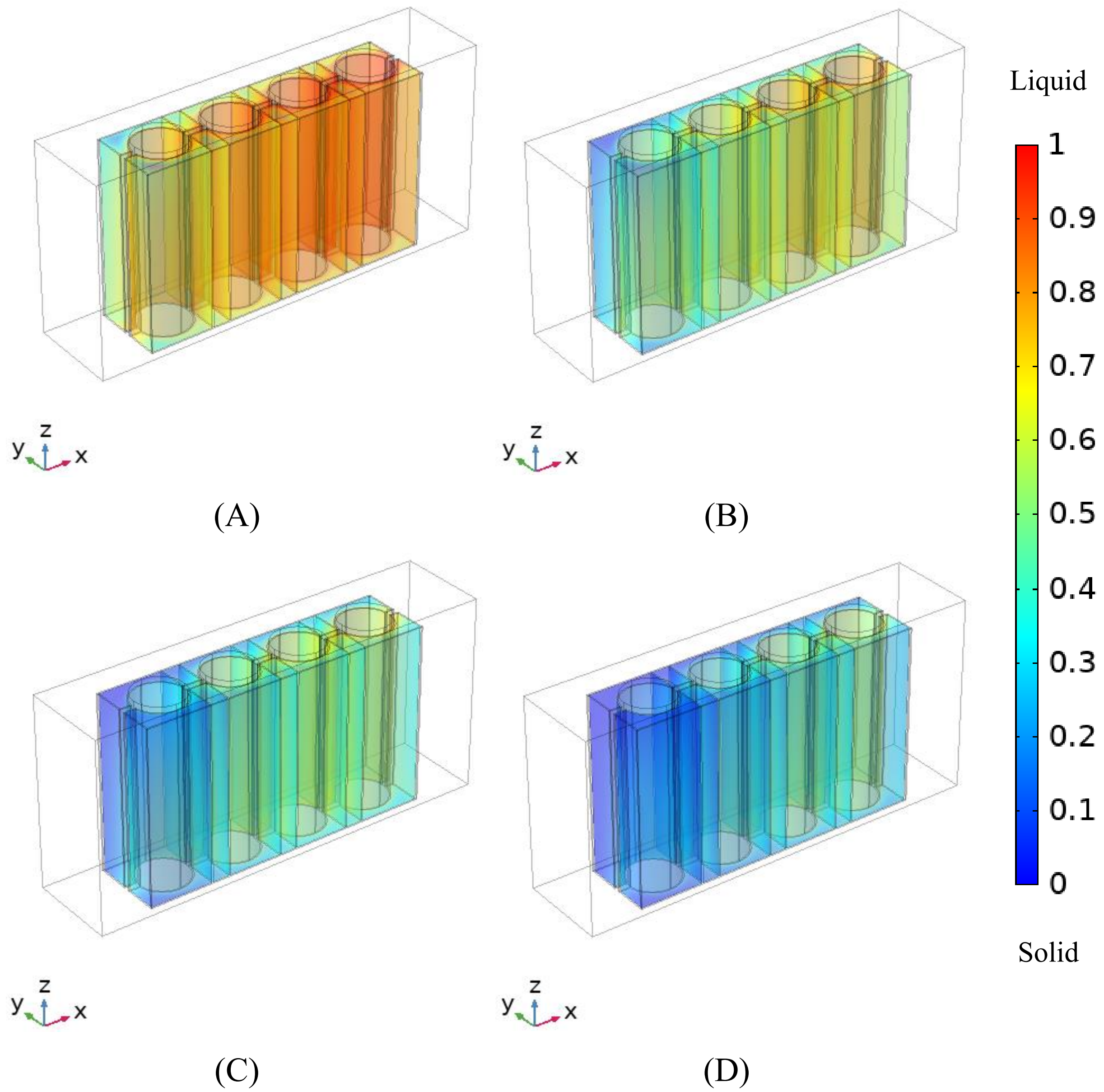

Figure (5.26) PCM liquid fraction contours for the PCM/Fin-Air-Model at the end of the discharge period under 2C and T_{in} of 40 ºC with various u_{in} of (A) $u_{in} = 0.75\ m/s$, (B) $u_{in} = 1.5\ m/s$, (C) $u_{in} = 2.25\ m/s$, (D) $u_{in} = 3\ m/s$.

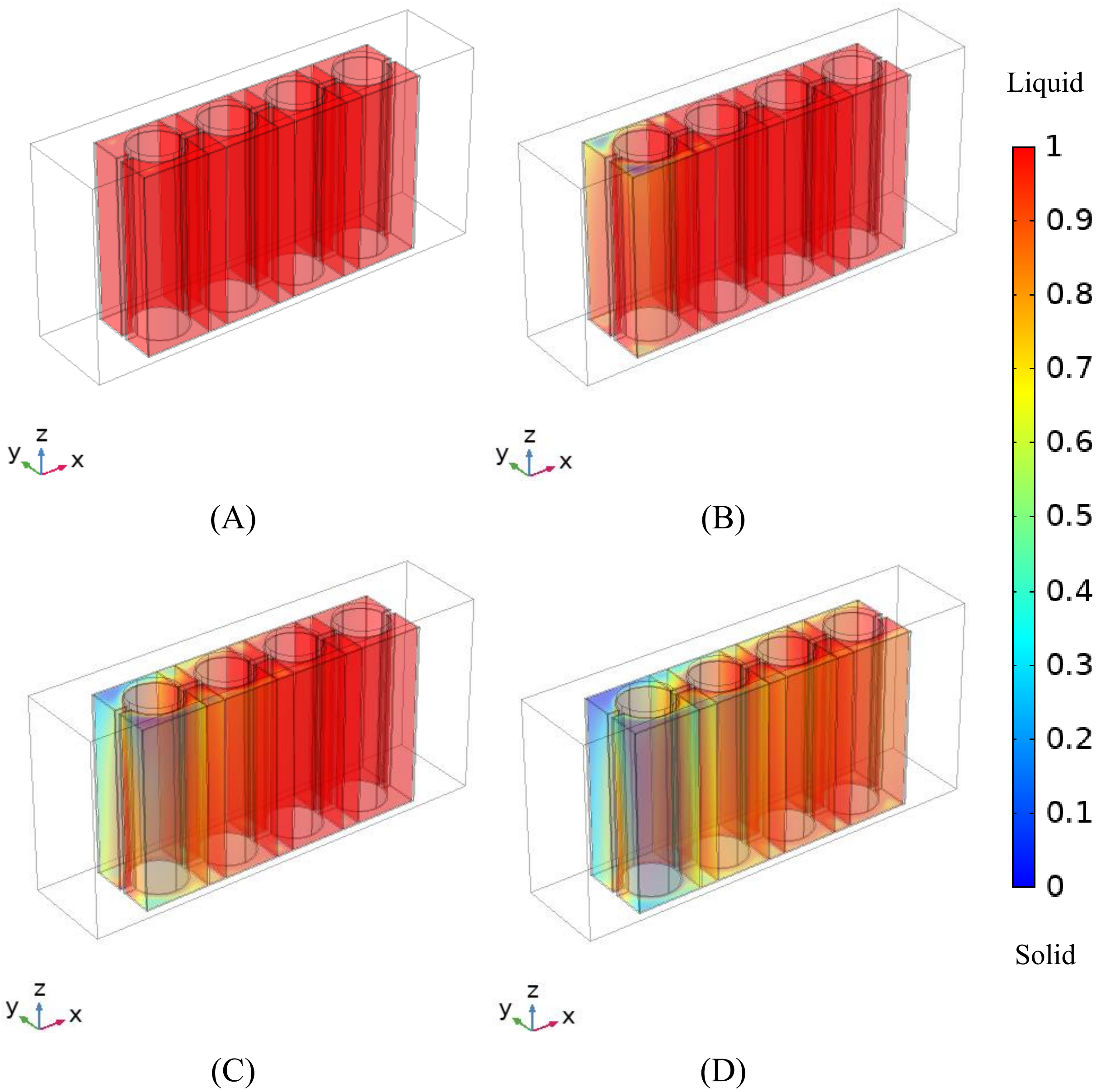

Figure (5.27) PCM liquid fraction contours for the PCM/Fin-Air-Model at the end of the discharge period under 3C and T_{in} of 40 ºC, with various u_{in} of (A) $u_{in} = 0.75\ m/s$, (B) $u_{in} = 1.5\ m/s$, (C) $u_{in} = 2.25\ m/s$, (D) $u_{in} = 3\ m/s$.

5.3.9 Effect of u_{in} variation on the ΔP using the PCM/Fin-Air-Model

Figures (5.28 A-D) show the pressure distribution contour at various u_{in} using PCM/Fin-Air-Model. It displays a high-pressure increase before the battery pack owing to the sudden obstruction by the PCM container and convergence of the airflow area, then the airflow tends to pass through the gap space between container rows, resulting in an increase in the airflow velocity and a decrease in the pressure. Then the pressure decreases gradually due to the friction losses until it leaves the battery pack. The maximum ΔP across the battery pack were 18, 68, 148, and 263 Pa for u_{in} of 0.75, 1.5, 2.25, and 3 m/s, respectively.

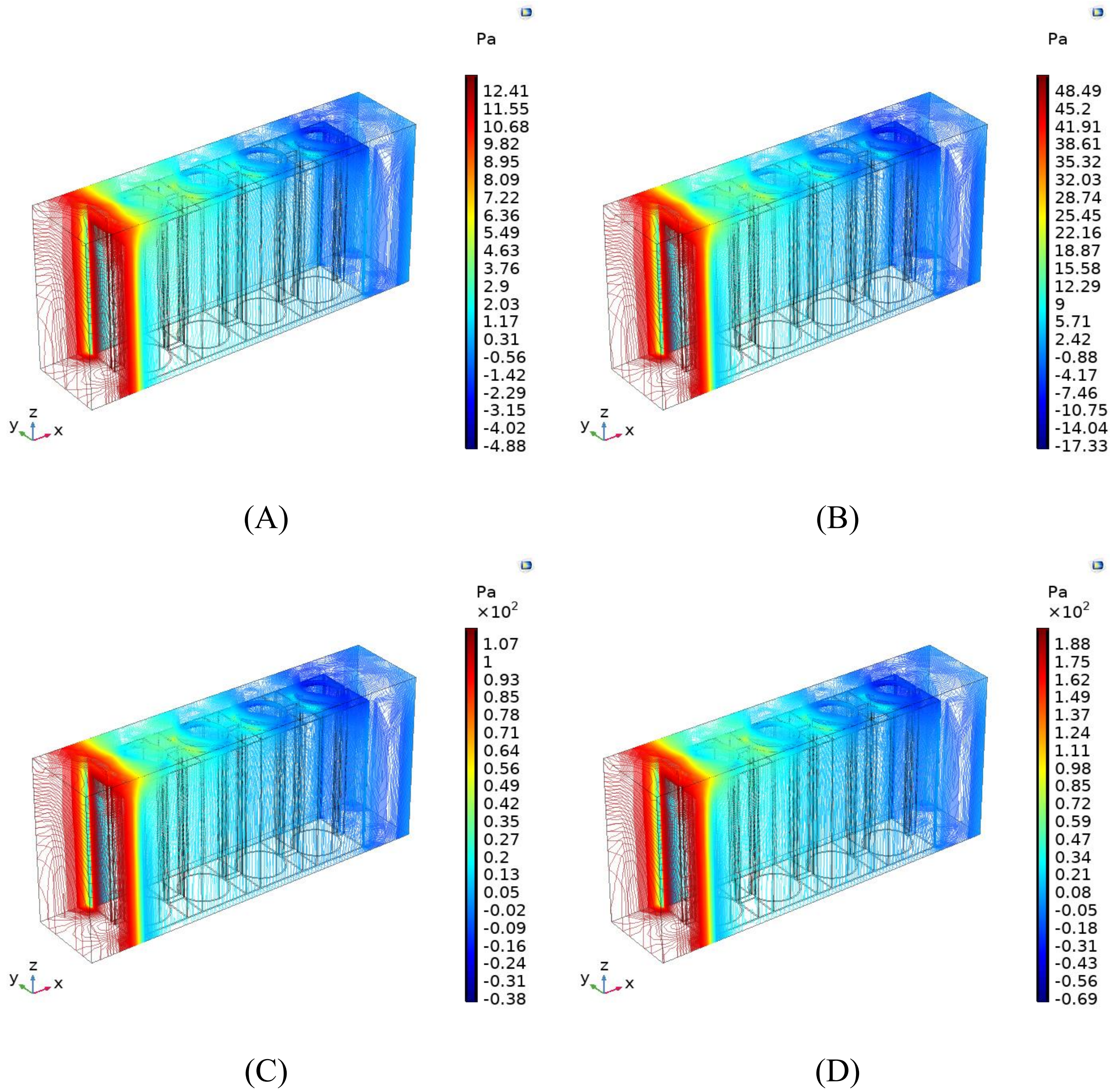

(A) (B)

(C) (D)

Figure (5.28) Pressure distribution contours for PCM/Fin-Air-Model with various u_{in} of (A) u_{in}=0.75 m/s (B) u_{in}=1.5 m/s (C) u_{in}=2.25 m/s (D) u_{in}=3 m/s.

5.3.10 Effect of T_{in} variation on the T_{max} using the HP-Model

Figures (5.29 A-D) show the variation in the T_{max} at u_{in} of 0.75 m/s and various T_{in} of 25, 30 35, and 40 ºC under C-rates of 1, 2, and 3C. The figures show an increase in the T_{max} with increasing the T_{in} and C-rates. At 1C the T_{max} has a low-rate increase and it remains below the safety temperature limit, where the largest values of T_{max} through the discharge period were 29.8, 34.8, 39.8, and 44.8 ºC for T_{in} of 25, 30, 35, and 40 ºC, respectively, that indicates the battery pack can operate safely for 1C-rate at an u_{in} of 0.75 m/s.

At 2C rate, the T_{max} increases significantly during the initial stage of the discharging period, followed by a slower rate of increase until the end of the discharging period. Furthermore, the T_{max} reached the upper level of the acceptable temperature limit of (50 ºC) at a high T_{in} of 40 ºC. The largest values of T_{max} were 36.4, 41.5, 46.6 and 51.7 ºC for T_{in} of 25, 30, 35 and 40 ºC, respectively.

At the 3C rate, the T_{max} shows the largest acceleration in the increasing rate through all the discharge periods owning the high heat generation. Furthermore, the T_{max} exceeds the upper level of safety temperature limit at the high T_{in} of 35 and 40 ºC, where the largest values of T_{max} at the end of the discharge period were 45.9, 50.9, 56.1, and 59.8 ºC for T_{in} of 25, 30, 35 and 40 ºC, respectively.

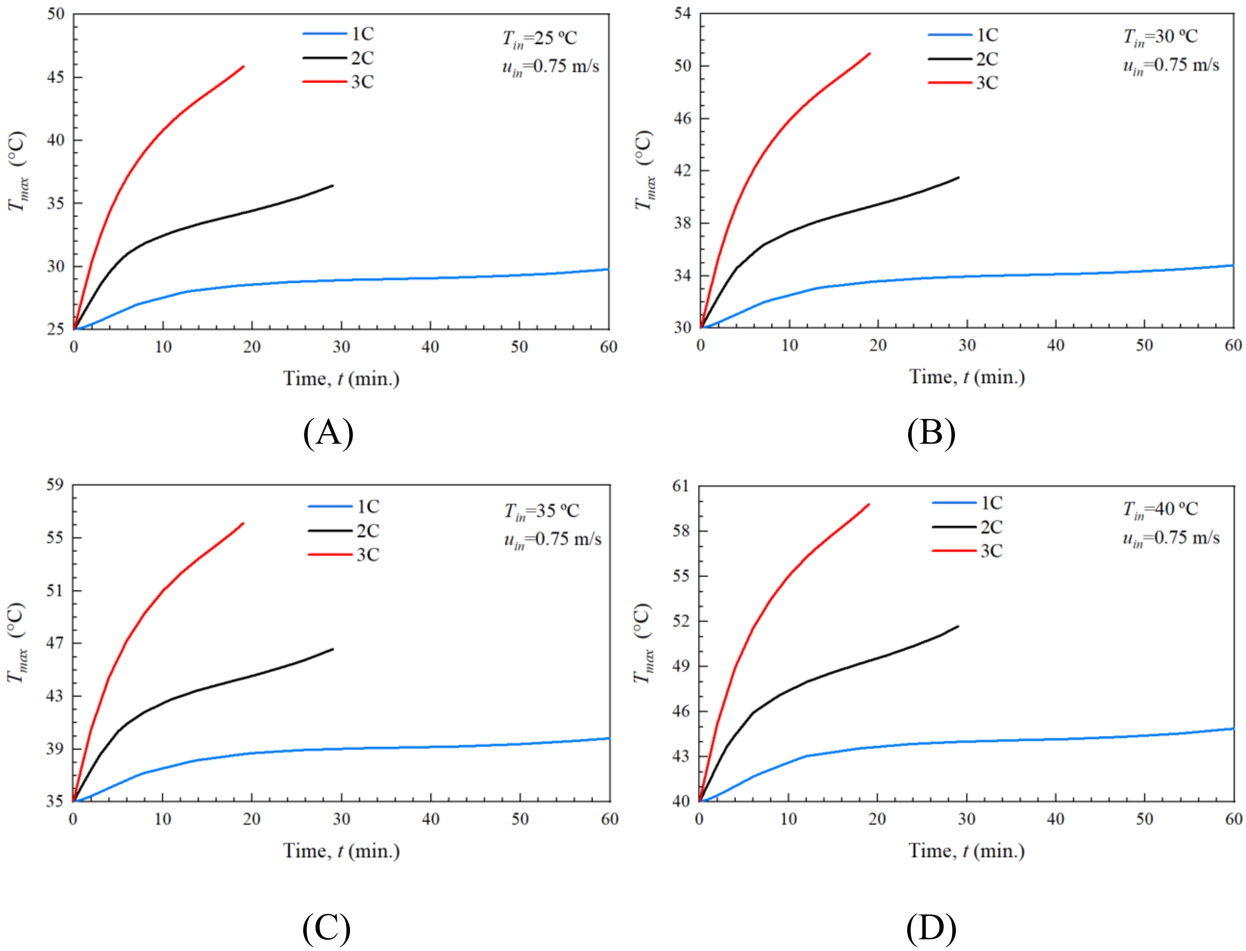

Figure (5.29) Variation of T_{max} using the HP-Model at u_{in} of 0.75 m/s and various C-rates for (A) T_{in} = 25 ℃, (B) T_{in} = 30 ℃, (C) T_{in} = 35 ℃, (D) T_{in} = 40 ℃.

5.3.11 Effect of u_{in} variation on the T_{max} and ΔT_{max} using the HP-Model

Figures (5.30 A and B) show the variation in the T_{max} and ΔT_{max} at T_{in} of 40 ºC and 3C rate for various u_{in} of 0.75, 1.5, 2.25, and 3 m/s. As shown in Figure (5.30 A), the changes in u_{in} had little effect on the T_{max} at the beginning of the discharge period up to t=3 mins. This was due to the small temperature difference between the air cooling and the HP condenser at the start of the discharging process, which was attributed to the HP thermal resistance. Subsequently, the variations in the u_{in} significantly affect the T_{max}, leading to a decreasing it as the u_{in} increases and this effect intensifies throughout the remainder of the discharge period.

Furthermore, the u_{in} increase in the range of 0.75-1.5 m/s has a significant effect on T_{max} and ΔT_{max} while it has the slightest effect when u_{in} increases in the range of 2.25-3 m/s. The largest value of T_{max} at the end of the discharge period are 59.8, 56.2, 54.5, and 53.6 ºC for u_{in} of 0.75, 1.5, 2.25, and 3 m/s, respectively.

In contrast, the model has a good temperature distribution through the battery pack, where the largest value of ΔT_{max} at the end of the discharge period are 2.9, 2.3, 1.9, and 1.7 ºC for u_{in} of 0.75, 1.5, 2.25, and 3 m/s, respectively, as shown in the Figure (5.30 B).

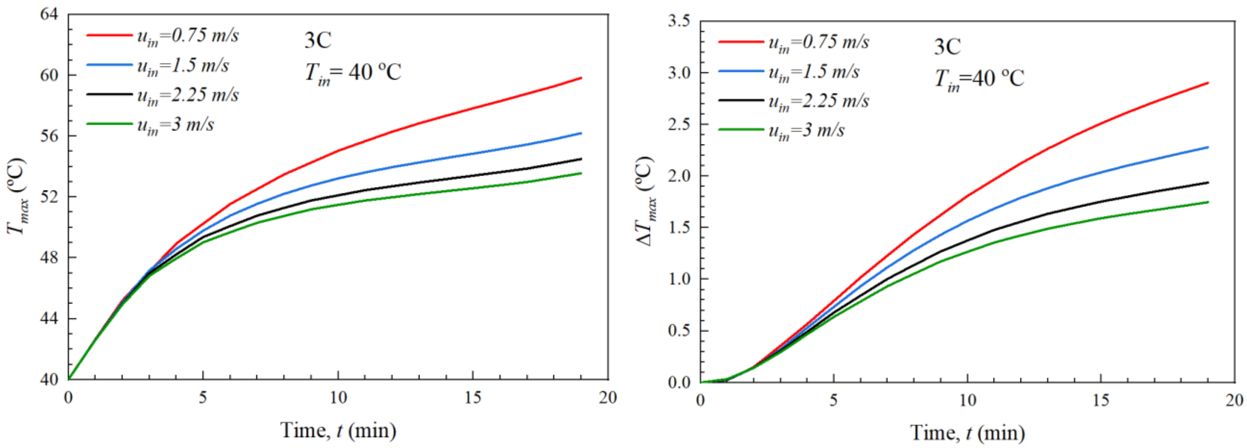

(A) (B)

Figure (5.30) Variation of (A) T_{max} and (B) ΔT_{max}, at 3C rate and T_{in} of 40 °C under various u_{in} using the HP-Model.

Moreover, Figures (5.31 A-D) show the temperature contours at the end of the discharge rate for the 3C rate, across the battery pack and HPs using various u_{in} values and T_{in} of 40 ºC. The figures show a continuous increase of temperature gradient from the battery cells, HP evaporator section then to the condenser section where the heat generation is rejected to the out by cooling air, as well as, the first HP and battery cells have the lower temperature gradient due to its location next to the airflow inlet section.

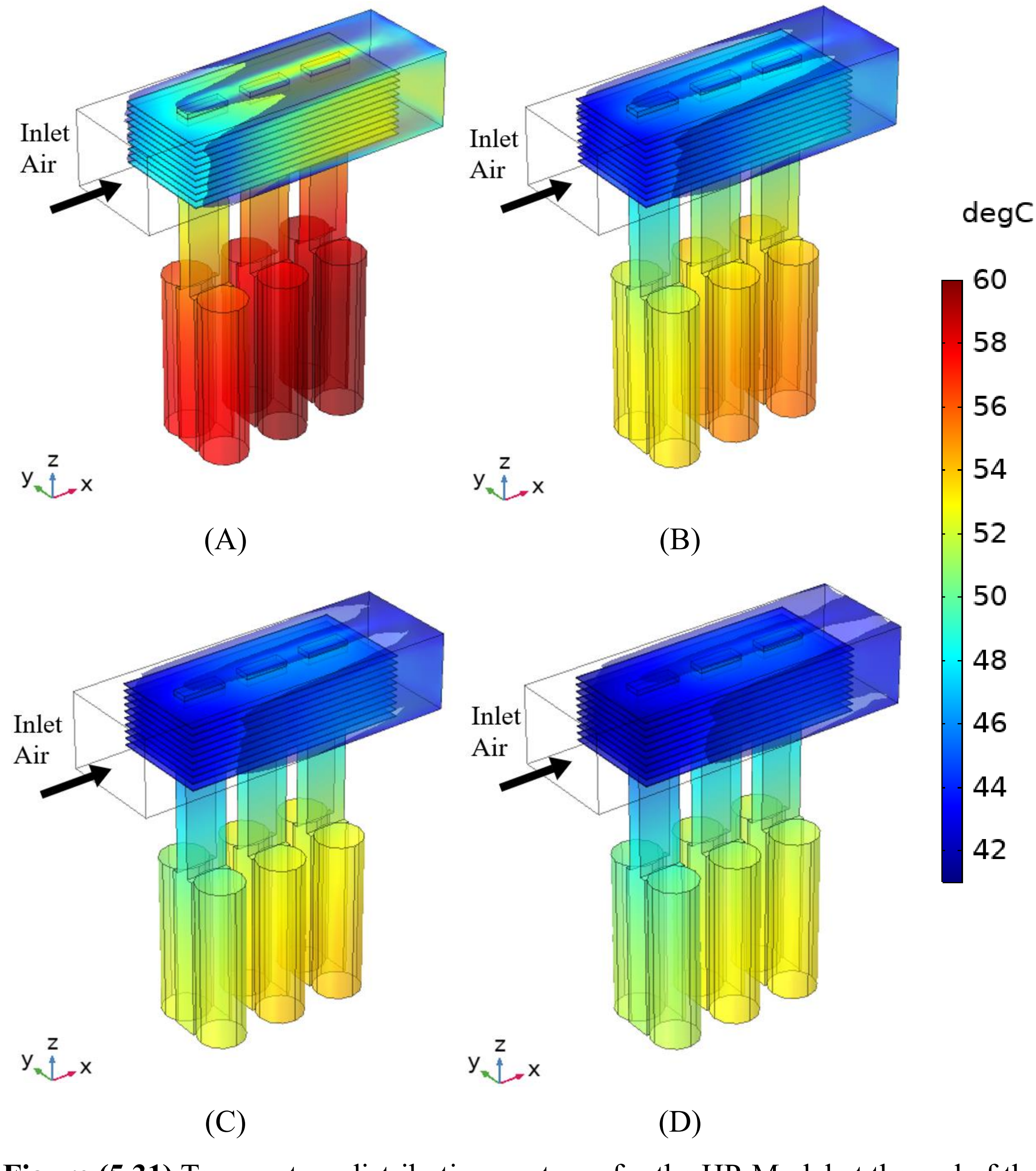

Figure (5.31) Temperature distribution contours for the HP-Model at the end of the discharge period under 3C and T_{in} of 40 ºC with various u_{in} of (A) u_{in}=0.75 m/s (B) u_{in}=1.5 m/s (C) u_{in}=2.25 m/s (D) u_{in}=3 m/s.

5.3.12 Effect of u_{in} variation on the ΔP using the HP-Model

Figures (5.32 A-D) show the pressure distribution contour at various u_{in} using HP-Model. It displays an increase in the pressure before the finned HP condenser owing to the convergence of the airflow area, then the airflow passes through the space between fins, resulting in an increase in the pressure drops. Then the pressure decreases gradually due to the friction losses until it leaves the condenser section.

The maximum ΔP across the battery pack were 5.3, 14, 26, and 41 Pa for u_{in} of 0.75, 1.5, 2.25, and 3 m/s, respectively. Furthermore, the HP-Model displays the lowest pressure loss as compared with the Air-Model and PCM/Fin-Air-Model, owing to the finned HP condenser design which has a lower contraction area in the air flow pass.

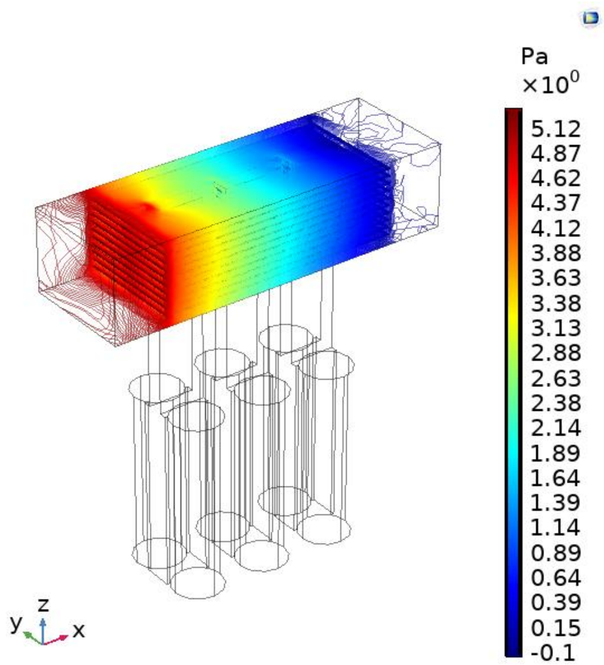

(A)

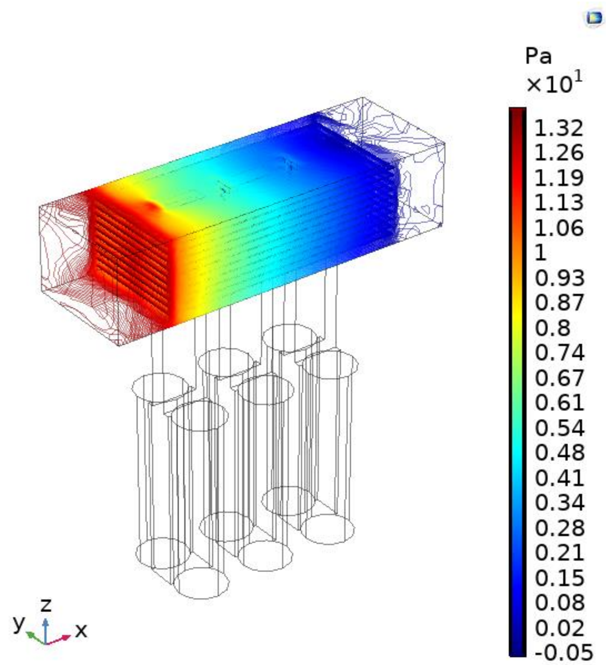

(B)

Continuous

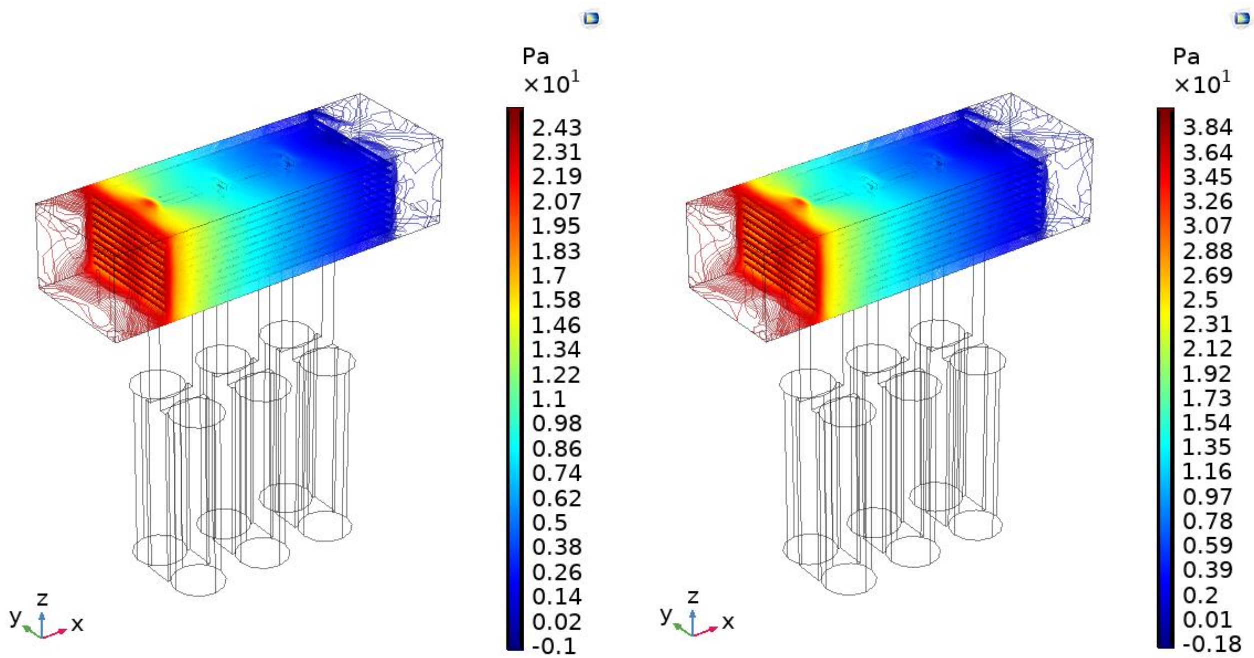

(C) (D)

Figure (5.32) Pressure distribution contours for HP-Model with various u_{in} of (A) $u_{in} = 0.75\ m/s$, (B) $u_{in} = 1.5\ m/s$, (C) $u_{in} = 2.25\ m/s$, (D) $u_{in} = 3\ m/s$.

5.3.13 Effect of T_{in} variation on the T_{max} using the HP/PCM-Model

Figures (5.33 A-D) show the variation in the T_{max} at u_{in} of 0.75 m/s and various T_{in} of 25, 30 35, and 40 ºC under C-rates of 1, 2, and 3C. The 1C rate is not studied in this model due to the low heat generation. The figures demonstrated that the T_{max} increases with increasing the T_{in} and C-rates. At 2C the T_{max} remains below the safety temperature limit throughout the discharge periods where the largest value of T_{max} were 36.4, 41.4, 44. 5 and 47.5 ºC for T_{in} of 25, 30, 35, and 40 ºC, respectively, as shown in Figures (5.33 A-D). This indicates the battery pack can operate safely for 2C-rate at an u_{in} of 0.75 m/s. At the 3C the T_{max} of the battery cell remains within the safety temperature limit at low T_{in} of 25, 30, and 35 ºC, where the largest value of T_{max} were 43.8, 46.3, and 49.7 ºC for T_{in} of 25, 30, and 35 ºC, respectively, as shown in Figures (5.33 A-C). While it exceeds the upper level of safety temperature limit at the high T_{in} of 40 ºC, where it reached 52.9 ºC, as shown in Figure (5.33 D).

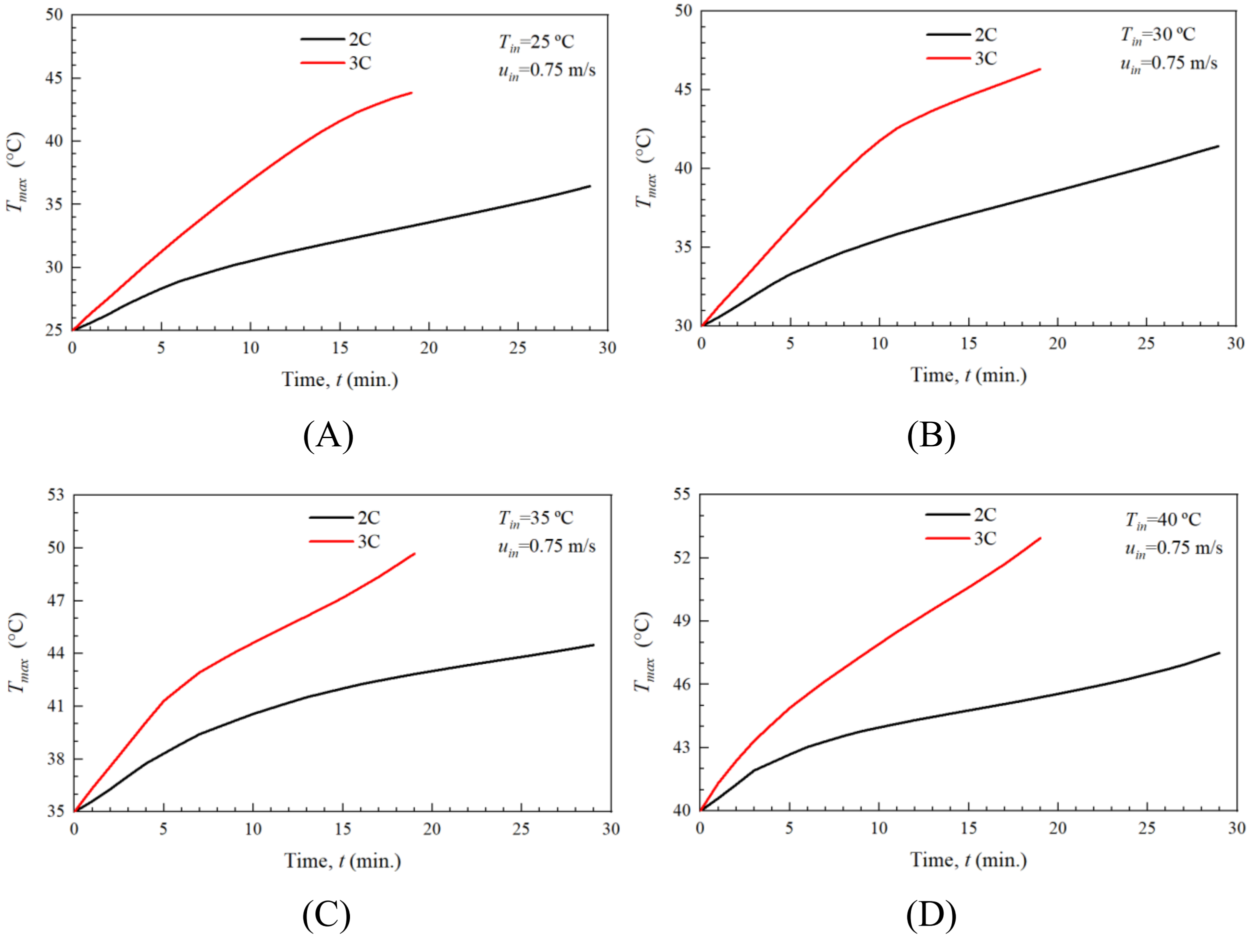

Figure (5.33) Variation of T_{max} using the HP/PCM-Model at u_{in} of 0.75 m/s and various C-rates under (A) T_{in}=25 ºC (B) T_{in}= 30 ºC (C) T_{in}= 35 ºC (D) T_{in}= 40 ºC.

5.3.14 Effect of u_{in} variation on the T_{max} and ΔT_{max} using the HP/PCM-Model

Figures (5.34 A and B) show the T_{max} and ΔT_{max} variations at T_{in} of 40 ºC for various u_{in} of 0.75, 1.5, 2.25, and 3 m/s under 3C rates. As shown in Figure (5.34 A) the changes in u_{in} had little influence on the T_{max} at the beginning of the discharge period. This was due to the small temperature difference between the air cooling and the HP condenser at the start of the discharging process, which was attributed to the HP thermal resistance, as well as, due to the phase change occurring in the PCM.

Then the variation in the T_{max} effecting by inlet air velocity change increase continuously until the end of the discharge period. Furthermore, the u_{in} increase has a slight effect on T_{max} and ΔT_{max} especially when it increases in the range between 2.25-3 m/s, meaning the thermal performance of the model became more stable when the u_{in} reached 2.25 m/s, as well as, due to the PCM integrated effect. The largest value of T_{max} at the end of the discharge period are 52.9, 51.3, 50.5, and 50.1 ºC for u_{in} of 0.75, 1.5, 2.25, and 3 m/s, respectively. In contrast, the model produces a good temperature distribution throughout the battery cells as shown in Figure (5.34 B), where the largest value of ΔT_{max} at the end of the discharge period are 1.8, 1.6, 1.4, and 1.3 ºC for u_{in} of 0.75, 1.5, 2.25, and 3 m/s, respectively.

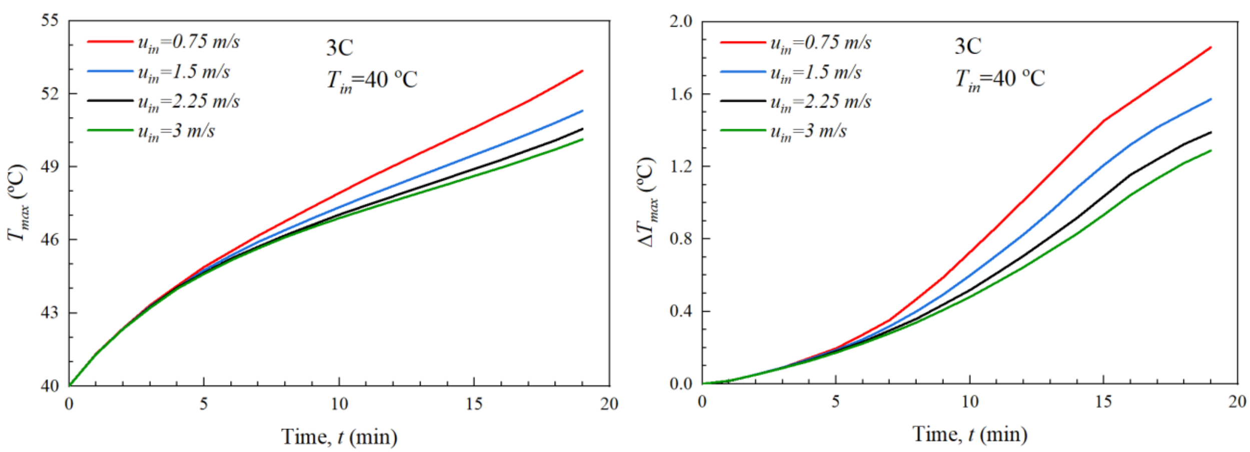

Figure (5.34) Variation of (A) T_{max} and (B) ΔT_{max}, at 3C rate and T_{in} of 40 °C under various u_{in} using the HP/PCM-Model.

Furthermore, Figures (5.35 A-D) show the temperature gradient contour at the end of the discharge rate of 3C rates across the battery pack under various u_{in} and 40 ºC operation temperature. As the discharge rate progresses, the heat generation from the battery cells is continuously transferred outwards. Some of this heat is stored in the PCM, while the other is transferred out of the battery pack through HP. Therefore, the figure shows a continuous increase of temperature gradient from the battery cells, the HP evaporator section then to the HP condenser section where the heat is rejected to the out by cooling air, as well as, from the battery cell towards the PCM.

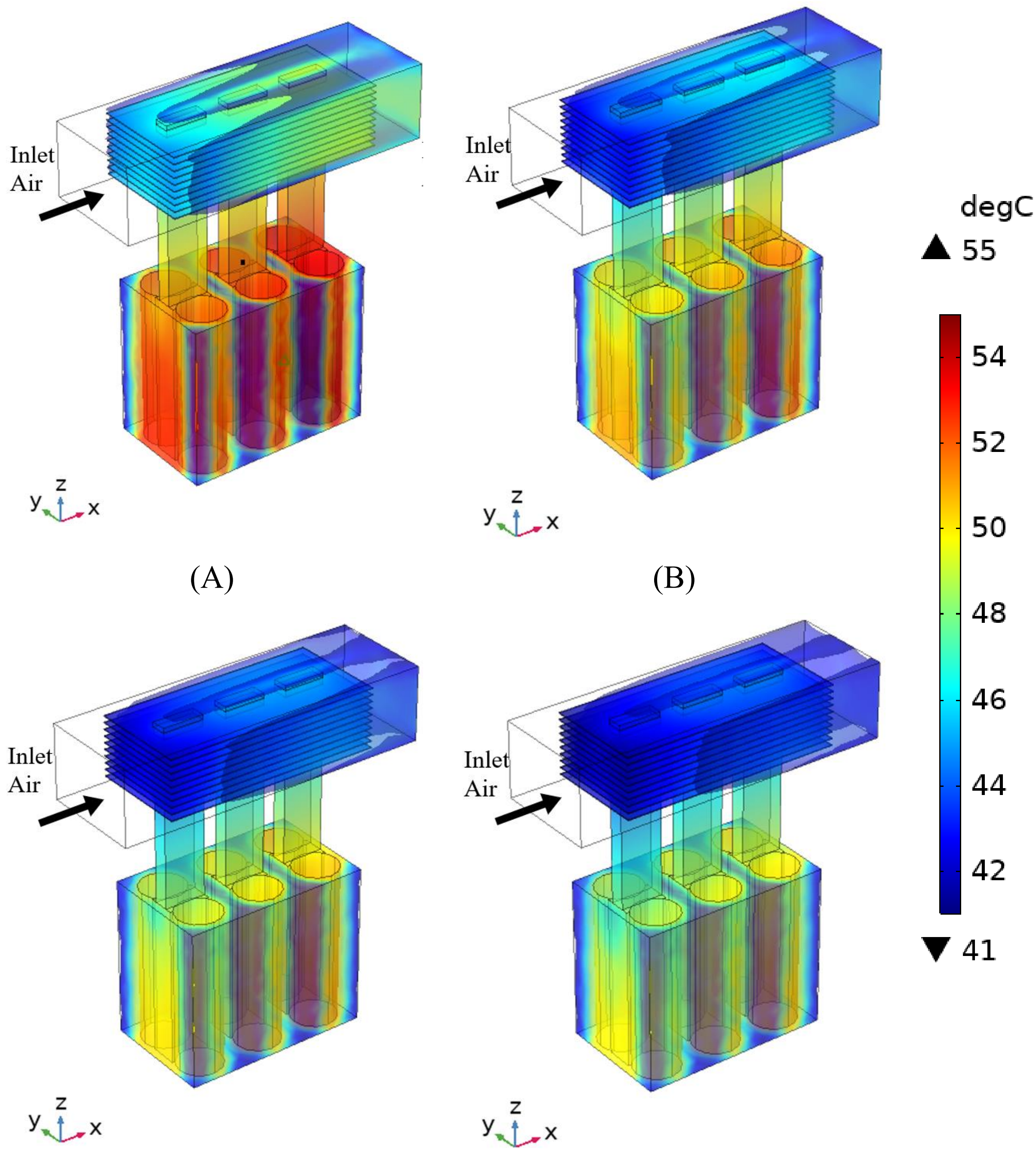

Figure (5.35) Temperature distribution contours for the HP/PCM-Model at the end of the discharge period under 3C and T_{in} of 40 ºC, and various u_{in} of (A) $u_{in} = 0.75\ m/s$, (B) $u_{in} = 1.5\ m/s$, (C) $u_{in} = 2.25\ m/s$, (D) $u_{in} = 3\ m/s$.

5.3.15 Effect of u_{in} variation on the PCM liquid fraction and temperature distribution using the HP/PCM-Model

Figures (5.36 A and B) illustrate the variation in the average liquid fraction of PCM at T_{in} of 40 ºC and various u_{in} of 0.75, 1.5, 2.25, and 3 m/s under 2C and 3C discharge rates. The figure shows that the increase in the u_{in} has a slight reduce the PCM liquid fraction rate, especially at the 3C rate, where the increase in the u_{in} from 0.75 to 3 m/s can reduce the liquid fraction of PCM from 0.621 to 0.435 and from 0.877 to 0.772 at the end of the discharge period for 2 and 3C, respectively. This owing to the small direct contact area between the HP evaporator section and PCM, as well as, to the low thermal conductivity of PCM.

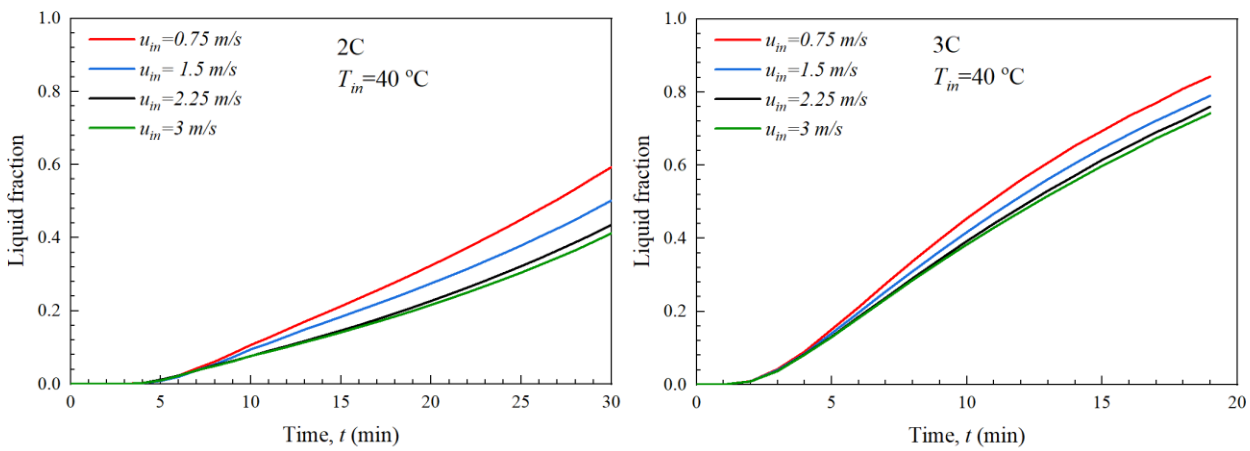

(A) (B)

Figure (5.36) Variation of the average liquid fraction using the HP/PCM-Model at T_{in} of 40 °C under various u_{in} and C-rates of (A) 2C and (B) 3C.

For further clarity, Figures (5.37) and (5.38) show the contours of the PCM liquid fraction within the battery pack at the end of the discharge period under 2C and 3C rates at T_{in} of 40 ºC and various u_{in}. Figures (5.37 A-D) illustrate the liquid fraction at a 2C rate with various u_{in} values of 0.75, 1.5, 2.25, and 3 m/s, respectively. At a low u_{in} of 0.75 m/s, a thick layer of liquid PCM is formed close to the battery cells due to the low heat rejection rate. As u_{in} increases to 1.5 m/s, the amount of liquid PCM is reduced to a thin layer close to the battery cells. In contrast, the layer of the liquid PCM is observed to almost disappear when further increases in u_{in} to 2.25 and 3 m/s.

In contrast, Figures (5.38 A-D) illustrates the liquid fraction at a 3C rate with various u_{in} values of 0.75, 1.5, 2.25, and 3 m/s, respectively. It demonstrates that a thick layer of liquid PCM is formed around all the battery cells in all u_{in} values condition with slight variation in thickness. Furthermore, the PCM melting process is not completed although the T_{max} of the battery pack exceeds the higher limit of the PCM melting point temperature.

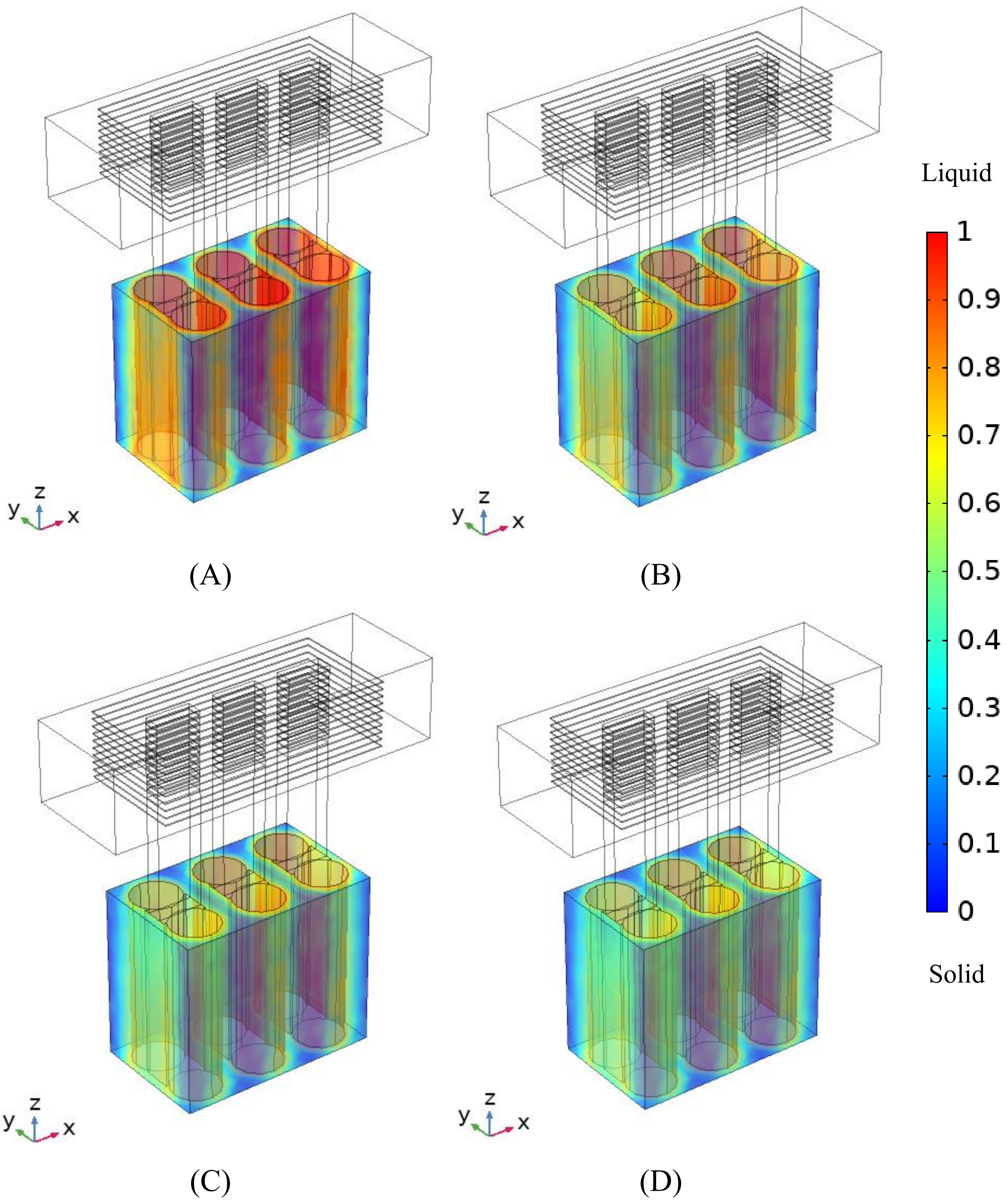

Figure (5.37) PCM liquid fraction contours for the HP/PCM-Model at the end of the discharge period under 2C and T_{in} of 40 ºC, and various u_{in} of (A) $u_{in} = 0.75\ m/s$, (B) $u_{in} = 1.5\ m/s$, (C) $u_{in} = 2.25\ m/s$, (D) $u_{in} = 3\ m/s$.

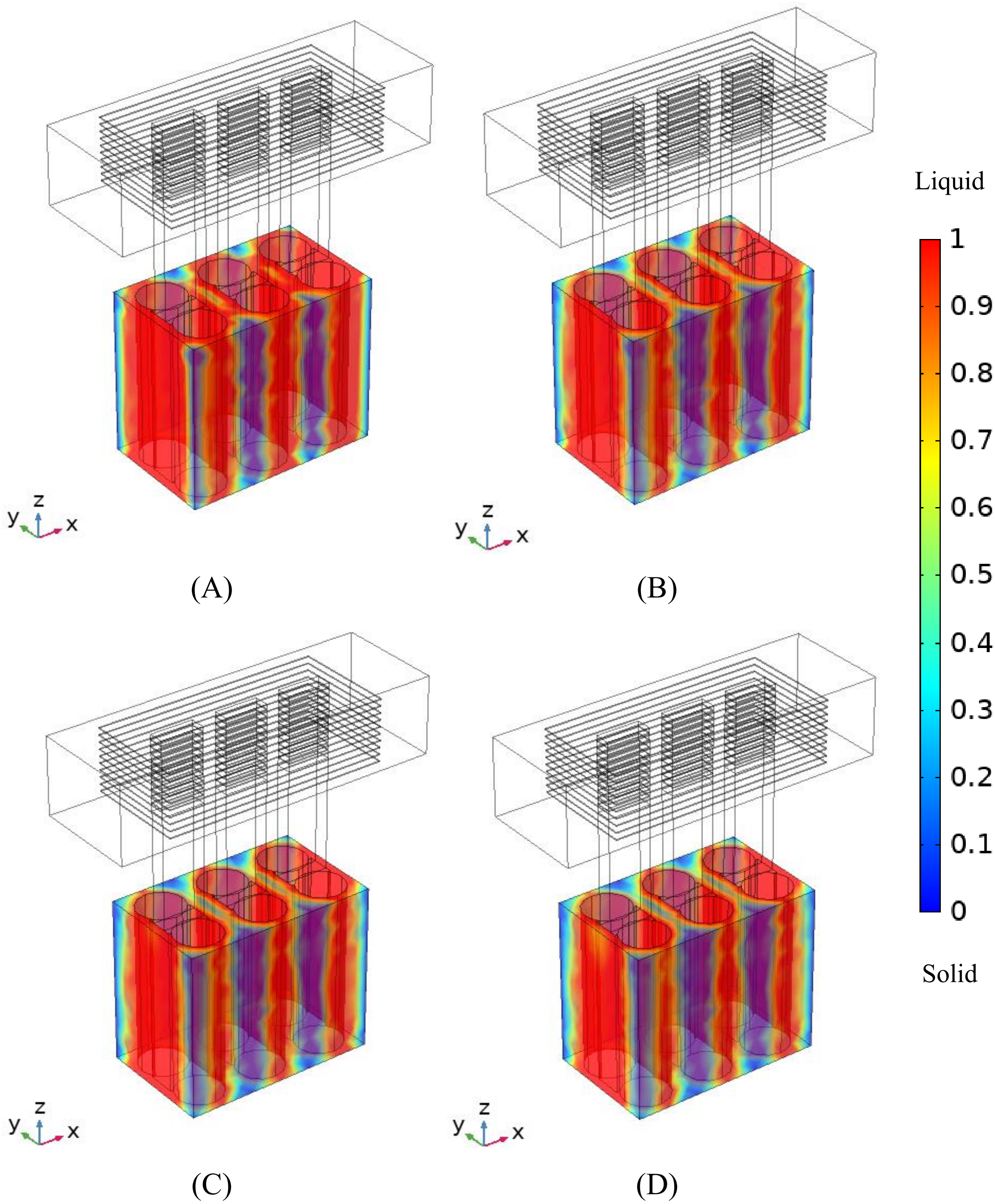

Figure (5.38) PCM liquid fraction contours for the HP/PCM-Model at the end of the discharge period under 3C and T_{in} of 40 ºC, and various u_{in} of (A) $u_{in} = 0.75\ m/s$, (B) $u_{in} = 1.5\ m/s$, (C) $u_{in} = 2.25\ m/s$, (D) $u_{in} = 3\ m/s$.

5.3.16 Numerical results comparison with the previous studies

To justify the effectiveness of the thermal performance of the HP/PCM-Model and PCM/Fin-Air-Model, their simulation results are compared with the previous simulation results of Sutheesh et al. [97] and Kavasogullari et al. [44]. The Sutheesh model consists of 21 copper HPs inserted in the space between the cylindrical 18650 Li-ion batteries which are submerged in a PCM container, and the condenser HPs are cooled with forced air. In contrast, the Kavasogullari model consists of twenty-one cylindrical 18650 Li-ion batteries, each battery was wrapped by a 4 mm thickness aluminum shell filled with PCM and, placed in the air duct. The comparison is conducted under the 3C rate. The simulated result of the present models produces a good thermal performance as compared with the Sutheesh and Kavasogullari models as shown in Figure (5.39).

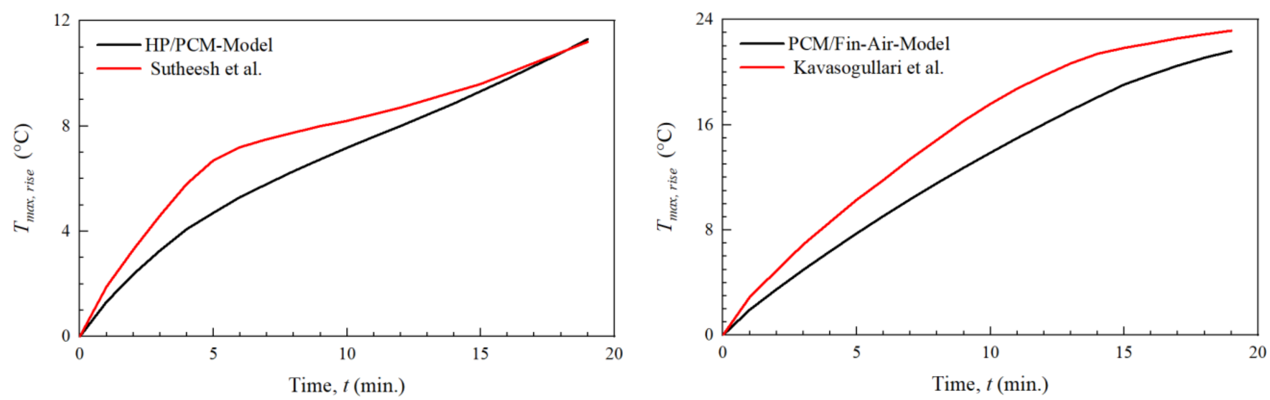

(A) (B)

Figure (5.39) Comparison of (A) HP/PCM-Model against Sutheesh et al. [97] and (B) PCM/Fin-Air-Model against Kavasogullari et al. [44].

5.4 Numerical and Experimental Results Validation

To validate the simulation models, the numerical results obtained by the COMSOL simulation approach were compared with the experimental results obtained by the present study. Figure (5.40) displays the T_{max} variation with time for various models at T_{in} and u_{in} of 40 ºC and 1.5 m/s, respectively. The figure demonstrated an acceptable agreement between the numerical and experimental results, with maximum deviations of 3.8, 6, 2.3, 2, and 2.7% for Air-Model, PCM-Model, PCM/Fin-Air-Model, HP-Model, and HP/PCM-Model, respectively.

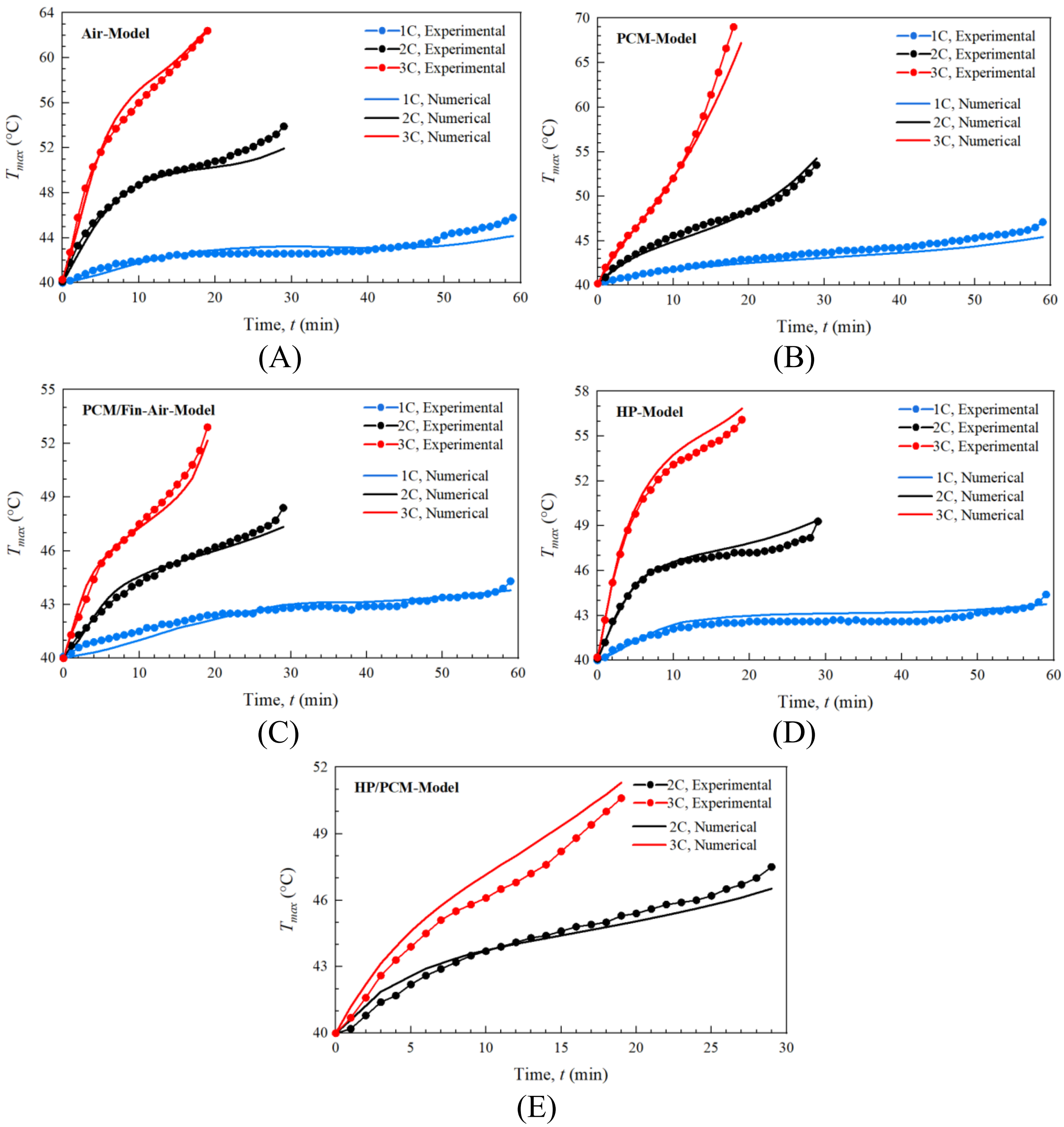

Figure (5.40) Comparison of T_{max} variation with time between the experimental and numerical results for (A) Air-Model, (B) PCM-Model, (C) PCM/Fin-Air-Model (D) HP-Model (E) HP/PCM-Model.

Chapter Six

Conclusions and Recommendations

Chapter Six

Conclusions and Recommendations

6.1 Conclusions

In this study, two novel hybrid models for cooling Li-ion batteries 18650-type $LiCoO_2$ are designed and investigated experimentally and numerically. They were tested under various operating conditions and compared with other conventional models, as well as, with other hybrid previous models.

The main conclusions are summarized as follows:

1- The novel hybrid models produce a good thermal performance as compared with the other previous hybrid models.

2- The present hybrid models can effectively enhance the thermal performance of BTMS by keeping the T_{max} within a suitable operation temperature range, compared with the conventional models, especially at a high C-rate.

3- The present hybrid models have good temperature uniformity through the battery pack where the ΔT_{max} stays below 4.2 °C at 3C rate and $u_{in} = 0.75\ m/s$.

4- The increase rate in the u_{in} has a slight effect on the T_{max} and ΔT_{max} using the present hybrid models, while it has a significant effect using Air-Model, where the T_{max} reduce by 5.3, 12.8 and 30 % as the u_{in} increase from 0.75 to 3 m/s for PCM/HP-Model, PCM/Fin-Air-Model, and Air-Model respectively.

5- The HP/PCM-Model can reduce the T_{max} by 6.7, 19.6, and 18.9 % than the case of the Air-Model and by 5.1, 10.3, and 26.6% than the case of the PCM-Model at C-rates of 1, 2, and 3C, respectively. While the PCM/Fin-Air-Model can reduce the T_{max} by 6, 18.3, and 15.2 % than the case of the Air-Model and by 4.4, 8.8, and 23.3% than the case of the PCM-Model at C-rates of 1, 2, and 3C, respectively.

6- The HP/PCM-Model has the lowest ΔP, and P_{fan} than the other models, where it can minimize the percentage P_{fan} by 94 and 90 % than PCM/Fin-Air-Model and Air-Model, respectively, at $u_{in} = 1.5\ m/s$.

7- The use of PCM coupled with HP reduces the T_{max} by 1.7, 1.8, and 7.6% at 1, 2, and 3C rates, respectively, as well as, it reduces the ΔT_{max} within the battery pack by 53, 12 and 31%, respectively.

8- Furthermore, the fitted equations of battery non-uniform heat generation rates have been found, and the average heat rate generation for a single battery cell at 1, 2, and 3C rates were 0.54 W, 2.06 W, and 4.05 W, respectively.

9- The average heat pipe's thermal resistances are 2.5, 1.7, and 1.2 °C/W at discharge rates of 1, 2, and 3C, respectively.

10- The HP/PCM-Model exhibits an excellent thermal performance with the lowest power consumption, especially at a high C-rate, as well as it can offer a safe working temperature for the Li-ion batteries. This is because the large heat transfer area of the grooved evaporator contacts with the batteries and finned condenser which efficiently absorbs the heat generation from the batteries and releases it to the forced air, as well as the additional heat generation is stored in the PCM, especially at a high discharge rate.

6.2 Recommendations for Future Work

Based on the findings of this study, the integration of HP and PCM plays an important role in enhancing the BTMS thermal performance. In contrast, the use of pure PCM integration in the HP evaporator section has some weaknesses which can be recommended for future work to improve its thermal performance as follows:

1- Improved the PCM thermal conductivity by adding the composed material to accelerate the rate of heat transfer to all parts of the PCM, which may reduce the T_{max} at a high C-rate.
2- Study the effect of the inclination angle of HP on its thermal performance.
3- Improve the thermal performance of HP by adding nano-material to the HP working fluid.

References

References:

[1] S. Ma Modi Jianga,1, Peng Taoa, Chengyi Songa, Jianbo Wua, Jun Wangb, Tao Denga, Wen Shang, "Temperature effect and thermal impact in lithium-ion batteries: A review," Progress in Natural Science: Materials International, vol. 28, no. 6. Elsevier B.V., pp. 653–666, Dec. 01, 2018. doi: https://doi.org/10.1016/j.pnsc.2018.11.002.

[2] J. Chen, J. Chen, S. Kang, Jiaqiang E, Z. Huang, K. Wei, B. Zhang, H. Zhu, Y. Deng, F. Zhang, G. Liao, "Effects of different phase change material thermal management strategies on the cooling performance of the power lithium-ion batteries: A review," Journal of Power Sources, vol. 442. Elsevier B.V., Dec. 01, 2019. doi: https://doi.org/10.1016/j.jpowsour.2019.227228.

[3] P. van den Bossche, F. Vergels, J. van Mierlo, J. Matheys, and W. van Autenboer, "SUBAT: An assessment of sustainable battery technology," Journal of Power Sources, vol. 162, no. 2 SPEC. ISS., pp. 913–919, Nov. 2006, doi: https://doi.org/10.1016/j.jpowsour.2005.07.039.

[4] M. Faizan, S. Pati, and P. Randive, "Implications of novel cold plate design with hybrid cooling on thermal management of fast discharging lithium-ion battery," Journal of Energy Storage, vol. 53, Sep. 2022, doi: https://doi.org/10.1016/j.est.2022.105051.

[5] Z. Guo, Q. Xu, and M. Ni, "A numerical study on the battery thermal management system with mini-channel cold plate considering battery aging effect," Applied Thermal Engineering, vol. 219, Jan. 2023, doi: https://doi.org/10.1016/j.applthermaleng.2022.119564.

[6] M. Ghiji, V. Novozhilov, K. Moinuddin, P. Joseph, I. Burch, B. Suendermann and G. Gamble, "A review of lithium-ion battery fire suppression," Energies, vol. 13, no. 19. MDPI AG, Oct. 01, 2020. doi:

https://doi.org/10.3390/en13195117.

[7] C. Y. Jhu, Y. W. Wang, C. Y. Wen, and C. M. Shu, “Thermal runaway potential of LiCoO2 and Li(Ni1/3Co1/3Mn1/3)O2 batteries determined with adiabatic calorimetry methodology,” Applied Energy, vol. 100, pp. 127–131, 2012, doi: https://doi.org/10.1016/j.apenergy.2012.05.064.

[8] L. H. Saw, Y. Ye, A. A. O. Tay, W. T. Chong, S. H. Kuan, and M. C. Yew, “Computational fluid dynamic and thermal analysis of Lithium-ion battery pack with air cooling,” Applied Energy, vol. 177, pp. 783–792, Sep. 2016, doi: https://doi.org/10.1016/j.apenergy.2016.05.122.

[9] I. Hunt, “Thermal effects and management of lithium ion batteries for automotive applications,” 2017, Ph.D. Thesis.

[10] F. Chen, R. Huanga, C. Wangc, X. Yua, H. Liua, Q. Wua, K. Qiana, R. Bhagat, “Air and PCM cooling for battery thermal management considering battery cycle life,” Applied Thermal Engineering, vol. 173, Jun. 2020, doi: https://doi.org/10.1016/j.applthermaleng.2020.115154.

[11] J.-M. Tarascon and M. Armand, “Issues and challenges facing rechargeable lithium batteries,” 2001. [Online]. Available: www.nature.com.

[12] S. Panchal, “Experimental Investigation and Modeling of Lithium-ion Battery Cells and Packs for Electric Vehicles”, 2016, Ph.D. Thesis.

[13] S. Abbas, Z. Ramadan, and C. W. Park, “Thermal performance analysis of compact-type simulative battery module with paraffin as phase-change material and flat plate heat pipe,” International Journal of Heat and Mass Transfer, vol. 173, Jul. 2021, doi: https://doi.org/10.1016/j.ijheatmasstransfer.2021.121269.

[14] D. M. Weragoda, G. Tian, A. Burkitbayev, K. H. Lo, and T. Zhang, “A comprehensive review on heat pipe based battery thermal management

systems," Applied Thermal Engineering, vol. 224. Elsevier Ltd, Apr. 01, 2023. doi: https://doi.org/10.1016/j.applthermaleng.2023.120070.

[15] Y. Yang, L. Chen, L. Yang, and X. Du, "Numerical study of combined air and phase change cooling for lithium-ion battery during dynamic cycles," International Journal of Thermal Sciences, vol. 165, Jul. 2021, doi: https://doi.org/10.1016/j.ijthermalsci.2021.106968.

[16] P. Ping, Y. Zhang, D. Kong, and J. Du, "Investigation on battery thermal management system combining phase changed material and liquid cooling considering non-uniform heat generation of battery," Journal of Energy Storage, vol. 36, Apr. 2021, doi: https://doi.org/10.1016/j.est.2021.102448.

[17] G. Chen, Y. Shi, H. Ye, and H. Kang, "Experimental study on phase change material based thermal management design with adjustable fins for lithium-ion battery," Applied Thermal Engineering, vol. 221, Feb. 2023, doi: https://doi.org/10.1016/j.applthermaleng.2022.119808.

[18] P. G. Zadeh, E. Gholamalizadeh, Y. Wang, and J. D. Chung, "Electrochemical modeling of a thermal management system for cylindrical lithium-ion battery pack considering battery capacity fade," Case Studies in Thermal Engineering, vol. 32, Apr. 2022, doi: https://doi.org/10.1016/j.csite.2022.101878.

[19] S. Shahid and M. Agelin-Chaab, "A review of thermal runaway prevention and mitigation strategies for lithium-ion batteries," Energy Conversion and Management: X, vol. 16. Elsevier Ltd, Dec. 01, 2022. doi: https://doi.org/10.1016/j.ecmx.2022.100310.

[20] A. Samba, "Battery Electrical Vehicles-Analysis of Thermal Modelling and Thermal Management." [Online]. Available: https://hal.archives-ouvertes.fr/tel-01298416

[21] K. S. Kshetrimayum, Y. G. Yoon, H. R. Gye, and C. J. Lee, "Preventing heat propagation and thermal runaway in electric vehicle battery modules using

integrated PCM and micro-channel plate cooling system," Applied Thermal Engineering, vol. 159, Aug. 2019, doi: https://doi.org/10.1016/j.applthermaleng.2019.113797.

[22] A. Mitra, R. Kumar, D. K. Singh, and Z. Said, "Advances in the improvement of thermal-conductivity of phase change material-based lithium-ion battery thermal management systems: An updated review," Journal of Energy Storage, vol. 53, Sep. 2022, doi: https://doi.org/10.1016/j.est.2022.105195.

[23] Y. S. Duh, Y. Sun, X. Lin, J. Zheng, M. Wang,Y. Wang, X. Lin, X. Jiang, Z. Zheng, S. Zheng, G. Yu, "Characterization on thermal runaway of commercial 18650 lithium-ion batteries used in electric vehicles: A review," Journal of Energy Storage, vol. 41. Elsevier Ltd, Sep. 01, 2021. doi: https://doi.org/10.1016/j.est.2021.102888.

[24] S. Chavan, R. Rudrapati, B. Venkateswarlu, S. Woo Joo, and S. Chul Kim, "An innovative approach to multi-response optimization of battery thermal management systems using multi-desirability function approach," Applied Thermal Engineering, vol. 236, Jan. 2024, doi: https://doi.org/10.1016/j.applthermaleng.2023.121835.

[25] P. Saechan and I. Dhuchakallaya, "Numerical study on the air-cooled thermal management of Lithium-ion battery pack for electrical vehicles," Energy Reports, vol. 8, pp. 1264–1270, Apr. 2022, doi: https://doi.org/10.1016/j.egyr.2021.11.089.

[26] M. Yacoub Al Shdaifat, R. Zulkifli, K. Sopian, and A. Adel Salih, "Basics, properties, and thermal issues of EV battery and battery thermal management systems: Comprehensive review," Proceedings of the Institution of Mechanical Engineers, Part D: Journal of Automobile Engineering, vol. 237, no. 2–3. SAGE Publications Ltd, pp. 295–311, Feb. 01, 2023. doi: https://doi.org/10.1177/09544070221079195.

[27] A. Wazeer, A. Das, C. Abeykoon, A. Sinha, and A. Karmakar, “Phase change materials for battery thermal management of electric and hybrid vehicles: A review,” Energy Nexus, vol. 7, Sep. 2022, doi: https://doi.org/10.1016/j.nexus.2022.100131.

[28] Z. Rao, Z. Qian, Y. Kuang, and Y. Li, “Thermal performance of liquid cooling based thermal management system for cylindrical lithium-ion battery module with variable contact surface,” Applied Thermal Engineering, vol. 123, pp. 1514–1522, 2017, doi: https://doi.org/10.1016/j.applthermaleng.2017.06.059.

[29] L. Zhao, W. Li, G. Wang, W. Cheng, and M. Chen, “A novel thermal management system for lithium-ion battery modules combining direct liquid-cooling with forced air-cooling,” Applied Thermal Engineering, vol. 232, Sep. 2023, doi: https://doi.org/10.1016/j.applthermaleng.2023.120992.

[30] S. Mazyar and H. Moghaddam, “Designing battery thermal management systems (BTMS) for cylindrical Lithium-ion battery modules using CFD.”

[31] I. K. Lokhande and N. Tiwari, “Enhancing lithium-ion battery cooling efficiency using composite phase change material packed mini-chambers: A numerical study,” Journal of Energy Storage, vol. 72, Nov. 2023, doi: https://doi.org/10.1016/j.est.2023.108749.

[32] H. Behi, D. Karimi, M. Behi, M. Ghanbarpourd, J. Jaguemont, M. A. Sokkeh, F. H. Gandoman, M. Berecibar, J. V. Mierlo, “A new concept of thermal management system in Li-ion battery using air cooling and heat pipe for electric vehicles,” Applied Thermal Engineering, vol. 174, Jun. 2020, doi: https://doi.org/10.1016/j.applthermaleng.2020.115280.

[33] P. Peng, Y. Wang, and F. Jiang, “Numerical study of PCM thermal behavior of a novel PCM-heat pipe combined system for Li-ion battery thermal management,” Applied Thermal Engineering, vol. 209, Jun. 2022, doi: https://doi.org/10.1016/j.applthermaleng.2022.118293.

[34] D. Brough and H. Jouhara, "The aluminium industry: A review on state-of-the-art technologies, environmental impacts and possibilities for waste heat recovery," International Journal of Thermofluids, vol. 1–2. Elsevier B.V., Feb. 01, 2020. doi: https://doi.org/10.1016/j.ijft.2019.100007.

[35] Y. Azizi and S. M. Sadrameli, "Thermal management of a LiFePO4 battery pack at high temperature environment using a composite of phase change materials and aluminum wire mesh plates," Energy Conversion and Management, vol. 128, pp. 294–302, Nov. 2016, doi: https://doi.org/10.1016/j.enconman.2016.09.081.

[36] M. M. Hamed, A. El-Tayeb, I. Moukhtar, A. Z. Dein, and E. H. Abdelhameed, "A review on recent key technologies of lithium-ion battery thermal management: External cooling systems," Results in Engineering, vol. 16. Elsevier B.V., Dec. 01, 2022. doi: https://doi.org/10.1016/j.rineng.2022.100703.

[37] C. Liu, Xu D, Weng J, Zhou S, Li W, Wan Y, Jiang S, Zhou D, Wang J, and Huang Q, "Phase change materials application in battery thermal management system: A review," Materials, vol. 13, no. 20. MDPI AG, pp. 1–37, Oct. 02, 2020. doi: https://doi.org/10.3390/ma13204622.

[38] P. Cicconi, P. Kumar, and P. Varshney, "A support approach for the modular design of li-ion batteries: A test case with PCM," Journal of Energy Storage, vol. 31, Oct. 2020, doi: https://doi.org/10.1016/j.est.2020.101684.

[39] Z. Ling, Z. Zhang, G. Shi, X. Fang, L. Wang, X. Gao, Y. Fang, T. Xu, S. Wang, X. Liu, "Review on thermal management systems using phase change materials for electronic components, Li-ion batteries and photovoltaic modules," Renewable and Sustainable Energy Reviews, vol. 31. Elsevier Ltd, pp. 427–438, 2014. doi: https://doi.org/10.1016/j.rser.2013.12.017.

[40] Y. Wang, P. Penga, W. Caoa, T. Donga, Y. Zhengb, B. Leic, Y. Shic, F. Jiang, "Experimental study on a novel compact cooling system for cylindrical lithium-ion battery module," Applied Thermal Engineering, vol. 180, Nov. 2020, doi: https://doi.org/10.1016/j.applthermaleng.2020.115772.

[41] Q. Huang, X. Li, G. Zhang, J. Zhang, F. He, and Y. Li, "Experimental investigation of the thermal performance of heat pipe assisted phase change material for battery thermal management system," Applied Thermal Engineering, vol. 141, pp. 1092–1100, Aug. 2018, doi: https://doi.org/10.1016/j.applthermaleng.2018.06.048.

[42] Z. Leng, Y. Yuan, X. Cao, W. Zhong, and C. Zeng, "Heat pipe/phase change material coupled thermal management in Li-ion battery packs: Optimization and energy-saving assessment," Applied Thermal Engineering, vol. 208, Feb. 2022, doi: https://doi.org/10.1016/j.applthermaleng.2022.118211.

[43] J. Wang, W. Mei, B. Mao, and Q. Wang, "Investigation on the temperature control performance and optimization strategy of a battery thermal management system combining phase change and liquid cooling," Applied Thermal Engineering, vol. 232, Sep. 2023, doi: https://doi.org/10.1016/j.applthermaleng.2023.121080.

[44] B. Kavasoğullari, M. E. Karagöz, A. S. Yildiz, and E. Biçer, "Numerical investigation of the performance of a hybrid battery thermal management system at high discharge rates," Journal of Energy Storage, vol. 73, Dec. 2023, doi: https://doi.org/10.1016/j.est.2023.108982.

[45] Z. Leng, Y. Yuan, X. Cao, C. Zeng, W. Zhong, and B. Gao, "Heat pipe/phase change material thermal management of Li-ion power battery packs: A numerical study on coupled heat transfer performance," Energy, vol. 240, Feb. 2022, doi: https://doi.org/10.1016/j.energy.2021.122754.

[46] M. A. Bamdezh, G. R. Molaeimanesh, and S. Zanganeh, "Role of foam anisotropy used in the phase-change composite material for the hybrid thermal management system of lithium-ion battery," Journal of Energy Storage, vol. 32, Dec. 2020, doi: https://doi.org/10.1016/j.est.2020.101778.

[47] W. Yang, F. Zhou, H. Zhou, Q. Wang, and J. Kong, "Thermal performance of cylindrical lithium-ion battery thermal management system integrated with mini-channel liquid cooling and air cooling," Applied Thermal Engineering, vol. 175, Jul. 2020, doi: https://doi.org/10.1016/j.applthermaleng.2020.115331.

[48] F. Liu, F. Lan, and J. Chen, "Dynamic thermal characteristics of heat pipe via segmented thermal resistance model for electric vehicle battery cooling," Journal of Power Sources, vol. 321, pp. 57–70, Jul. 2016, doi: https://doi.org/10.1016/j.jpowsour.2016.04.108.

[49] Y. Gan, L. He, J. Liang, M. Tan, T. Xiong, and Y. Li, "A numerical study on the performance of a thermal management system for a battery pack with cylindrical cells based on heat pipes," Applied Thermal Engineering, vol. 179, Oct. 2020, doi: https://doi.org/10.1016/j.applthermaleng.2020.115740.

[50] A. A. A. Hakeem and D. Solyali, "Empirical thermal performance investigation of a compact lithium-ion battery module under forced convection cooling," Applied Sciences (Switzerland), vol. 10, no. 11, Jun. 2020, doi: https://doi.org/10.3390/app10113732.

[51] K. Kirad and M. Chaudhari, "Design of cell spacing in lithium-ion battery module for improvement in cooling performance of the battery thermal management system," Journal of Power Sources, vol. 481, Jan. 2021, doi: https://doi.org/10.1016/j.jpowsour.2020.229016.

[52] M. W. Nazar, N. Iqbal, M. Ali, H. Nazir, and M. Z. bin Amjad, "Thermal management of Li-ion battery by using active and passive cooling method,"

Journal of Energy Storage, vol. 61, May 2023, doi: https://doi.org/10.1016/j.est.2023.106800.

[53] H. Zhou, F. Zhou, Q. Zhang, Q. Wang, and Z. Song, "Thermal management of cylindrical lithium-ion battery based on a liquid cooling method with half-helical duct," Applied Thermal Engineering, vol. 162, Nov. 2019, doi: https://doi.org/10.1016/j.applthermaleng.2019.114257.

[54] W. Wei, Z. Luo, S. Qiao, J. Zhai, and Z. Lei, "Analysis and design of module-level liquid cooling system for rectangular Li-ion batteries," International Journal of Heat and Mass Transfer, vol. 225, Jun. 2024, doi: https://doi.org/10.1016/j.ijheatmasstransfer.2024.125435.

[55] P. Jha, M. Hussain, and M. K. Khan, "Numerical evaluation of nanofluid-based indirect liquid cooling of a Li-ion battery pack using equivalent circuit model under static and dynamic loading conditions," International Communications in Heat and Mass Transfer, vol. 159, Dec. 2024, doi: https://doi.org/10.1016/j.icheatmasstransfer.2024.108079.

[56] Z. Rao, S. Wang, M. Wu, Z. Lin, and F. Li, "Experimental investigation on thermal management of electric vehicle battery with heat pipe," Energy Conversion and Management, vol. 65, pp. 92–97, Jan. 2013, doi: https://doi.org/10.1016/j.enconman.2012.08.014.

[57] A. Greco, D. Cao, X. Jiang, and H. Yang, "A theoretical and computational study of lithium-ion battery thermal management for electric vehicles using heat pipes," Journal of Power Sources, vol. 257, pp. 344–355, Jul. 2014, doi: https://doi.org/10.1016/j.jpowsour.2014.02.004.

[58] F. M. Nasir, M. Z. Abdullah, and M. A. Ismail, "Experimental Investigation of Water-Cooled Heat Pipes in the Thermal Management of Lithium-Ion EV Batteries," Arabian Journal for Science and Engineering, vol. 44, no. 9, pp. 7541–7552, Sep. 2019, doi: https://doi.org/10.1007/s13369-019-03851-5.

[59] W. Liu, Z. Jia, Y. Luo, W. Xie, and T. Deng, "Experimental investigation on thermal management of cylindrical Li-ion battery pack based on vapor chamber combined with fin structure," Applied Thermal Engineering, vol. 162, Nov. 2019, doi: https://doi.org/10.1016/j.applthermaleng.2019.114272.

[60] A. Alihosseini and M. Shafaee, "Experimental study and numerical simulation of a Lithium-ion battery thermal management system using a heat pipe," Journal of Energy Storage, vol. 39, Jul. 2021, doi: https://doi.org/10.1016/j.est.2021.102616.

[61] T. Wang, S. Tan, C. Guo, H. Su, C. Guo, and Y. Jiang, "Experimental study on U-shape flat thermosyphon for thermal management of power battery," Journal of Mechanical Science and Technology, vol. 35, no. 9, pp. 4193–4200, Sep. 2021, doi: https://doi.org/10.1007/s12206-021-0831-6.

[62] J. E, F. Yi, W. Li, B. Zhang , H. Zuo, K. Wei, J. Chen, H Zhu, H. Zhu, Y. Deng, "Effect analysis on heat dissipation performance enhancement of a lithium-ion-battery pack with heat pipe for central and southern regions in China," Energy, vol. 226, Jul. 2021, doi: https://doi.org/10.1016/j.energy.2021.120336.

[63] U. Han, S. Lee, Y. J. Jun, and H. Lee, "Experimental investigation on thermal performance of battery thermal management system with heat pipe assisted hybrid fin structure under fast charging conditions," Applied Thermal Engineering, vol. 230, Jul. 2023, doi: https://doi.org/10.1016/j.applthermaleng.2023.120840.

[64] M. Zheng, Y. Liu, Z. Ma, Y. Li, D. Li, Z. Lu, H.Song, X. Guo, W. Shao, "Numerical study on power battery thermal management system based on heat pipe technology," Energy Reports, vol. 9, pp. 350–361, Dec. 2023, doi: https://doi.org/10.1016/j.egyr.2022.11.187.

[65] Z. Sun, R. Fan, F. Yan, T. Zhou, and N. Zheng, "Thermal management of the lithium-ion battery by the composite PCM-Fin structures," International Journal

of Heat and Mass Transfer, vol. 145, Dec. 2019, doi: https://doi.org/10.1016/j.ijheatmasstransfer.2019.118739.

[66] N. Zheng, R. Fan, Z. Sun, and T. Zhou, "Thermal management performance of a fin-enhanced phase change material system for the lithium-ion battery," International Journal of Energy Research, vol. 44, no. 9, pp. 7617–7629, Jul. 2020, doi: https://doi.org/10.1002/er.5494.

[67] G. Srivastava, R. Nandan, and M. K. Das, "Thermal runaway management of Li ion battery using PCM: A parametric study," Energy Conversion and Management: X, vol. 16, Dec. 2022, doi: https://doi.org/10.1016/j.ecmx.2022.100306.

[68] H. Behi, D. Karimi, M. Behi, N. Nargesi, M. Aminian, A. Ghanbarpour, F. Mirmohseni, J. V. Mierlo, M. Berecibar, "An Enhanced Phase Change Material Composite for Electrical Vehicle Thermal Management," Designs, vol. 6, no. 5, Oct. 2022, doi: https://doi.org/10.3390/designs6050070.

[69] Y. Li, Z. Zhou, L. Hu, M. Bai, L. Gao, Y. Li, X. Liu, Y. Li, Y Song, "Experimental studies of liquid immersion cooling for 18650 lithium-ion battery under different discharging conditions," Case Studies in Thermal Engineering, vol. 34, Jun. 2022, doi: https://doi.org/10.1016/j.csite.2022.102034.

[70] A. C. Budiman, S. Kaleg, Sudirja, Amin, And A. Hapid, "Passive thermal management of battery module using paraffin-filled tubes: An experimental investigation," Engineering Science and Technology, an International Journal, vol. 29, May 2022, doi: https://doi.org/10.1016/j.jestch.2021.06.011.

[71] H. Chen, A. Abidi, A. K. Hussein, O. Younis, M. Degani, and B. Heidarshenas, "Investigation of the use of extended surfaces in paraffin wax phase change material in thermal management of a cylindrical lithium-ion battery: Applicable

in the aerospace industry," Journal of Energy Storage, vol. 45, Jan. 2022, doi: https://doi.org/10.1016/j.est.2021.103685.

[72] Z. Sun, Y. Guo, C. Zhang, J. Whitehouse, Q. Zhou, H. Xu, C Wang, "Experimental study of battery passive thermal management system using copper foam-based phase change materials," International Journal of Thermofluids, vol. 17, Feb. 2023, doi: https://doi.org/10.1016/j.ijft.2022.100255.

[73] Y. Li, Z. Chen, Y. Feng, M. Liu, C. Kang, K. Yang, J. Yuan, C. Qiu, H. Shi, Y. Jiang, "A novel petal-type battery thermal management system with dual phase change materials," International Journal of Heat and Mass Transfer, vol. 207, Jun. 2023, doi: https://doi.org/10.1016/j.ijheatmasstransfer.2023.123989.

[74] S. Sudhakaran, M. Terese, Y. Mohan, A. D. Thampi, and S. Rani, "Influence of various parameters on the cooling performance of battery thermal management systems based on phase change materials," Applied Thermal Engineering, vol. 222, Mar. 2023, doi: https://doi.org/10.1016/j.applthermaleng.2022.119936.

[75] S. Wang, D. Zhang, C. Li, J. Wang, J. Zhang, Y. Cheng, W. Mei, S. Cheng, P. Qin, Q. Duan, J. Sun, Q. Wang, "Numerical optimization for a phase change material based lithium-ion battery thermal management system," Applied Thermal Engineering, vol. 222, Mar. 2023, doi: https://doi.org/10.1016/j.applthermaleng.2022.119839.

[76] G. Jiang, J. Huang, M. Liu, and M. Cao, "Experiment and simulation of thermal management for a tube-shell Li-ion battery pack with composite phase change material," Applied Thermal Engineering, vol. 120, pp. 1–9, 2017, doi: https://doi.org/10.1016/j.applthermaleng.2017.03.107.

[77] P. Qin, M. Liao, D. Zhang, Y. Liu, J. Sun, and Q. Wang, "Experimental and numerical study on a novel hybrid battery thermal management system integrated forced-air convection and phase change material," Energy

Conversion and Management, vol. 195, pp. 1371–1381, Sep. 2019, doi: https://doi.org/10.1016/j.enconman.2019.05.084.

[78] D. Kong, R. Peng, P. Ping, J. Du, G. Chen, and J. Wen, “A novel battery thermal management system coupling with PCM and optimized controllable liquid cooling for different ambient temperatures,” Energy Conversion and Management, vol. 204, Jan. 2020, doi: https://doi.org/10.1016/j.enconman.2019.112280.

[79] R. D. Jilte, R. Kumar, M. H. Ahmadi, and L. Chen, “Battery thermal management system employing phase change material with cell-to-cell air cooling,” Applied Thermal Engineering, vol. 161. Elsevier Ltd, Oct. 01, 2019. doi: https://doi.org/10.1016/j.applthermaleng.2019.114199.

[80] Q. Huang, Z. Zhong, X. Li, G. Zhang, D. Wei, W. Yuan, J. Zhang, D. Zhou, “Experimental and Numerical Investigation on an Integrated Thermal Management System for the Li-Ion Battery Module with Phase Change Material,” International Journal of Photoenergy, vol. 2020, 2020, doi: https://doi.org/10.1155/2020/4695419.

[81] C. Hu, H. Li, Y. Wang, X. Hu, and D. Tang, “Experimental and numerical investigations of lithium-ion battery thermal management using flat heat pipe and phase change material,” Journal of Energy Storage, vol. 55, Nov. 2022, doi: https://doi.org/10.1016/j.est.2022.105743.

[82] A. E. Anqi, C. Li, H. A. Dhahad, K. Sharma, E. ATTIA, A. Abdelrahman, A. G. Mohammed, S. Alamri, A. A. Rajhi, “Effect of combined air cooling and nano enhanced phase change materials on thermal management of lithium-ion batteries,” Journal of Energy Storage, vol. 52. Elsevier Ltd, Aug. 25, 2022. doi: https://doi.org/10.1016/j.est.2022.104906.

[83] Q. Gu, G. Li, and Z. Wu, “The analysis on the battery thermal management system with composite phase change materials coupled air cooling and fins,”

Journal of Energy Storage, vol. 56, Dec. 2022, doi: https://doi.org/10.1016/j.est.2022.105977.

[84] A. Fu, Z. Zhang, J. Lin, Y. Zou, C. Qin, C. Xu, P. Yan, K. Zhou, J. Hao, X. Yang, Y. Cheng, D. Wu, Y. Yang, M. Wang, J. Zheng, "Highly stable operation of LiCoO2 at cut-off ≥ 4.6 V enabled by synergistic structural and interfacial manipulation," Energy Storage Materials, vol. 46, pp. 406–416, Apr. 2022, doi: https://doi.org/10.1016/j.ensm.2022.01.033.

[85] Y. S. Duh, X. Liu, X. Jiang, C. S. Kao, L. Gong, and R. Shi, "Thermal kinetics on exothermic reactions of a commercial LiCoO2 18650 lithium-ion battery and its components used in electric vehicles: A review," Journal of Energy Storage, vol. 30. Elsevier Ltd, Aug. 01, 2020. doi: https://doi.org/10.1016/j.est.2020.101422.

[86] D. Pedersen, M. Lybbert, and R. Warren, "Life Cycle Analysis of LiCoO2/ Graphite Batteries with Cooling using Combined Electrochemical-Thermal Modeling," Resources, Conservation and Recycling, vol. 180, May 2022, doi: https://doi.org/10.1016/j.resconrec.2022.106204.

[87] L. K. Singh, G. Mishra, A. K. Sharma, and A. K. Gupta, "A numerical study on thermal management of a lithium-ion battery module via forced-convective air cooling," International Journal of Refrigeration, vol. 131, pp. 218–234, Nov. 2021, doi: https://doi.org/10.1016/j.ijrefrig.2021.07.031.

[88] N. S. Spinner, R. Mazurick, A. Brandon, S. L. Rose-Pehrsson, and S. G. Tuttle, " Analytical, Numerical and Experimental Determination of Thermophysical Properties of Commercial 18650 LiCoO2 Lithium-Ion Battery," Journal of The Electrochemical Society, vol. 162, no. 14, pp. A2789–A2795, 2015, doi: https://doi.org/10.1149/2.0871514jes.

[89] Z. Hu, X. He, F. Restuccia, and G. Rein, "Numerical Study of Self-Heating Ignition of a Box of Lithium-Ion Batteries During Storage," Fire Technology,

vol. 56, no. 6, pp. 2603–2621, Nov. 2020, doi: https://doi.org/10.1007/s10694-020-00998-8.

[90] Ahmed Fouad Mahmood Al-Neama, “Serpentine Minichannel Liquid-Cooled Heat Sinks for Electronics Cooling Applications,” 2018, Ph.D. Thesis.

[91] E. M. Sparrow, J. P. Abraham, and W. J. Minkowycz, “Flow separation in a diverging conical duct: Effect of Reynolds number and divergence angle,” International Journal of Heat and Mass Transfer, vol. 52, no. 13–14, pp. 3079–3083, Jun. 2009, doi: https://doi.org/10.1016/j.ijheatmasstransfer.2009.02.010.

[92] ASHRAE, 1997 ASHRAE Handbook - Fundamentals. Atlanta, GA: American Society of Heating, Refrigerating and Air-Conditioning Engineers, 1997.

[93] Y. Gan, J. Wang, J. Liang, Z. Huang, and M. Hu, “Development of thermal equivalent circuit model of heat pipe-based thermal management system for a battery module with cylindrical cells,” Applied Thermal Engineering, vol. 164, Jan. 2020, doi: https://doi.org/10.1016/j.applthermaleng.2019.114523.

[94] H. M. Abd, O. R. Alomar, and M. M. M. Salih, “Improving the performance of solar air heater using a new model of V-corrugated absorber plate having perforations jets,” International Journal of Energy Research, vol. 46, no. 6, pp. 8130–8144, May 2022, doi: https://doi.org/10.1002/er.7715.

[95] C. Li, Y. Ding, Z. Zhou, Y. Jin, X. Ren, C. Cao, H. Hu, “Parameter optimization and sensitivity analysis of a Lithium-ion battery thermal management system integrated with composite phase change material,” Applied Thermal Engineering, vol. 228, Jun. 2023, doi: https://doi.org/10.1016/j.applthermaleng.2023.120530.

[96] P. M. Sutheesh, R. B. Nichit, and B. Rohinikumar, “Numerical investigation of thermal management of lithium-ion battery pack with nano-enhanced phase change material and heat pipe,” Journal of Energy Storage, vol. 77, Jan. 2024, doi: https://doi.org/10.1016/j.est.2023.109972.

Appendices

Appendix:

A.1 Thermocouples Calibrations

All thermocouples were tested and calibrated against mercury thermometers using standard procedures to ensure reliable data before their use in experimentation. The thermocouples and mercury thermometer were placed in a water container equipped with an electrical heater and a mixing fan to achieve a uniform temperature rise. Temperature values from both the thermocouples and mercury thermometers were recorded at specific increments in water temperature. Figures (A-a) through (A-12) display the measured values and their associated uncertainties.

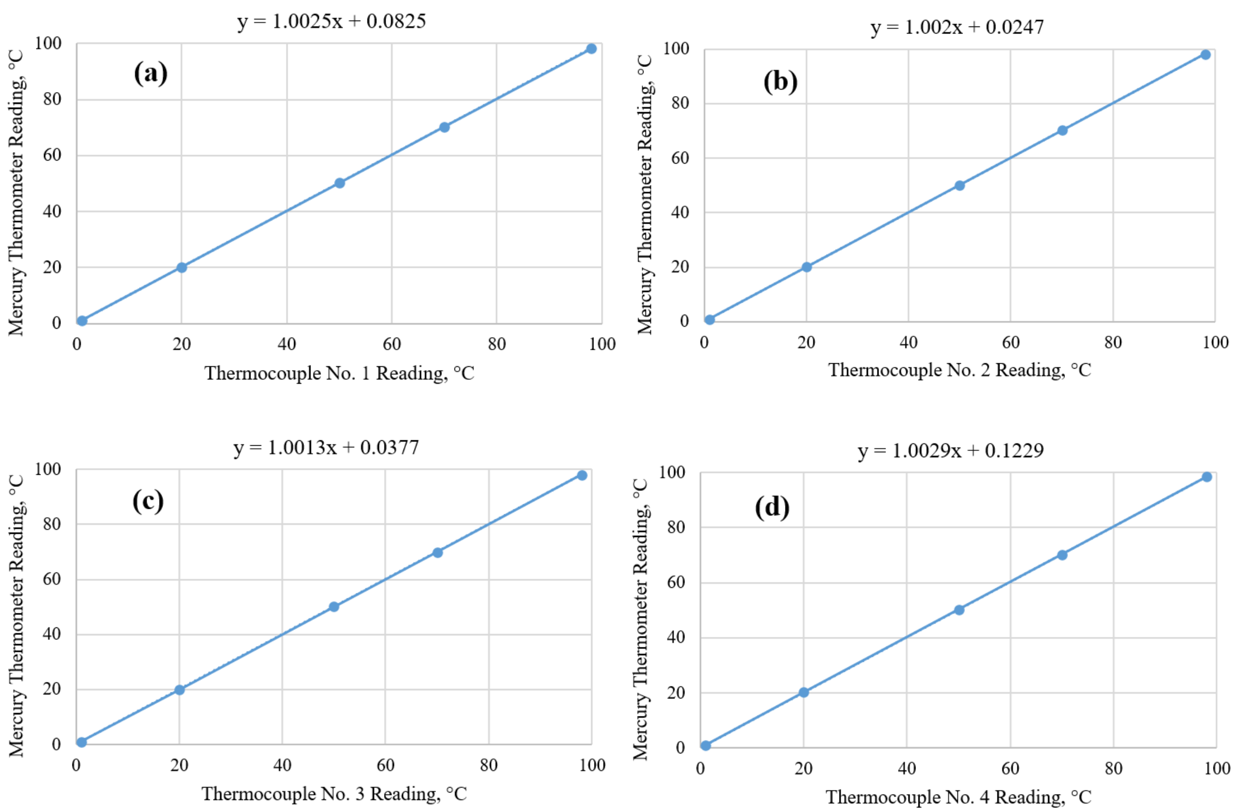

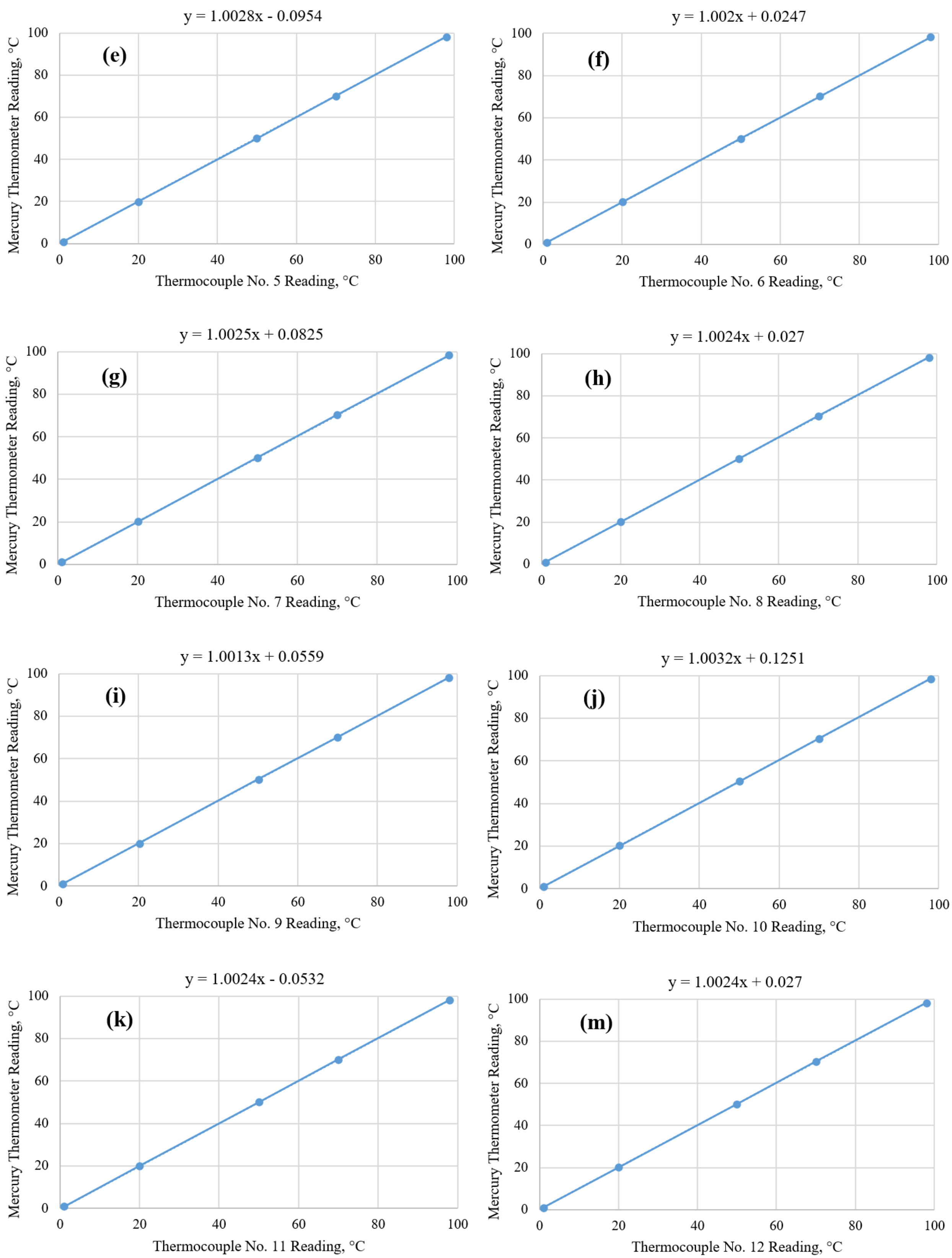

Figure (A.1) Thermocouples measured values and their uncertainties equations.

A.2 Pressure and Velocity Device Calibration

For the pressure and velocity measurement device, the calibration was based on the certificate test report from the device manufacturer, a copy of which is attached below.

TROTEC
AT WORK.

Werkskalibrierzeugnis
Calibration test report
Certificat d'étalonnage

Hiermit wird bescheinigt, dass dieses Trotec-Erzeugnis in Übereinstimmung mit dem OM-Handbuch der Trotec GmbH & Co. KG nach DIN EN ISO 9001/9002 gefertigt wurde. Die Bestellvorgaben wurden eingehalten. Die Ausführung und Anzeigegenauigkeit der Geräte/Systeme wurde im Rahmen der Trotec Kalibrier- und Qualitätssicherungs-maßnahmen überwacht. Die Überprüfung ergab keine Beanstandung.

This is to certify. that this Trotec product has been tested according to the TQM to the Trotec GmbH &Co. KG manual in accordance with DIN EN ISO 9001/9002. Ordering specifications are complied with. Execution of instruments / systems as well as testing of accuracy was carried out following TROTEC calibration and quality assurance procedures. Inspection was successfully passed.

Par ce document, nous certifions qua le produit correspondant a bien été testé suivant les normes TQM de Trotec GmbH & Co. KG en accord avec la norme DIN EN ISO 9001/9002. Les conditions stipulées dans la commande ont été remplies. La réalisation des appareils / systèmes ainsi que les tests da précision ont été fait an concordance avec les procédés de qualité et d'étalonnage Trotec.

Typ/Type/Type: **TA400**

Genauigkeit/Accuracy/Précision :
V: ±2.5 % (@ 10 m/s)
T: ±1.0 °C (@ 0 – 50 °C)
P: ±0.3 % FSO* (@ 25 °C)

Serien Nr./Serial Nr./N° de Série: 190611241

Kalibriereinheit (Referenz)/Calibration unit (Reference)/
Équipement d'étalonnage (référence):

Fabrikat/ brand/Modèle:	TIANJIN METEOROLOGICAL INSTRUMENT WORKS
Zertifikat-Nr./Certificate-No./ N° de certificat	LKK201709037/ NSC201730134
Serien Nr./Serial Nr./N° de série	05005
Genauigkeit/Accuracy/Précision:	+/-0.2m/s
Kal.-datum/Cal.-date/ Date d'étalonnage	2017-11-20
Standards/Standards/Normes:	JJG431-1986 Regulation

Umgebungsbedingungen/Environmental conditions/
Les conditions environnementales :

Temp [°C]: 25℃

Rel. Hum [%]: 55%RH

Datum/Date/Date: 2019-06-28

1 / 3

*FSO = Full Scale Output

TROTEC
AT WORK.

Messergebnisse/Measuring results/Les mesures: Velocity

Nr.	Messbereich/ Range/ plage de mesure [m/s]	Referenz/ Reference/ Référence [m/s]	Toleranz/ Tolerance/ Permissivité [m/s]	Messwert/ Reading/ Valeur mesurée [m/s]	Abweichung/ Deviation/ Écart [m/s]	Status/ Status/ Résultat
1	1 – 80.0	10	+/-0.25	10.02	+0.02	Passed

Messergebnisse/Measuring results/Les mesures: Temperature

Nr.	Messbereich/ Range/ plage de mesure [°C]	Referenz/ Reference/ Référence [°C]	Toleranz/ Tolerance/ Permissivité [°C]	Messwert/ Reading/ Valeur mesurée [°C]	Abweichung / Deviation/ Écart [°C]	Status/ Status/ Résultat
1	0 - 50.0	5	+/-1.0	4.7	-0.3	Passed
2	0 - 50.0	10	+/-1.0	9.9	-0.1	Passed
3	0 - 50.0	25	+/-1.0	25.2	+0.2	Passed
4	0 - 50.0	50	+/-1.0	49.5	-0.5	Passed

Messergebnisse/Measuring results/Les mesures: Pressure

Nr.	Messbereich/ Range/ plage de mesure [Pa]	Referenz/ Reference/ Référence [Pa]	Toleranz/ Tolerance/ Permissivité [Pa]	Messwert/ Reading/ Valeur mesurée [Pa]	Abweichung / Deviation/ Écart [Pa]	Status/ Status/ Résultat
1	1 – 5000	10	+/15	9	-1	Passed
2	1 – 5000	50	+/15	48	-2	Passed
3	1 – 5000	100	+/15	99	-1	Passed
4	1 – 5000	1000	+/15	999	-1	Passed
5	1 – 5000	2500	+/15	2498	-2	Passed
6	1 – 5000	5000	+/15	5000	+0	Passed

Kalibrierung erfolgreich bestanden. ☑
Inspection was successfully passed ☑
L'appareil a été vérifié. Aucunemesure corrective nécessaire ☑

Das Gerät liegt außerhalb der Kalibriervorgaben. ☐
Inspection failed ☐
L'appareil ne satisfait pas aux critères du test. ☐

2 / 3

TROTEC
AT WORK.

Prüfer
Checked by
Verificateur
Peng Xingen

Qualitätssicherung
Quality Control
Assurance Qualité
Li Menglong

3 / 3

KONTAKT

PERSÖNLICH HAFTENDE GESELLSCHAFTERIN

B.1 PCM Data Sheet

The data sheet below contains the PCM properties that are used in the present study.

Data sheet RUBITHERM

RT47

RUBITHERM® RT is a pure PCM, this heat storage material utilising the processes of phase change between solid and liquid (melting and congealing) to store and release large quantities of thermal energy at nearly constant temperature.
The RUBITHERM® phase change materials (PCM's) provide a very effective means for storing heat and cold, even when limited volumes and low differences in operating temperature are applicable.

Properties for RT-line:
- high thermal energy storage capacity
- heat storage and release take place at relatively constant temperatures
- no supercooling effect, chemically inert
- long life product, with stable performance through the phase change cycles
- melting temperature range between -9 °C and 100 °C available

The most important data:	Typical Values	
Melting area	41-48 main peak: 46	[°C]
Congealing area	48-41 main peak: 47	[°C]
Heat storage capacity ± 7,5%	160	[kJ/kg]*
Combination of latent and sensible heat in a temperatur range of 39°C to 54°C.	46	[Wh/kg]*
Specific heat capacity	2	[kJ/kg·K]
Density solid at 15°C	0,88	[kg/l]
Density liquid at 80°C	0,77	[kg/l]
Heat conductivity (both phases)	0,2	[W/(m·K)]
Volume expansion	12	[%]
Flash point	>180	[°C]
Max. operation temperature	65	[°C]

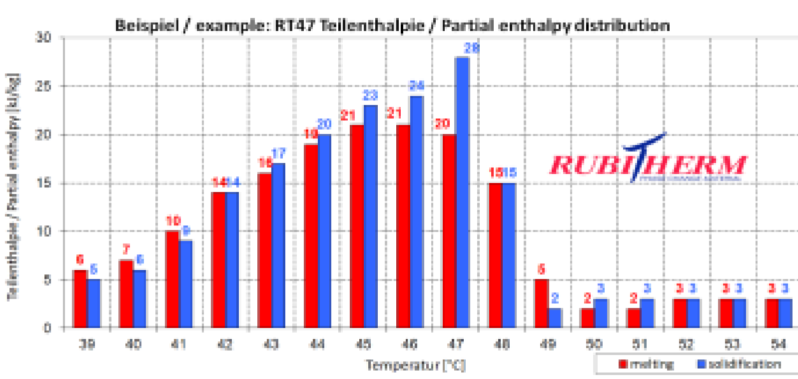

Rubitherm Technologies GmbH
Imhoffweg 6
D-12307 Berlin
phone: +49 (30) 7109622-0
E-Mail: info@rubitherm.com
Web: www.rubitherm.com

The product information given is a non-binding planning aid, subject to technical changes without notice.
Version: 09.10.2020

**Measured with 3-layer-calorimeter.*

C.1 Calculation of the Uncertainty

C.1.1 Uncertainty of ΔT_{max}

The uncertainties of the ΔT_{max} is determined as follows:

$$\Delta T_{max} = T_{max} - T_{min} \tag{C.1}$$

$$\frac{\partial \Delta T_{max}}{\partial T_{max}} = 1$$

$$\frac{\partial \Delta T_{max}}{\partial T_{min}} = -1$$

For example, the T_{max} equal 50 °C and T_{min} equal 45 °C, then ΔT_{max} equal 5 °C.

As the accuracy of the temperature data logger is equal to 0.2 %, the $w_{T_{max}}$ and $w_{T_{min}}$ determine as:

$$w_{T_{max}} = 50 \times \frac{0.2}{100} = 0.1\ \%$$

$$w_{T_{min}} = 45 \times \frac{0.2}{100} = 0.09\ \%$$

Then using equation (4.8)

$$w_{\Delta T_{max}} = \left[\left(\frac{\partial \Delta T_{max}}{\partial T_{max}}\right)^2 w_{T_{max}}^2 + \left(\frac{\partial \Delta T_{max}}{\partial T_{min}}\right)^2 w_{T_{min}}^2\right]^{1/2} \tag{4.8}$$

$$w_{\Delta T_{max}} = [(1)^2 \times 0.1^2 + (-1)^2 \times 0.09^2]^{1/2}$$

$$w_{\Delta T_{max}} = \pm 0.134\ ℃\text{, or}$$

$$w_{\Delta T_{max}} = \frac{0.134}{5} \times 100\ \% = 2.68\ \%$$

C.1.2 Uncertainty of $\dot{m}_a$

The uncertainties of the $\dot{m}_a$ is determined as follows:

$$\dot{m}_a = \rho \times u \times A_d \tag{4.3}$$

$$\dot{m}_a = 1.095 \times 1.5 \times (0.11 \times 0.07) = 0.0126 kg/s$$

$$\frac{\partial \dot{m}_a}{\partial \rho} = u \times A_d = 1.5 \times 0.0077 = 0.01155$$

$$\frac{\partial \dot{m}_a}{\partial u} = \rho \times A_d = 1.095 \times 0.0077 = 0.00843$$

$$\frac{\partial \dot{m}_a}{\partial A_d} = u \times \rho = 1.5 \times 1.095 = 1.642$$

As the accuracy of the airflow device and area measurement equal to 2.5 % and 5%, respectively, the w_u and w_{A_d} determine as:

$$w_u = 1.5 \times \frac{2.5}{100} = 0.0375$$

$$w_{A_d} = 0.0077 \times \frac{2}{100} = 0.000154$$

$$w_\rho = 1.095 \times \frac{3}{100} = 0.033$$

Then using equation (4.9)

$$w_{\dot{m}_a} = \left[\left(\frac{\partial \dot{m}_a}{\partial \rho}\right)^2 w_\rho^2 + \left(\frac{\partial \dot{m}_a}{\partial u}\right)^2 w_u^2 + \left(\frac{\partial \dot{m}_a}{\partial A_d}\right)^2 w_{A_d}^2\right]^{1/2} \tag{4.9}$$

$$w_{\dot{m}_a} = [(0.01155)^2 \times 0.033^2 + (0.00843)^2 \times 0.0375^2 + (1.642)^2 \times 0.000154^2]^{1/2}$$

$w_{\dot{m}_a} = \pm$ 0.000556 kg/s or

$$w_{\dot{m}_a} = \frac{0.000803}{0.0126} \times 100\ \% = 4.4\ \%$$

C.1.3 Uncertainty of $\dot{Q}_{gen}$

The uncertainties of the $\dot{Q}_{gen}$ is determined as follows:

$$\dot{Q}_{gen} = \frac{1}{V_b}(Q_a + Q_b) \qquad (4.1)$$

$$\dot{Q}_{gen} = \frac{1}{V_b}\left(\dot{m}_a \times c_{p,a} \times \Delta T_a + m_b \times c_{p,b} \times \frac{\Delta T_b}{\Delta t}\right)$$

$$\dot{Q}_{gen} = \frac{1}{0.0002}(0.0126 \times 1007 \times 2.7 + 12 \times 0.046 \times 830 \times 0.028) = 234{,}600 \text{ W/m}^3$$

$$\frac{\partial \dot{Q}_{gen}}{\partial \dot{m}_a} = \frac{1}{V_b}\left(c_{p,a} \times \Delta T_a\right) = \frac{1}{0.0002}(1007 \times 2.7) = 13{,}594{,}000$$

$$\frac{\partial \dot{Q}_{gen}}{\partial c_{p,a}} = \frac{1}{V_b}(\dot{m}_a \times \Delta T_a) = \frac{1}{0.0002}(0.0126 \times 2.7) = 170$$

$$\frac{\partial \dot{Q}_{gen}}{\partial \Delta T_a} = \frac{1}{V_b}\left(\dot{m}_a \times c_{p,a}\right) = \frac{1}{0.0002}(0.0126 \times 1007) = 63{,}441$$

$$\frac{\partial \dot{Q}_{gen}}{\partial m_b} = \frac{1}{V_b}\left(c_{p,b} \times \frac{\Delta T_b}{\Delta t}\right) = \frac{1}{0.0002}(830 \times 0.028) = 116{,}200$$

$$\frac{\partial \dot{Q}_{gen}}{\partial c_{p,b}} = \frac{1}{V_b}\left(m_b \times \frac{\Delta T_b}{\Delta t}\right) = \frac{1}{0.0002}(12 \times 0.046 \times 0.028) = 77$$

$$\frac{\partial \dot{Q}_{gen}}{\partial \frac{\Delta T_b}{\Delta t}} = \frac{1}{V_b}\left(m_b \times c_{p,b}\right) = \frac{1}{0.0002}(12 \times 0.046 \times 830) = 2{,}290{,}800$$

As the accuracy of the measurement parameters are determine as,

$w_{\dot{m}_a} = 0.000556$ kg/s

$w_{c_{p,a}} = 1 \frac{J}{kg\ ℃}$

$w_{\Delta T_a} = 0.134$ ℃

$$w_{m_b} = 0.001\ kg$$

$$w_{c_{p,b}} = 20\ \frac{J}{kg\ ℃}$$

$$w_{\frac{\Delta T_b}{\Delta t}} = 0.028 \times \frac{0.2}{100} = 0.000056\ ℃$$

Then using equation (4.10)

$$w_{\dot{Q}_{gen}} = [(13{,}594{,}000)^2 \times 0.000556^2 + (170)^2 \times 1 + (63{,}441)^2 \times 0.134^2 + (116{,}200)^2 \times 0.001^2 + (77)^2 \times 20^2 + (2{,}290{,}800)^2 \times 0.000056^2]^{1/2}$$

$$w_{\dot{Q}_{gen}} = \pm\ 11{,}481\ \mathrm{W/m^3}\ \text{or}$$

$$w_{\dot{Q}_{gen}} = \frac{11{,}481}{234{,}600\ \mathrm{W/m^3}} \times 100\ \% = 4.9\ \%$$

Journal of Energy Storage 84 (2024) 110963

Contents lists available at ScienceDirect

Journal of Energy Storage

journal homepage: www.elsevier.com/locate/est

Research papers

Experimental comparison of the Li-ion battery thermal management systems using a new hybrid model of flat heat pipe coupled with phase change materials

Hareth Maher Abd [a,b,*], Abdual Hadi N. Khalifa [b], Ahmed J. Hamad [b]

[a] *Engineering Technical College of Mosul, Northern Technical University, Iraq*
[b] *Engineering Technical College/Bagdad, Middle Technical University, Iraq*

ARTICLE INFO

Keywords:
Heat pipe
Lithium-ion batteries
Phase change materials
Battery thermal management systems

ABSTRACT

The usage of an effective battery thermal management system (BTMS) to achieve optimal lithium-ion battery operation and prevent thermal runaway is essential. The usage of heat pipes (HPs) is considered one of the most effective techniques to cool batteries due to its high thermal conductivity. In this study, a BTMS equipped with a new model of flat HP coupled with phase change material (PCM) is experimentally investigated. The new flat HP consists of a double circular grooved evaporator and a finned condenser. The thermal performance of the new model is compared with the pure PCM model, air cooling model, and the same HP without the PCM combination. Different BTMS models are examined using various discharge rates (1C, 2C, and 3C) and air velocities, at 35 °C ambient temperature. The results indicated that the new model displays a good cooling performance, especially at high discharge rates and it can provide better protection for the batteries. Where the new model can reduce maximum operating temperature (T_{max}) at 3C by 20.1 % and 21.1 % than the Air-Model and pure PCM-Model, respectively. Furthermore, the largest value of T_{max} and maximum temperature difference using the new model did not exceed 48.1 °C and 1.8 °C, respectively. Additionally, we found the adding of the PCM to the new HP model can reduce the T_{max} by 4 °C at 3C.

1. Introduction

The increased use of internal combustion engines has resulted in severe issues of energy scarcity and climate pollution, where the quantity of energy produced from fossil fuels contributes to around 80 % of the energy produced [1]. That incentivizes many countries to develop more efficient and sustainable energy technologies, which have become one of the most pressing needs of our time. Recently, with the invention of lithium-ion (Li-ion) batteries, electric vehicles (EVs) have emerged as potential solutions to these issues, as well as new ways to store electrical energy from alternative energy sources and then reduce fossil fuel consumption [2]. Li-ion batteries have gained popularity due to their unique characteristics, which include a long life cycle, high voltage capability, rapid charging/discharge rate, and high energy density of up to 180 Wh/kg when compared to other batteries of the same size and weight [3,4]. In contrast, when the Li-ion battery is used, it produces a significant heat rate owing to the electrochemical reactions which cause an increase in the battery's temperature that affects the battery's longevity and vehicle safety [5]. However, to avoid battery thermal runaway and ensure the safety of operation, they must be kept below 60 °C [6]. Other studies [7,8] demonstrate that the best operation temperature range is between (20–50 °C). Another study shows the battery capacity at 50 °C was marginally higher than 25 °C due to the reduction in the internal resistance of the lithium-ion battery [9]. Furthermore, the maximum temperature difference (ΔT_{max}) of battery packs must be limited below 5 °C to avoid the occurrence of aging variance and individual deformation, which reduces battery lifetime [10,11].

As a result, the battery thermal management system (BTMS) is critical for a reliable and safe operation of electric cars to create a proper and controllable operating temperature of the batteries [12]. According to the cooling mediums, currently, there are five types of cooling systems; air cooling system, liquid cooling system, phase change material (PCM) cooling system, heat pipe (HP) cooling system, and combined cooling system.

In the air-cooling system, forced air convection is used to take away the heat generated from the battery. It is commonly used in commercial

* Corresponding author at: Engineering Technical College of Mosul, Northern Technical University, Iraq.
E-mail address: harethmaher2018@ntu.edu.iq (H.M. Abd).

https://doi.org/10.1016/j.est.2024.110963
Received 10 September 2023; Received in revised form 25 November 2023; Accepted 12 February 2024

Received: 23 December 2023 | Revised: 29 February 2024 | Accepted: 4 April 2024

DOI: 10.1002/est2.625

RESEARCH ARTICLE

ENERGY STORAGE WILEY

Hybrid battery thermal management system of phase change materials integrated with aluminum fins and forced air

Hareth Maher Abd[1,2] | Ahmed J. Hamad[2] | Abdual Hadi N. Khalifa[2]

[1]Engineering Technical College of Mosul, Northern Technical University, Mosul, Iraq

[2]Engineering Technical College of Bagdad, Middle Technical University, Iraq

Correspondence
Hareth Maher Abd, Engineering Technical College of Mosul, Northern Technical University, Mosul, Iraq.
Email: harethmaher2018@ntu.edu.iq

Abstract

Due to its high self-heat rate, most researchers have avoided using lithium cobalt oxide ($LiCoO_2$) in their work, although, major car companies use it to power some car models because of its high-power density. A thermal management system benefits from phase change material (PCM) and serves as a reliable cooling system to ensure the safety, performance, and lifespan of Li-ion batteries. In this study, we conducted an experimental investigation of a new hybrid battery thermal management system (BTMS) using PCM combined with aluminum fins and forced air to enhance the cooling performance of Li-ion battery type 18 650 $LiCoO_2$. Furthermore, the hybrid model's thermal behaviors are compared with other models that use only air or PCM for cooling. The cooling performance of different BTMS models was tested under a high temperature of 40°C and various discharge rates, as well as, various air velocities. The results demonstrate that the hybrid model effectively minimizes the battery heat accumulation and can reduce the maximum operating temperature by 1.5°C, 5.5°C, and 9.5°C compared to the air-cooling model and by 2.8°C, 5.1°C, and 16.1°C compared to the PCM model for discharge of 1C, 2C, and 3C rates, respectively. Furthermore, the maximum temperature difference within the battery pack did not surpass 3.1°C with our hybrid model. Moreover, the use of our model has a significant advantage in minimizing the air-cooling power consumption by 89%.

KEYWORDS

BTMS, $LiCoO_2$, Li-ion batteries, phase change materials

1 | INTRODUCTION

The increasing demand for the internal combustion engine led to significant problems in the form of pollution and energy shortages, where almost 80% of the energy generation comes from fossil sources.[1] This motivated many researchers to find more sustainable, efficient energy technologies, which have become one of the urgent necessities in the present time.[2] In recent years, with the development of lithium-ion batteries, alternative methods have emerged to alleviate these issues and to discover new ways of storing more energy from renewable sources, thereby reducing reliance on fossil fuels.[3] Among all types of batteries, Li-ion batteries became the most attractive battery type due to their unique features, comprising the high energy density, quick charge/discharge rate, extended life cycle, and high voltage capabilities compared with other batteries of similar size and

The 6th Scientific Conference for Postgraduate Engineering Research (SCPER2024)

Baghdad, Iraq, 25-26 December 2024

Letter of Acceptance and Invitation

Date: October 22, 2024

Paper ID: 111

Paper Title:

Numerical Study on the Lithium-ion Battery Cooling System Using Forced Air and Phase Change Material Coupled with Aluminum Fins

Dear Hareth Maher Abd, Abdual Hadi N. Khalifa, Ahmed J. Hamad

With the heartiest congratulations, I am pleased to inform you that based on the recommendations of the reviewers, your paper identified above has been accepted for publication and oral presentation by *the 6th Scientific Conference for Postgraduate Engineering Research (SCPER 2024)*. Your paper will be published in the *AIP Conference Proceedings*.

Herewith, the Conference Organizing Committee sincerely invites you to present your paper at the conference to be held at the Middle Technical University / Engineering Technical College, Baghdad, Iraq, 25-26 December 2024.

We look forward to your participation in the SCPER 2024.

Yours sincerely,

Prof. Dr. Nabil Jamil Yasin

SCPER 2024 Organizing Committee, Baghdad, Iraq.

https://scper24.tecb.mtu.edu.iq/

الخلاصة

إن شحن وتفريغ بطاريات الليثيوم أيون يؤدي الى انبعاث طاقة حرارية. تزداد مقدار هذه الطاقة مع ازدياد معدلات الشحن والتفريغ للبطارية. تمثل هذه الطاقة المنبعثة عائق رئيسيا لاستخدام بطاريات الليثيوم أيون. لذلك، فإن استخدام نظام الإدارة الحرارية للبطارية يعد امرا ضروري للغاية لضمان التشغيل الأمثل لها. يمكن للانظمة الحرارية الهجينة التي تتكون من نظام تبريد نشط وسلبي أن توفر المزيد من السيطرة على درجة حرارة خلايا البطاريات مقارنة بالاستخدام المنفرد لانظمة التبريد.

في هذه الدراسة، تم اجراء دراسة تجريبية وعددية لنموذجين هجينين جديدين للسيطرة على درجة حرارة البطاريات يعتمدان على استخدام مادة متغيرة الطور كنظام تبريد سلبي مقترن بنظام تبريد نشط أخر. يستخدم النموذج الأول والمسمى (PCM/Fin-Air-Model) مادة متغيرة الطور مع الهواء القسري لطرد الحرارة الزائدة خارج المنظومة مع اضافة زعانف من الألومنيوم الى المادة متغيرة الطور لزيادة الموصلية الحرارية لها. بينما يستخدم النموذج الثاني تصميما جديدًا من أنابيب الحرارة المسطحة التي تحتوي على مكثف مزعنف ومبخر ذو أخدودين دائريين على جانبيه بالإضافة إلى استخدام مادة متغيرة الطور في قسم المبخر ويطلق على هذا النموذج (HP/PCM-Model). تم اختيار المادة متغيرة الطور نوع-Rubitherm RT47 ذو درجة انصهار معتدلة تتراوح مابين 41-48 درجة مئوية. تم تصميم النماذج الهجينة لتبريد حزمة من البطاريات مكون من 12 بطارية أسطوانية من نوع $LiCoO_2$-18650 مرتبة في ثلاثة صفوف يحوي كل صف على اربعة بطاريات. تمت مقارنة الأداء الحراري للنماذج الجديدة مع نماذج تقليدية أخرى وهي: نموذج يستخدم مادة متغيرة الطور فقط ويسمى (PCM-Model)، ونموذج يستخدم الهواء القسري فقط ويسمى (Air-Model)، ونفس النموذج (HP/PCM-Model) ولكن بدون استخدام مادة متغيرة الطور والمسمى (HP-Model) . تم اختبار جميع النماذج باستخدام معدلات تفريغ مختلفة (1، 2، 3) قدرة تفريغ، وسرعات هواء مختلفة (0.75، 1.5، 2.25، 3) متر/ثانية ودرجات حرارة تشغيل مختلفة ايضا (25، 30، 35، 40) درجة مئوية.

تم اجراء المحاكاة العددية باستخدام نماذج ثلاثية الأبعاد مبنية باستخدام برنامج COMSOL Multiphysics 5.6وتم التحقق من صحتها بالمقارنة مع النتائج التجريبية.

أشارت النتائج التجريبية إلى أن النماذج الهجينة الجديدة تُظهر أداء تبريد جيدًا، وخاصةً عند معدل تفريغ مرتفع مقارنة بالنماذج التقليدية التي أصبحت غير كافية لتبريد البطارية عند التفريغ العالي. يقلل PCM/HP-Model من الحد الأقصى لدرجة حرارة التشغيل عند التفريغ بمقدار 3C بنسبة 19.8% مقارنة

بنموذج Air-Model ونسبة 26.6% مقارنة بنموذج PCM-Model ونسبة 9.8% مقارنة بنموذج HP-Model. بينما يقلل PCM/Fin-Air-Model من الحد الأقصى لدرجة حرارة التشغيل بنسبة 15.2%مقارنة بنموذج Air-Model ونسبة 23.3% مقارنة بنموذج PCM-Model ونسبة 4.6% مقارنة بنموذج HP-Model .علاوة على ذلك، لم يتجاوز الفرق في درجة الحرارة بين خلايا البطاريات في PCM/HP-Model و PCM/Fin-Air-Model القيم 1.9 و4.2 درجة مئوية على التوالي. بالإضافة إلى ذلك، يتمتع نموذجHP/PCM-Model بأقل فرق بالضغط بين الهواء الداخل والخارج (ΔP) واستهلاك للطاقة مقارنة بالنماذج الأخرى.

اثبتت النتائج العددية أن زيادة سرعة الهواء لها تأثير طفيف على تبريد البطارية باستخدام النماذج الهجينة الجديدة بينما لها تأثير كبير على تبريد البطارية باستخدام Air-Model، حيث تنخفض T_{max} درجة الحرارة العظمى للبطارية بنسبة 5.3% و12.8 و30 مع زيادة سرعة الهواء من 0.75 إلى 3 متر/ثانية في PCM/HP-Model ونموذج PCM/Fin-Air-Model ونموذج Air-Model على التوالي. يؤدي زيادة سرعة الهواء من 0.75 إلى 3 متر/ثانية إلى تقليل نسبة طور السائل للمادة متغيرة الطور من 0.877 إلى 0.772 ومن 1.0 إلى 0.748 في نهاية فترة 3C في PCM/HP-Model و PCM/Fin-Air-Model على التوالي. لا يُنصح باستخدام PCM-Model لمعدل 3C حتى عند درجة حرارة تشغيل منخفضة تبلغ 25 درجة مئوية. كما أظهرت النتائج أن HP/PCM-Model يُظهر أداءً حراريًا أفضل واستهلاكًا أقل للطاقة، وخاصة عند معدل تفريغ مرتفع 3 قدرة تفريغ، كما أنه يمكن أن يوفر درجة حرارة عمل آمنة لبطاريات الايثيوم. تظهر النتائج العددية اتفاقًا جيدًا مع البيانات التجريبية، مع انحرافات قصوى قدرها 3.8، 6، 2.3، 2، و2.4٪ لنموذج الهواء، PCM-Model، PCM/Fin-Air- Model، HP-Model، HP/PCM- Model ، على التوالي.

جمهورية العراق

وزارة التعليم العالي والبحث العلمي

الجامعة التقنية الوسطى

الكلية التقنية الهندسية– بغداد

تقييم نماذج نظام التبريد الهجين لحزمة بطاريات المركبة الكهربائية في ظل ظروف المناطق الحارة

رسالة مقدمة

إلى مجلس الكلية التقنية الهندسية- بغداد وهي جزء من

متطلبات نيل شهادة دكتوراه فلسفة في اختصاص

هندسة الحراريات

من قبل الطالب

حارث ماهر عبد

بكالوريوس هندسة تقنيات والتبريد 2004

ماجستير هندسة تكييف وتثليج 2012

أشراف

د. احمد جاسم حمد

أستاذ

د. عبدالهادي نعمة خليفة

أستاذ

2024 كانون الاول

1446 جماد الاخرة